SURFACES, INTERFACES AND COATINGS TECHNOLOGY

EDITED BY
ALESSIO BOSIO

Surfaces, Interfaces and Coatings Technology

The book Surfaces, Interfaces, and Coatings Technology is a compilation of recent research advances covering fundamental aspects of chemistry and physics occurring at surfaces and interfaces.

Editor: Alessio Bosio

ISBN: 978-81-953047-3-8

Year Published 2024

Publisher: Vide Leaf

Electronic version of the book can be accessed online at www.videleaf.com

Table of Contents

Book Chapter

Regenerable Antibacterial Cotton Fabric by Plasma Treatment with Dimethylhydantoin: Antibacterial Activity against *S. aureus*

Chang-E Zhou[1,2], Chi-wai Kan[3]*, Jukka Pekka Matinlinna[4] and James Kit-hon Tsoi[4]

[1]College of Textile Science and Engineering, Jiangnan University, China
[2]Jiangsu Lianfa Textile Co., Ltd., China
[3]Institute of Textiles and Clothing, The Hong Kong Polytechnic University, China
[4]Dental Materials Science, Faculty of Dentistry, The University of Hong Kong, China

***Corresponding Author:** Chi-wai Kan, Institute of Textiles and Clothing, The Hong Kong Polytechnic University, China

Published **February 24, 2020**

This Book Chapter is a republication of an article published by Chi-wai Kan, et al. at Coatings in January 2017. (Zhou, C.-E.; Kan, C.-W.; Matinlinna, J.P.; Tsoi, J.K.-H. Regenerable Antibacterial Cotton Fabric by Plasma Treatment with Dimethylhydantoin: Antibacterial Activity against S. aureus. Coatings 2017, 7, 11.)

How to cite this book chapter: Chang-E Zhou, Chi-wai Kan, Jukka Pekka Matinlinna, James Kit-hon Tsoi. Regenerable Antibacterial Cotton Fabric by Plasma Treatment with Dimethylhydantoin: Antibacterial Activity against *S. aureus*. In: Surfaces, Interfaces and Coatings Technology. Hyderabad, India: Vide Leaf. 2020.

Acknowledgments: This work is financially supported by the Research Grants Council of The Hong Kong Special Administrative Region, China (Project No. PolyU 5173/11E), The Hong Kong Polytechnic University, the Natural Science Foundation of China (51703084), China Postdoctoral Science Foundation (Project No. 2019M661725), Postdoctoral Scientific Research Projects of Jiangsu Province (Project No. 2019K011),Youth Foundation of Jiangnan University (1062050205190950) and 2018 Jiangsu Province “dual creative Doctor” Foundation (Project No. 1066010241180650).

Author Contributions: Chi-wai Kan proposed the project. Chang-E. Zhou wrote the main manuscript text. Chang-E. Zhou and Chi-wai Kan performed the experiments and analyzed the results. Jukka Pekka Matinlinna and James Kit-hon Tsoi advised the technical content and revised the language of the manuscript. All authors reviewed the manuscript.

Conflicts of Interest: The authors declare no conflict of interest.

Abstract

This study examined the influence of variables in a finishing process for making cotton fabric with regenerable antibacterial properties against Staphylococcus aureus (S. aureus). 5,5-dimethylhydantoin (DMH) was coated onto cotton fabric by a pad-dry-plasma-cure method. Sodium hypochlorite was used for chlorinating the DMH coated fabric in order to introduce antibacterial properties. An orthogonal array testing strategy (OATS) was used in the finishing process for finding the optimum treatment conditions. After finishing, UV-Visible spectroscopy, Scanning Electron Microscopy (SEM), and Fourier Transform Infrared Spectroscopy (FTIR) were employed to characterise the properties of the treated cotton fabric,

including the concentration of chlorine, morphological properties, and functional groups. The results show that cotton fabric coated with DMH followed by plasma treatment and chlorination can inhibit S. aureus and that the antibacterial property is regenerable.

Keywords

Plasma; Regenerable; Antibacterial; Cotton; DMH

Introduction

Antibacterial finishing is of enormous importance in the textile industry because fibres are susceptible to microorganisms, including bacteria and fungi, which are nourished by sweat, sebum, and food stains, as well as the fibres themselves [1-4]. These microorganisms can cause odor, staining, deterioration of textiles, and infection, allergies, and diseases. Cotton is a natural cellulosic fibre which has the ability to absorb and retain moisture and promote the growth of microorganisms [5,6]. Therefore, antibacterial finishing for cotton fabric is imperative. To achieve safety and health properties, antibacterial cotton fabric is grafted or coated with bactericides (e.g., chitosan, quaternary ammonium salts, chlorine and chloramines, etc.) [7-11], or loaded with heavy metal ions (silver, copper, zinc) [12-15]. However, it is found that the uptake and durability of these compounds are difficult to manage because they leach from the textiles easily [7]. These chemicals are always loaded onto cotton fabrics with the help of other chemicals, such as cross-linking agents, initiators, and catalysts, but the incompatibility of antibacterial agents with other chemicals and the toxicity of these antibacterial agents to humans and aquatic animals are also important weaknesses that need to be addressed [7]. In order to reduce chemical consumption, protect the environment, and improve the quality of textiles, researchers have worked hard to find innovative solutions. Plasma treatment is one of the methods used to improve textile manufacturing processes. Plasma technology has already been used by the textile industry for surface modification and for imparting permeability and biocompatibility [16-19]. Plasma is a medium composed of ions,

free electrons, photons, neutral atoms, and molecules in ground and excited states [20]. These particles, generated from the dissociation of inert gases under electrical energy, gain their own energy from an imposed electric field and lose this energy when they collide with the material surface. During the surface collision, chemical bonds in the material surface are ruptured and free radical groups are created on the material surface. These particles are chemically active and can introduce new functional groups on the surface of the material which can be used as precursors for polymerisation; a reaction between the substrate and the monomer [20]. Plasma treatment applied in textile processes replaces application of some chemicals, thereby reducing the amount of chemicals used during production. This reduces the environmental effects of textile production. The main advantage of plasma treatment is that it just changes the surface properties without affecting the bulk properties of substrates [21,22].

Finishing of cotton fabric with chloramine (pad-dry-cure) with the aid of plasma treatment is proposed because of environmental concerns. The chloramine is changed from 5,5-dimethylhydantoin (DMH), a chemical with an amide structure, to an N-halamine structure by chlorination. The chlorine in chloramine can be regenerated through chlorination after consumption by bacteria (Figure 1). This finishing method makes antibacterial textiles regenerable. In the reaction, chlorine in the N-halamine structure is not stable due to the inductive effect of the carbonyl (C=O) [23]. It can attach to bacteria easily to change the osmotic pressure of the bacteria and kill it. At that time, the chlorine in N-halamine is substituted with a hydrogen ion. However, the chlorine in N-halamine can be obtained again by chlorination of sodium hypochlorite. Therefore, this finishing process improves the lifespan of the antibacterial properties of cotton fabric. In addition, the chemical structure of DMH is simple and the reagent itself is inexpensive and easily available. In our preliminary study [24], we found that plasma treatment can improve the pad-dry-cure process for introducing DMH to cotton fabric to achieve good antibacterial effects. The plasma process can be carried out at different stages of the pad-dry-cure process, i.e., plasma-pad-dry-cure (CPD); pad-plasma-dry-cure

(CWPD), and pad-dry-plasma-cure (CDPD) [24], in order to make cotton fabric with antibacterial properties [24]. Experimental results reveal that CDPD treatment can provide the best antibacterial effect against S. aureus compared with CPD, CWPD, and even the "pad-dry-cure" process without plasma treatment (CD). Further studies were conducted in order to optimize the treatment conditions for CD [25], CPD [26], and CWPD [27] but the optimum condition for the CDPD process has not been reported yet. Therefore, the optimum condition for the CDPD process is investigated in this study.

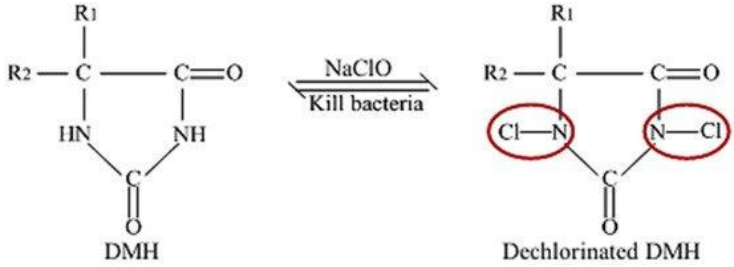

Figure 1: Reversible redox reaction of DMH (red circles show the N-halamine structure) [25].

Experimental Methods

Fabric and Chemicals

100% woven cotton fabric, completely desized, scoured, and bleached, was used in this study (fabric weight = 260 g/m^2; 54 threads/cm in warp and 25 threads/cm in weft). Non-ionic detergent, Diadavin EWN-T 200% (Tanatex, Leverkusen, Germany) (2%), was used for cleaning the fabric at pH 7 at 50 °C for 30 min. After cleaning, the fabric was rinsed with deionised water to remove detergent, oil, and impurities and dried at 80 °C for 20 min [23-27]. The cleaned fabric was then conditioned at 65% ± 2% relative humidity and 20 ± 2 °C for at least 24 h prior to further use. 5,5-Dimethyl hydantoin (DMH) (97%), sodium hypochlorite (5% active chlorine content), potassium iodide, glacial acetic acid (>99.8%), and starch indicator (1% in H_2O) were purchased from Sigma-Aldrich.

Plasma Treatment

Atmospheric pressure plasma (APP) treatment was conducted after drying during the conventional pad-dry-cure process. Plasma generator Atomflo-200 (Surfx Technology, Redondo Beach, CA, USA) was used for APP treatment of the cotton fabric. The plasma discharge was ignited by low radio frequency at 13.56 MHz. In the APP treatment system, the plasma jet was placed vertically above the fabric (Figure 2) [23-27]. As described in detail previously [23-27], helium (flow rate = 9.6 L/min) and nitrogen (flow rate = 0.15 L/min) were used as the carrier gas and reactive gas, respectively. The APP discharge power was 80 W, the jet distance was 5 mm, and the movement speed of the fabric was 0.2 m/s.

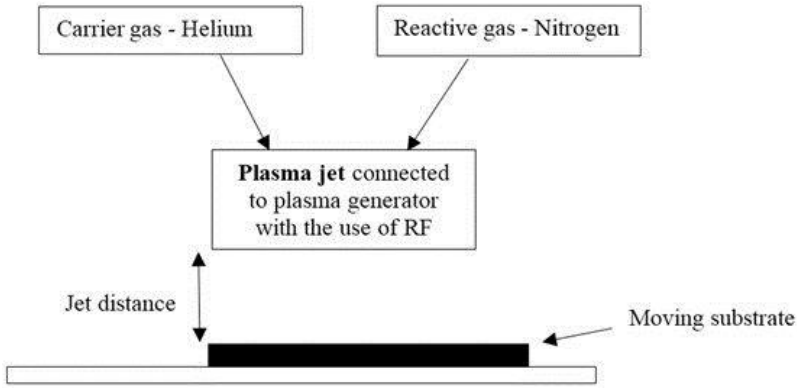

Figure 2: Schematic diagram of the Atmospheric pressure plasma (APP) treatment.

Optimizing the Treatment Condition for Coating DMH on Cotton Fabric

For the coating of DMH, cotton fabric was first padded with DMH (with concentrations of 2%, 4%, or 6%) until a wet pick up of 80% was achieved. The DMH padded cotton fabric was then dried at 80 °C for 5 min, similar to previous studies [24-27]. The dried fabric was then treated with plasma and cured at 120 °C, 140 °C, or 160 °C for 5 min (i.e., pad-dry-plasma-cure). The fabric samples treated with the same coating process were

subsequently chlorinated at room temperature with sodium hypochlorite solution with different active chlorine contents of 0.8%, 1.0%, or 1.2%, in order to transform some of the amino groups on the pad-dry-plasma-cure treated cotton fabric into N-halamines [24-27]. After chlorination with sodium hypochlorite, these fabrics were rinsed thoroughly with deionised water in order to ensure that no free chlorine remained in the chlorinated fabric. To test the free chlorine, the water after rinsing the chlorinated fabric was tested with KI/starch solution. If no blue color was observed in the rinsing water, this indicated that no free chlorine remained in the fabric [24-27]. After the chlorination process, the cotton fabrics were conditioned at 65% ± 2% relative humidity and 20 ± 2 °C for at least 24 h prior to use [26,27].

Orthogonal array testing strategy (OATS) analysis was used for determining the optimum treatment conditions [25-29]. Four variables which have been used previously [25-27] were adopted, i.e., the concentration of DMH, curing temperature, concentration of the bleaching solution, and the duration of chlorination and their respective effects on antibacterial properties were investigated. Table 1 summarises the variables and levels used in the OATS analysis and Table 2 shows the experimental arrangements (nine test runs were conducted).

Table 1: Variables and levels used in OATS [25-27].

Level	**Variables**			
	Concentration of DMH (%)	**Curing Temperature (°C)**	**Concentration of Bleaching Solution (%)**	**Time of Chlorination (min)**
	A	**B**	**C**	**D**
I	2	120	0.8	20
II	4	140	1.0	40
III	6	160	1.2	60

Table 2: Arrangement of experiment [25-27].

Test Run	Variables			
	Concentration of DMH (%)	Curing Temperature (°C)	Concentration of Bleaching Solution (%)	Time of Chlorination (min)
	A	B	C	D
1	I	I	I	I
2	I	II	II	II
3	I	III	III	III
4	II	I	II	III
5	II	II	III	I
6	II	III	I	II
7	III	I	II	II
8	III	II	I	III
9	III	III	II	I

Antibacterial Property

Antibacterial activity of the samples was tested referring to the AATCC Test Method 147-2011. S. aureus (ATCC 6538, purchased from Tin Hang Technology Ltd in Hong Kong) was used as the model bacteria [4,30-32]. The bacteria were inoculated in a blood agar plate purchased from Tin Hang Technology Ltd in Hong Kong and incubated at 37 °C for 24 h. A bacterial suspension was prepared in Brain-Heart Infusion (BHI) (Oxoid, purchased from Thermo Fisher Scientific HK Ltd., Hong Kong, China) broth by harvesting the cells from the blood agar plate and its optical density was measured with a UV-Vis spectrophotometer (DU 730, Beckman Coulter HK Ltd., Hong Kong, China) (wavelength at 660 nm) to 0.5 McFarland standard. Then, the suspension was diluted 100-fold. After that, the diluted suspension was inoculated on new sterile blood agar plates using the Autoplate 4000 microprocessor-controlled Spiral Platter (Advanced Instruments, Inc., Norwood, MA, USA), and untreated and freshly prepared treated samples (20 mm × 20 mm) were placed on the seeded agar surfaces. After standing for 5–10 min, these plates were placed in the aerobic incubator and incubated at 37 °C for 48 h. Finally, clear zones were observed to evaluate the antibacterial activity of the samples. The antimicrobial activity of each sample was tested three times, and the mean value of the width of three clear zones was used to evaluate the antimicrobial activity of the fabric.

Active Chlorine Content of Chlorinated DMH Coated in Cotton Fabric

A colorimetric method was used for evaluating the active chlorine content of chlorinated DMH coated on cotton fabric, as described previously [24-27]. The available active chlorine content of the fabric was determined based on the absorbance measured by the Lambda 18 UV-Visible spectrophotometer (Perkin Elmer, Waltham, MA, USA) at wavelength (λ_{max} = 427.60 nm). A calibration curve was prepared by measuring the absorbance of three standard sodium hypochlorite solutions. In the calibration curve, absorbance is plotted against concentration (the best fit equation of the calibration curve is $y = 30.401x - 50.84$; $R^2 = 0.9918$). Based on the calibration curve, the concentration of active chlorine of the DMH coated fabric samples can be obtained [24-27].

Regenerability

The regenerability of chlorine in the cotton fabric was tested by washing using the AATCC Test Method 61-1A [25-27]. The antibacterial activity of samples before washing, after washing (termed as AW), and after re-chlorination was tested (termed as AW + CH). The conditions for re-chlorination were the same as the first chlorination process.

Chemical Composition of DMH Coated Fabric

Fourier transform infrared spectroscopy was used for evaluating the chemical properties of DMH coated fabrics. A Spectrum 100 with attenuated total reflection mode was used for obtaining the FTIR spectra. The spectra were obtained using 16 scans between 650 and 4000 cm^{-1} with a resolution of 4 cm^{-1}. For obtaining better spectra with low noise, the second derivative of the spectra was obtained, for further analysis of the chemical composition of DMH coated fabric [25-27].

Scanning Electron Microscopy (SEM)

Surface morphology of the cotton fabric was evaluated by SEM (JEOL Model JSM-6490, JEOL USA, Inc., Peabody, MA, USA) with imaging up to 300,000× with a high resolution of 3 nm. Samples (5 mm × 5 mm) were pasted on a metal round table with conducting resin. They were then placed in the vacuum pump of the SEM. The surface images of fabrics were obtained by the SEM operated at an accelerating voltage of 20 kV and magnification of the image was set at 4000× to 5000×.

Tearing Strength

Tearing strength of untreated fabrics, fabrics coated with DMH (CD), and fabric coated with DMH with plasma treatment (CDPD) was measured in accordance with the American Society for Testing and Materials (ASTM) D1424-09 "Standard Test Method for Tearing Strength of Fabrics by Falling-Pendulum Type (Elmendorf) Apparatus" with an Elmatear Digital Tear Tester (James H. Heal & Co. Ltd., Halifax, UK). Three samples per fabric type for both the warp (for tearing across the weft) and the weft (for tearing across the warp) direction were tested. The dimensions of the samples were about (75 ± 2) mm × (100 ± 2) mm based on the template in accordance with the requirements in ASTM D 1424-09 [33]. The results of the tearing strength were represented in newton (N).

Results

Optimised Treatment Condition for Antibacterial Finishing

In this study, the mean value of the width of four clear zones in a fabric (Figure 3) is used to evaluate the antibacterial activity of the fabric against S. aureus and is termed mean clear width. A wider clear width indicates the antibacterial activity is more pronounced. The mean clear width of the bacteria against S. aureus was obtained from the nine specimens generated by the OATS technique and the result of orthogonal analysis, where T_{mn} refers to the sum of the evaluation indexes of all levels (n, n = I, II, III) in each factor (m, m = A, B, C), such that TAI = 1.156 +

1.090 + 1.611 = 3.857 is the sum of level I of factor A; TCII = 1.090 + 1.062 + 1.258 = 3.410 is the sum of level II of factor C; and K_{mn} implies the mean value of T_{mn}, such that KAI = TAI/3 = 3.857/3 = 1.286 is the mean value of TAI; KCII = TCII/3 = 3.410/3 = 1.137 is the mean value of TCII, and all are shown in Table 3. In addition, T is the sum of the evaluation indexes, w_i, which is an evaluating indicator for antimicrobial activity of cotton fabrics evaluated by the AATCC Test Method 147-2011; and the range of factors in each column, $R = Max(K_j) - Min(K_j)$, indicates the function of the corresponding factor [34]. The larger value of R corresponds to a greater impact of the level of the factor on the experimental index. Therefore, the impact of every factor on the final treatment effect can be distinguished clearly on the comprehensive condition that every factor changes.

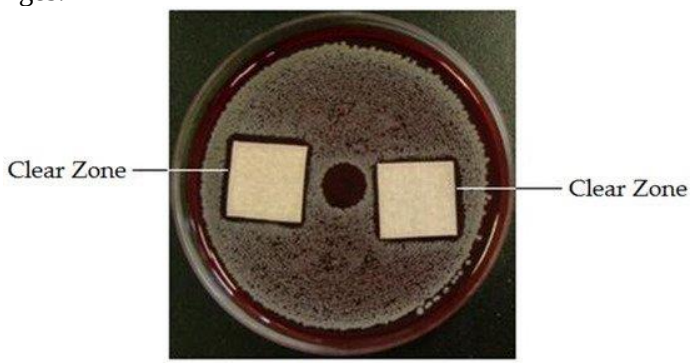

Figure 3: Example of the clear zone of the sample against bacteria [24].

Table 3: Orthogonal table for optimizing the antibacterial property of cotton fabric coated with DMH.

Test Run	Parameters				Results
	Concentration of DMH (%)	Temperature of Curing (°C)	Concentration of Bleaching Solution (%)	Time of Chlorination (min)	Mean clear width against *S. aureus* (mm)
	A	B	C	D	w_i
1	I	I	I	I	1.156
2	I	II	II	II	1.090
3	I	III	III	III	1.611
4	II	I	II	III	1.062
5	II	II	III	I	1.338
6	II	III	I	II	0.879
7	III	I	III	II	1.468

8	III	II	I	III	1.601
9	III	III	II	I	1.258
T_{mI}	3.857	3.686	3.636	3.752	$T_{mn} = \Sigma 9i = 1^{wi}$
T_{mII}	3.279	**4.029**	3.410	3.437	–
T_{mIII}	**4.327**	3.748	**4.417**	**4.274**	$K_{mn} = 1/3T_{mn} = 1/3\ \Sigma 9i = 1^{wi}$
K_{mI}	1.286	1.229	1.212	1.251	–
K_{mII}	1.093	**1.343**	1.137	1.146	–
K_{mIII}	**1.442**	1.249	**1.472**	**1.425**	–
R	*0.349*	*0.114*	*0.335*	*0.279*	$R = \text{Max}(K_{mI}, K_{mII}, K_{mIII}) - \text{Min}(K_{mI}, K_{mII}, K_{mIII})$

Figures in bold exhibit the highest value among all values of different variables used while italics show the level of importance of each variable.

Based on Table 3, all the four variables used, i.e., (i) concentration of DMH; (ii) curing temperature; (iii) concentration of bleaching solution; and (iv) time of chlorination, in the antibacterial finishing process can have different effects on antibacterial activity of cotton fabric coated with DMH in the CDPD process. The order of importance of these variables based on the OATS analysis is concentration of DMH > concentration of bleaching solution > time of chlorination > curing temperature. According to the results of the OATS analysis, the optimum conditions for DMH coating on cotton fabric in the CDPD process are: (i) concentration of DMH is 6%; (ii) curing temperature is 140 °C; (iii) concentration of bleaching solution is 1.2%; and (iv) time of chlorination is 60 min. In order to verify these optimum conditions, cotton fabric was treated under the optimum conditions and it was found that the mean clear width was 1.798 mm and this width is the widest when compared with the nine specimens' results in Table 3. Therefore, the optimum conditions were determined and the cotton fabric was treated under these optimum conditions for further evaluation of regenerability, by FTIR-ATR and SEM.

The effect of process variables including (i) concentration of DMH; (ii) time for curing; (iii) concentration of bleaching solution; and (iii) time of chlorination on the antimicrobial results was investigated (Figure 4). The effect of the concentration of DMH on the antibacterial property is shown in

Figure 4a; mean clear width reduces with an increase of the concentration of DMH when the concentration of DMH is lower than 4%, while it increases when the concentration of DMH increases beyond 4%. As shown in Figure 4b, the mean clear width increases with the increase of the curing temperature until it reaches 140 °C, but it reduces with the increase of the curing temperature beyond 140 °C (Figure 4b). As shown in Figure 4c, when the concentration of the bleaching solution is below 1%, the mean clear width reduces with the increase of the concentration of the bleaching solution. Moreover, if the bleaching solution concentration is higher than 1%, the mean clear width increases further. Figure 4d shows that the mean clear width of the finished cotton fabric decreases with the increase of the time of chlorination up to 40 min. After exceeding 40 min, the mean clear width starts increasing.

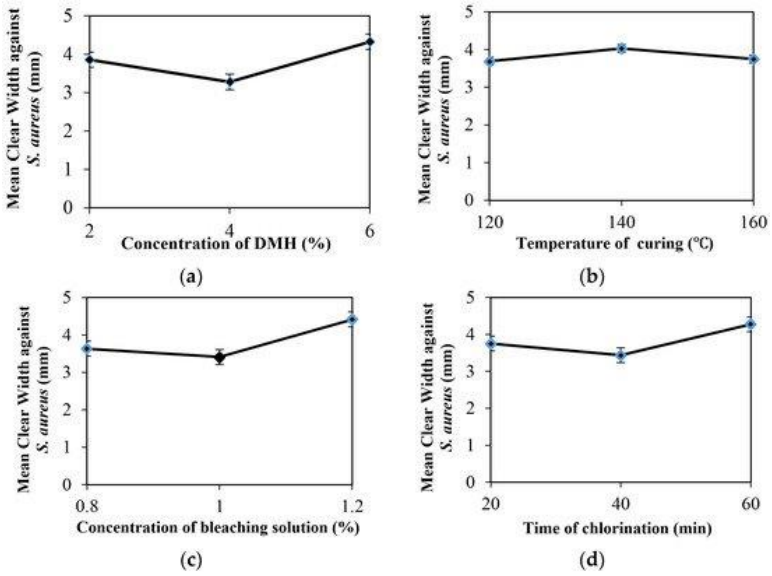

Figure 4: Effect of (**a**) concentration of DMH; (**b**) curing temperature; (**c**) concentration of the bleaching solution; and (**d**) time of chlorination on the antibacterial property of cotton fabric coated with DMH.

Relationship between the Antibacterial Property and the Concentration of Chlorine on Cotton Fabric

Figure 5 shows the relationship between the antibacterial property and the concentration of chlorine on cotton fabric. It is noted that the mean clear width becomes wider with an increase of the concentration of chlorine on DMH coated cotton fabric. The relationship is logarithmic with a logarithmic equation of y = 0.933ln(x) + 0.0155 (R^2 = 0.91301). That is because steric hindrance of the functional groups decreases the chlorination of N-containing groups by sodium hypochlorite [35,36].

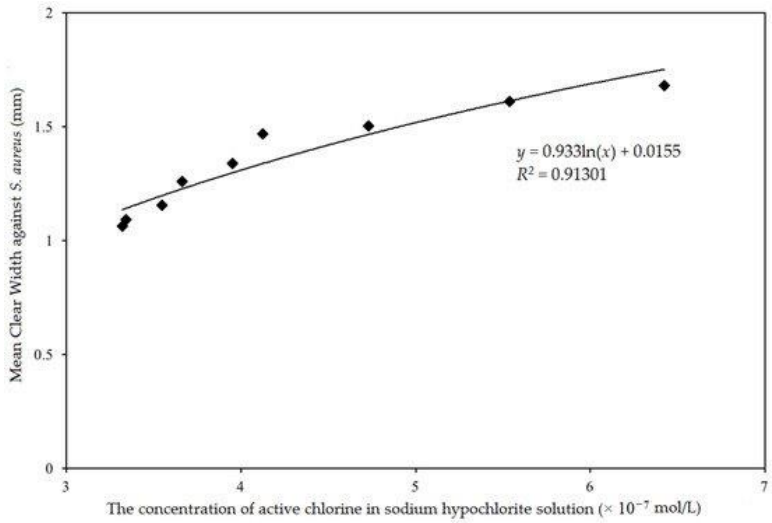

Figure 5: Relationship between the antibacterial property and the concentration of chlorine on cotton fabric.

Regenerability

Regenerability makes antibacterial textiles environmentally-friendly, besides prolonging the service life of the fabric. Figure 6 shows the regenerability of cotton fabric with plasma treatment (symbol: CDPD) and without plasma treatment (symbol: CD). In Figure 6, the mean clear width of fabric with plasma treatment is wider than for fabric without plasma treatment whether before

washing (washing time = 0 in Figure 6), after washing (symbol: AW), or re-chlorination (symbol: AW + CH). According to Figure 6, the antibacterial activity of cotton fabric with plasma treatment after re-chlorination is approximately the same as that before washing. However, the antibacterial activity of fabric without plasma treatment decreases after washing and re-chlorination, compared with that before washing. It is also found that the mean clear width of fabric without plasma treatment after washing decreases significantly when compared to that with plasma treatment after washing.

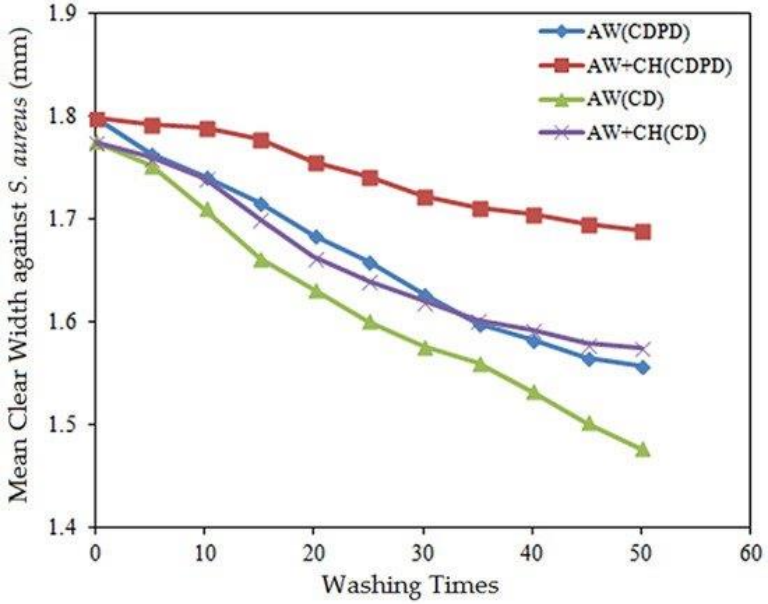

Figure 6: Antimicrobial effect of fabric finished with pad-dry-plasma-cure (CDPD) and pad-dry-cure (CD) processes before washing, after washing (AW), and after re-chlorination (AW + CH).

FTIR-ATR

FTIR-ATR is used to determine the existence and the content of chemical groups on the finished substrates. In this experiment, characteristic groups of DMH, amide II, and C=O and other chemical groups related to N_2 plasma treatment were determined. Figure 7 is the second derivative FTIR-ATR spectrum of the untreated cotton fabric (Figure 7a), cotton fabric treated with

plasma (Figure 7b), cotton fabric coated with DMH with plasma treatment (Figure 7c) and cotton fabric coated with DMH without plasma treatment (Figure 7d). Compared with Figure 7a, the peaks at around 1550 cm^{-1} are assigned to N–H (amine II) deformation in Figure 7b–d. The absorbance bands in the 1755 cm^{-1} region of Figure 7b–d indicate the stretching vibrations of C=O [36,37,38,39,40]. The absorbance peak of C=O in Figure 7b belongs to the stretching vibration of the carboxyl groups. Absorbance peaks of C=O in Figure 7d are derived from DMH and the absorbance peaks of C=O in Figure 7c include the stretching vibration of the carboxyl groups and amides. Absorbance peaks at 3304 cm^{-1} represent the stretching vibrations of N–H [24]. The absorbance peak of C=O and N–H (amine II) in Figure 7c is higher than that in Figure 7b,d according to coordinates of the absorbance peaks, which means fabrics finished with the pad-dry-plasma-cure process increase the content of C=O and N–H (amine II) groups on the basis of the Beer-Lambert law [24]. Therefore, finishing process with plasma treatment can modify the fabric surface by carboxyl groups and amides.

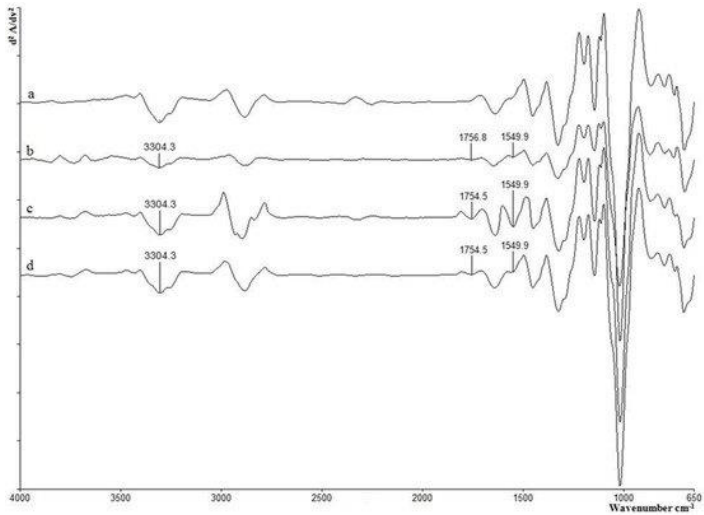

Figure 7: Second derivative FTIR spectrum of (**a**) untreated cotton fabric; (**b**) cotton fabric treated with plasma; (**c**) cotton fabric coated with DMH through the 'pad-dry-cure' method with plasma treatment (CDPD); and (**d**) cotton fabric coated with DMH through the 'pad-dry-cure' method (CD).

SEM

SEM was employed to observe the variations of physical characteristics on the surface of modified substrates. Figure 8 shows a SEM picture of untreated cotton fabric (Figure 8a), cotton fabric coated with DMH through the "pad-dry-cure" method (CD) (Figure 8b), and cotton fabric coated with DMH through the 'pad-dry-plasma-cure' method (CDPD) (Figure 8c). As shown in Figure 8, the surface of the cotton fibres is smooth even before coating, while the surface of cotton fibres coated with DMH is not smooth. Compared with the distribution of DMH on fabric without plasma treatment (Figure 8b), DMH is more evenly distributed on the surface of fibres treated with plasma (Figure 8c). This may be caused by the etching effect, that is, species generated in a plasma generator possess active energy, which collides with material surfaces to remove some line-structures on the fibre surfaces [23,41,42].

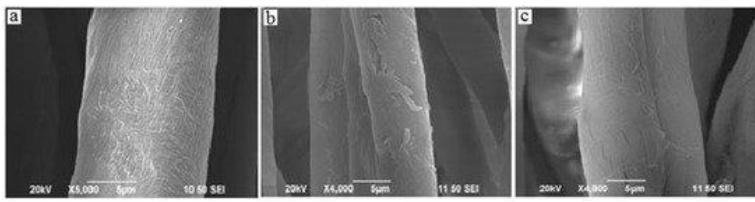

Figure 8: SEM picture of (**a**) untreated cotton fabric; (**b**) cotton fabric coated with DMH through the "pad-dry-cure" method (CD); and (**c**) coated with DMH through the 'pad-dry-cure' method with plasma treatment (CDPD).

Tearing Strength

Tearing strength of the untreated fabric, fabric coated with DMH (CD), and fabric coated with DMH with plasma treatment (CDPD) is shown in Table 4. Compared with the untreated fabric, the tearing strength of the cotton fabrics decrease about 5% in the warp direction and 10% in the weft direction after coating with DMH with or without plasma treatment. The tearing strength of cotton fabric without plasma treatment is nearly the same as that with plasma treatment. That is to say, the etching effect of the plasma treatment has no significant influence on the

tearing strength when plasma treatment is carried out after drying.

Table 4: Tearing strength of the untreated cotton fabric and cotton fabric finished with pad-dry-plasma-cure (CDPD) and pad-dry-cure (CD) processes both in the warp and weft direction.

Sample	Untreated	CD	CDPD
Tearing strength in warp direction (N)	15.42	14.63	14.60
Tearing strength in weft direction (N)	10.4	9.42	9.60

Discussion

In this study, it was found that N_2 plasma treatment functionalises the cotton fabric with N-containing groups and C=O groups, according to the FTIR study [43]. The formation of carboxyl groups on fabric after plasma treatment is caused by the oxidation of hydroxyl groups by particles in N_2 plasma, and they can react with amide groups in a hydantoin ring [44]. The higher absorbance peak of C=O in Figure 7c means the content of C=O in Figure 7c is 1.7 times higher than that in Figure 7b and 1 time in Figure 7d. According to the Beer-Lambert law, $A = \log_{10} (I_0/I) = abc$ (where A is the absorbance of functional groups; I_0 is the intensity of source radiation; I is the intensity of transmitted radiation; a is the absorpitivity co-efficient, b is the thickness of the path length; and c is the concentration of the absorber), the height of a second-derivative peak in the FTIR spectrum is proportional to the square of the original peak height with an opposite sign [44].

In addition, plasma treatment imparts an etching effect on the material surface leading to the formation of grooves and cracks [45]. In this study, the fabric is first covered by DMH in a pad-dry-plasma-cure process, and when the plasma particles reach the surface of the fabric, they initially interact with DMH. Thus, distribution and coating of DMH onto cotton fabrics is improved by plasma treatment. Meanwhile, the cracks and DMH on the fabric increase the surface friction and roughness, which restricts the sliding action of the yarn during tearing and leads to lower

tearing strength [23,46,47]. However, the DMH attached to the fabric decreases the etching effect of plasma treatment which prevents the tearing strength of the fabric from declining. Therefore, N_2 plasma treatment introduces N-containing groups and improves the content of DMH on cotton fabric, which increases the content of chlorine and enhances the antibacterial effect as well as its regenerability [24]. The plasma treatment applied after drying is a feasible way for improved functional finishing of cotton fabric.

It was also discovered that the process variables affect the antibacterial properties of cotton fabric finished with DMH. Firstly, the higher concentration of the DMH solution results in the aggregation of molecules of DMH, which affects the distribution and adhesion of DMH on fabric, resulting in a decrease of the mean clear width with an increase in the concentration of DMH. However, when the concentration of DMH is high enough, the aggregated DMH can cover a larger surface area and more DMH can be coated on the fabric. This explains why the mean clear width increases with the concentration of DMH until the DMH concentration reaches 6% [25,26]. Secondly, the melting point of DMH is around 175 °C and thus with a high curing temperature, the DMH can get detached from the fabric surface leading to poor fixation of DMH on fabric [25,26]. So DMH may be dissolved in water easily during the subsequent finishing process. Therefore, the DMH content on the fabric and chlorine decrease with the increase of the curing temperature, and the resultant antibacterial properties decrease. Generally speaking, a higher concentration of the bleaching solution provides more chlorine to interact with the DMH in the cotton fabric. Therefore, the chlorine concentration of fabric increases with an increase in the concentration of the bleaching solution [25], but this assumption could not be verified by the outcome as depicted in Figure 4c. Generally speaking, chlorine in sodium hypochlorite has a strong oxidising ability which is considered able to damage functional moieties, such as potential aldehyde groups on the cotton fabric [26]. This damage may contribute to the occurrence of decreased antibacterial efficacy of the treated fabrics when fabrics are chlorinated with higher concentration of sodium hypochlorite

solution. In this study, the N-containing groups came from two sources: DMH and N_2 plasma [41]. N-containing groups in DMH are chlorinated easily due to the effect of steric hindrance of functional groups in cellulose molecules [26]. When the concentration of sodium hypochlorite is lower than 1%, chlorine is consumed by the N-containing groups in DMH and functional groups on the cotton fabric. With the increase of the bleaching solution concentration, redundant chlorine has the chance to react with N-containing groups introduced by N_2 plasma [25]. This explains why the mean clear width is nearly stable with an increase in the bleaching solution concentration when the bleaching solution concentration is lower than 1%, and why it increases with the increase in concentration of the bleaching solution after the concentration exceeds 1%. The last factor is the time of chlorination. Because there are two sources of N-containing groups, at the beginning of chlorination, N-containing groups in DMH are chlorinated by sodium hypochlorite due to the steric hindrance of vicinal chemical groups of N-containing groups introduced by the nitrogen plasma on cotton fabrics [35,36]. However, the N-Cl structure in DMH is not stable. N-Cl bonds are hydrolysed (reverse reaction, Figure 1) with extension of the time of chlorination [48]. Functional groups in DMH are potentially destroyed by the strong oxidising ability of sodium hypochlorite. Meanwhile, nitrogen plasma introduces N-containing groups which are transferred into the N-halamine structure with the extension of chlorination time [24,25,26,27]. Therefore, the mean clear width of cotton fabric increases after the initial decrease.

It is demonstrated that the antibacterial activity is proportional to the concentration of chlorine on the finished cotton fabric. Therefore, the effective method to improve the antibacterial property of cotton fabric is to increase the amount of chlorine on the cotton fabric.

Conclusions

The pad-dry-plasma-cure process for coating DMH on cotton fabric followed by chlorination with sodium hypochlorite inhibits the bacteria, S. aureus, effectively. The optimum

treatment conditions of the antibacterial finishing process as identified in this research are (i) concentration of DMH = 6%; (ii) curing temperature = 140 °C; (iii) concentration of bleaching solution = 1.2%; and (iv) time of chlorination = 60 min. In the future, the finishing process can be optimized further by variance analysis through orthogonal experiments considered with interaction and error terms.

The antibacterial property of cotton fabric coated with DMH with the aid of plasma treatment followed by chlorination is regenerable, durable, and stable. The appearance, distribution, and content of DMH on cotton fabrics are enhanced by plasma treatment. Nitrogen plasma also introduces nitrogen-containing groups onto the surface of cotton fabrics, which enhances the antibacterial activity directly. Meanwhile, plasma treatment has no significant effect on the tearing strength of cotton fabric coated with DMH through the pad-dry-plasma-cure process.

With the regenerable antibacterial property, the cotton fabric can be potentially used for healthcare products in which a bleaching agent containing chlorine may be used as a sterilisation agent during the washing process. However, in future work, it is recommended to use X-ray photoelectron spectroscopy (XPS) to detect the variation of the chemical elements quantitatively. This characterization technique provides a more precise result of the variation of chemical elements on the surface of materials. In order to ensure the safety of finished fabrics that come in contact with humans, cytotoxicity testing should be performed, on account of the chlorine involved in the finishing process.

References

1. Thanh NVK, Phong NTP. Investigation of antibacterial activity of cotton fabric incorporating nano silver colloid. J. Phys. 2009; 187: 1–7.
2. Kenawy E, Abdel-Fattah YR. Antimicrobial properties of modified and electrospun poly (vinyl phenol). Macromol. Biosci. 2002; 2: 261–266.
3. Lala NL, Ramaseshan R, Bojun L, Sundarrajan S, Barhate RS, et al. Fabrication of nanofibers with antimicrobial

functionality used as filters: Protection against bacterial contaminants. Biotechnol. Bioeng. 2007; 97: 1357–1365.
4. Gouda M, Ibrahim N. New approach for improving antibacterial functions of cotton fabric. J. Ind. Text. 2008; 37: 327–339.
5. Lim S, Hudson SM. Application of a fiber-reactive chitosan derivative to cotton fabric as an antimicrobial textile finish. Carbohydr. Polym. 2004; 56: 227–234.
6. Abidi N, Hequet E, Cabrales L. Changes in sugar composition and cellulose content during the secondary cell wall biogenesis in cotton fibers. Cellulose. 2010; 17: 153–160.
7. Chen S, Chen S, Jiang S, Xiong M, Luo J, et al. Environmentally friendly antibacterial cotton textiles finished with siloxane sulfopropylbetaine. ACS Appl. Mater. Interfaces. 2011; 3: 1154–1162.
8. Sun G, Xu X, Bickett JR, Williams JF. Durable and regenerable antibacterial finishing of fabrics with a new hydantoin derivative. Ind. Eng. Chem. Res. 2001; 40: 1016–1021.
9. Liu S, Sun G. Durable and regenerable biocidal polymers: Acyclic N-halamine cotton cellulose. Ind. Eng. Chem. Res. 2006; 45: 6477–6482.
10. Ye W, Xin JH, Li P, Lee KD, Kwong T. Durable antibacterial finish on cotton fabric by using chitosan-based polymeric core-shell particles. J. Appl. Polym. Sci. 2006; 102: 1787–1793.
11. Son Y, Kim B, Ravikumar K, Lee S. Imparting durable antimicrobial properties to cotton fabrics using quaternary ammonium salts through 4-aminobenzenesulfonic acid-chloro-triazine adduct. Eur. Polym. J. 2006; 42: 3059–3067.
12. Hebeish A, El-Naggar ME, Fouda MMG, Ramadan MA, Al-Deyab SS, et al. Highly effective antibacterial textiles containing green synthesized silver nanoparticles. Carbohydr. Polym. 2011; 86: 936–940.
13. Lee H, Yeo S, Jeong S. Antibacterial effect of nanosized silver colloidal solution on textile fabrics. J. Mater. Sci. 2003; 38: 2199–2204.
14. Perelshtein I, Applerot G, Perkas N, Wehrschuetz-Sigl E, Hasmann A, et al. CuO-cotton nanocomposite: Formation,

morphology, and antibacterial activity. Surf. Coat. Technol. 2009; 204: 54–57.
15. Jia B, Mei Y, Cheng L, Zhou J, Zhang L. Preparation of copper nanoparticles coated cellulose films with antibacterial properties through one-step reduction. ACS Appl. Mater. Interfaces. 2012; 4: 2897–2902.
16. Leroux F, Perwuelz A, Campagne C, Behary N. Atmospheric air-plasma treatments of polyester textile structures. J. Adhes. Sci. Technol. 2006; 20: 939–957.
17. Zhou CE, Kan CW. Plasma-assisted regenerable chitosan antimicrobial finishing for cotton. Cellulose. 2014; 21: 2951–2962.
18. Hegemann D. Plasma polymerization and its applications in textiles. Indian J. Fibre Text. Res. 2006; 31: 99–115.
19. Bertaux E, Le Marec E, Crespy D, Rossi R, Hegemann D. Effects of siloxane plasma coating on the frictional properties of polyester and polyamide fabrics. Surf. Coat. Technol. 2009; 204: 165–171.
20. Abidi N, Hequet E. Cotton fabric graft copolymerization using microwave plasma. I. Universal attenuated total reflectance-FTIR study. J. Appl. Polym. Sci. 2004; 93: 145–154.
21. Virk RK, Ramaswamy GN, Bourham M, Bures BL. Plasma and antimicrobial treatment of nonwoven fabrics for surgical gowns. Text. Res. J. 2004; 74: 1073–1079.
22. Morent R, De Geyter N, Verschuren J, De Clerck K, Kiekens P, et al. Non-thermal plasma treatment of textiles. Surf. Coat. Technol. 2008; 202: 3427–3449.
23. Zhou CE, Kan CW, Yuen CWM, Lo KYC, Ho CP, et al. Regenerable antimicrobial finishing of cotton with nitrogen plasma treatment. BioResources. 2016; 11: 1554–1570.
24. Zhou CE, Kan CW. Plasma-enhanced regenerable 5,5-dimethylhydantoin (DMH) antibacterial finishing for cotton fabric. Appl. Surf. Sci. 2015; 328: 410–417.
25. Zhou CE, Kan CW. Optimizing rechargeable antimicrobial performance of cotton fabric coated with 5,5-dimethylhydantoin (DMH). Cellulose. 2015; 22: 879–886.
26. Zhou CE, Kan CW, Yuen CWM. Orthogonal analysis for rechargeable antimicrobial finishing of plasma pretreated cotton. Cellulose. 2015; 22: 3465–3475.

27. Zhou CE, Kan CW, Yuen CWM, Matinlinna JP, Tsoi JKH, et al. Plasma treatment applied in the pad-dry-cure process for making rechargeable antimicrobial cotton fabric that inhibits S. Aureus. Text. Res. J. 2015; 86: 2202–2215.
28. Kan CW. Evaluating antistatic performance of plasma-treated polyester. Fibers Polym. 2007; 8: 629–634.
29. Kan CW, Yuen CWM, Wong WY. Optimizing color fading effect of cotton denim fabric by enzyme treatment. J. Appl. Polym. Sci. 2011; 120: 3596–3603.
30. Sathianarayanan M, Bhat N, Kokate S, Walunj V. Antibacterial finish for cotton fabric from herbal products. Indian J. Fibre Text. Res. 2010; 35: 50–58.
31. Scholz J, Nocke G, Hollstein F, Weissbach A. Investigations on fabrics coated with precious metals using the magnetron sputter technique with regard to their anti-microbial properties. Surf. Coat. Technol. 2005; 192: 252–256.
32. Mohammadkhodaei Z, Mokhtari J, Nouri M. Novel anti-bacterial acid dyes derived from naphthalimide: Synthesis, characterisation and evaluation of their technical properties on nylon 6. Coloration Technol. 2010; 126: 81–85.
33. Daoud WA, Xin JH, Tao XM. Superhydrophobic silica nanocomposite coating by a low-temperature process. J. Am. Ceram. Soc. 2004; 87: 1782–1784.
34. Chuanwen C, Feng S, Yuguo L, Shuyun W. Orthogonal analysis for perovskite structure microwave dielectric ceramic thin films fabricated by the RF magnetron-sputtering method. J. Mater. Sci. 2010; 21: 349–354.
35. Kocer HB, Akdag A, Ren X, Broughton RM, Worley SD, et al. Effect of alkyl derivatization on several properties of N-halamine antimicrobial siloxane coatings. Ind. Eng. Chem. Res. 2008; 47: 7558–7563.
36. Qian L, Sun G. Durable and regenerable antimicrobial textiles: Synthesis and applications of 3-methylol-2,2,5,5-tetramethyl-imidazolidin-4-one (MTMIO). J. Appl. Polym. Sci. 2003; 89: 2418–2425.
37. Wang L, Xie J, Gu L, Sun G. Preparation of antimicrobial polyacrylonitrile fibers: Blending with polyacrylonitrile-co-3-allyl-5,5-dimethylhydantoin. Polym. Bull. 2006; 56: 247–256.

38. El-Newehy MH, Al-Deyab SS, Kenawy E, Abdel-Megeed A. Nanospider technology for the production of nylon-6 nanofibers for biomedical applications. J. Nanomater. 2011; 2011: 626589.
39. Sun X, Cao Z, Porteous N, Sun Y. An N-halamine-based rechargeable antimicrobial and biofilm controlling polyurethane. Acta Biomater. 2012; 8: 1498–1506.
40. Kocer HB, Worley S, Broughton R, Huang T. A novel N-halamine acrylamide monomer and its copolymers for antimicrobial coatings. React. Funct. Polym. 2011; 71: 561–568.
41. Yoon NS, Lim YJ, Tahara M, Takagishi T. Mechanical and dyeing properties of wool and cotton fabrics treated with low temperature plasma and enzymes. Text. Res. J. 1996; 66: 329–336.
42. Wong KK, Tao XM, Yuen CWM, Yeung KW. Low temperature plasma treatment of linen. Text. Res. J. 1999; 69: 846–855.
43. Silva SS, Luna SM, Gomes ME, Benesch J, Pashkuleva I, et al. Plasma surface modification of chitosan membranes: Characterization and preliminary cell response studies. Macromol. Biosci. 2008; 8: 568–576.
44. Max JJ, Chapados C. Infrared spectroscopy of aqueous carboxylic acids: Comparison between different acids and their salts. J. Phys. Chem. A 2004; 108: 3324–3337.
45. Karahan H, Özdoğan E. Improvements of surface functionality of cotton fibers by atmospheric plasma treatment. Fibers Polym. 2008; 9: 21–26.
46. Cheng SY, Yuen CWM, Kan CW, Cheuk KKL, Daoud WA, et al. Influence of atmospheric pressure plasma treatment on various fibrous materials: Performance properties and surface adhesion analysis. Vacuum. 2010; 84: 1466–1470.
47. Kan CW, Chan K, Yuen CWM. A study of the oxygen plasma treatment on the serviceability of a wool fabric. Fibers Polym. 2004; 5: 213–218.
48. Sun G, Worley SD. Chemistry of durable and regenerable biocidal textiles. J. Chem. Educ. 2005; 82: 60–64.

Book Chapter

Selective Grafting of Polyamines to Polyether Ether Ketone Surface during Molding and Its Use for Chemical Plating

Jürgen Nagel*, Philipp Zimmermann, Simona Schwarz and Kornelia Schlenstedt

Leibniz-Institut für Polymerforschung Germany

***Corresponding Author:** Jürgen Nagel, Leibniz-Institut für Polymerforschung Dresden e.V., Hohe Straße 6, 01069 Dresden, Germany

Published **March 16, 2020**

This Book Chapter is a republication of an article published by Jürgen Nagel, et al. at Coatings in September 2018. (Nagel, J.; Zimmermann, P.; Schwarz, S.; Schlenstedt, K. Selective Grafting of Polyamines to Polyether Ether Ketone Surface during Molding and Its Use for Chemical Plating. Coatings 2018, 8, 333.)

How to cite this book chapter: Jürgen Nagel, Philipp Zimmermann, Simona Schwarz, Kornelia Schlenstedt. Selective Grafting of Polyamines to Polyether Ether Ketone Surface during Molding and Its Use for Chemical Plating. In: Surfaces, Interfaces and Coatings Technology. Hyderabad, India: Vide Leaf. 2020.

Author Contributions: Conceptualization & supervision, J.N.; Sample preparation, characterization and plating, P.Z.; electro kinetic investigations, S.S.; Microscopic and spectroscopic investigations, K. S.

Funding: This research received no external funding.

Acknowledgements: The authors wish to thank Mrs. Anja Caspari for thorough measurements of the zeta potentials. Mr. Renè Weihrauch from University of Applied Science in Zittau is thanked for measurements of the metal layer thicknesses by RFA.

Conflicts of Interest: The authors declare no conflict of interest.

Abstract

We present a new approach of surface functionalization of PEEK that is carried out during the molding step. Thin films of polymers with different functional groups were applied to the surface of a mold and brought in close contact with a PEEK melt during injection molding. The surfaces of the produced parts were characterized after solidification. Only those PEEK surfaces that were in contact with polymers bearing primary amino groups exhibited a wettability for water. Obviously, the thin polymer film was grafted to the surface by a chemical reaction initiated by the high melt temperature. The formation of azomethine bonds between PEEK and the polyamine by coupling to the ketone groups was proposed. The other amino groups in the molecule were still in function after the molding process. They adsorbed different anionic molecules and anionic charged nanoparticles from aqueous solutions. The surfaces could be chemically plated by copper and nickel with high adhesion.

Keywords

PEEK; Adhesion; Surface Modification; Injection Molding; Plating; Hydrogel Layers

Introduction

PEEK is a high performance thermoplastic polymer that features a high modulus and mechanical strength even at high temperature and a high chemical stability. It is flame resistant, and the combustion is self-quenching. Moreover, it is physiologically harmless. Therefore, it is used in medical devices and artificial replacements, e.g. for bone and dental implants. The chemical stability is used in devices for chemical industry and food industry. Its high mechanical strength at relatively low density and its flame resistance are advantageous for aviation and for the construction of vehicles. Its stiffness is a result of the high content of aromatic hydrocarbon rings in the molecule. Unfortunately, this makes PEEK sensitive to ultra violet radiation. That is one reason, why a coating of PEEK parts is often required. Design aspects are another reason. However, PEEK surfaces are rather non-polar, and a surface modification is required for high adhesion of coatings [1,2]. The polymerization of dopamine results in a modified surface, which is able to immobilize proteins, but the mechanical adhesion of the poly dopamine would not be sufficient for bonding a thick metal layer [3]. A direct grafting method was developed that takes advantage of the reactivity of the ketone group [4]. Here polyvinyl alcohol was attached via the formation of acetals. Then, glycidyl groups were attached to the hydroxyl groups of polyvinyl alcohol, and finally a diamine was attached via the glycidyl groups. Thus, this way is rather expensive, and the modification effect was not stable over a long period of time. Treatment with different types of plasma is often used for modifying the surfaces of polymers. An efficient method with high industrial relevance is the flame impingement. Treatment with defined plasmas, e.g. low pressure plasma, atmospheric plasma, or corona, in the presence of different gases gives a better control of the chemical modification [5-17]. However, only the PEEK segments on the outermost surface layer are converted to functional groups like carboxyl, hydroxyl, carbonyl, and amide. Control of composition is difficult. Since PEEK absorbs ultraviolet irradiation, it was used for chemical surface modification and grafting [18-20]. Due to the high-energy

treatments a high diversity of different functional groups are formed on the surface, but the effect is usually not permanent [21,22]. The combination of plasma treatment and grafting a functional polymer layer from the PEEK surface results in reliable surface modification, but with high operating expense [23]. A high adhesion of a metal layer is supported by a micro structure on the surface. This can be realized by plasma etching, chemical etching, laser etching or mechanical etching, e.g. with sandblast [24,26]. There are other processes in use, but all of them require an additional processing step. Any pre-treatment step require production space, investment, and running costs, e.g. for materials, energy, and labor expense. Integrating the surface modification with the molding step would be very efficient. This was demonstrated, e.g. by structuring the part surface using a micro structured mold surface [27].

In our paper, we present an approach for the chemical surface modification that is carried out during injection molding of the part. It is based on the deposition of a thin film of a functional and reactive polymer, the so-called modifier, on the mold surface of an injection molding machine. The high temperature of the melt is used to initiate a coupling reaction. Treatment in melt state features additional advantages over part treatments. e.g. a high mobility of chain segments and a higher excluded volume. Side reactions are minimized due to the rapid cooling and the small reaction time. The effect is much larger compared to the pre-treated surfaces due to grafting of a relatively thick functional polymer layer to the thermoplastic surface. The reaction proceeds in only one step and is integrated in the molding step of the part. The important issue is to identify a reactant and a suitable reaction pathway for the thermoplastic under consideration. Solutions for polycarbonate (PC), polypropylene (PP), grafted PP, Polystyrene (PS), and polyamide (PA) were already published [28-33]. The carbonate group in PC was reacted with polyethylene imine during molding under formation of a urethane bond, resulting in a relatively thick layer of a functional polymer on the PC surface. Parts rinsed in water did not dewet due to the high hydrophilicity. PP was modified by radical grafting of acrylic

acid. The high reactivity of a cyclic carboxylic anhydride was used to graft a maleic anhydride-ethylene copolymer to PA 6. PS contains electron-rich phenyl rings. Here, we applied Friedel-Crafts acylation using mixed anhydrides to attach a polycarboxylic acid on the melt surface during 3D printing. In this paper, we tested different functional groups for chemical coupling onto PEEK surfaces. A reaction pathway is proposed. Finally, chemical plating was carried out, which demonstrates the effect of surface modification for industrial use. This application is of high impact, as a metal composite with PEEK would support its usage for lightweight construction parts in vehicles, aircrafts and spacecraft. Moreover, this type of surface modification of PEEK may also be used for other applications.

Experimental

The different types of polymer modifiers (polyallyl amine, PAAm, Mw 65 kg mol^{-1}; hyper branched polyethylene imine, PEI, M_w 700 kg mol^{-1}; polyvinyl alcohol, PVA, M_w 23 kg mol^{-1}, degree of hydrolysis 89%; polyacrylic acid, PAc, M_w 450 kg mol^{-1}) and $CuSO_4$• 5 H_2O were supplied by SigmaAldrich, Germany. PEEK (Vestakeep 3300, Evonik Industries AG, Germany) was used as thermoplastic material. It was dried at 160 °C for 4 hours in vacuum. Melt and mold temperatures were 360 and 160 °C, respectively. Typical molding conditions as suggested by the manufacturer were used.

The general processing steps are explained in figure 1. Fundamental molding investigations were carried out in the first stage with a small Boy injection molding machine (BOY 22 A HV, Dr. Boy GmbH & Co. KG, Germany). The L/D ratio of the screw, screw speed, and pressure were 20, 60 min^{-1}, 400 MPa, respectively. It was equipped with an in-house build mold having an inlay with a magnetic substrate holder in which mirror-polished steel substrates with a diameter of 50 mm were mounted before each injection cycle [34]. The substrates were covered with a layer of the appropriate modifier by spin-coating in advance. This approach had the advantage that the applied modifier layer on the substrate can be characterized. The layer thickness on the substrate was measured by ellipsometry using

a Multiskop 8.8 ellipsometer (Optrel GbR, Germany). After injection of PEEK and solidification, the substrate was separated from the formed part. Both surfaces were characterized. Dynamic contact angles against water were measured using an OCA35 XL (DataPhysics Instruments GmbH, Germany). The zeta potential of the polymer surfaces was measured with an electro kinetic analyzer EKA (Anton Paar GmbH, Austria). Some samples were dipped into a 10^{-3} M solution of eosin Y in water at pH 9 for 10 minutes to test the dye adsorption.

SEM-EDX investigations were made with an Ultra Plus Gemini microscope (Carl Zeiss SMT GmbH, Germany) using an XFlash 5060 F EDX detector (Bruker Nano GmbH, Germany). Prior to the characterization, the parts were rinsed in copper sulfate solution for marking the amino groups, exploiting the complex formation between amino groups and the copper ions. After rinsing in water to remove excess copper ions and drying, they were coated with a Pt layer of 3 nm thickness by sputtering using a Leica EM SCD 050 (Leica Microsysteme GmbH, Germany).

Samples for plating experiments were prepared on the injection molding machine Ergotech 100/420-310 (Sumitomo-Demag Plastics Machinery GmbH, Germany). The L/D ratio of the screw, injection pressure, rate, holding pressure and time and cooling time were 20, 600 MPa, 35 mm s^{-1}, 350 bar, 1 s, 25 s, respectively. The modifier films were directly spray-coated from aqueous solutions on one side of the mold using an air brush at each cycle. The amount of dry modifier on the mold surface was calculated by volume and concentration of used solution per injection. It was about 250 mg m^2. The prepared plates used for metallization experiments were rinsed in water for 6 hours under stirring to remove unbound modifier. The plates were shaken first in a colloidal solution of gold nanoparticles (AuNP) for 30 minutes. The synthesis of the AuNP was made using a classical approach [34]. After rinsing with water and drying, the plates were dipped in a copper bath, consisting of a solution of 6.25 g l^{-1} $CuSO_4$•5 H_2O, 8 g l^{-1}

EDTA, and 0.11 g l^{-1} $NaBH_4$ at room temperature. The pH of this solution was adjusted to 12 by adding NaOH. Plating with nickel was realized using a commercial nickel bath (SurTec International GmbH, Germany)
The metal layer thickness was measured by x-ray fluorescence analysis (XFA) using a Fischerscope Xray Xan 220 (Helmut Fischer GmbH + Co KG, Germany). The metallized plates were cut with a cross-hatch (Erichsen Mehrschneidegerät 295/I with 6 blades, Erichsen GmbH & Co. KG). An adhesive tape was fixed on the metal layer and then pulled off at an angle of 90 degrees.

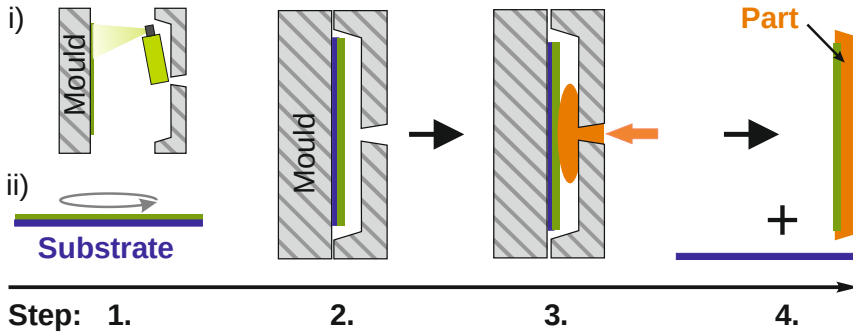

Figure 1: Processing steps of surface modification during molding. 1. Formation of thin film (10-100 nm) of modifier by either (i) spray-coating or (ii) spin-coating; 2. Modifier layer on mounted substrate or directly on mold surface; 3. Injection of the PEEK melt while initiating a coupling reaction, see also graphical abstract figure; 4. Demolding with transfer of the modifier layer to the part.

Results and Discussion

The thicknesses of the modifier layers on the substrates prior to molding are listed in table 1. The modifier layer thickness was measured again after injection molding and removing of the PEEK part. The comparison with the thicknesses before molding revealed, that they did not change significantly in the case of PAc. Obviously, no transfer of PAc from the substrate to the PEEK surface took place during molding. Thus, PAc did not interact with the PEEK melt. The same behavior was observed for the PVA layer. Obviously, no interaction between

PEEK and PVA did occur either. On the other hand, the thickness of the PEI layer was reduced very much during molding. The PAAm layer was transferred almost completely. Obviously, only thin layers of polymers bearing primary amino groups were transferred to the PEEK surface during molding.

Table 1: Characteristics of the PEEK part surfaces.

Sample type	Layer thickness / nm [a]		Contact angle / degrees [b]	
	after preparation	after molding	advancing	receding
PEEK	-	-	80	52
PEEK-PAc	36	34	83	52
PEEK-PVA	18	18	83	53
PEEK-PEI	115	14	68	<10
PEEK-PAAm	79	2	84	<10

[a] on substrate, after deposition; [b] of molded part, after extraction in ethanol, details in Table S-1

Eosin Y was adsorbed only on surfaces modified with PAAm or PEI using the described process, but neither on samples without such modification nor on plain PEEK. This suggests the formation of a cationic surface on PEEK. Obviously, the polyamine-modified surface is charged positively by adsorption of protons from water and formation of ammonium functions. Thus the negatively charged dye adsorbed on this surface due to electrostatic interactions. The adsorbed dye could not be removed by rinsing with water, see also figure S-1.

The EDX spectrum of plain PEEK shows only signals for C,O in figure 2. It did not show any copper signal. The spectra of parts modified with PEI exhibited intense peaks of Cu (L) as well as S (K) after dipping in copper sulfate solution, pointing to chemisorption of copper due to formation of a very stable chelate complex with amino groups. This is an indication, that the amino groups were still functional and accessible, despite the thermal treatment during molding. The copper was evenly distributed on the PEEK surface, as shown in figure S-2.

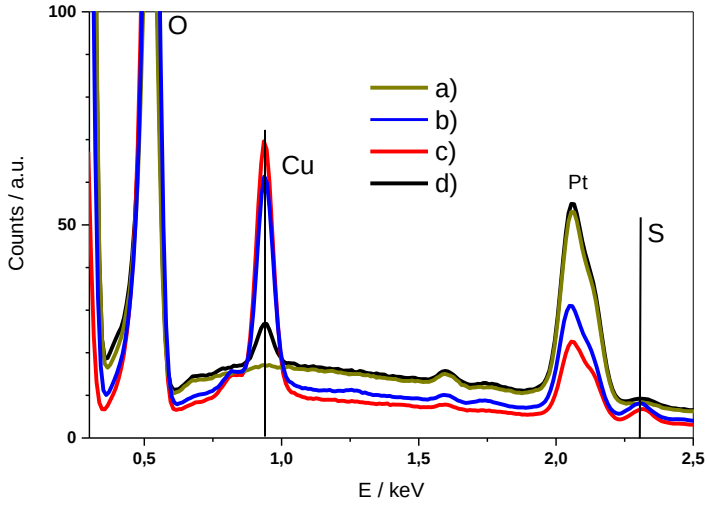

Figure 2: EDX spectra of PEEK samples, treated with $CuSO_4$ solution. A) Plain PEEK; b) PEEK surface modified with PEI during molding; c) after extraction in ethanol; d) after extraction in water at pH 3. The signals are marked with assigned elements. The Pt signals stem from the preparation procedure.

The parts were then extracted in ethanol for 6 hours in a Soxhlet apparatus. The extraction was intended to remove any unbound material. Ethanol is a good solvent for PAAm but do not swell or dissolve PEEK. Water was avoided as solvent because it could result in charging the PEEK surface, which would enhance the adsorption of PAAm due to electrostatic attraction, which was not intended. Moreover, water could result in hydrolyzation of some bonds. These samples were characterized by the following experiments.

The EDX spectrum of the sample modified with PEI after marking with copper exhibited a strong signal of copper that was only slightly smaller than that of the surface before extraction. Consequently, only a low amount of the polyamine was removed. This pointed to a covalent coupling of the polyamine layer according to figure 3.

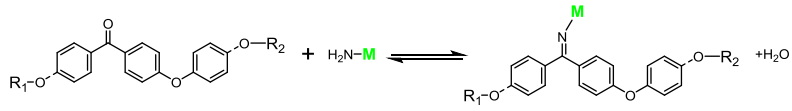

Figure 3: Schema of chemical coupling of a primary amino compound (the modifier M) to PEEK.

The dynamic contact angles were measured. The advancing angles of the differently prepared samples in table 1 equaled almost those of the plain PEEK. The same relation was observed for the receding angles of samples treated with PAc and PVA. Thus, these polymers did not modify the PEEK surface during the proposed approach. However, the samples modified with PAAm or PEI exhibited receding angles lower than 10 degrees and in a range that could not be reliably measured. In addition, parts dipped into water did not dewet after drawing off the water. Swelling of a hydrophilic polymer layer may be an explanation for the high hysteresis [35]. A similar behavior was already studied at the surface modification of PC with polyamines during molding [29]. There, the amino groups were coupled onto the PC backbone by formation of an urethane bond.

Some of the parts modified with PAAm or PEI and extracted in ethanol were additionally extracted for four hours in a Soxhlet apparatus in aqueous hydrochloride acid solution of pH 3. The surfaces of these parts did not show any of the properties and behavior of that of those surfaces without this treatment. No staining, no wetting by water, almost no shift of the isoelectric point (see figure S-3) and no adsorption of copper did occur, as the EDX spectrum in figure 2 revealed. Obviously, the polyamines were completely removed by acid catalyzed hydrolysis in aqueous environment as suggested in figure 3. Such a reaction is typical for azomethine bonds. Thus, the assumption of chemical grafting of the polyamines during molding by the primary amino groups according to figure 3 is supported by this experiment.

Since the PAAm and PEI layers could not be removed by extraction in ethanol, chemical coupling of primary amino groups to ketone groups of the PEEK surface by formation of azomethine bonds was assumed. This assumption is supported by the fact that compounds with other functional groups (hydroxyl, carboxylic acid) were not transferred. The reactions between PEEK and primary amino compounds in solution at high temperature were studied extensively under different conditions in the literature [36-39]. Alternatively, the surfaces of PEEK plates were reacted in solutions of different components at elevated temperature [40,41]. Reasonable conversion was achieved there after many hours reaction time.

In contrast to the proposed reactions, our experiments were carried out under different conditions. The reaction temperature on melt-mold contact was high, i.e. about 300 °C. However, the reaction time during injection molding was much smaller due to the rapid cooling than in the solution experiments, and the concentration of reactive groups (ketone and amino) was much higher. Thermal simulations revealed a reaction time at high temperature of about 1 µs [42]. Hence, a reaction takes place only in a very small layer along the melt-modifier interface with a thickness of about 1 nm [43]. Interdiffusion is limited also by the immiscibility of the two materials. Thus, only molecular groups that come into close contact immediately after the melt hits the modifier layer on the mold can take part in a reaction. Therefore, the concentrations of those reactive groups in the interphase have to be high. In the case of PEEK, PEI and PAAm the concentrations of ketone groups and primary amino groups, respectively, are very high because not only the end groups but every repeating unit carries a reactive group. The reactivity of the components, the high concentrations and the high temperature on the one hand and the transferred layer and its stability against solvent extraction on the other hand pointed to a reactive coupling of the modifiers over the primary amino groups. However, a direct proof of the reaction product will not be possible due to the low amount of products formed in the small interface layer. Moreover, even the plain PEEK is poorly soluble in almost all

solvents, preventing the use of standard analytical tools like nuclear magnetic resonance spectroscopy. It is somewhat soluble in special solvents only at very high temperature (about 300 °C). The reaction products in the surface layer are even less soluble due to the formation of cross-links between many ketone groups of PEEK and many amino groups of the polyamine. Nevertheless, the solubility and chemical behavior point to the formation of a chemical bond according to figure 3 as suggested by the reaction mechanism taken from literature.

Further investigations were carried out with parts with larger surface areas. The plates were cut in small pieces and extracted in ethanol in a Soxhlet apparatus for 6 hours to remove unbound modifier. The zeta potential of the resulting plain PEEK surface was positive at low pH values and decreased with the pH value as shown in figure 4. The isoelectric point was at pH=4. The zeta potential was constant at high pH with values of less than -32 mV, which is typical for a non-polar polymer surface. The curve of the PEEK surface modified with PAAm was shifted to higher values. The isoelectric point was at about pH=5. This suggests a more cationic surface than that of plain PEEK. The zeta potential then decreased continuously with pH. In contrast to the plain PEEK surface, no constant value was approached in the measurement range. This pointed to functional groups, e.g. amino groups, within a finite polymer layer bound on the surfaces. The isoelectric point shifted even more to about 8 for the PEEK surface modified with PEI. The maximum potential in the acid range was about 40 mV, which was higher than in the case of PAAm. This revealed a complete change of the electro kinetic behavior compared to unmodified PEEK.

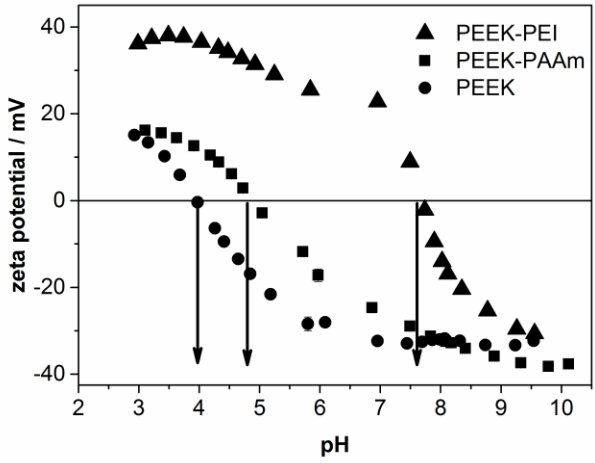

Figure 4: Zeta potentials of PEEK plates and plates chemically modified during molding with PEI or PAAm, respectively. After extraction in ethanol. The arrows point to the isoelectric points.

The plates modified with PAAm or PEI, respectively, were rinsed in a solution of gold nanoparticles (AuNP, size about 20 nm), which were prepared according to the description in a previous paper [34]. The red color of the surfaces revealed adsorption of AuNP only at the modified surface regions, i.e. where a polyamine layer was bound, see also figure S-4. These parts were then rinsed in the copper bath. After 60 minutes at room temperature a copper layer had formed. This layer had the typical view of massive copper. The thickness was about 0.3 µm. The adsorbed AuNP were used here as catalytic seeds for chemical plating. The cross-hatch test did not show any delamination of the copper film, and there was no delamination after peeling off an adhesive tape, pointing to a high adhesion, see figure 5. The cross-hatch test had a value of zero. Similar experiments were carried out using a nickel bath with a rinsing time in the nickel solution of 10 minutes, resulting in deposition of a nickel layer of 0.1 µm with high adhesion. In contrast, no adsorption of AuNP and, consequently, no formation of a metal layer took place on a plain PEEK surface. Moreover, the covalently grafted polyamine layers can be used for attaching

different organic layers, e.g. hydrogel layers, see supplementary materials.

Figure 5: Photograph of a PEEK-copper composite made by chemical plating, after cross-hatch and peel test.

Conclusions

It was shown that polyamines bearing primary amino groups can be grafted to the surface of PEEK parts during molding. Grafting took place exploiting the melt temperature for initiating a chemical reaction, where the ketone groups of PEEK and the primary amino groups were connected under formation of azomethine bonds. The chemical properties and behavior of these modified PEEK surfaces were dominated by the attached polyamines. The polyamine layer adsorbed gold seeds. The use of other seeds may also be possible, e.g. Pd or Ag. The seeds and the functional surface can then be used for chemical plating of PEEK with Cu or Ni, e.g. for protective or decorative coatings or for electromagnetic shielding. Those metal-PEEK composites will support the application of PEEK in light-weight constructions. Moreover, plating only takes place at sites, where the modifier was applied to the mold prior to injection of the melt. Consequently, site-selective plating and the formation of metal structures on surface becomes possible, like for the production of molded interconnected devices or circuit boards. The thermal stability of PEEK would enable soldering of those circuit boards.

The high adhesion may be a result of the strong attraction of copper and nickel ions because the polyamines are strong

chelating ligands of these metal ions. Probably, there are also strong interactions to metals, which supported high adhesion of the metal film [11]. These films are useful for the deposition of different metal layers by conventional galvanic plating processes.

References

1. Laurens P, Sadras B, Decobert F, Arefi-Khonsari F, Amouroux J. Enhancement of the adhesive bonding properties of PEEK by excimer laser treatment. Int. J. of Adhes. Adhes. 1998; 18: 19–27.
2. Ma R, Tang T. Current Strategies to Improve the Bioactivity of PEEK. Int. J. Mol. Sci. 2014; 15: 5426–5445.
3. Kwon G, Kim H, Gupta KC, Kang IK. Enhanced Tissue Compatibility of Polyetheretherketone Disks by Dopamine-Mediated Protein Immobilization. Macromol. Res. 2018; 26: 128–138.
4. Kim KH, Im SH, Park BJ. Long-term stable hydrophilic surface modification of poly(ether ether ketone) via the multilayered chemical grafting method. J. Appl. Polym. Sci. 2018; 135: 4604.
5. Rochford ETJ, Poulsson AHC, Salavarrieta Varela J, Lezuo P, Richards RG, et al. Bacterial adhesion to orthopaedic implant materials and a novel oxygen plasma modified PEEK surface. Colloid Surf. B-Biointerfaces. 2014; 113: 213–222.
6. Al-Maliki H, Zsidai L, Samyn P, Szakal Z, Keresztes R, et al. Effects of atmospheric plasma treatment on adhesion and tribology of aromatic thermoplastic polymers. Polym. Eng. Sci. 2018; 58: E93–E103.
7. Salerno S, Piscioneri A, Laera S, Morelli S, Favia P, et al. Improved functions of human hepatocytes on NH3 plasma-grafted PEEK-WC-PU membranes. Biomaterials. 2009; 30: 4348–4356.
8. Stefanikova R, Kretkova T, Kuzminova A, Hanus J, Vaidulych M, et al. Influence of atmospheric pressure dielectric barrier discharge on wettability and drying of

poly(ether-ether-ketone) foils. Polym. Degrad. Stabil. 2018; 150: 114–121.
9. Tsougeni K, Vourdas N, Tserepi A, Gogolides E, Cardinaud C. Mechanisms of Oxygen Plasma Nanotexturing of Organic Polymer Surfaces: From Stable Super Hydrophilic to Super Hydrophobic Surfaces. Langmuir. 2009; 25: 11748–11759.
10. Schroder K, Meyer-Plath A, Keller D, Besch W, Babucke G, et al. Plasma-induced surface functionalization of polymeric biomaterials in ammonia plasma. Contrib. Plasma Phys. 2001; 41: 562–572.
11. Briem D, Strametz S, Schroder K, Meenen NM, Lehmann W, et al. Response of primary fibroblasts and osteoblasts to plasma treated polyetheretherketone (PEEK) surfaces. J. Mater. Sci.-Mater. Med. 2005; 16: 671–677.
12. Gomathi N, Sureshkumar A, Neogi S. RF plasma-treated polymers for biomedical applications. Curr. Sci. 2008; 94: 1478–1486.
13. Tsougeni K, Papageorgiou D, Tserepi A, Gogolides E. "Smart'"' polymeric microfluidics fabricated by plasma processing: controlled wetting, capillary filling and hydrophobic valving." Lab Chip. 2010; 10: 462–469.
14. Ha SW, Hauert R, Ernst KH, Wintermantel E. Surface analysis of chemically-etched and plasma-treated polyetheretherketone (PEEK) for biomedical applications. Surf. Coat. Technol. 1997; 96: 293–299.
15. Iqbal HMS, Bhowmik S, Benedictus R. Surface modification of high performance polymers by atmospheric pressure plasma and failure mechanism of adhesive bonded joints. Int. J. Adhes. Adhes. 2010; 30: 418–424.
16. Inagaki N, Tasaka S, Horiuchi T, Suyama R. Surface modification of poly(aryl ether ether ketone) film by remote oxygen plasma. J. Appl. Polym. Sci. 1998; 68: 271–279.
17. Awaja F, Cools P, Lohberger B, Nikiforov AY, Speranza G, et al. Functionalized, biocompatible, and impermeable nanoscale coatings for PEEK. Mater. Sci. Eng. C-Mater. Biol. Appl. 2017; 76: 865–870.

18. Mathieson I, Bradley RH. Improved adhesion to polymers by UV/ozone surface oxidation. Int. J. Adhes. Adhes. 1996; 16: 29–31.
19. Liu S, Zhu Y, Gao H, Ge P, Ren K, et al. One-step fabrication of functionalized poly(etheretherketone) surfaces with enhanced biocompatibility and osteogenic activity. Mater. Sci. Eng. C-Mater. Biol. Appl. 2018; 88: 70–78.
20. Ishihara K, Fukazawa K, Inoue Y, Koyama J, Mori Y, et al. Reliable surface modification of dental plastic substrates to reduce biofouling with a photoreactive phospholipid polymer. J. Appl. Polym. Sci. 2018; 135: 46512.
21. Rymuszka D, Terpiłowski K, Borowski P, Holysz L. Time-dependent changes of surface properties of polyether ether ketone caused by air plasma treatment: Air plasma treatment of polyether ether ketone. Polym. Int. 2016; 65: 827–834.
22. Morent R, De Geyter N, Leys C, Gengembre L, Payen E. Study of the ageing behaviour of polymer films treated with a dielectric barrier discharge in air, helium and argon at medium pressure. Surf. Coat. Technol. 2007; 201: 7847–7854.
23. Noiset O, Schneider YJ, Marchand-Brynaert J. Fibronectin adsorption or and covalent grafting on chemically modified PEEK film surfaces. J. Biomater. Sci.-Polym. Ed. 1999; 10: 657–677.
24. Riveiro A, Soto R, Comesana R, Boutinguiza M, del Val J, etal. Laser surface modification of PEEK. Appl. Surf. Sci. 2012; 258: 9437–9442
25. Rotel M, Zahavi J, Tamir S, Buchman A, Dodiuk H. Pre-bonding technology based on excimer laser surface treatment. Appl. Surf. Sci. 2000; 154: 610–616.
26. Lee KS, Shin MS, Lee JY, Ryu JJ, Shin SW. Shear bond strength of composite resin to high performance polymer PEKK according to surface treatments and bonding materials. J. Adv. Prosthodont. 2017; 9: 350–357.

27. Lee JA, McCarthy TJ. Polymer surface modification: Topography effects leading to extreme wettability behavior. Macromol. 2007; 40: 3965–3969.
28. Nagel J, Scheidler D, Hupfer B, Bräuer M, Pleul D, et al. Investigations on the formation of composites by injection molding of PA6 and different grafted polypropylenes and their blends. J. Appl. Polym. Sci. 2006; 100: 2992–2999.
29. Nagel J, Bräuer M, Hupfer B, Grundke K, Schwarz S, et al. Investigations on the reactive surface modification of polycarbonate by surface-reactive injection molding. J. Appl. Polym. Sci. 2004; 93: 1186–1191.
30. Brunotte R, Mennig G, Nagel J. In-situ Surface Modification of Polycarbonate During Injection Moulding J. Appl. Polym. Sci. 2004; 93: 1186-1191.
31. Nagel J, Brunotte R, Hupfer B, Grundke K, Lehmann D, et al. Investigations into the Chemical Modification of Polyolefin Surfaces by Radical Reactions during Molding. Macromol. React. Eng. 2007; 1: 480–487.
32. Brunotte R, Nagel J, Mennig G, Heinrich G, Gehde M. Polyolefin Surface Modification During Injection Molding Using Radical Reactions in Liquid Phase. Macromol. React. Eng. 2014; 8: 412–417.
33. Nagel J, Zimmermann P, Schubert O, Simon F, Schlenstedt K. Coupling of carboxylic groups onto the surface of polystyrene parts during fused filament fabrication. Appl. Surf. Sci. 2017; 422: 28–31.
34. Kroschwald F, Nagel J, Janke A, Simon F, Zimmerer C, et al. Gold nanoparticle layers from multi-step adsorption immobilised on a polymer surface during injection molding. J. Appl. Polym. Sci. 2016; 133: 43608.
35. Ruiz-Cabello FJM, Rodríguez-Valverde MA, Cabrerizo-Vilchez MA. Contact Angle Hysteresis on Polymer Surfaces: An Experimental Study. J. Adh. Sci. Technol. 2011; 25: 2039–2049.
36. Manolakis I, Cross P, Colquhoun HM. Direct Iminization of PEEK. Macromolecules. 2011; 44: 7864–7867.
37. Yurchenko ME, Huang J, Robisson A, McKinley GH, Hammond PT. Synthesis, mechanical properties and chemical/solvent resistance of crosslinked poly(aryl-ether–

ether–ketones) at high temperatures. Polymer. 2010; 51: 1914–1920.
38. Wright M. Glyoxalated n-vinylamine. 2016.
39. Thompson SA, Farris RJ. A novel method for crosslinking polyetheretherketone. J. Appl. Polym. Sci. 1988; 36: 1113–1120.
40. Becker M, Lorenz S, Strand D, Vahl CF, Gabriel M. Covalent Grafting of the RGD-Peptide onto Polyetheretherketone Surfaces via Schiff Base Formation. Sci. World J. 2013; 2013: 616535.
41. Franchina NL, McCarthy TJ. Surface modifications of poly(ether ether ketone). Macromolecules. 1991; 24: 3045–3049.
42. Nagel J, Heinrich G. Temperature transitions on the surface of a thermoplastic melt during injection moulding and its use for chemical reactions. Int. J. Heat Mass Transfer. 2012; 55: 6890–6896.
43. Helfand E, Tagami Y. Theory of the interface between immiscible polymers. J. Polym. Sci. Part B: Polymer Letters. 1971; 9: 741–746.

Supplementary Materials:

Supplementary Materials can be accessed online at https://videleaf.com/wp-content/uploads/2020/02/SICT-19-03_Supplementary-Information.pdf

Book Chapter

A Photovoltaic Overview: from Crystalline to Thin-Film

Alessio Bosio*

University of Parma, Department of Mathematical, Physical and Computer Science, Italy

***Corresponding Author:** Alessio Bosio, University of Parma, Department of Mathematical, Physical and Computer Science, Parma, Italy

Published **December 30, 2020**

This Book Chapter is a republication of an article published by Alessio Bosio, et al. at Coatings in April 2020. (Bosio, A.; Pasini, S.; Romeo, N. The History of Photovoltaics with Emphasis on CdTe Solar Cells and Modules. Coatings 2020, 10, 344.)

How to cite this book chapter: Alessio Bosio. A Photovoltaic Overview: from Crystalline to Thin-Film. In: Surfaces, Interfaces and Coatings Technology. Hyderabad, India: Vide Leaf. 2020.

Conflicts of Interest: The author declares no conflict of interest.

Abstract

A brief overview of photovoltaic technologies, starting from the first results obtained on monocrystalline materials, passing

through epitaxial technologies up to the most sophisticated polycrystalline thin-film solar cells, is presented. Particular emphasis is given to the cadmium telluride (CdTe) technology since, among thin-film, CdTe has achieved a truly impressive development that can commercially compete with silicon, which is still the king of the market. Solar cells made on a laboratory scale have reached efficiencies close to 22%, while modules made with fully automated in-line machines show efficiencies above 18%. This success represents the result of over 40 years of research, which led to effective and consolidated production processes. Based on a large literature survey on photovoltaics and on the results of research developed in our laboratories, we present the fabrication processes of both CdTe polycrystalline thin-film solar cells and photovoltaic modules. The most common substrates, the constituent layers, their interaction, the interfaces and the different "tricks" necessary to obtain highly efficient devices will be analyzed. A realistic industrial production process will be analytically described. Moreover, environmental aspects, end-of-life recycling and the life cycle assessment of CdTe-based modules will be deepened and discussed.

Keywords

CdTe; CdS; CdSe; Polycrystalline; Thin Film; PV Modules; Recycling; Life Cycle Assessment

Introduction

Solar cells and photovoltaic (PV) modules have been intensively studied since the 1950s, when a Si-based p/n junction, able to convert sunlight into electrical energy, was made for the first time. Since then, many steps for obtaining more and more efficient devices have been made, both with laboratory-scale solar cells and with commercial PVmodules.

Many different materials were studied, which gave rise to their respective technologies. Others have been abandoned due to the inability to obtain power conversion efficiencies (PCE) high enough to be used in large-scale industrial production, or

because they did not produce devices that were sufficiently stable overtime [1,2]. Among the most successfully technologies are certainly those based on single- and multi-crystalline Si [3,4], widely used in terrestrial PV generators and multi-junctions based on GaAs technology, which are essentially used for space applications[3].

In addition to Si technology, alternative materials and production processes have been developed in order to easily realize solar devices. The research was pushed towards the optimization of the PCE/cost ratio, decreasing the amount of constituent materials and using easily available low-cost substrates, such as soda-lime glass, polymers or thin metallic foils. This was the beginning of the thin-film technology, which demonstrated its potential when a fully automated in-line machine produced the first PV module based on amorphous Si (a-Si) [5].The success of this technology is mainly due to two other materials: CdTe and $Cu(In,Ga)Se_2$(CIGS) which, thanks to the high efficiency obtained in recent years both on laboratory scale and in large modules[3], have completely replace a-Si. Nowadays, a-Si finds its principal use in consumer electronics, such as calculators, watches, toys and gadgets, while the PV market is almost completely governed by multi crystalline silicon (mc-Si), relegating thin film technology to a small percentage of the market. This is firstly due to the fact that Si technology was the first implemented at an industrial level, secondly thin film technology developed high-efficiency modules only in the last ten years, when the PV market was already well-established. However, thin film technology, with its CdTe and CIGS diamond tips, is gaining more and more space in the PV market due to its excellent performance and the over-time stability achieved in recent years.

Nowadays, the increasing demand for environmentally friendly technologies pushes research towards new absorber materials made of non-polluting and abundant elements on the earth's crust such as: Cu_2ZnSnS_4 (CZTS), SnS and Sb_2Se_3 between inorganics and perovskites and polymers among organic substances. The research on these systems is still young; for this

reason, the final performance and the over-time stability of the solar cells based on these absorbers have certainly improved.

In this work, we will only deal with thin-film technology applied to inorganic materials. In particular, we will present the CdTe/CdS system, giving a comprehensive description of all the constituent layers, the strategic choices made in over thirty years of research and the discovered tricks needed to enhance the final performance of the solar cell. The article is organized with the first section dedicated to a brief history of the inorganic photovoltaic world. The second section describes the CdTe/CdS system, the different deposition methods, the main characteristics of the constituent layers and how their mutual interactions control the final results. A portion of this section is dedicated to the latest innovations, which have led to solar cells having efficiencies high enough to compete with the other players on the PV market. The third section describes the passage from laboratory scale to the large production level, with particular attention to the industrialization of the manufacturing process. The fourth section is dedicated to the end-of-life of CdTe-based modules, considering the environmental dangerousness of some constituent elements, together with some comments on the life cycle analysis (LCA) of the whole production process. The article finishes with the Conclusion, in which the major accomplishments, some open problems with their solutions, and potential future developments are highlighted.

Inorganic Photovoltaics: A Brief History

In 1839, Edmond Becquerel [6] discovered the photovoltaic effect while performing experiments with an electrolytic cell composed of two metal electrodes: the conclusion was that some materials, notably platinum, produced small amounts of electric current when exposed to sunrays. In 1873, the British engineer Willoughby Smith [7] discovered the photoconductivity of selenium (the element varied its electrical conductivity following the illumination of the surface). Ten years later, Charles Fritts [8] invented the first solar cell by using selenium, which showed a PCE of 1%, too low for practical applications.

Silicon (Si)

It was only in 1941, that Russel Ohl produced and patented the first silicon cell [9–11], which was more efficient than the selenium one. Ohl's intuition was further developed by three colleagues from Bell Laboratories, Gerald Pearson, Calvin Fuller and Daryl Chapin [12], who built the first photovoltaic cell capable of converting solar energy into enough electricity to power a small electrical device, a radio transmitter (Figure 1a). This progress was only possible because the people involved had a good understanding of quantum processes [13] while they were developing the necessary manufacturing techniques. In a few years, silicon-based photovoltaic cells were developed with a PCE of 15%, which made the first practical application possible, including, in 1958, the artificial satellite Vanguard I, the first large-scale equipment furnished with silicon photovoltaic cells [14]. In the last sixty years, silicon technology has progressed up to an efficiency of about 26.7% on small cells (Figure 1b) and 24.4 % on large photovoltaic modules [3]. These results are based on monocrystalline silicon technique (mono-Si), essentially developed with the Czochralsky growth process [15].

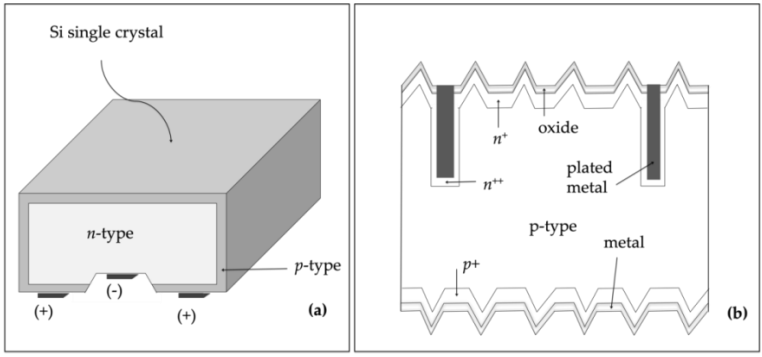

Figure 1: (**a**) first modern silicon cell, reported in 1954 [12], fabricated on single-crystalline silicon wafers with the pn junction formed by dopant diffusion. (**b**)Passivated Emitter Rear Locally-diffused (PERL) silicon cell, with light trapping, back-reflector and buried contacts, which took efficiency close to 27%.

This growth technique has found widespread use in the production of electronic chips and, while producing silicon

crystals of excellent quality, is a very energy-intensive and time-consuming technique. Electronics have overcome these problems by developing the "Very Large-scale Integration" (VLSI) technology, namely, many devices can be made using a low quantity of the precious Si single crystals. Photovoltaics, on the other hand, must use very large devices to recover energy from the sun. From this point of view, single-crystal silicon technology is not particularly suitable for use in photovoltaics. In fact, over time, an alternative technology has been developed that uses multicrystalline silicon (multi-Si) [4]. To obtain multi-Si, a less sophisticated growth technique is used, the so-called Siemens method [16]. However, this process is able to supply solar cells with an efficiency of the order of 22% on a laboratory scale and an efficiency of about 20% on large-size modules.

However, Si technology dominates the PV market with a mono-Si and multi-Si share of 60.8 and 32.2 respectively, covering 93% of the worldwide production.

Gallium Arsenide (GaAs)

In the second part of the last century, in parallel with silicon technology, other materials capable of producing sophisticated devices including high-efficiency solar cells, were studied. In particular, in 1954 Welker published a first work showing the behavior of a GaAs "photocell" as a function of illumination intensity. In 1955, Gremmelmaier [17] reported the characteristics of two polycrystalline GaAs solar cells, which had measured efficiencies of 1% and 4% while illuminated with "sea-level sunlight". Gremmelmaier expected a higher efficiency if monocrystalline GaAs was used. This material shows some intrinsic advantages with respect to silicon, such as a direct energy gap whose value is well-suited to sunlight and better withstands bombardment by ionizing radiation, making it suitable for space use. Unfortunately, GaAs is particularly sensitive to structural defects and its performance strongly depends on the intrinsic quality of the single crystal. It was necessary to wait 10 years in order to develop epitaxial growth techniques that were able to produce a small solar cell showing an efficiency of 13% [18], which is quite low compared to the

theoretical efficiency of 26% [19]. It was already known [20] that the direct recombination process, occurring in poor-quality GaAs crystals, limits the cell output. Moreover, it was shown that a high surface recombination velocity was the most probable origin of the poor performance practically obtained for GaAs cells [21]. A heteroface cell, consisting of a p-type $Ga_{1-x}Al_xAs$ or InGaP layers on a p/nGaAs cell (Figure 2a) represented the keystone to overcoming the problems related to interface states [22,23]. The great boost due to the strong demand for space cells to be installed in the ever-increasing number of telecommunications satellites meant that the GaAs technology could reach the production of 5000 cells per week with an area of 2 cm × 4 cm. This was made possible because the technology passed from the liquid phase epitaxy (LPE), developed in the 1970s in the Hughes Research Lab (HRL), to the metal organic chemical vapor deposition (MOCVD) technology developed in the 1980s by Applied Solar Energy Corp. (ASEC). The key points of this technology were [24,25]:

- Monocrystalline Ge substrate that, in addition to allowing an epitaxial growth of GaAs, provides a p/n junction sensitive to infrared light;
- Epitaxial GaAs layer, thin enough to allow infrared light to reach the junction with Ge, grown by MOCVD process;
- Upper AlGaAs layer with the primary function of eliminating surface defects and acting as a window layer for the cell;
- Antireflecting bi-layer (SiO_2+Al_2O_3) coating with the double function of minimizing the sunlight reflection and preventing any damage to the underneath AlGaAs layer due to humidity;
- Interdigitated metal (Ti–Pd–Ag) external contacts. In order to avoid any possible diffusion of metal atoms into the active layers, a capping p+ GaAs coating was deposited between AlGaAs and the contacts.

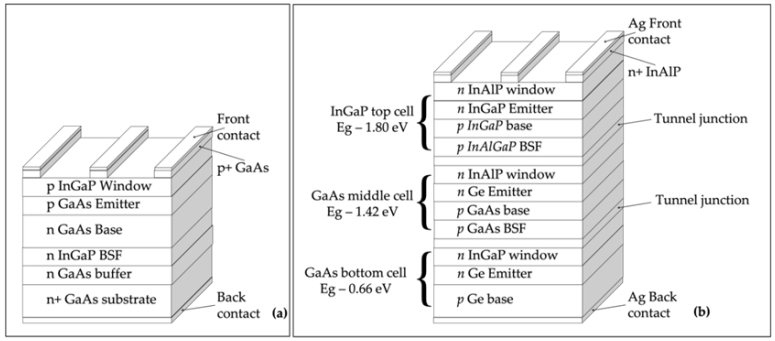

Figure 2: (**a**) GaAs single junction (SJ) with an InGaP Back Surface Field (BSF) layer. (**b**) GaAs-based triple junction (3-J) suitable for harvesting sunlight in a wide range from 0.69 to 1.87 μm.

In the1990s, dual-junction solar cells based on Ge/GaAs/AlGaAs system showed an efficiency, under extraterrestrial condition, of about 20%. In this period, many satellites were supplied with GaAs-based solar modules. GaAs panels with an efficiency over 20% represent an attractive choice for low-earth orbit (LEO) satellites [26], where the aerodynamic drag represents a problem, it is mandatory to use panels that are as small as possible; moreover, transport in orbit with a launch vehicle requires objects that are as light as possible. These considerations confirm that GaAs-based technology is widely accepted for space application. Furthermore, the MOCVD growth technique showed that only a small additional growth time is needed for adding a top cell and a tunnel diode to a bottom GaAs cell, increasing the interest in cascade cells. The higher efficiency exhibited by these cells, although costlier on cell scale, lead to a considerable reduction in the weight and costs of the whole system, making them even more attractive for space uses. On the contrary, the only way to exploit this technology for terrestrial use is to couple solar cells with light concentration systems making up for the higher cost of the system with less use of the material [27,28].

Nowadays, triple junction (3-J) GaAs-based solar cells (Figure 2b) under a concentration of 508 (508 times the irradiance of 1 sun) show an efficiency of 46% over a designed area of 0.05 cm^2. Four junctions (4-J) minimodule (10 cells) under 230 suns exhibit an efficiency of 41.4% over an aperture area of 121.8

cm^2. Multijunctions (nGaP/GaAs/InGaAs) for space use show an efficiency of the order of 31.2% under AM 1.5 [3]. At the same time, since the end of the 1970s, GaAs thin-film solar cells technology was developed [29], demonstrating its competitiveness both in terms of long-term stability and reasonable cost [30], reaching an efficiency of 29.1% (aperture area of 0.998 cm^2) in recent years [3].The main process adopted for the realization of the GaAs thin layer consists of the epitaxial lift-off (ELO) method to separate the GaAs film from the substrate. Production costs are appreciably reduced by re-using the substrate [31–33].

Copper Sulfide (Cu_2S)

Thin film technology wasn't implemented only for crystalline epitaxial growth. Materials with good photovoltaic responses both in amorphous and polycrystalline form have been studied since 1954, when Reynolds published a first work on the CdS/Cu_2S heterojunction (Figure 3a) [1,2]. This first polycrystalline thin-film solar cell raised many expectations when, around the 1980s, a 10% photovoltaic conversion efficiency was achieved using ZnCdS as a window material coupled with Cu_2S [34]. By replacing CdS with ZnCdS, the interface states introduced by the lattice mismatch between CdS and Cu_2S were almost completely removed. However, this cell did not have the success that the pioneers expected due to over-time instability problems. Briefly, Cu_2S is not a stable material when subjected to the electric field of the p/n junction; in fact, it frees Cu atoms, which form metallic filaments that channel the reverse current, causing the destruction of the junction barrier [35]. For this reason, this system was slowly abandoned, and the researchers began to take an interest in two other excellent photovoltaic materials: CdTe and $CuInSe_2$.

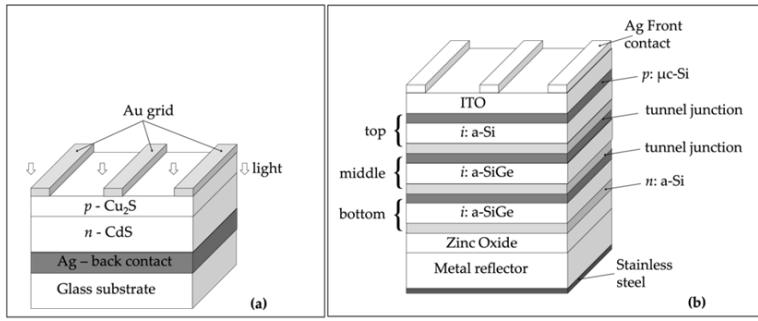

Figure 3*:* (**a**) schematic representation of the front-wall Cu_2S/CdS solar cell in which light enters the device from the top. Solar cells made with Cu_2S layer, topotaxially grown on CdS, exhibited an efficiency close to 10%. (**b**) a-SiGe-based triple junction, which exhibited a stabilized total-area efficiency of 12.1% on laboratory scale.

Hydrogenated Amorphous Silicon (a-Si:H)

In 1975, within extensive research on amorphous semiconductors, it was unexpectedly discovered that the a-Si:H alloy can be doped with substitutional impurities such as boron (p-type) and phosphorus (n-type) [36]. Immediately after this, a solar cell exhibiting a 2.4% efficiency was realized [37]. The intrinsic disorder of the amorphous phase is effective in a lot of defects, which limit the mobility and the mean lifetime, contributing to the recombination of the photogenerated carriers. For this reason, a less defective intrinsic material (i:a-Si) was used as an absorber layer. In the following years, a-Si:H-based solar cells were produced both in substrate or in superstrate configuration, which means a p-i-n or n-i-p system, respectively. It became clear that the final productivity of the cell was strongly influenced by a consistent degradation of its PV parameters as a consequence of the light exposure (Light Induced Degradation (LID)), which creates metastable states in the energy gap. The recombination of photogenerated electron–hole pairs releases enough energy to break a weak bond, producing a pair of dangling-bond defects. To prevent the recombination of the two neighboring broken bonds a hydrogen atom moves from an adjacent Si–H bond. Annealing at temperatures of about 150 °C for one hour restores the original condition, allowing the hydrogen atoms to return to their original positions. In other

words, the absence of a long-range order and the presence of dangling bonds produce states in the energy gap that prevent charge carriers to move freely [38,39]. Subsequent studies have clarified that this behavior was due in part to the large number of defects generated from the amorphous nature of the material and partly caused by interfaces; a-Si is usually grown by a plasma-enhanced chemical vapor deposition process (PECVD) in which silane is dissociated into an RF plasma [40]. The final quality of the material is determined by plasma chemistry and growth kinetics, which is highly influenced by temperature. In order to improve the film quality, the p-i-n stack was deposited at a temperature just below the amorphous-to-microcrystalline transition; to improve the interface quality, a tandem junction was realized, bringing together an a-Si:H top and microcrystalline μc-Si:H bottom cell (micromorph-cell). In this tandem cell, the different values of the energy gap of a-Si:H (1.7 eV) and μc-Si:H (1.1 eV) allows the exploitation of a wider region of the solar spectrum [41]. Starting from 1990, a new system based on three subcells integrated in a single device (triple junction) was considered, in order to improve the collection of the photogenerated carriers. The triple junction (3-J) was realized in a n-i-p sequence in which the topmost subcell exploits a typical a-Si:H-based sequence, while the middle and the bottom subcells were based on an a-Si–Ge:H alloy [42]. The Ge content was controlled in order to obtain an energy gap width of 1.6 and 1.4 eV for the middle and the bottom subcells respectively. 3-J devices (Figure 3b), realized on laboratory scale, exhibited an initial active-area efficiency of 14.6%, corresponding to a stabilized total-area efficiency of 12.1%, very similar to the best performance of micromorph tandem cells. For these solar cells, initial and stabilized, are significant for their performance before and after light-induced degradation, respectively.

The modest performance of these cells caused many market losses. This technology covered only 0.3% of the annual photovoltaic production in 2017.

Copper Indium Gallium Diselenide ($CuInGaSe_2$)

The development of $CuInSe_2$ (CIS) solar cells started in the early 1970s, when a 12% efficient solar cell based on a p-type CIS single crystal coupled with a n-type CdS thin film was realized [43]. Only few years later, the first entirely thin-film solar cell based on CIS/CdS exhibiting a 5.7% efficiency was realized [44]. Many efforts were made in order to improve the photovoltaic performance of this solar cell, involving several laboratories and researchers, but it took more than 30-40 years to realize CIS-based thin film solar cells that were efficient enough to compete with the most studied silicon-based ones. During these years, some important modifications were introduced in stoichiometry and in the growth process of the CIS film in order to completely exploit its potential. In particular, Ga was added to form $CuIn_xGa_{(1-x)}Se_2$(CIGS), whose energy band gap can be adjusted by the percentage of Ga incorporation [45]. By exploiting the higher band gap of the quaternary compound, the photovoltage (V_{oc}) increased and a reduced recombination in the conduction band of CdS was observed. All this work led to a 17.7% efficiency solar cell in 1996 [46]. MgF_2 antireflecting coating and a ZnO window layer helped to improve the photocurrent (I_{sc}), resulting in an 18.8% efficient device [47]. By gradually changing the Ga and In concentration inside the CIGS layer, a band gap grading was obtained. The interface with CdS was formed with a very thin CIGS layer with a higher Ga concentration, resulting in an increased built-in potential, which means an enhanced photovoltage (V_{oc}). By raising the In concentration in the remaining CIGS material, the energy band gap was lowered; as a consequence, the I_{sc} increased. This engineered band gap profile attained a larger diffusion length in the minority carriers and reduced recombination in the space-charge region, leading to a 19.2% efficient ZnO/CdS/CIGS solar cell in 2003 [48]. The energy band gap profile was definitively stressed when, approaching the back contact, the Ga concentration was increased inside the CIGS layer. Consequently, a larger energy gap in the back-contact region was realized and a mirror for the minority carriers was obtained, increasing their diffusion length [49,50]. In this favorable condition, a 19.9% efficient solar cell was realized in 2008 [51].

In 2010, an efficiency of 20.3% was reached [52], definitively overcoming the 20% psychological barrier. Three years later, the Swiss Federal Laboratories for Materials Science and Technology (EMPA) obtained a 20.4 efficiency CIGS-based solar cell on a flexible polymeric substrate (Figure 4a) [53]. This impressive result opened the route to the roll-to-roll continuous production of completely flexible PV modules.

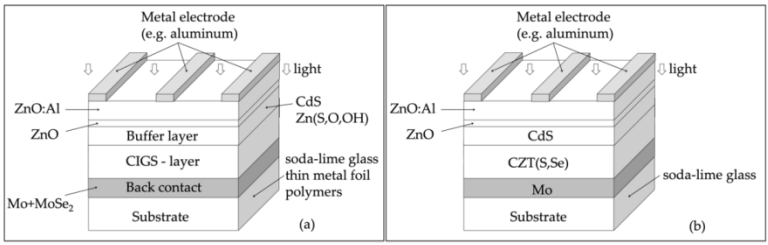

Figure 4: (**a**) CIGS solar cell which evidenced the possibility of using different types of substrates. (**b**) CZTSSe solar cell; the stacked layers are almost the same, except for the absorber.

In the same year, substituting the CdS buffer with a more environmental sustainable Zn(O,S) layer and improving the CIGS film by using potassium doping, an efficiency of 20.8% was reached [54]. The efficiency became 21.7% [55] by optimizing the alkali post-deposition treatment of the cell. Recently, a CIGS-based solar cell world record efficiency of 23.35% was achieved by Solar Frontier [56] over a designated area of about 1 cm^2. The use of $Cu(In,Ga)(Se,S)_2$, together with a high-temperature heavy alkali (Cs) post-treatment of the absorber layer, results in a reduced defect density. The enhanced quality of the $Cu(In,Ga)(Se,S)_2$ allows the opportunity to benefit from the effects of a wider absorber bandgap. Consequently, the reverse saturation current density decreases, producing an important enhancement in photovoltage and fill factor (FF), leading to the world record efficiency result.

Today, CIGS technology, with an annual production of around 1.8 GWp, covers a market share of 1.9%, which is principally supported by three producers: Miasolè, Solibro and Solar Frontier.

Within the past ten years, the photovoltaic world has realized that 20% efficiency is more than enough to guarantee the so-called grid parity, or to make photovoltaics widely competitive with traditional energy sources [57–59]. To significantly affect the world energy market, the production volume of photovoltaic modules must be a few terawatts/year (TW/yr). TW-scale production implies a correct availability of the constituent elements. For CIGS technology, the greatest risk is represented by the availability of indium (In), since it is even more widely used in expensive devices such as flat panel displays (FPD) [60,61]. In this condition, the estimates predict that the demand for In will exceed the supply, when CIGS manufacturing volumes will reach 100 GW/yr. From this point of view, it is mandatory to exploit other materials, whose constituents are more available on the earth crust. For example, we have to consider that the abundance of Cu, Zn, Sn, and Sulphur is 68,79, 2.2, and 420 ppm respectively, which is considerably higher compared to that of In, Cd, Te of 0.16, 0.15, and 0.001 ppm, respectively.

$Cu_2ZnSn(S,Se)_4$-(CZTSSe)

Ternary and quaternary chalcopyrites ($CuInSe_2$ and $Cu(In,Ga)Se_2$) represent a promising solution, but the increase in the prices of rare metals (In and Ga) heavily influences the cost-efficiency ratio.

Another opportunity is offered by replacing rare metals with cheap and widespread zinc and tin, and different new materials are considered for replacing CIGS and CdTe. Among them, one of the kesterite family, namely $Cu_2ZnSn(S,Se)_4$ (CZTSSe), has become intriguing as an alternative absorber in thin film solar cells. CZTSSe exhibits a native p-type conductivity, high optical absorption coefficient ($>10^4 cm^{-1}$ in the visible part of the solar spectrum) and tunable direct band gap in the (1.0/1.5) eV range, depending on the S and Se concentration [62–64].

In 1996, the first CZTS-based cell exhibiting an efficiency of 0.66% was realized [65]. In the following decades, the knowledge of the material improved and, as a consequence, the

performance of the solar cell increased too, reaching an efficiency of 12.6% in 2013 [66]. Different physical and chemical techniques are used for the deposition of the CZTSSe layer. Among them, the most common are: RF sputtering with post-deposition treatment in S and/or Se atmosphere at high temperature (> 500 °C), thermal evaporation, pulsed laser deposition, spray pyrolysis, spin coating, sol-gel. The best performing cell has been obtained by IBM, making use of a simple nano particle ink-based process. All these different manufacturing methods indicate a cost-effective approach for this technology, but they are not effective in terms of the finished device's performance. In fact, it was clear from the beginning that one of the main problems affecting this material is the possibility of generating many stoichiometric defects during growth both in bulk material and in the form of thin film. The similar ionic radii of Cu and Zn promote the formation of Cu_{Zn} and Zn_{Cu} anti sites, which are characterized by having the lowest energy among the acceptor and donor defects. Given the high concentration of these native defects, compensation is offered through the formation of anti site pairs $[Cu_{Zn}^{-} + Zn_{Cu}^{+}]$ distinguished by a very small formation energy. This cations disorder into the kesterite crystal lattice could be the reason for a poor performance, showing a reduction in the photovoltage and fill factor. Recently, improvements in open circuit voltage have been obtained by reducing the number of antisite defects via cation substitution with Cd, Mn, Ba, Fe, Ni and Co, demonstrating that a better control of stoichiometry is needed for obtaining high efficiencies [67]. Moreover, the most efficient CZTSSe-based devices are processed by reacting precursors at atmospheric pressure; these methods are effective in reducing the re-evaporation of high-vapor pressure compounds, such as SnSe, Cu_2SnSe_3, Zn, Se and S, and in providing good control of the CZTSSe stoichiometry. This solar cell was born with the purpose of replacing the more expensive and less sustainable CIGS and, although they have a lot in common (Figure 4b), they are still far from the remarkable performance of CIGS-based cells. One possible explanation consists in considering the different role of the grain boundaries (GB) inside CIGS and CZTSSe. Some studies have recognized GBs as the origin of the extraordinary performance of CIGS. In this material, crystal defects and

impurities present at GBs act as traps for majority carriers (holes for p-type CIGS), generating a depletion region [68–70]. The resulting electrostatic barrier repels holes from the GBs, assists electrons in reaching the n-type layers, enhancing the charge carrier collection, and prevents the recombination of the photogenerated electron-hole pairs. On the contrary, GBs in CZTS polycrystalline films act as recombination center for the electron–holes pairs and, to date, an effective method for their passivation has not yet been found.

The history of the development of the champion module efficiencies for silicon and thin-film technologies is depicted in Figure 5, together with their manufacturer, while the current performances are shown in Table 1.

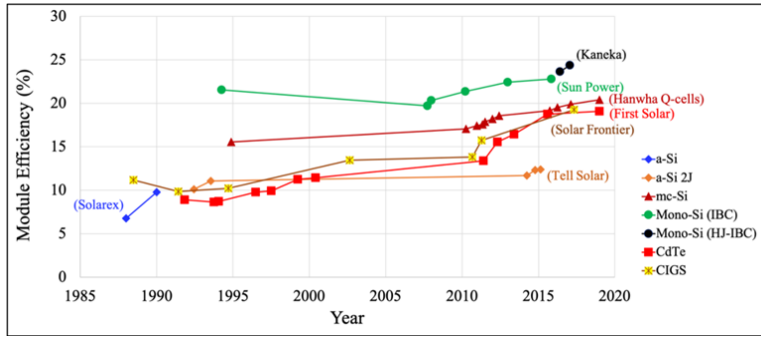

Figure 5: History of the development of the champion module efficiencies for terrestrial technologies plotted from 1988 to the present. For each technology is reported the manufacturer of the module that holds the world efficiency record. Acronym explanation: a-Si 2J = amorphous silicon double-junction cells, mc-Si = multi crystalline silicon, mono-Si (IBC) = single-crystal silicon with inter digitated back contacts, mono-Si (HJ-IBC) = single-crystal silicon with amorphous silicon heterojunction contacts made on the back of the cell. Data reported from https://www.nrel.gov/pv/module-efficiency.html.

Table 1: Photovoltaic Conversion Efficiency (PCE) of the best solar cells and commercial modules collected for different technologies. The confirmed PCE data are measured under the global AM1.5 spectrum (1000 W/m^2) at 25°C (IEC 60904-3:2008, ASTM G-173-03 global). Data reported from [3] and from www.nrel.gov/pv/cell-efficiency.html.

Solar Cells										
Parameters/ Producers	**Si Single-Crystal**	**Si Multi-Crystal**	**GaAs SJ**	**GaAs 3-J**	**GaAs 6-J**	**Cu_2S**	**CIS**	**CIGS**	**CZTS**	CdTe
PCE [%]	26.7	23.2	32.8	37.9	47.1[§]	10.0	15.4	23.35	12.6	22.1
Area[cm^2]	79*	247.79***	1000**	1047**	0.099	≈1.0	100.0***	1043*	0.4209**	0.4798*
Producer	Kaneka	Trina Solar	LG Electronics	Sharp	NREL	IEC	IPE	Solar Frontier	IBM	First Solar
Modules										
PCE [%]	24.4	20.4	–	31.2	–	–	–	18.6	–	19.0
Area[cm^2]	13 177*	14 818**	–	968*	–	–	–	10 858**	–	23 573*
Producer	Kaneka	Hanwa Q Cells	–	Sharp	–	–	–	Miasolé	–	First Solar

* (da) = designated illumination area; ** (ap) = aperture area; *** (t) = total area; § 6-J = six-junction with concentrator (143X)

CdTe-Based Technology

In the previous paragraph we presented the world of inorganic PV, except for the CdTe system. In the following, we will extensively describe the CdTe-based solar cell and modules, departing from the research which started in the 1960s and moving on to the technological aspects inherent the module production.

CdTe is considered as a very good material to serve as an absorber in solar cells, due to its direct energy gap (1.45 eV), which is nearly ideal for photovoltaic energy conversion, corresponding to the maximum of the solar spectrum. Its high optical absorption coefficient allows the incident light, with energy above its band-gap, to be totally absorbed within 1 μm from the surface. A CdTe-based solar cell could exhibit a photocurrent of 30.5 mA/cm^2 when illuminated with 100 mW/cm^2 sunlight, offering a theoretical maximum efficiency close to 30%. Historically, the best performances were typically obtained with heterojunction in which the n-type partner was cadmium sulfide (CdS). Some different attempts were tried when p-type CdTe single crystals were coupled with In_2O_3 [71], ZnO [72] or a very thin n-type CdTe layer [73], obtaining a 13.8% maximum efficiency. The success of this material was not obtained by means of single crystal but, on the contrary, by exploiting one of its best characteristics, namely the possibility to produce a complete solar cell by simply using thin-film technology. In fact, CdTe/CdS total thin film heterojunction led to a 6% efficiency solar cell and this result has been known since 1972 [74]. However, the psychological limit of 10% efficiency was overcome in the 1980s only after a heat treatment in chlorine atmosphere was applied to the CdTe/CdS stacked layers [75]. In the following ten years, devices with efficiency close to 17% were made by optimizing both the front and the back contacts [76,77]. This was followed by a period of stasis in photovoltaic performance, in part due to intrinsic difficulties, such as the impossibility of extrinsically doping polycrystalline CdTe thin films and partly due to the fact that many researchers have devoted their activities to the technological transfer of production processes from laboratory to industrial scale.

Around 2010, the photovoltaic conversion efficiency began to increase again, reaching values close to 20% in a short time. The continuous increase in efficiency is largely due to the optimization of the layers making up the antireflecting coating (ARC), the transparent electrical contact and the window layer, as well as a careful choice of the glass substrate. This led to a substantial increase in the photocurrent, going from 26.1 mA/cm^2 for a cell with 17.6% efficiency [77] to a 28.59 mA/cm^2 photocurrent for a cell with 19.6% efficiency, corresponding to a rather modest increase in photovoltage [3]. Unfortunately, there aren't any details in the literature concerning these remarkable results. However, it seems clear that the photocurrent increase is not only due to a very good optimization of the light harvesting, but also to an accurate management of the CdTe energy gap in order to extent the absorption to longer wavelengths. $CdTe_{(1-x)}(S,Se)_x$ alloys show energy band gap values smaller than CdTe when $x \leq 0.05$, corresponding to a maximum increase in the cutoff wavelength of about 15 nm. The corresponding increase in photocurrent can be evaluated in 1 mA/cm^2. Moreover, the use of a $CdTe_{(1-x)}(S,Se)_x$ mixed compound reduces the lattice mismatch at the metallurgical junction, resulting in enhanced charge transport properties. In 2015, a solar cell based on a $CdTe_{(1-x)}(S,Se)_x$ thin film exhibited a world efficiency record of (22.1 ±0.5)%, showing the following parameters measured under the global AM1.5 spectrum (1000 W/m^2) at 25 °C:V_{oc} = 0.8872 V, I_{sc} = 31.69 mA/cm^2, fill factor = 0.785 over a designated illumination area of 0.4798 cm^2 [3,78].

The fabrication process of this solar cell is particularly suitable to be implemented in a large area, fully automated, in-line production. This is made possible by the electrical in-series integration of the cells directly inside the production process (monolithically integrated) by means of a robotic laser scribing. This technology realized a 11% efficient module in 2002 by depositing the CdTe thin film with the electrodeposition technique [79]. In the years 2010–2011, the number of factories able to produce tens of megawatts/years of CdTe modules were 10 units worldwide. The production was based on the close-spaced vapor transport (CSVT) or close-spaced sublimation (CSS) techniques for the deposition of the CdTe layer and an

average module efficiency ranging from 10% to 12% was announced. At the end of 2012 a 14.4% efficient device was reported, which became 16.1% at the beginning of 2013. In March 2014, a 17.5% efficient module was obtained, followed by a world efficiency record of (18.6 ± 0.5)% in 2015. The photovoltaic parameters of such a module, taken under the global AM1.5 spectrum (1000 W/m^2) at a cell temperature of 25 °C, are: V_{oc} = 110.6 V, I_{sc} = 1.533 A and fill factor = 0.742 over a designated illumination area of 7038 cm^2 [3]. Commercial modules with an efficiency of 18.2% are now available on the market [81]. First Solar, with a 2.4 GWp annual production, covers 2.3% of the market share.

The Solar Cell

A CdTe-based solar cell is typically realized with very thin stacked layers, arranged in such a way to form a high-quality heterojunction. When CSS or CSVT techniques are used, CdTe thin films naturally grow as p-type and are forced to select a n-type partner to make the p-n junction. The architecture of the heterojunction allows sunlight to pass through the n-type layer to reach CdTe where photogeneration takes place. To date, the best-found configuration is the CdS/CdTe system, where CdS is the "window", while CdTe is the "absorber". For this reason, the thickness of CdS film is never more than 100 nm to ensure excellent transparency. The free carrier concentration of both the window and absorber films ensures that the electric field mostly falls into the absorber material, so that all the photogenerated electron–hole pairs can be separated and pushed towards the external electrical contacts. These auxiliary layers complete the device, ensuring the passage of the photocurrent. High-efficiency CdS/CdTe solar cells are produced in a superstrate configuration, which means light passes through the substrate and the front contact is as transparent and conductive as possible. Instead, the back-contact, which is generally opaque, has to ensure the ohmicity with p-type CdTe in order to efficiently harvest all the photocurrents (Figure 6a).

In substrate configuration, the manufacturing sequence starts with the back contact, followed by the CdTe/CdS films, ending

with the transparent electrical contact (Figure 6b). This configuration is particularly intriguing since it allows devices to be made on opaque substrates such as metal and polymeric foils, paving the way for the production of flexible, light and cost-effective modules. Moreover, flexible substrates enable the roll-to-roll technique, which is very suited for vehicle- and building-integrated photovoltaics (VIPV and BIPV). It is undeniable that this architecture could overcome one of the problems of superstrate configuration; in fact, CdTe doping and CdTe/CdS junction formation are separated production steps, which could be individually optimized. On the contrary, one of the unsolved issues is the formation of an ohmic back-contact, which is partly resolved by the introduction of a buffer layer between the metallic part of the contact and the CdTe surface. By using Te/MoO_3 and Cu_xTe as buffer layers, coupled with a Mo metal contact, solar cells exhibiting efficiencies in the range (13.6-11.3)% are obtained [82,83]. Furthermore, individual cells, monolithically integrated inside a module, require the electrical insulation of the metal substrate from the back-contact, otherwise series interconnection would not be possible, as the system has a common electrode. This dielectric film also acts as a barrier against the diffusion of metal atoms from the substrate into the absorber layer and, consequently, to the junction region. Al_2O_3 or SiO_2 films, 100 nm thick, directly sputtered onto the metallic substrate, are excellent buffer layers from both these points of view.

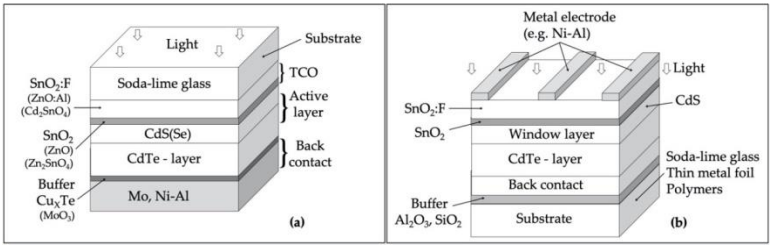

Figure 6: The CdTe/CdS solar cell; (**a**) superstrate configuration (light enters through the substrate), (**b**) substrate configuration (substrates could be opaque).

The final behavior of the CdTe-based solar cell strongly depends on the interaction among the constituent layers, which depend on the deposition order, highlighting that the layer sequence is

crucial. CdTe/CdS solar cells realized in substrate configuration are younger compared with the superstrate ones, and a lot of research on the layer interaction, diffusion, interfaces, back-contact and doping issue should be done.

We are principally interested in superstrate configuration, since the best performances are obtained by solar cells fabricated following this arrangement.

Briefly summarizing, the main steps of the production process are: (i) to deposit cadmium and tellurium as inexpensively as possible, (ii) to activate the system in chlorine environment at high temperature, (iii) to couple a window layer to the absorber layer to form an efficient heterojunction. The other production steps are typical of thin-film technology such as the choice of the electrical contacts, whose principal requirements are to be as conductive as possible and to be transparent to sunlight in case of the front contact. Since we are dealing with superstrate configuration, the substrate must be chosen to ensure maximum light transparency for the whole useful life of the solar cell.

Now, we will review each of the production steps and the main requirements the individual materials should have.

The Substrate

Rigid glass is normally used in the superstrate production of high-efficiency cells and modules. Since solar light passes through the substrate, glass has to be as transparent as possible in order to minimize parasitic light absorption. The most common commercial glasses are generally known as “soda-lime glass” (SLG). Silica (SiO_2) is the principal component of this type of glass (up to 75% - 76%), making it particularly resistant to thermal shocks, but its high melting point and its viscosity make processing difficult. To simplify the manufacturing process, other substances are added. One is “soda”, or sodium oxide (Na_2O) (14%), for lowering the glass transition temperature. Nevertheless, soda makes glass unwantedly water-soluble and, in order to provide a better chemical stability, “lime” or calcium oxide (CaO) is also added (9%). In addition, magnesium oxide

(MgO) and alumina (Al_2O_3), contribute to durability (see Table 2). Inexpensive minerals such as trona, sand, and feldspar are typically used in place of pure chemicals, making soda lime glass really cost-effective. Unfortunately, when starting with minerals, some impurities, such as Fe_2O_3 and MnO_2, which are responsible for a transparency decrease in the visible part of the solar spectrum, are un-intentionally introduced. For this reason, iron-free glasses are normally used in CdTe technology, gaining 8% transparency at short wavelengths ($\lambda < 300$ nm) [84].

Table 2: By weight composition of commercial soda-lime glass. In iron-free glass, iron oxide (Fe2O3) is discarded from the starting material.

Oxide	**SiO_2**	**Na_2O**	**CaO**	**MgO**	**Al_2O_3**	**K_2O**	**TiO_2**	**SO_3**	**Fe_2O_3**	**Others**
Weight [%]	72.85	12.42	8.15	4.09	1.27	0.47	0.37	0.18	0.10	0.10

Some attempts to employ flexible substrates were made by using polymers, such as the Dupont's polyimide, which permits a high-rate roll-to-roll technology in order to produce large-area, very light photovoltaic devices at reasonably low costs. The optical transparency of standard SLG and polyimide are comparable at long wavelengths, but below 530 nm polyimide transmittance is not enough for PV application, despite thin foils being used (Figure 7a). This turns into a photocurrent loss of at least 3 mA/cm^2. For this reason, together with the temperature limitation, solar cells realized with this polymer never exhibit an efficiency over 13.8% [85].

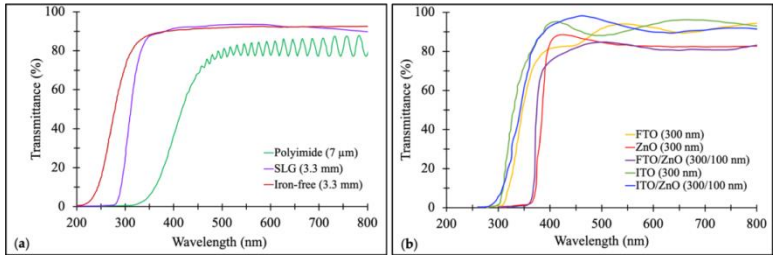

Figure 7: Transmittance spectra of: (**a**) commonly used substrates such as soda-lime glass (SLG) and polyimide; (**b**) SLG (3.3 mm thick) covered with only ITO or FTO and SLG covered with ITO or FTO coupled with ZnO as a high-resistivity transparent (HRT) layer.

The Transparent Electrode

In thin-film photovoltaic technology, one of the most severe requirements is the use of transparent and conductive electrodes, capable of letting light pass through, which must reach the underlying active layers and must be electrically conductive in order to efficiently collect the photogenerated carriers without introducing unnecessary series resistances. Transparent and conductive oxides (TCO) are high-performing, exhibiting transparencies close to 90% in the wavelength range of the visible light and electrical conductivity up to $10^4\ \Omega^{-1}\cdot cm^{-1}$. A high electrical conductivity and high transparency to visible light seem to be contradictory. In fact, these requirements need opposite properties in terms of band gap, which must be:

- Large enough to avoid optical absorption;
- Small enough to allow the filling of the conduction band by a near-free electron at the working temperature.

Concerning the optical transparency, the low-energy limit is set by the width of the energy band gap. On the other hand, the electrical conductivity needs heavy doping, which often means a degenerate condition characterized by the Fermi level inside the conduction band. In this condition, the energy gap, evidenced by the absorption of light, is wider when compared with the fundamental one, according to the Burstein–Moss effect [86].

The most common TCOs used in CdTe technology, are: Sn-doped In_2O_3 (ITO), F-doped SnO_2 (FTO), Al-doped ZnO (AZO) and Cd_2SnO_4 (CTO). These TCOs are near-degenerate semiconductors, but only ITO exhibits a typical free-carrier absorption in the near-infrared (NIR) region of the solar spectrum. This drawback, together with the indium scarcity [87], implies that ITO is not widely used in PV industrial production. All these TCOs are coupled with high-resistivity transparent oxide buffer layers (HRT's) with the aim of reducing shunt effects coming from pinholes in active layers hindering the diffusion of impurities from TCOs or from the substrate. The transmittance of some of these TCO is reported in Figure 7b. On laboratory scale, un-doped SnO_2, In_2O_3 and ZnO are HRT layers

commonly coupled with ITO, while FTO is generally paired with pure SnO_2 and CTO is combined with Zn_2SnO_4 (ZTO) [88]. The typical bilayer structure of these TCOs change the chemical and physical interaction between the front contact and the window layer, as is seen when ZnO and CdS, brought at high temperature, form an intermixing layer, which modifies the optical properties of both films.

The Window Layer

The most used n-type partner with CdTe is cadmium sulfide (CdS), which exhibits n-type conduction due to stoichiometry defects, such as sulfur vacancies, which are formed during the film growth. With an energy gap of 2.42 eV, it allows sunlight to pass up to a wavelength of 512 nm, inhibiting the passage of the near ultraviolet light to which SLG substrate and TCO layers are still transparent. Moreover, self-doping is effective in obtaining resistivity of the order of (10^6-10^7) $\Omega \cdot$cm, the same order of magnitude obtained with CdTe films. A golden rule for the formation of a p/n junction in efficient solar cell is that the electric field falls principally into the p-type region (CdTe). As the mobility of electrons in CdS is significantly greater than the mobility of holes in CdTe, this requirement is satisfied only if the density (p) of the p-type carriers in CdTe is appreciably less than the density (n) of the n-type carriers in CdS. In dark conditions, this rule is not satisfied, but under light, where the solar cell works, the photoconductivity of CdS helps to distribute the electric field into the CdTe film. Concerning the transparency of the wavelengths of sunlight, which are shorter than the gap cutoff, since nothing can be done about the absorption coefficient (α), it is only possible to work on the optical density ($\alpha \cdot d$) by using extremely thin films, allowing the passage of light despite the high value of the absorption coefficient ($t < d$, $t \leq 100$ nm, where d is the average absorption length and t is the film thickness).

In order to better exploit the visible spectrum of sunlight, window materials with a wider energy band gap were studied. The ZnCdS system, varying the energy band gap from 2.42 (CdS) up to 3.6 eV (ZnS), seemed a good candidate. The

expected increase in the photovoltaic parameters (V_{oc} and I_{sc}) of the ZnCdS/CdTe solar cells did not take place [89]. The most reliable explanation is that interface defects have increased because the Zn–Cd–S–Te system is not as favorable as the Cd–S–Te one in reducing the structural defects responsible for the recombination of the photogenerated carriers. In fact, it is now accepted by many researchers that CdS is crucial for obtaining solar cells with excellent performances, despite the high lattice mismatch with CdTe (≈10%). This drawback is overcome since the deposition high temperature of CdTe guarantees a strong interaction between the two materials. As a consequence, an intermixed layer is formed, minimizing the lattice mismatch and the interface states resulting from structural defects.

Since the quality of the solar cell strongly depends on the interaction between the active layers, the deposition techniques used for the film growth play an essential role. The techniques generally used for the deposition of both the active layers can be divided into low (L-T) and high temperature (H-T).

CdS is normally deposited at a substrate temperature below (L-T) or above (H-T) 200 °C. RF sputtering, chemical bath deposition (CBD) and high vacuum thermal evaporation (HVTE) belong to L-T processes, while close-spaced sublimation (CSS) and close-spaced vapor transport (CSVT) are H-T deposition procedures.

The CBD process gives high-quality CdS films characterized by a very high density and compactness which are pin-hole free, but as-deposited films are not suitable for the formation of an efficient junction when coupled with CdTe [90,91]. A heat-treatment at 400°C is needed to remove the Cd and S excesses naturally present in the L-T deposited films. This treatment is also effective in changing the crystalline structure from a hexagonal-cubic mixed phase to a more stable unique wurtzite phase.

On a laboratory scale, this method offers excellent results, but in industrial production sputtering and H-T processes are generally

preferred since CBD is a low-speed process and it produces a large amount of waste, which must be expensively recycled.

CdS films can be sublimated at temperatures above 700 °C in a high-vacuum chamber and deposited on a substrate held at a temperature below 200 °C. As in the case of the CBD deposition, an annealing at a temperature of 400 °C, under vacuum or in a hydrogen atmosphere, is needed to remove stoichiometry defects and to obtain the necessary chemical stability. Unfortunately, CdS films deposited with this technique have low compactness with a high density of pinholes.

For this reason, very thick CdS layers (≈300 nm) must be used to produce efficient solar cells, but with unavoidable photocurrent loss due to poor light collection.

The HVTE technique is used for producing flexible PV modules, where a thin polymeric foil is used as a substrate, which can withstand temperatures up to 400 °C [92].

Sputtering is considered a L-T deposition technique even though the surface of the growing film is constantly bombarded by electrons and impinging atoms, which exchange their kinetic energy and promote typical high-temperature effects. In fact, the RF sputtering deposition is not suitable to produce CdS films with the proper quality and chemical stability to be used in CdTe-based solar cells. Only reactive RF sputtering, introducing oxidizing atoms into the process chamber, such as fluorine- or oxygen-containing gases, produce high-quality CdS films which are able to form a good CdS/CdTe heterojunction. What happens in the sputtering discharge when a hydrofluorocarbon or oxygen gas is added to the process gas (Ar) is well known: the glow discharge ionizes the decomposed elements of the reactive gas, producing free fluorine or oxygen ions [93]. Some of these, being electronegative, become negative ions and, as a consequence, they hit the surface of the growing film, which could be considered the positive electrode for the main part of the RF period. These ions have sufficient energy to sputter-back the weakly bonded Cd and S atoms on the surface of the CdS film. As a result, a stoichiometric, dense and better-crystallized

film is obtained with a great improvement in optical and structural quality. Moreover, fluorine or oxygen ions could react with CdS, forming CdF_2 or $CdSO_3$, respectively. These are excellent dielectric insulating materials, principally segregated into the grain boundaries of the polycrystalline CdS film, contributing to their passivation. The same segregation on the surface of the growing CdS film may adjust the interaction with CdTe during its high-temperature deposition (Figure 8b). Among the H-T deposition technique, CSS is the most popular and CdS films obtained with this process exhibit superior qualities, even though depositions carried out in pure Ar provide low-density films with many pinholes. If oxygen is added into the process chamber, the deposition equilibrium is substantially altered and the growth slows down, since the grain boundaries of the growing film are decorated with oxides ($CdSO_4$, $CdSO_3$) [94]. As a consequence, a denser film without pinholes is easily obtained. In this case, the CdS surface is covered by a mixed $CdSO_4$-$CdSO_3$ thin layer. High-efficiency solar cells are obtained when, CdS films deposited with CSS in Ar + O_2 process gases, are annealed in an H_2 atmosphere (Figure 8a).

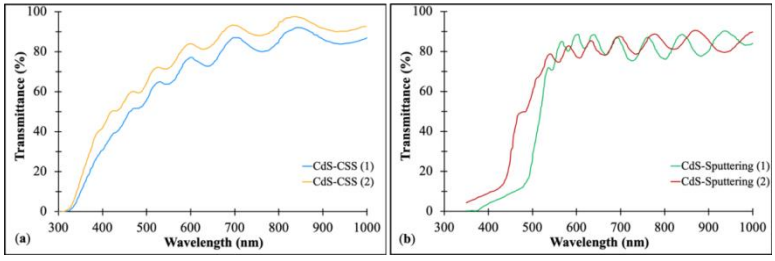

Figure 8: Transmittance spectra of: (**a**) 300 nm thick CdS film prepared by CSS in Ar + O_2atmosphere: (1) as-deposited, (2) after annealing for 30 min at 420 °C in 400 mbar of Ar containing 20% of H_2; (**b**) 80 nm thick sputtered CdS film: (1) deposited in pure argon and (2) deposited in argon + CHF_3. The shift toward shorter wavelengths of the absorption edge demonstrates the helpful effect of deposition in the presence of fluorine.

The Absorber Layer

Homojunction, heterojunction, p-i-n and Schottky barrier have been historically investigated for CdTe-based solar cell production [95–97]. It was immediately clear that heterojunction

is the most efficient structure, probably due to the intermixing layer formed during CdTe deposition or during post-deposition heat-treatments. This layer, removing the structural native defects, makes the window/absorber interface very close to a homojunction exhibiting an ideality factor close to unity. This homojunction-like behavior characterizes the high-efficiency CdTe polycrystalline thin-film solar cells, confirming that the recombination centers are far away from the junction, i.e., the depletion layer is virtually free of interface states.

Typically, L-T and H-T deposition technologies are both widely used to produce CdTe thin films.

The highest efficient devices are generally obtained by H-T processes, in particular CSS (Figure 9) and CSVT, which are industrially implemented for the production of commercially available 18% efficiency CdTe-based modules. Due to the high deposition temperature, the polycrystalline films are characterized by large, columnar and slightly defective grains with an average dimension in the range of (5/10) μm for film thickness of about (6/8) μm. These techniques allow high growth rates (up to some μm/min) at the expense of a homogeneous growth of the crystalline grains. As an immediate consequence, wide grains, with a lot of pinholes in the middle, are routinely obtained although, the film thickness is already very large.

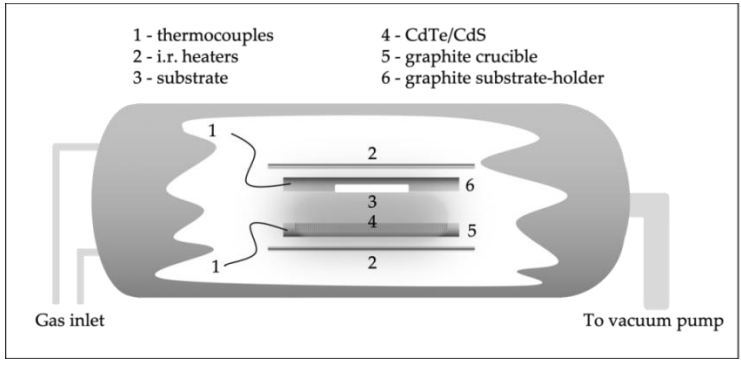

Figure 9: Not in scale outline of the CSS system for the deposition of CdTe and CdS films. The distance between crucible (5) and substrate (6) is of the order of 0.5 cm.

In this form, it is very hard to extrinsically dope CdTe, because any attempt carried out to date has highlighted the tendency of p-type dopants to segregate into the grain boundaries, generating short-circuit paths that kill the junction. With only the intrinsic doping, due to stoichiometric native defects, the typical dark p-type conductivity, shown by CSS-deposited CdTe films, is of the order of $(10^{-4}/10^{-5})$ $\Omega^{-1}\cdot cm^{-1}$. By considering the absorption coefficient, the visible light penetrates into the CdTe layer up to 1 μm. Due to photo-generation, this part becomes more conductive (10^{-2} $\Omega^{-1}\cdot cm^{-1}$), while the rest of the film, persisting in dark conditions, cannot change its electrical conductivity. This corresponds to a series resistance which afflicts the device, inhibiting the complete collection of the photocurrent.

From this point of view, it is mandatory to reduce the thickness of the CdTe layer, since a thickness of around 2 μm is more than enough to absorb all the visible light, considering that CdTe exhibits an absorption coefficient in the range of $(10^4/10^5)$ cm^{-1}. This thickness is optimal both for optical and electrical requirements, even though it's very difficult to obtain CSS-deposited pinhole-free films with the requested quality and compactness.

In order to avoid these two unpleasant drawbacks, oxygen is generally added to the inert gas in the CSS or CSVT process chamber. Due to the presence of CdO and TeO_2 species, an increased surface diffusion of the incoming Cd and Te atoms is expected; as a consequence, a less defective CdSTe layer could be formed. The presence of oxygen affects the nucleation process, increasing the number of nucleation sites and promoting a denser growth of the CdTe film. In these conditions, a small amount of $CdTeO_3$ is formed, performing an appreciated passivation effect of the grain boundaries [98].

A similar result is obtained if oxygen is added to the Ar process gas during the CdTe sputtering deposition by using a ceramic target. In both cases, a reduction in the grain size is clearly evidenced and a deep profiling analysis, made by secondary ion mass spectroscopy (SIMS), put in evidence a Te-rich surface concerning the CSS-film, while the sputtered CdTe layer shows

a Cd-rich stoichiometry on the surface [99]. The sputtered film exhibits a n-type conductivity of about 10^{-3} $\Omega^{-1}\cdot cm^{-1}$. A sputtered thin film, deposited on top of a CSS-deposited one, is mainly segregated into the grain boundaries, filling in all the pinholes and giving rise to a p-n junction formed between the grain boundaries and the bulk. This beneficial passivation efficiently acts as a mirror for the minority carriers, increasing their lifetime and preventing shunt paths in the junction region.

In recent years, an attractive hypothesis about the optimization of the photovoltaic parameters of the CdS/CdTe solar cell has been considered. In particular, it is known that a solar cell under AM 1.5 G reaches maximum efficiency when the energy gap of the absorber layer is 1.34 eV [19,100]. From this point of view, the energy gap of CdTe is slightly wider, being 1.5 eV. Following this idea, First Solar improved the efficiency of the CdTe-based solar cells by using $CdTe_{(1-x)}Se_x$ as an absorber material. In fact, by adjusting the stoichiometric composition x, a graded profile of the energy gap could be obtained. According to [101], when $x \approx 0.4$, the energy gap of the $CdTe_{0.6}Se_{0.4}$ alloy is 1.4 eV and a better collection of the solar light extended to a longer wavelength compared to the pure CdTe is observed. An engineered profile of the energy gap could be effective in improving the photocurrent if a $CdTe_{(1-x)}Se_x$ alloy is used in the front region, while maintaining the photovoltage in the bulk of the CdTe layer. Moreover, when a CdS/$CdTe_{(1-x)}Se_x$ heterojunction is made, it was found that the thickness of the CdS layer can be drastically reduced or the layer can be avoided, decreasing the parasitic absorption in the high-energy region of the solar spectrum, and obtaining an increasing photocurrent [102]. Additional improvements can be obtained if the CdS layer is replaced with MgZnO, a material with which CdTe and $CdTe_{(1-x)}Se_x$ have a better alignment to the energy band. This material is characterized by a better transparency in the high-energy region with respect to CdS [103,104]. Furthermore, a greater passivation effect of the defects due to the presence of Se is effective for a longer lifetime of the charge carrier in $CdTe_{(1-x)}Se_x$ compared to CdTe [105]. By adopting these measures, solar cells with an efficiency of over 22% were obtained, including the world record [3].

These excellent results are a consequence of more than 20 years of research focused on all the aspects that influence solar cell behavior, including materials, interfaces, deposition techniques, electrical contacts, substrates and last but not least, production techniques which must be intrinsically easy enough to scale up to the industrialization of large modules.

However, alternative ways to achieve high efficiency devices should not be overlooked. In fact, high-efficiency solar cells have also been made on flexible polymeric substrates, where the basic requirement is a low process temperature.

CdTe and CdS films, deposited by HVTE at a temperature of about 200 °C with a typical thickness of (2/3) μm, show very good smoothness and compactness with a characteristic grain size of (100/500) nm [106]. The dimension of crystallites suggests that the mobilities and lifetimes of the charge carriers are very low, and not suitable to form an efficient p-njunction capable of properly collecting the photogenerated carriers.

Never, as in this case, is a post-deposition treatment, the so-called "chlorine treatment" needed. This heat-treatment has the ability to reduce the stacking faults, misfit dislocations and grain boundaries, increasing, accordingly, the crystalline grain size [107]. By using commercial FTO-covered SLG substrates, all HVTE-deposited CdS/CdTe solar cells exhibit efficiencies of about 15%. The efficiency is lowered to 12% if a polyimide substrate is used [108].

Among the L-T techniques, the electrodeposition of semiconducting materials was originally presented in the 1970s [109,110]. Only in the early 1980s was an all thin-film electrodeposited CdTe-based solar cell developed, exhibiting a notable efficiency of 8% [90,111,112]. Recently, a record efficiency of 15.3% has been announced, exploiting a different device architecture. Normally, the electrodeposited CdTe layer exhibits a n-type conductivity. As a consequence, the active junction is shifted at the back-contact, which forms a Schottky barrier with CdTe. An innovative SLG/FTO/n-CdS/n-CdTe/p-CdTe/Au layer sequence was implemented for producing the

record solar cell. The main improvement is represented by a buried-homojunction close to the back-contact. The presence of a p-type CdTe thin film at the back-contact allows for better control of the junction position inside the absorber layer, resulting in an enhanced barrier height and photogenerated carrier collection [113].

RF magnetron sputtering deposition is a simple technique for industrial coating needs after being scaled down to laboratory requirements. For this reason, the opposite path is considered obvious and sputtering technique is increasingly considered a key process when a high-density film with good adhesion to the substrate is requested [114]. When CdS and CdTe compounds are deposited, the electro-optical properties of the films strongly depend on the sputtering parameters as well as the sputtering power, Ar and reactive gas pressure, bias voltage, substrate temperature, target-to-substrate distance, etc. This great variety of process parameters allows a very fine-tuning of the physical characteristics of the growing film. Exploiting the excellent coverage and high density of the sputtering-deposited films, a 2μm thick CdTe layer is used to realize very thin solar cells [115]. By suitably adjusting the chlorine treatment, CdTe thin films with crystalline grains large enough for achieving high-efficiency solar cells could be obtained. Following this philosophy, in the early 2000s a 14% efficient solar cell has been produced [116].

The Heat-Treatment

It is not important which technology is used to deposit the CdTe layer; whether it is LT or HT, the result obtained is always the same, i.e., very limited conversion efficiency. Evidently the as-deposited material does not have a suitable crystalline quality to obtain a good device, since it is characterized by a large number of structural defects, which hinder the motion of the charge carriers promoting the recombination of the photogenerated electron–hole pairs.

For this reason, in CdTe technology an annealing, at a temperature in the range (350/400) °C, in chlorine atmosphere, is

currently used. This treatment is inspired by the monocrystalline vapor phase growth of II-VI compounds, in which the transport agent is a halogen gas, normally chlorine. Historically, chlorine is supplied by depositing a $CdCl_2$ on the top of the CdTe film. A first attempt was made by vapor depositing a $CdCl_2$ thin film or by drop-casting a Cl-salt/methanol solution followed by an air-anneal. At the treatment temperature, the surface of the CdTe film becomes mobile due to the vapor pressure, and the following process is normally assumed to occur:

$$CdTe(s) + CdCl_2(s) \rightarrow 2Cd(g) + \tfrac{1}{2}Te_2(g) + Cl_2(g) \rightarrow CdCl_2(g) + CdTe(s) \quad (1)$$

During the annealing, CdTe re-crystallizes, changing its morphology (Figure 10). A better-organized crystalline matrix is formed, small grains disappear and the CdS/CdTe interface is re-organized, removing the typical defects due to the lattice mismatch [117]. Moreover, treated samples exhibit a very good response in the long wavelength region of the visible light. These photons are absorbed far away from the CdS/CdTe region and the photogenerated electron–hole pairs must live long enough to reach the external electrical contacts. This is possible only if recombination is negligible, which means an absence of structural defects.

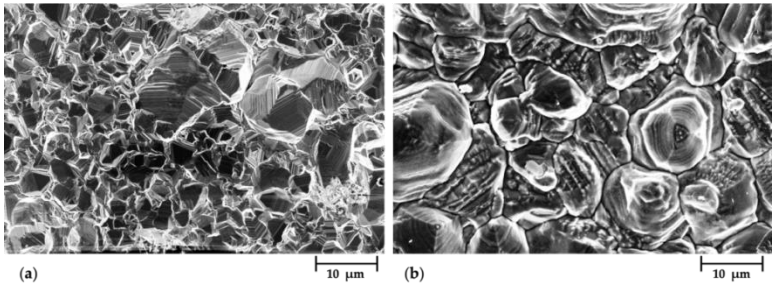

Figure 10: SEM images of CdTe film morphology (**a**) before, and (**b**) after chlorine-treatment with Ar + HCl + fluorine-containing gas (R-23).

As a chlorine supplier, other Cl-based salts have been used; among them, the most popular are NH_4Cl, NaCl, $MgCl_2$, $ZnCl_2$ [118–121]. These Cd-free salts are more environmentally sustainable than $CdCl_2$. Recent studies have been demonstrated

that the replacement of costly and toxic $CdCl_2$ could be made by using nontoxic and more cost-effective $MgCl_2$ [122] without losing solar cell performance.

A good alternative to Cl-salts is represented by halogen gas, which is able to release chlorine radicals in the heat-treatment ambient at the annealing temperature. Since Cl-containing gases are very aggressive with CdTe surface, the re-crystallization process becomes extremely critical [99,123,124]. The reaction returns under control if a fluorinated hydrocarbon is added into the treatment chamber. In the presence of F_2 or F-based radicals a fluorine compound, such as CdF_2, could be formed. The presence of CdF_2 is effective in lowering the growth rate of the Cl-containing counterparts ($CdCl_2$), resulting in the decreased reactivity of all the system.

All studies, regarding chlorine heat-treatment, unequivocally claim that the solar cell efficiency strictly depends on how effective the re-crystallization of the CdTe grains is, and on the quality of the intermixing layer at the junction region. These results reveal that the lower dissociation energy of the salt molecules promote greater recrystallization and, in turn, higher conversion efficiency.

These findings help to choose the best candidate for substituting $CdCl_2$ and underline that Cl-containing gases, with the addition of fluorinated hydrocarbons, could be a good option.

The Back-Contact

One of the criticisms encountered in the high-efficiency CdS/CdTe solar cell production is the realization of an ohmic, stable over-time, back-contact. Commonly, many production processes make use of a Cu-containing compound, such as Cu–Au alloy, Cu_2Te, ZnTe:Cu and Cu_2S [125–128]. Excluding the Cu–Au bilayer, the electrical contact is finished with the deposition of a metallic layer such as Mo, Ni–V or graphite paste.

The diffusion of copper into the CdTe layer reduces its resistivity, promoting the formation of a very low resistance ohmic contact suitable for high-performance solar cells.

Devices made with contacts not containing Cu show a high series resistance, principally due to the non-ohmic contact. For this reason, the highest efficiency solar cells have been made, exploiting the presence of some Cu-based compound at the back-contact.

Typically, a chemical attack in Br_2-methanol or in a mixture of HNO_3/HPO_3 acids is performed, which leaves the surface of the CdTe film as Te-rich. A Te-rich surface promotes the correct band alignment between the valence band of CdTe and the work function of the metal contact and/or the electronic affinity of a degenerate semiconductor, through the formation of a low-resistance tunneling barrier.

Since copper is very reactive with Te, a thin layer of Cu_2Te is formed at the interface between CdTe and the back-contact, which limits the copper diffusion into the grain boundaries of the absorber film. Unfortunately, Cu_2Te is not sufficiently stable since it releases copper atoms directly in contact with the surface of the CdTe film, triggering the usual diffusion into the grain boundaries. To overcome this regrettable problem, a fine control of the amount of copper, directly in contact with the Te-rich surface of the CdTe layer, is mandatory. Different solutions are proposed; the most reliable make use of a very thin layer of Cu (0.5 nm) or of a buffer layer, which acts as a filter for the diffusion of the Cu atoms. In both cases, the formation of a Cu_xTe layer is needed to ensure a good quality contact and to break the Cu diffusion, but Cu_xTe behaves like a stable material only if $x \leq 1.4$. This condition is achieved by placing a buffer layer, based on M_2Te_3, between the very thin layer of Cu and the surface of CdTe (where M = Sb, Bi, As)[129,130]. Two different phenomena are present: (i) the M atoms can bind the tellurium excess, forming a M_2Te_3 or Cu_xTe degenerate interface layer, confirming the fundamental role of a CdTe Te-rich surface. (ii) An air heat-treatment of the whole system, carried out at a temperature of 200 °C for 15 min, promotes the formation of an

oxide into the grain boundaries of the CdTe layer, which contributes to the passivation of the grain boundaries by removing their capacity to recombine the charge carriers. A similar result is obtained if a ZnTe film is used as a buffer layer [131].

This is a general recipe; if respected, an efficient and durable solar cell is routinely realized, allowing the industrial production of CdTe-based large modules.

The Industrial Production

At present, an in-line, fully automated machine is able to produce large CdTe modules (≈1 m^2) with a cycle time of about 1 min. The mainly exploited technologies are CSS or CSVT for the deposition of the CdTe layer and sputtering for the remaining films. Exploiting the thin-film technology, the in-line production machine carries out the monolithical series-integration of solar cells, by selective laser scribing of constituent layers at different stages of the production steps. In this way, a soda-lime glass enters the machine at the first stage and a finished PV module comes out from its last section (Figure 11). A typical engineered process consists of the following main steps [80]:

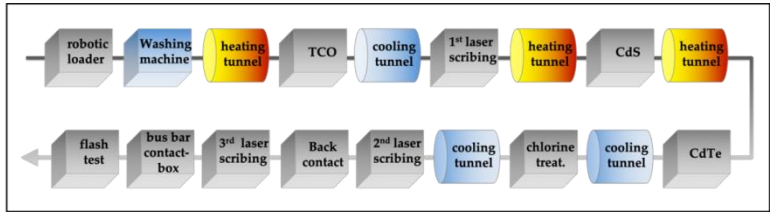

Figure 11: Flow diagram of a fully automated in-line process for the production of CdTe/CdS based PV modules.

Substrate Cleaning: The first stage of the in-line production machine is a robotic loader connected with a washing machine. The substrate, typically iron-free SLG is washed by means of pressurized deionized water jet and then dried in a filtered hot air stream.

1st-Heating Tunnel: The SLG substrate moves on a rail in vertical or horizontal position according to the operations it needs. The glass enters evacuated chambers at a 10^{-6} mbar residual pressure to be heated up to the deposition temperature of the TCO layer. The heating must be very uniform to avoid thermal shocks, which could cause glass break. Considering that glass moves at a speed of 1 m/s and it cannot be heated with a rate greater than 25 °C/min, the heating tunnel must be at least 7 m long if the deposition will take place at a temperature of 200 °C or 14 m if the temperature should be 400 °C. The heating system is equipped with infrared (IR) lamps and a PID system controls the power supply through the temperature feedback.

Sputtering TCO: In case TCO consists of the ITO + ZnO bi-layer, the deposition takes place at 400 °C to guarantee the correct stability of the stacked films. The sputtering chambers are equipped with a number of targets sufficient to deposit 500 nm of ITO and 150 nm of ZnO in the transit time of the SLG substrate. Typically, four ITO targets, and two for ZnO, are enough to accomplish this task.

The targets, in a vertical position, are of the cylindrical-rotating type to efficiently use up to 95% of the starting material. ITO and ZnO targets are deposited by means of a DC- and RF-sputtering power supply, respectively. If commercially TCO-coated SLG substrates are used, this deposition step is not present in the first part of the production machine.

1st Cooling Tunnel: Since the next operation is the first laser scribing, temperature must be decreased up to 25 °C. The substrate, covered with the front contact, comes out from the sputtering chamber and enters into the cooling tunnel. The cooling rate is very similar to the heating one, and also, in this case, the tunnel is 14 m long.

1st Laser Scribing: In order to define how large a solar cell is, an IR or ultraviolet laser (UV), able to eliminate the TCO along parallel lines, at a distance of 1 cm one from each other, 40/60 μm wide, is typically used (Figure 12). The industrial solution for this purpose is a Q-switched (ns regime) diode-pumped solid-

state laser (DPSSL), working at wavelengths of 1064 or 266 nm (third harmonic) depending on the IR or UV cutting, respectively. The lasing medium for the DPSSLs is a neodymium-doped yttrium aluminum garnet ($Nd:Y_3Al_5O_{12}$), the so-called Nd:YAG. For a CdTe-module with an area of 1 m^2, a scribing length of about 100 m has to be done in 1 min. This is made possible only if the laser beam moves with a speed of 2 m/s, which includes the time loss due to the motion inversion that must be carried out for cutting each cell [132].

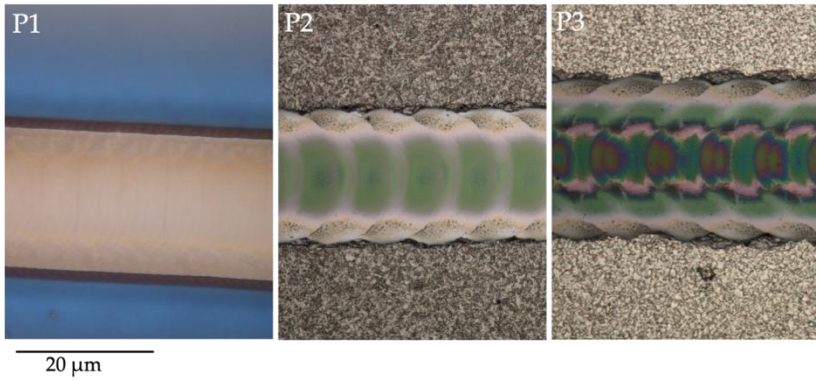

Figure 12: Optical microscope pictures of P1-P2-P3 scribes taken with a magnification of 1000×; P1, P2 and P3 cut TCO, CdS/CdTe and back-contact layers, respectively. Substrate is a 3.3 mm thick SLG.

2^{nd}-Heating Tunnel: Before the deposition of the window layer, the temperature of the TCO-covered SLG must reach 200°C. This heating tunnel, 7 m long, is equipped as the previous one.

Sputtering of CdS Layer: A planar RF sputtering equipped with at least three CdS ceramic targets, provides the deposition of the window layer. The typical deposition rate (DR) is more than 2nm/s, supplied by a RF power density of 3.5 W/cm^2. As an alternative to the sputtering technique, chemical bath deposition (CBD) could be implemented for the deposition of the CdS layer. Since CBD is carried out at very low temperatures (60/80) °C, the preceding heating tunnel is not necessary and the deposition occurs inside thermostatic baths containing the saturated solution.

3rd-Heating Tunnel: Deposition of the CdTe film by CSS or CSVT requires a temperature of about 500 °C; consequently, the SLG covered with TCO + CdS layers runs into a heating tunnel, while the temperature varies from 200 to 500 °C.

CSS of the CdTe Layer: CSS requires a substrate temperature of 500 °C and a crucible temperature of 600 °C if an Ar pressure of 1 mbar is used as a process gas. The number of crucibles is congruent with respect to the DR. Fortunately, this technique allows a very high DR (8/10 μm/min), which enables the deposition of relatively thick CdTe films (6 μm) within the production cycle time.

2nd Cooling Tunnel: The next step is the so-called chlorine treatment, which is carried out at a temperature of about 400 °C. This tunnel, with a length of 4 m, can lower the temperature from 500 °C to the typical temperature of the Cl_2-treatment, in the range of (360/400) °C.

Chlorine Treatment: This is a special section of the in-line production machine, since Cl_2 or Cl-radicals are very aggressive, especially at very high temperatures. If Cl–F-containing gases (Freon) are used, this step is performed in a vacuum chamber whose walls are internally coated with HCL-resistant ceramics. The final pressure of the Ar-Freon mixture is about 500 mbar and the total length of the treatment station is about 25 m.

Chlorine could be also supplied by dipping the CdS/CdTe system into tanks containing the $CdCl_2$-methanol solution. On the contrary, $CdCl_2$ could be additionally deposited by simple sublimation; in that case, this treatment section is furnished by vacuum thermal evaporators. In this situation, $CdCl_2$ is supplied at a low temperature and a cooling tunnel in front of this section, with a heating tunnel after the $CdCl_2$ deposition is needed.

3rd Cooling Tunnel: However, chlorine is supplied, the CdS/CdTe system, after having covered the entire cooling tunnel, lowering the temperature from 400 °C to room temperature, enters a washing machine in which splashes of

demineralized hot water remove any $CdCl_2$ residue and/or oxides formed during the Cl-treatment.

2nd Laser Scribing: This patterning step selectively removes the active layers close to one edge of each cell delineated by the first scribing (Figure 11). The laser action only has to remove the CdS and CdTe semiconductors, leaving the unchanged, completely cleaned surface of the underneath TCO. The laser scribing of the CdS/CdTe layers could be done facing the film surface or from the glass side. These strategies are employed with opaque or transparent substrates, respectively. In both cases, a green laser (wavelength = 515 nm) is efficiently used. Cycle time imposes a cutting speed of 2 m/s to perform a 100 m-long scribing in less than a minute.

Sputtering of Back-Contact: Back-contact consists of Mo or Ni–V films and the deposition is normally carried out at room temperature. The sputtering chamber is equipped with a sufficient number of cylindrical-rotating targets to perform the film deposition in the requested cycle time. The metallic films are deposited by a DC power density of 5 W/cm^2, which is able to deposit the 500-nm-thick back-contact in less than 1 min (DR $\geq$ 30 Å/s). Before the deposition of metallic films, buffer layers are added between the CdTe surface and the metallic films to achieve an ohmic contact. The M_2Te_3 and Cu films are deposited by means of a DC sputtering with a power density of about 3 W/cm^{2}for M_2Te_3 and 1.5 W/cm^2, corresponding to a DR of about 30 and 5 Å/s, respectively.

3rd Laser Scribing: This scribing removes the back-contact and the active stacked films close to the 2nd scribing keeping the underneath TCO layer as unchanged as possible (Figure 11). In this way, every cell is series-connected with its adjacent one. The main problem regarding this patterning, is to avoid the thermal damage of the CdS/CdTe films, which could form shunt paths in the junction region. This effect could be minimized if a very short pulse laser is used in order to avoid, as much as possible, the heat-affected zone (HAZ). This laser has the following characteristics: wavelength = 1064 nm, average max power = 5W at 50 kHz, energy per pulse = 160 μJ at 30 kHz, pulse width

= 500 ps at 30 kHz. This laser ensures a cutting speed of 2 m/s, which is able to perform a 100 m-long scribing in less than a minute.

Bus-Bar, Contact Box, Lamination: The production line ends with the installation of bus bars and a junction box with the external cables. Lastly the lamination operation, using a thin ethylene-vinyl acetate sheet (EVA) placed between two glasses. Lamination requires keeping the module at a temperature of about 165 °C for several minutes; this operation is effective in curing the diffusion/reaction of Cu with the M_2Te_3 material to form the desired Cu_xTe inside the back-contact. In this case, the upper glass, placed on the sunny side of the PV module, is normally a tempered glass, which makes the module particularly robust and hail-resistant.

Final Flash-Test and Packaging: The finished PV module is subjected to the so-called flash test to learn the electrical output power and the characteristic photovoltaic parameters. The measurement is performed with a pulsed solar simulator under standard conditions (1000 W/m^2, AM 1.5 G, 25 °C). The test results are printed on an adhesive label, which is automatically attached to the back of the panel, following the appropriate IEC standard. The tested modules are automatically divided into 5W output power classes and packaged in order to be shipped to their final destination.

Recycling and Life Cycle Assessment

Independent studies have shown that metallic cadmium is much more toxic compared to the CdTe compound, and massive doses of CdTe taken by oral inhalation have been shown to be about nine times lower than the toxicity of elemental cadmium[133].

Starting material processing, modules production, the operation of the PV plants and removal at their end of life, releases two orders of magnitude less cadmium emissions compared to the most modern thermoelectric power plants.

Concerning environmental issues, some of the main characteristics of CdTe are: (i) it is a non-flammable solid, (ii) it is insoluble in water, (iii) a melting point in air close to 1100 °C (higher than the typical temperature of an outdoor fire), (iv) at high temperature with oxygen (air), it forms an oxide, $CdTeO_3$, which is even more stable than CdTe itself. Moreover, CdTe modules are of the glass–glass laminated type and CdS-CdTe materials are retained in the molten glass if exposed to temperature in excess of the softening point of the encapsulant glasses [134]. Encapsulating Cadmium in the form of CdTe inside photovoltaic modules represents a safe alternative for using cadmium with respect to the commonly practiced use. In other words, this is a safe way to sequester cadmium from the environment. Replacing fossil-fuel electricity with CdTe-based PV plants results in a reduction in all the life cycle impact categories. In fact, CdTe modules have the lowest environmental impact from the harmful emissions point of view, showing the smallest ecological footprint compared to the other thin-film and cost-competitive Si technologies[135]. Increasingly, efficient cells and modules decline the availability concern, which is common to all thin-film technologies. The ever-decreasing use of CdTe might have an impact on tellurium primary demand, which could decrease regardless of the growth of the CdTe-technology market. Detractors of photovoltaic technologies assert that ground-mounted photovoltaic systems are very impactful from the soil transformation point of view. Since PV plants do not require extraction of fuel during their life cycle and the occupation of soil decreases with the increasing plant lifespan and PCE of modules, we can conclude that CdTe, among thin film technologies, is the best related to the land transformation impact.

The large amount of water required in the production of electricity from fossil and nuclear sources poses a serious supply problem, especially in those areas of the planet where water is a very precious resource. PV technology needs significantly lower water consumption than the full life cycle of thermoelectric power plants [136]. The amount of water used to produce one MWh of electricity from a PV source is the third lowest after wind and hydroelectric. Among the PV sources, CdTe-based

technology shows a lower water consumption than the more common multi-Si technology, due to the production of ultra-pure Si. A common implication for all the PV technologies is the recycling of modules at the end of their useful life; this not only from the point of view of the environmental impact but also in terms of the efficient recovery of raw materials. Cadmium, being a toxic element, must be recovered regardless of the economic implications, while the recovery of tellurium is seen as an additional benefit.

With a worldwide installed capacity close to 200 GW, recycling is mandatory for the future management of extensive PV waste volumes in order to safely recover costly materials.

In general, thin film technology is a feasible, environmentally friendly way to produce electricity. In particular, CdTe production represents a safe way to remove Cd from the environment.

Conclusion

Ever since the first photovoltaic device was made in the 1950s, it was immediately clear that this technology could be used to produce electricity. The first devices were built for space applications, allowing the development of telecommunication satellites on an international scale.

Since then, many different materials have been studied and related different technologies have been developed. Actually, the photovoltaic market, based on single and polycrystalline Si technology, has been developed since the 1980s. Quite quickly, very high-performance Si-based devices, with photovoltaic conversion efficiencies close to 25%, were realized. At the same time, other materials, made with epitaxial techniques, entered the world of PVs. Devices based on materials of the III-V family, such as GaAs, have given rise to even more efficient solar cells. At present, complex devices made with these materials, as well as multi-junction cells, exhibit an efficiency above 35% and up to 45% if sunlight concentrators are adopted. These technologies

are very expensive and are typically used to supply energy to space missions.

At the same time, alternative technologies were developed with the aim of maximizing the cost–efficiency ratio to make photovoltaics truly competitive with traditional energy sources.

Thin-film technology is well-suited to accomplishing this task, and devices based on different materials have been developed. Nowadays, sophisticated solar cells, in which the absorber layer is $CuInGaSe_2$ or CdTe, achieved efficiencies of 23.35% and 22.1%, respectively. These technologies, which are very competitive with respect to the Si-based one, will allow the development of PV at very low prices, reaching the so-called "Grid-Parity" in many countries, i.e., electricity is produced with photovoltaics at a lower price than the electricity produced by traditional fossil sources.

CdTe technology, which has several advantages compared to its competitors, is particularly promising; in fact, CdTe has one of the lowest costs of all the finished modules per peak watt. The high scalability of the production process, as well as the low production cost and not-problematic recycling of modules at their end of life, allow an extremely low cost per watt, making this technology the most competitive on the PV market. Despite this, CdTe technology represents a very small portion of production on the global market scale, while Si is still the undisputed king of the market.

CdTe production could receive a further boost if some still-open problems could be solved and easily implemented in the production process.

A reduction in the CdTe layer thickness, grain boundaries passivation, back-contact quality and stability, CdTe doping, and control of interface defects are only few of the main problems that can be improved. In this direction, some remarkable steps concerning the recombination of the charge carriers and the engineering of the energy gap have been made. For example, the addition of selenium in the production process allows for the

realization of PV modules with a photovoltaic conversion efficiency greater than 18%, representing one of the best results among commercial thin-film technology.

References

1. Gill WD, Bube RH. Photovoltaic properties of Cu_2S-CdS heterojunctions. J. Appl. Phys. 1970; 41: 3731.
2. Devaney W, Barnett A, Storti G, Meakin J. The design and fabrication of CdS/Cu_2S cells of 8.5-percent conversion efficiency. IEEE Trans. Electron Devices. 1979.
3. Green MA, Hishikawa I, Dunlop ED, Levi DH, Hohl-Ebinger J, et al. Solar cell efficiency tables (Version 54). Prog. Photovolt. Res. 2019; 27: 565–575.
4. Khattak CP, Schmid F. Growth of silicon ingots by HEM for photovoltaic applications. In: Khattak CP, Ravi KV, editors. Silicon Processing for Photovoltaics II, Amsterdam. Amsterdam: Elsevier. 1987.
5. Hanak JJ. Monolithic solar cell panel of amorphous silicon. Sol. Energy. 1979; 23: 145–147.
6. Becquerel AE. Mémoiresur les effetsélectriquesproduits sous l'influence des rayonssolaires. C. R. 1839, 9, 561–567.
7. Willoughby S. Selenium: Its Electrical Qualities and the Effect of Light Thereon. London: Hayman Bros. and Lilly Printers. 1877; 1–21.
8. Fritts C. On the Fritts selenium cell and batteries. Nostrands Eng. Mag. 1885; 32: 388–395.
9. Ohl R. Light Sensitive Electric Device. U.S. Patent 2402662. 1941.
10. Ohl R. Light-Sensitive Electric Device Including Silicon. U.S. Patent 2443542. 1941.
11. Kingsbury E, Ohl R. Photoelectric properties of ionically bombarded silicon. Bell Syst. Tech. J. 1952; 31: 802–815.
12. Chapin D, Fuller C, Pearson G. A new silicon p-n junction photocell for converting solar radiation into electrical power. J. Appl. Phys. 1954; 25: 676–677.
13. Shockley W. Electrons and Holes in Semiconductors. New York: D. van Nostrand. 1953.
14. Easton RL, Votaw MJ. Vanguard I IGY Satellite (1958 Beta). Rev. Sci. Instrum. 1959; 30: 70–75.

15. Czochralski J. Einneuesverfahrenzurmessung der kristallisationsgeschwindigkeit der metalle. Z. Phys. Chem. 1918; 92: 219.
16. Langhammer W. A Method for Producing High-Purity Silicon. Germany Patent DE1222481B. 1958.
17. Gremmelmaier R. GaAs-photoelement. Z. Phys. Chem.1955; 10: 501.
18. Gobat A, Lamorte M, Mclver G. Characteristics of high-conversion-efficiency gallium arsenide solar cells. IRE Trans. Mil. Electron. 1962; 20.
19. Shockley W, Queisser HJ. Detailed balance limit of efficiency of p-n junction solar cells. J. Appl. Phys. 1961; 32: 510.
20. Lofersky J. Recent research on photovoltaic solar energy converters. Proc. IEEE. 1963; 51: 667–674.
21. Ellis B, Moss TS. Calculated efficiencies of practical gaas and si solar cells including the effect of built-in electric fields. Solid State Electron. 1970; 13: 1.
22. Woodall J, Hovel H. High-efficiency $Ga_{1-x}Al_xAs$-GaAs solar cells. Appl. Phys. Lett. 1990; 21: 379.
23. Hovel H, Woodall J. $Ga_{1-x}Al_xAs$ p-p-n heterojunction solar cells. J. Electrochem. Soc. 1973; 120: 1246.

Iles PA. Manufacturing Technology for GaAs Solar Cell Applied Solar Energy Corporation Final Review to U.S. Air Force on A.F. Contract F33615-81-C-5150. 1986. Available Online at: https://ntrs.nasa.gov/archive/nasa/casi.ntrs.nasa.gov/19970010878.pdf

24. Iles PA, Chang KI, Leung D, Yeh YCM. The role of the AlGaAs Window layer in GaAs Hetero face Solar Cells. In Proceedings of the 18th IEEE Photovoltaic Specialist Conference, Las Vegas, NV, USA. 1985; 304.
25. Brambilla L, Caon A, Contini R, D'Accolti G, Rossi E, et al. GaAs Photovoltaic Technology Application: Arsene Solar Array. In Proceedings of the 23rd IEEE Photovoltaic Specialists Conference, Louisville, KY, USA. 1993; 1453.
26. Swanson RM. The promise of Concentrators. Prog. Photvolt. Res. Appl. 2000; 8: 93–111.

27. Bosi M, Pelosi C. The potential of III-V semiconductors as terrestrial photovoltaic devices. Prog. Photovolt. Res. Appl. 2007; 15: 51–68.
28. Konagai MSM, Takahashi K. High efficiency GaAs thin film solar cells by peeled film technology. J. Crys. Growth. 1978; 45: 277–280.
29. Lin Q, Huang H, Jing Y, Fu H, Chang P, et al. Flexible photovoltaic technologies. J. Mater. Chem. 2014; 2: 1233–1247.
30. Adams J, Elarde V, Hains A, Stender C, Tuminello F, et al. Demonstration of multiple substrate reuses for inverted metamorphic solar cells. In Proceedings of 38th IEEE PV Specialists Conf. (PVSC). Austin, TX, USA. 2012.
31. Bauhuis GJ, Mulder P, Haverkamp EJ, Schermer JJ, Bongers E, et al. Wafer reuse for repeated growth of III-V solar cells. Prog. Photovolt. Res. Appl. 2010; 18: 155–159.
32. Lee K, Zimmerman JD, Xiao X, Sun K, Forrest SR. Reuse of GaAs substrates for epitaxial lift-off by employing protection layers. J. Appl. Phys. 2012; 111: 033527–0033532.
33. Hall RB, Birkmire RW, Phillips JE, Meakin JD. Thin-film polycrystalline $Cu_2S/Cd_{1-x}Zn_x$solar cells of 10% efficiency. Appl. Phys. Lett. 1981; 38: 925.
34. Brandhorst HW, Bernatowicz DT. The Degradation of Cu_2S-CdS Thin Film Solar Cells Under Simulated Orbital Conditions. In Proceedings of the International Colloquium on Solar Cells. Toulouse, France.1970.
35. Spear WE, le Comber PG. Substitutional doping of amorphous silicon. Solid State Commun. 1975; 17: 1193–1196.
36. Carlson DE, Wronski CR. Amorphous silicon solar cell. Appl. Phys. Lett. 1976; 28: 671.
37. Staebler DL, Wronski CR. Reversible conductivity changes in discharge-produced amorphous Si. Appl. Phys. Lett. 1977; 31: 291–294.
38. Meier J, Dubail S, Fluckinger R, Fisher D, Keppner H, et al. Intrinsic microcrystalline silicon (μc-Si:H)—A promising new thin film solar cell material. In Proceedings of the 1st World Conference on Photovoltaic energy conversion. Waikoloa, HI, USA. 1994.

39. Matsuda A. Control of plasma and surface conditions for low defect density a-Si:H at high growth rates. In Proceedings of the Conference Record of the Twenty Fifth IEEE Photovoltaic Specialists Conference. Washington, DC. 1996.
40. Yang J, Guha S. Amorphous silicon alloy materials and solar cells near the threshold of microcrystallinity. MRS Online Proc. Libr. Arch. 1999; 557.
41. Yang J, Banerjee A, Guha S. Triple-junction amorphous silicon alloy solar cell with 14.6% initial and 13.0% stable conversion efficiencies. Appl. Phys. Lett. 1997; 70: 2975.
42. Wagner S, Shay JL, Migliorato P, Kasper HM. $CuInSe_2$/CdS heterojunction photovoltaic detectors. Appl. Phys. Lett. 1974; 434: 25.
43. Kazmerski LL, White FR, Ayyagari MS, Juang YJ, Patterson RP. Growth and characterization of thin film compound semiconductor photovoltaic heterojunctions. J. Vac. Sci. Technol. 1977; 14: 65.
44. Devaney WE, Chen WS, Stewart JM, Mickelsen R. Structure and properties of high efficiency ZnO/CdZnS/$CuInGaSe_2$ solar cells. Electron Devices IEEE Trans. 1990; 37: 428–433.
45. Tuttle JR, Ward JS, Duda A, Berens TA, Contreras MA, et al. The performance of Cu (In, Ga) Se_2-based solar cells in conventional and concentrator applications. MRS Proc. 1996.
46. Contreras M, Egaas B, Ramanathan K, Hiltner J, Swartzlander A, et al. Progress toward 20% efficiency in Cu(In,Ga)Se_2 polycrystalline thin-film solar cells. Prog. Photovolt. Res. Appl. 1999; 7: 311–316.
47. Ramanathan K, Contreras M, Perkins C, Asher S, Hasoon F, et al. Properties of 19.2% efficiency ZnO/CdS/$CuInGaSe_2$ thin-film solar cells. Prog. Photovolt. Res. Appl. 2003; 11: 225–230.
48. Menossi D, Bosio A, Romeo N. Key Developments in $CuInGaSe_2$ Thin Film Solar Cell. Saarbrüchen: LAP LAMBERT Academic Publishing. 2014.
49. Rosa G, Bosio A, Menossi D, Romeo N. How the starting precursor influences the properties of

polycrystallinecuingase$_2$ thin films prepared by sputtering and selenization. Energies. 2016; 9.
50. Repins I, Contreras MA, Egaas B, DeHart C, Craig JS, et al. 19.9%- efficient ZnO/CdS/CuInGaSe$_2$ solar cell with 81·2% fill factor. Prog. Photovolt. Res. Appl. 1999; 7: 311–316.
51. Jackson P, Hariskos D, Lotter E, Paetel S, Wuerz R, et al. New world record efficiency for Cu (In, Ga) Se$_2$ thin- film solar cells beyond 20%. Prog. Photovolt. Res. Appl. 2011; 19: 894–897.
52. Chirilă A, Reinhard P, Pianezzi F, Bloesch P, Uhl AR, et al. Potassium-induced surface modification of Cu(In,Ga)Se$_2$ thin films for high-efficiency solar cells. Nat. Mater. 2013; 12: 1107–1111.
53. Jackson P, Hariskos D, Wuerz R, Wischmann W, Powalla M. Compositional investigation of potassium doped Cu(In,Ga)Se$_2$ solar cells with efficiencies up to 20.8%. Phys. Status Solidi RRL. 2014; 8: 219–222.
54. Jackson P, Hariskos D, Wuerz R, Kiowski O, Bauer AM, et al. Properties of Cu(In, Ga)Se$_2$ solar cells with new record efficiencies up to 21.7%.Phys. Status Solidi RRL. 2014; 9: 28–31.
55. Solar Frontier Achieves World Record Thin-Film Solar Cell Efficiency of 23.35%. 17 January 2019. Available online at: http://www.solar-frontier.com/eng/news/2019/0117_press.html
56. Bazilian M, Onyeji I, Liebreich M, MacGill I, Chase J, et al. Re-considering the economics of photovoltaic power. Renew. Energy. 2013; 53: 329–338.
57. Hernández-Moro J, Martínez-Duart JM. Analytical model for solar PV and CSP electricity costs: Present LCOE values and their future evolution. Renew. Sustain. Energy Rev. 2013; 20: 119–132.
58. Ueckerdt F, Hirtha L, Luderer G, Edenhofer O. System LCOE: What are the costs of variable renewables? Energy. 2013; 63: 61–75.
59. Feltrin A, Freundlich A. Material considerations for terawatt level deployment of photovoltaics. Renew. Energy. 2008; 33: 180–185.

60. Andersson BA. Materials Availability for large-scale thin-film photovoltaics. Prog. Photovolt. Res. Appl. 2000; 8: 61–76.
61. Guo Q, Ford GM, Yang WC, Walker BC, Stach EA, et al. Fabrication of 7.2% efficientCZTSSesolar cells using CZTS nanocrystals. J. Am. Chem. Soc. 2010; 132: 17384–17386.
62. Repins I, Beall C, Vora N, DeHart C, Kuciauskas D, et al. Co-evaporated $Cu_2ZnSnSe_4$films and devices. Sol. Energy Mater. Sol. Cells. 2012; 101: 154–159.
63. Bag S, Gunawan O, Gokmen T, Zhu Y, Todorov TK, et al. Low band gap liquid-processed CZTSe solar cell with 10.1% efficiency. Energy Environ. Sci. 2012; 5: 7060–7065.
64. Katagiri H, Jimbo K, Maw WS, Oishi K, Yamazaki M, et al. Development of CZTS-based thin film solar cells. Thin Solid Films. 2009; 517: 2455–2460.
65. Wang W, Winkler MT, Gunawan O, Gokmen T, Todorov TK, et al. Device characteristics of CZTSSethin- film solar cells with 12.6% efficiency. Adv. Energy Mater. 2014; 4: 1301465.
66. Kumar MS, Madhusudanan SP, Batabyal SK. Substitution of Zn in Earth- Abundant $Cu_2ZnSn(S,Se)_4$ based thin film solar cells—A status review.Sol. Energy Mater. Sol. Cells. 2018; 185: 287–299.
67. Metzger WK, Gloeckler M. The impact of charged grain boundaries on thin-film solar cells and characterization. J. Appl. Phys. 2005; 98: 063701.
68. Rau U, Taretto K, Siebentritt S. Grain boundaries in $Cu(In,Ga)(Se, S)_2$ thin-film solar cells. Appl. Phys. A2009; 96: 221.
69. Jiang CS, Noufi R, Ramanathan K, Abu Shama J, Moutinho HRM, et al. Does the local built-in potential on grain boundaries of $Cu(In,Ga)Se_2$ thin films benefit photovoltaic performance of the device? Appl. Phys. Lett. 2004; 85: 2625.
70. Nakazawa T, Takamizawa K, Ito K. High efficiency indium oxide/cadmium telluride solar cells. Appl. Phys. Lett. 1987; 50: 279.
71. Aranovich JA, Golmayo D, Fahrenbruch AL, Bube RH. Photovoltaic properties of ZnO/CdTeheterojunctions prepared by spray pyrolysis. J. Appl. Phys. 1980; 51: 4260–4268.

72. Arroyo JM, Marfaing Y, Cohen-Solal G, Triboulet R. Electric and photovoltaic properties of CdTepnhomojunctions. Sol. Energy Mater. 1979; 171: 171–180.
73. Bonnet D, Rabenhorst H. New results on the development of a thin film p-CdTe/n-CdS heterojunction solar cell. In Proceedings of the Conference Record of the 9th IEEE Photovoltaic Specialists Conference. Silver Springs, Atlantic City, NJ, USA. 1972.
74. Tyan YS, Albuerne EA. Efficient thin film CdS/CdTe solar cells. In Proceedings of the 16th IEEE Photovoltaic Specialist Conference. New York, NY, USA. 1982.
75. Britt J, Ferekides C. Thin- film CdS/CdTe solar cell with 15.8% efficiency. Appl. Phys. Lett. 1993; 62: 2851–2852.
76. Wu X, Keane JC, Dhere RG, Dehert C, Albin DS, et al. 16.5% Efficient CdS/CdTe Polycrystalline Thin-Film Solar cell. In Proceedings of the17th European Photovoltaic Solar Energy Conference. Munich, Germany. 2001.
77. First Solar Establishes New World Record for CdTe Efficiency, 23 February 2016. Available online at: https://www.solarpowerworldonline.com/2016/02/24939/
78. Cunningham D, Rubcich M, Skinner D. Cadmium telluride PV module manufacturing at BP Solar. Prog. Photovolt. Res. Appl. 2002; 10: 159–168.
79. Bosio A, Menossi D, Mazzamuto S, Romeo N. Manufacturing of CdTe thin film photovoltaic modules. Thin Solid Films. 2011; 519: 7522–7525.
80. FirstSolar.Com. Series 6 Datasheet. Available online at: http://www.firstsolar.com/-/media/First-Solar/Technical-Documents/Series-6-Datasheets/Series-6-Datasheet.ashx
81. Gretener C, Perrenoud J, Kranz L, Kneer L, Schmitt R, et al. CdTe/CdS thin film solar cells grown in substrate configuration. Prog. Photovolt. Res. Appl. 2013; 21: 1580–1586.
82. Dhere R, Duenow J, DeHart C, Li J, Kuciauskas D, et al. Development of substrate structure CdTe photovoltaic devices with performance exceeding 10%. In Proceedings of the Photovoltaic Specialists Conference, 38th IEEE. Austin, TX, USA. 2012.

83. Bosio A, Rosa G. Past present and future of the thin film CdTe/CdS solar cells. Sol. Energy. 2018; 175: 31–43.
84. Salavei A, Artegiani E, Piccinelli F, di Mare S, Menossi D, et al. Flexible CdTe solar cells on polyimide and flexible glass substrates. In Proceedings of the 31st European Photovoltaic Solar Energy Conference. Berlin/Heidelberg, Germany. 2015.
85. Moss T. The interpretation of the properties of indium antimonide. In Proceedings of the Physical Society, Section B. London, UK. 1954.
86. Kumar A, Zhou C. The race to replace tin-doped indium oxide: Which material will win? ACS Nano. 2010; 4: 11–14.
87. Wu X, Ribelin R, Dhere RG, Albin DS, Gessert TA, et al. High-efficiency $Cd_2SnO_4/Zn_2SnO_4/Zn_xCd_{1-x}S$/CdS/CdTe polycrystalline thin-film solar cells. In Proceedings of the Conference Record of the Twenty-Eighth IEEE Photovoltaic Specialists Conference. Anchorage, AK, USA. 2000.
88. Kartopu G, Clayton AJ, Brooks WS, Hodgson SD, Barrioz V, et al. Effect of window layer composition in $Cd_{1-x}Zn_xS$/CdTe solar cells. Prog. Photovolt. Res. Appl. 2014; 22: 18–23.
89. Ortega-Borges R, Lincot D. Mechanism of chemical bath deposition of cadmium sulfide thin films in the ammonia-thiourea system in situ kinetic study and mod- elization. J. Electrochem. Soc. 1993; 140: 3464–3473.
90. Dona JM, Herrero J. Chemical bath deposition of CdS thin films: An approach to the chemical mechanism through study of the film microstructure. J. Electrochem. Soc. 1997; 144: 4081–4091.
91. Salavei A, Rimmaudo I, Piccinelli F, Menossi D, Romeo N, et al. Flexible CdTe Solar Cells by a Low Temperature Process on ITO/ZnO Coated Polymers. In Proceedings of the 27th European Photovoltaic Solar Energy Conference and Exhibition. Frankfurt, Germany. 2012.
92. Romeo N, Bosio A, Canevari V. The role of CdS preparation method in the performance of CdTe/CdS thin film solar cell. In Proceedings of the 3rd World Conference on Photovoltaic Energy Conversion, WCPEC-3. Osaka, Japan. 2003.
93. Ferekides C, Ceekala V, Dugan K, Killian L, Oman D, et al. Recent advances in thin film CdTe solar cells. In

Proceedings of the AIP Conference. Lakewood, CO, USA. 1996.
94. Anthony T, Fahrenbruch A, Peters M, Bube R. Electrical properties of CdTe films and junctions. J. Appl. Phys. 1985; 57: 400–410.
95. Chu T, Chu S, Ang S. Electrical properties of CdS/CdTe heterojunctions. J. Appl. Phys. 1988; 64: 1233–1237.
96. Fahrenbruch A, Bube R. Fundamentals of Solar Cells: Photovoltaic Solar Energy Conversion. New York: Academic Press. 1983.
97. Bosio A, Romeo A, Romeo N. Polycrystalline CdTe thin films solar cells. In Alessio Bosio Alessandro Romeo. Thin Film Solar Cells: Current Status and Future Trends. New York: Nova Science Publishers Inc. 2011.
98. Bosio A, Rosa G, Menossi D, Romeo N. How the chlorine treatment and the stoichiometry influences the grain boundary passivation in polycrystalline CdTe thin films. Energies. 2016; 9: 254.
99. Rühle S. Tabulated values of the Shockley–Queisser limit for single junction solar cells. Sol. Energy. 2016; 130: 139–147.
100. Wei S, Zhang S, Zunger A. First-principles calculation of band offsets, optical bowings, and defects in CdS, CdSe, CdTe, and their alloys. J. Appl. Phys. 2000; 87: 1304–1311.
101. Mia M, Swartz C, Paul S, Sohal S, Grice C, et al. Electrical and optical characterization of CdTe solar cells with CdS and CdSe buffers—A comparative study. J. Vac. Sci. Technol.B. 2018; 36: 052904.
102. Kephart J, McCamy J, Ma Z, Ganjoo A, Alamgir F, et al. Band alignment of front contact layers for high-efficiency CdTe solar cells. Sol. Energy Mater. Sol. Cells. 2016; 157: 266–275.
103. Munshi A, Kephart J, Abbas A, Shimpi T, Barth K, et al. Polycrystalline CdTe photovoltaics with efficiency over 18% through improved absorber passivation and current collection. Sol. Energy Mater. Sol. Cells. 2018; 176.
104. Fiducia T, Mendis B, Li K, Grovenor C, Munshi A, et al. Understanding the role of selenium in defect passivation for highly efficient selenium-alloyed cadmium telluride solar cells. Nat. Energy. 2019; 504–511.

105. Romeo A, Bätzner D, Zogg H, Vignali C, Tiwari A. Influence of CdS growth process on structural and photovoltaic properties of CdTe/CdS solar cells. Sol. Energy Mater. Sol. Cells. 2001; 67: 311–321.
106. Moutinho H, Al-Jassim M, Abulfotuh F, Levi D, Dippo P, Dhere R, et al. Studies of Recrystallization of CdTe thin filmsafterCdCI, treatment. In Proceedings of the Conference Record of the Twenty Sixth IEEE Photovoltaic Specialists Conference. Anaheim, CA, USA. 1997.
107. Perrenoud J, Buecheler S, Tiwari AN. Flexible CdTe solar cells and modules: Challenges and prospects. In Proceedings of the SPIE. San Diego, CA, USA. 2009.
108. Danaher W, Lyons L. Photoelectrochemical cell with cadmium telluride film. Nature. 1978; 271: 139–139.
109. Kröger F. Cathodic deposition and characterization of metallic or semiconducting binary alloys or compounds. J. Electrochem. Soc. 1978; 125: 2028–2034.
110. Fulop G, Taylor R. Electrodeposition of semiconductors. Ann. Rev. Mater. Sci. 1985; 15: 197–210.
111. Basol B. High-efficiency electroplated heterojunction solar cell. J. Appl. Phys. 1984; 55: 601–603.
112. Ojo A, Dharmadasa I. 15.3% efficient graded bandgap solar cells fabricated using electroplated CdS and CdTe thin films. Sol. Energy. 2016; 136: 10–14.
113. Soliman MM, Shabana MM, Abulfotuh F. CdS/CdTe solar cell using sputtering technique. Renew. Energy. 1996; 8: 386–389.
114. Paudel N, Wieland K, Compaan A. Ultrathin CdS/CdTe solar cells by sputtering. Sol. Energy Mater. Sol.Cells. 2012; 105: 109–112.
115. Compaan AD, Gupta A, Lee S, Wang S, Drayton J. High efficiency, magnetron sputtered CdS/CdTe solar cells. Sol. Energy. 2004; 77: 815–822.
116. Bosio A, Romeo N, Mazzamuto S, Canevari V. Polycrystalline CdTe thin films for photovoltaic applications. Progress Cryst. Growth Charact. Mater. 2006; 52: 247–279.
117. Bayhan H. Investigation of the effect of $CdCl_2$ processing on vacuum deposited CdS/CdTe thin film solar cells by DLTS. J. Phys. Chem. Solids. 2004; 65: 1817–1822.

118. Hiie J. CdTe:$CdCl_2$:O_2 annealing process. Thin Solid Films. 2003; 431: 90–93.
119. Niles DW, Waters D, Rose D. Chemical reactivity of $CdCl_2$ wet-deposited on CdTe films studied by X-ray photoelectron spectroscopy. Appl. Surf. Sci. 1998; 136: 221–229.
120. Romeo N, Bosio A, Tedeschi R, Canevari V. A highly efficient and stable CdTe/CdS thin film solar cell. Sol. Energy Mater. Sol. Cells. 1999; 58: 209–218.
121. Major J, Treharne R, Phillips L, Durose K. A low-cost non-toxic post-growth activation step for CdTe solar cells. Nature. 2014; 511: 334.
122. Zhou T, Reiter N, Powell R, Sasala R, Meyers P. Vapor chloride treatment of polycrystalline CdTe/CdS films. In Proceedings of the 1994 IEEE 1st World Conference on Photovoltaic Energy Conversion—WCPEC. Waikiloa, HI, USA. 1994.
123. Qu Y, Meyers P, McCandless B. HCl vapor post-deposition heat treatment of CdTe/CdS films. In Proceedings of the Twenty Fifth IEEE Photovoltaic Specialists Conference. Washington, DC, USA. 1996.
124. Albright S, Jordan JF, Akerman B, Chamberlain RC. Developments on CdS/CdTe photovoltaic panels at Photon Energy, Inc. Sol. Cells. 1989; 27: 77.
125. Gessert TA, Mason AR, Sheldon P, Swartzlander A, Niles D, et al. Development of Cu-doped ZnTe as back-contact interface layer for thin-film CdS/CdTe solar cells. J. Vac. Sci. Technol. 1996; 14: 806.
126. Uda H, Ikegami S, Sonomura H. Compositional change of the Au–Cu_2Te contact for thin-film CdS/CdTe solar cells. Jpn. J. Appl. Phys. 1990; 29: 495.
127. McCandless BE, Qu Y, Birkmire RW. A Treatment to Allow Contacting CdTe with Different Conductors. In Proceedings of the First World Conference on Photovoltaic Energy Conversion. Waikoloa, USA. 1994.
128. Du M. First-principles study of back-contact effects on CdTe thin-film solar cells. Phys. Rev. B2009; 80: 205322.
129. Durose K, Boyle D, Abken A, Ottley C, Nollet P, et al. Key aspects of CdTe/CdS solar cells. Phys. Status Solidi. 2002; 229: 1055–1064.

130. Bosio A, Ciprian R, Lamperti A, Rago I, Ressel B, et al. Interface phenomena between CdTe and ZnTe:Cu back contact. Sol. Energy. 2018; 176: 186–193.
131. Bosio A, Sozzi M, Menossi D, Selleri S, Cucinotta A, et al. Polycrystalline CdTe thin film mini-modules monolithically integrated by fiber laser. Thin Solid Films. 2014; 562: 638–647.
132. Zayed P, Philippe S. Acute oral and inhalation toxicities in rats with Cadmium Telluride. Int. J. Toxicol. 2009; 28: 259–265.
133. Fthenakis VM, Fuhrmann M, Heiser J, Lanzirotti A, Fitts J, et al. Emissions and encapsulation of cadmium in CdTe PV modules during fires. Prog. Photovolt. Res. Appl. 2005; 13: 713–723.
134. Kim H, Cha K, Fthenakis VM, Sinha P, Hur T. Life cycle assessment of cadmium telluride photovoltaic (CdTe PV) systems. Sol. Energy. 2014; 103: 78–88.
135. Sinha P. Life cycle materials and water management for CdTe photovoltaics. Sol. Energy Mater. Sol. Cells. 2013; 119: 271–275.

Book Chapter

Effects of O_2 Plasma Treatments on the Photolithographic Patterning of PEDOT: PSS

Deng-Yun Zheng[1], Meng-Hsiang Chang[1], Ci-Ling Pan[1,2] and Masahito Oh-e[1]*

[1]Institute of Photonics Technologies, Department of Electrical Engineering, National Tsing Hua University, Taiwan
[2]Department of Physics, National Tsing Hua University, Taiwan

***Corresponding Author:** Masahito Oh-e, Institute of Photonics Technologies, Department of Electrical Engineering, National Tsing Hua University, 101 Sec. 2 Kuang-Fu Road, Hsinchu 30013, Taiwan

Published **April 21, 2021**

This Book Chapter is a republication of an article published by Masahito Oh-e, et al. at Coatings in December 2020. (Zheng, D.-Y.; Chang, M.-H.; Pan, C.-L.; Oh-e, M. Effects of O_2 Plasma Treatments on the Photolithographic Patterning of PEDOT:PSS. Coatings 2021, 11, 31.
https://doi.org/10.3390/coatings11010031)

How to cite this book chapter: Deng-Yun Zheng, Meng-Hsiang Chang, Ci-Ling Pan, Masahito Oh-e. Effects of O_2 Plasma Treatments on the Photolithographic Patterning of PEDOT:PSS. In: Alessio Bosio, editor. Surfaces, Interfaces and Coatings Technology. Hyderabad, India: Vide Leaf. 2021.

Author Contributions: Conceptualization, C.-L.P. and M.O.; methodology, D.-Y.Z. and M.O.; validation, D.-Y.Z.; formal analysis, D.-Y.Z. and M.O.; investigation, D.-Y.Z. and M.-H.C.; data curation, D.-Y.Z.; writing—original draft preparation, D.-Y.Z.; writing—review and editing, M.O.; visualization, M.O.; supervision, C.-L.P. and M.O.; project administration, C.-L.P. and M.O.; funding acquisition, C.-L.P. and M.O. All authors have read and agreed to the published version of the manuscript.

Funding: This work was supported by grants from the Ministry of Science and Technology (MOST), Taiwan, under Grant MOST 108-2221-E-007-094-MY2 as well as Grants MOST 108-2622-M-007-006-CC1 and 109-2622-M-007-007-CC1 for industrial–academic collaborations jointly funded by MOST and Profound Material Technology Co., Ltd., in Taiwan.

Conflicts of Interest: The authors declare no conflict of interest.

Abstract

Poly(3,4-ethylenedioxythiophene) polystyrene sulfonate (PEDOT:PSS) is known for its potential to replace indium–tin oxide in various devices. Herein, when fabricating finger-type PEDOT:PSS electrodes using conventional photolithography, the cross-sectional profiles of the patterns are U-shaped instead of rectangular. The films initially suffer from non-uniformity and fragility as well as defects owing to undesirable patterns. Adding a small amount of hydrolyzed silane crosslinker to PEDOT:PSS suspensions increases the mechanical durability of PEDOT:PSS patterns while lifting off the photoresist. To further improve their microfabrication, we observe the effects of two additional oxygen (O_2) plasma treatments on conventional photolithography processes for patterning PEDOT:PSS, expecting to observe how O_2 plasma increases the uniformity of the patterns and changes the thickness and U-shaped cross-sectional profiles of the patterns. Appropriately exposing the patterns photoresist to O_2 plasma before spin-coating PEDOT:PSS improves the wettability of its surface, including its sidewalls, and a similar treatment before lifting off the photoresist helps partially remove the spin-coated PEDOT:PSS

that impedes the lift-off process. These two additional processes enable fabricating more uniform, defect-free PEDOT:PSS patterns. Both increasing the wettability of the photoresist patterns before spin-coating PEDOT:PSS and reducing its conformal coverage are key to improving the photolithographic microfabrication of PEDOT:PSS.

Keywords

Microfabrication; Photolithography; Patterning; PEDOT:PSS; Plasma; Thickness; Film; Surface; Height Profile; Terahertz Device

Introduction

Advancing terahertz (THz) technology [1,2] requires developing many functional quasi-optical components for THz devices such as phase shifters [3–8], filters [9], phase gratings [10], and polarizers [11]; however, most of these device components use indium–tin oxide (ITO) or metal electrodes, the transmittance of which is not necessarily high enough for THz devices.

To improve transmittance characteristics, on one hand, finger-type ITO electrodes [12], which mitigate the absorption of light via ITO, have been fabricated by patterning flat ITO electrodes. On the other hand, materials with higher transmittance in the THz region such as graphene [13] are actively being attempted to replace ITO. For this purpose, poly(3,4-ethylenedioxythiophene) polystyrene sulfonate (PEDOT:PSS) [14–19] is a promising candidate, and patterning PEDOT:PSS as a microfabrication strategy has been well studied. PEDOT:PSS exhibits high transmittance in the THz region, and because of its solution-process capability, it can be patterned using photolithography. Under these circumstances, replacing the finger-type ITO electrodes with patterned PEDOT:PSS ones would attain even higher transmittance in the THz region. Therefore, we attempted to fabricate finger-type electrodes using PEDOT:PSS; however, the films suffered from non-uniformity and fragility as well as defects owing to undesirable patterns.

As wearable and portable electronics have continued to develop [20], PEDOT:PSS as a flexible transparent electrode has been gaining an important role in such optoelectronic devices [21]. For practical purposes, developing versatile patterning techniques is required for incorporating PEDOT:PSS into these optoelectronic devices. Micropatterning has been developed for organic materials, but some challenges have not yet been fully addressed; in particular, the surface morphology and electrical and optical properties of patterned PEDOT:PSS are adversely influenced by patterning processes. This is because organic materials, i.e., soft matter, that can be dissolved or dispersed in water or organic solvents are usually mechanically fragile and chemically sensitive. These difficulties have encouraged researchers to devise various approaches in different micro- and nanopatterning techniques to solve these problems and to ultimately achieve well-organized, uniformly patterned surfaces with fine structures.

In principle, photolithography is applicable to organic materials including PEDOT:PSS when the proper materials and processes are selected [16]. Traditional photolithography materials and processes can be used in the lift-off process. As another alternative method, using orthogonal solvents and corresponding photoresists enables creating submicrometer-scale PEDOT:PSS patterns [22,23]; however, they can potentially be damaged by aggressive organic solvents. In addition, PEDOT:PSS can be directly crosslinked by ultraviolet (UV) irradiation with an appropriate photoinitiator [24–26], but the resolution is limited to several micrometers. From the above-mentioned techniques, we choose traditional photolithography together with the lift-off process. In other words, we observe how PEDOT:PSS films can be patterned using traditional photolithography and how undesirable patterns or defects, if any, made by photolithographic processes can be altered and improved.

Plasma treatments are well known and offer many advantages in fabrication processes because they can modify the surface properties, but exposing a surface to plasma does not alter its bulk properties [27]. Plasma treatment can prime any surface for

secondary manufacturing processes by eliminating all traces of contamination. Therefore, we are interested in observing the correlation between plasma treatments and the surface structures and morphologies of photolithographic PEDOT:PSS patterns while exploring ways to improve their quality.

In this study, we aim to tackle the aforementioned problems, i.e., the non-uniformity and fragility of the films as well as defects owing to undesirable patterns, and to improve the quality of photolithographic PEDOT:PSS patterns. Although photolithography has already been established for PEDOT:PSS, some material- and process-related factors seem to affect the quality of the films and patterns. For this purpose, we introduce two additional O_2 plasma processes into traditional photolithography, and we analyze how each additional plasma treatment affects the PEDOT:PSS patterns, expecting to improve them by applying these two additional processes. From a practical perspective, exploiting these basic, unsophisticated fabrication processes while unveiling their effects helps further develop the photolithographic patterning of PEDOT:PSS thin films in a facile, familiar way.

Materials and Methods

Materials and Procedure

Soda-lime glass substrates with dimensions of 25 × 25 × 0.7 mm were sequentially sonicated in commercially available detergent RBS™ 35 Concentrate (Thermo Fisher Scientific, Waltham, MA, USA and deionized water (>18 MΩ·cm) for 15 min. To increase its hydrophilicity, the surface of the substrates was exposed to O_2 plasma with a power of 100 W and O_2 flowing at 15 sccm for 3 min using a Samco-ucp PC-300 plasma cleaner (Ruggell, Liechtenstein). A positive photoresist AZ4620 (Merck KGaA, Darmstadt, Germany) was spin-coated onto the substrates at 4000 rpm for 40 s and then baked at 90 °C for 7 min. The photoresist films were exposed to UV light for 7 s using an EVG®620 mask aligner. The photoresist films were developed in a developer solution AD-10 (Merck KGaA, Darmstadt, Germany) for 3 min.

Figure 1 illustrates the designed mask patterns of a unit cell together with an enlarged diagram of a corner of the electrode area showing a part of the finger-type electrodes near the edge. The total electrode dimensions are 14 × 13 mm, and each finger-type electrode is 20 µm wide with a 20 µm gap between neighboring electrodes. In practice, the four designed unit cells were laid out in a soda-lime mask with dimensions of 5 × 5 × 0.09 in (12.7 × 12.7 × 0.229 cm).

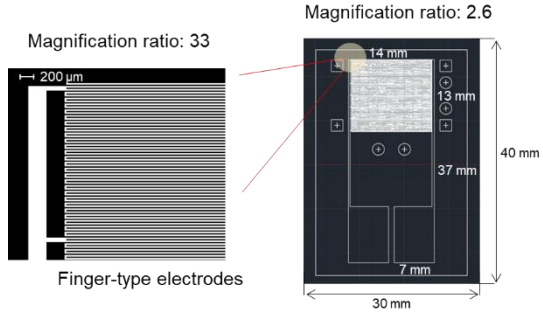

Figure 1: Designed mask pattern for a unit cell (right) and enlargement of the finger-type electrodes (left).

A PEDOT:PSS dispersion (PH1000, Heraeus Epurio Clevios™, Leverkusen, Germany) was filtered through a 0.45 µm syringe filter and then mixed with 0.2 wt % (3-glycidyloxypropyl)trimethoxysilane (GOPS) [28,29], a hydrolyzed silane crosslinker (Sigma-Aldrich, St. Louis, MO, USA). The suspension was sonicated for 30 min to homogenize the PEDOT:PSS dispersion, which was then spin-coated at 3000 rpm for 60 s onto the patterned photoresist. The spin-coated substrates were baked at 130 °C for 15 min and finally sonicated in acetone to lift off the photoresist.

In our modified process, two O_2 plasma treatments were independently added, one before spin-coating PEDOT:PSS and one before lifting off the photoresist. The O_2 plasma power and the O_2 flow rate were set to 100 W and 15 sccm, respectively, for both reaction ion etching (RIE) and plasma etching (PE) modes, and each operation time was varied. The latter mode is more isotropic and gentler, whereas in the former mode, the O_2 species are generated more vertically and hit the substrates more vigorously because of the potential between the electrodes in the chamber.

Measurements

A Dimension ICON scanning probe microscope system (Bruker, Billerica, MA, USA), which offers precisions of <0.15 Å nm for XY noise and <0.35 Å Z sensor noise, was used to measure the film thickness and probe its height profiles on the surface of the substrates. We prepared three samples for each set of conditions. For each sample, we measured at least three points in the upper, middle, and lower parts of the electrode area shown in Figure 1, and we measured each point three times. We also used a Quatek (Sheung Wan, Hong Kong) four-point probe test system, composed of a 5601TSR surface resistance tester and a QT-50 manual test console, to measure the surface resistance $R_s(\Omega)$ of films, from which the conductivity σ (S/cm) = $1/(R_s \cdot d)$ was deduced using the film thickness d (cm).

Results

Transferring an Image to the Photoresist and the Fragility of PEDOT:PSS Patterns

To draw a finger-type (stripe-type) image on the photoresist, a mask pattern (design drawing or pattern) is first transferred. The stripe-type-patterned photoresist works as a template or mold to create PEDOT:PSS patterns [16,30]. To this end, some process conditions are optimized using various quality engineering methods [31], i.e., by controlling the spin-coating rotational speed, baking temperature, UV-light-exposure time, and developing time, as described in the experimental section. Using these optimized conditions, we attain a high-quality patterned photoresist, and the patterns are transferred from the mask patterns with a gap of 20 μm between neighboring patterns. By using the image (pattern) of the photoresist, PEDOT:PSS is then patterned via microprocessing.

Initially, the PEDOT:PSS patterns were very mechanically fragile, especially in the lift-off process, during which the substrates were shaken in an acetone bath. To remove the photoresist patterns from the substrates, they were inevitably shaken, which presumably applied a frictional force to the PEDOT:PSS patterns on the substrates. In fact, the PEDOT:PSS

patterns were partially peeled off and bent out of the substrates, as shown in Figure 2. Simply immersing substrates in acetone, however, does not remove photoresist patterns from substrates; therefore, to avoid damaging the patterns, the films had to be strengthened. This fragility can be attributed to the weak anchoring of the PEDOT:PSS films to the surface of the substrates, although this technique is well known [28,29,32]. However, exposing the photoresist patterns to O_2 plasma did not mitigate this problem, so it had to be resolved using surfactants.

Specifically, GOPS, a hydrolyzed silane crosslinker, was used to improve the anchoring, as its epoxy group can react open under acidic conditions, yielding a hydroxyl group. When GOPS is added to PEDOT:PSS suspensions, the hydroxyl groups strongly interact with the sulfonic acid groups of PEDOT:PSS via hydrogen bonds. The trimethoxysilane groups of GOPS are hydrolyzed in acidic suspensions and become Si–OH groups, which form stable Si–O–Si bonds on the glass surface [32]. To reveal the effects of GOPS in the PEDOT:PSS suspensions, its concentration was varied, and the durability of the resulting PEDOT:PSS patterns was evaluated. As the GOPS concentration increased, fewer defects ended to appear in the PEDOT:PSS patterns. However, 3.0 wt % GOPS caused PEDOT:PSS to agglomerate, which was previously reported to hinder spin-coating [29]. Further, we confirmed that adding GOPS decreased the conductivity of the PEDOT:PSS films, suggesting a trade-off relationship between improving the durability and maintaining the conductivity of the PEDOT:PSS films. Figure 3 shows the relationship between the conductivity of PEDOT:PSS films and the GOPS concentration, which shows almost the same trend as that observed in previous work [28], although the initial conductivity without GOPS was slightly lower here. Based on these findings, we used 0.2 wt % GOPS in subsequent experiments because this concentration yielded PEDOT:PSS films that were sufficiently durable during the lift-off process.

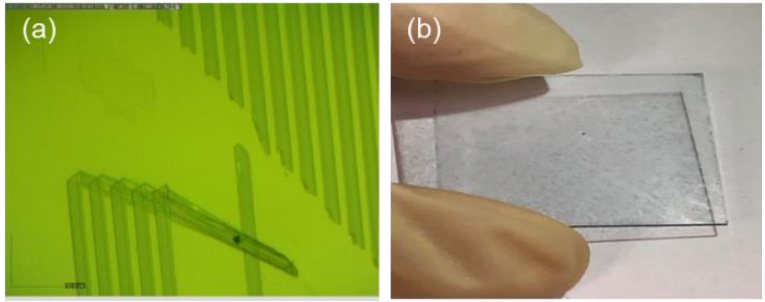

Figure 2: Poly(3,4-ethylenedioxythiophene) polystyrene sulfonate (PEDOT:PSS) film damaged when the substrate was shaken in an acetone bath during the lift-off process. (**a**) Image of the finger-type electrodes observed using an optical microscope. (**b**) Macroscale image of the entire substrate.

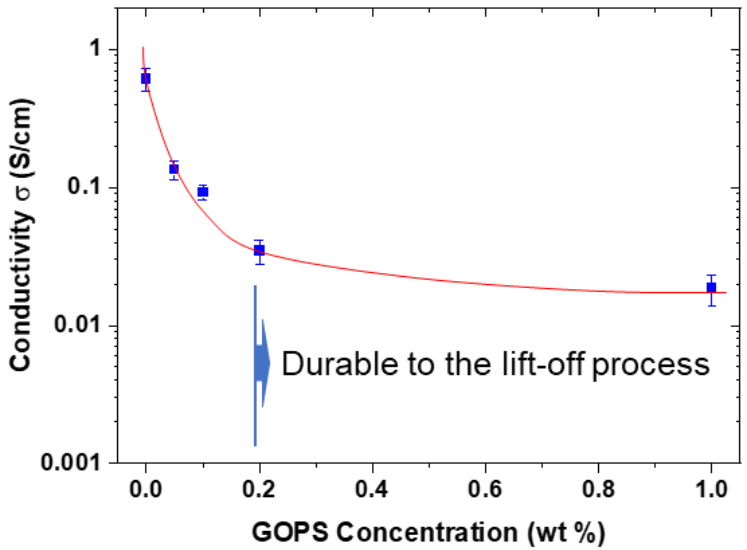

Figure 3: Changes in conductivity of PEDOT:PSS films when (3-glycidyloxypropyl)trimethoxy-silane (GOPS) is added to PEDOT:PSS suspensions. The solid curve is a visual guide.

Traditional Process for PEDOT:PSS

Figure 4 shows the two-dimensional height profiles of the PEDOT:PSS patterns obtained using the traditional process. Each sample was measured at several points in the sample, and

an average was taken at each position. Considering the photoresist patterns, we expect to observe a rectangular cross-section with a line width of 20 μm. Surprisingly, however, the actual profiles are U-shaped [33,34], with large variations in thickness at the center of the lines. The U-shaped profiles could be attributed to the evaporation of solvent and its corollary mass transfer [35]. If the surface of the photoresist has good wettability, the suspension spreads not only in the planar direction but also upward along the sidewalls of the photoresist. In addition, as the solvent evaporates, mass transfer occurs at the edge of the suspension on the sidewall of the photoresist, thereby leading to the U-shaped profiles at the edge. According to this mechanism, a higher concentration with higher viscosity would reduce the peak height of the U-shaped profiles, whereas better wettability, including on the sidewalls of the photoresist, would develop U-shaped profiles.

From another perspective, the bottom of the lines is approximately 30 μm, which is 1.5 times larger than the designed value. In contrast, the peak-to-peak width is almost 20 μm, suggesting that each peak must be determined by the sidewall of the patterned photoresist. Presumably, when PEDOT:PSS is spin-coated onto the patterned photoresist, PEDOT:PSS not only fills the spaces between the lines of the patterned photoresist but also covers the top of the photoresist. The PEDOT:PSS initially present on top of the photoresist can be connected to the PEDOT:PSS between the lines via conformal coverage. Therefore, even after the photoresist patterns are removed during the lift-off process, partially connected PEDOT:PSS would remain at the bottom of the patterns [30]. These observations suggest that removing the PEDOT:PSS from the top of the photoresist may help improve the quality and uniformity of the final PEDOT:PSS patterns.

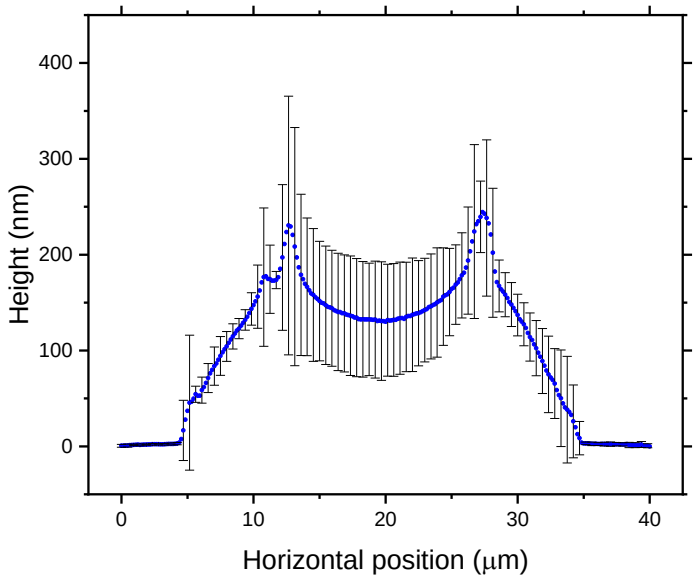

Figure 4: Height profiles of the patterned PEDOT:PSS lines made using the traditional process. The error bars show the difference in the maximum and minimum values at each position.

Adding an O_2 Plasma Treatment before Spin-Coating

O_2 plasma increases the hydrophilicity of surfaces. Contact angle measurements revealed that the surface of the patterned photoresist was rather hydrophobic, which prompted us to add an O_2 plasma treatment before spin-coating PEDOT:PSS, which would also remove the PEDOT:PSS from the top of the patterned photoresist. Figure 5 shows how PEDOT:PSS suspensions spread on the surface of the photoresist with and without an O_2 plasma treatment; clearly, increasing the O_2 plasma operation time further increased the wettability of the patterned photoresist surface.

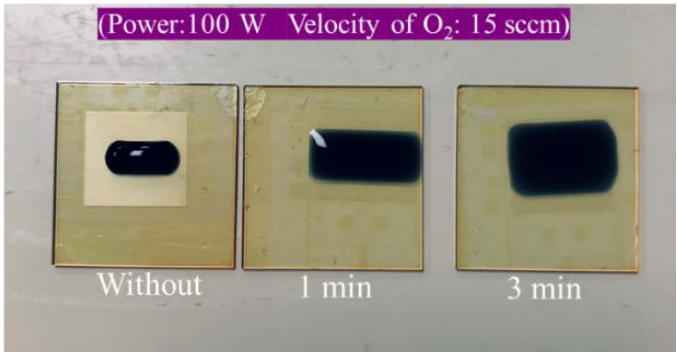

Figure 5: Effects of exposing O_2 plasma to the surface of the patterned photoresist on its wettability.

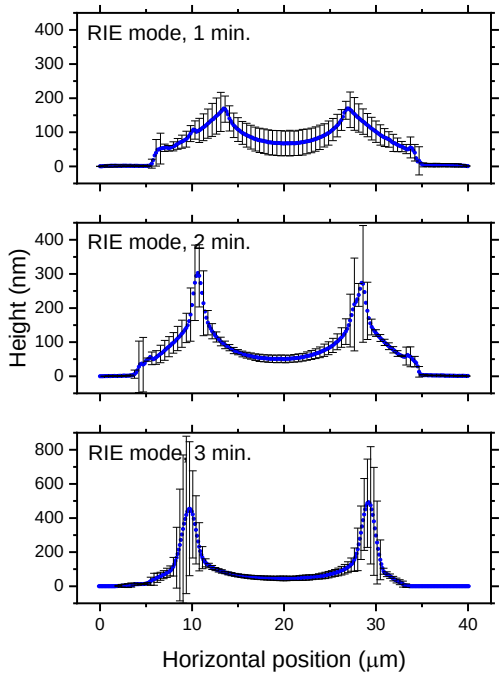

Figure 6: Height profiles of the patterned PEDOT:PSS lines made by plasma-treating the photoresist in reaction ion etching (RIE) mode before spin-coating PEDOT:PSS. The error bars show the maximum and minimum values at each position.

We found that adding the O_2 plasma treatment at this point during processing indeed improves the uniformity of the thickness. Figure 6 shows how the height profiles of the cross-sectional PEDOT:PSS patterns change when the patterned photoresist is plasma-treated in RIE mode before spin-coating it with PEDOT:PSS. As the operating time of the O_2 plasma treatment increases, the center of the lines becomes more uniform. Interestingly, however, the peaks that appear at the edge of each line become more pronounced with the increasing operating time, which suggests that the plasma-treated surface of the photoresist-patterned substrates indeed provides better wettability for PEDOT:PSS and hence better uniformity at the center of the lines. Specifically, the thickness variations at the center of the lines are improved, decreasing from ±33.9 to ±5.7 nm. Furthermore, O_2 plasma increases the wettability of the sidewalls of the photoresist patterns, and therefore, the peaks become more pronounced with the increasing operating time owing to the so-called coffee ring effect [35,36]. This finding can be verified by using a gentler O_2 plasma treatment in PE mode.

Figure 7 shows how the height profiles of the cross-sectional PEDOT:PSS patterns change when the photoresist is plasma-treated in PE mode before spin-coating PEDOT:PSS. In contrast to the results of the RIE O_2 plasma treatment, the thickness of PEDOT:PSS changes more mildly and gently, with little impact on the sidewalls of the photoresist pattern. Figure 8 compares the changes in thickness and its variability at the center of the PEDOT:PSS patterns when the patterned photoresist is plasma-treated in RIE or PE mode before spin-coating. In RIE mode, the O_2 plasma treatment is indeed vigorous and more rapidly reduces the film thickness. Presumably, this mode makes the surface of the photoresist more hydrophilic than PE mode, which is consistent with the results shown in Figure 5. Although in principle, the RIE plasma mode bombards the substrate surface more vertically, it also more severely affects the sidewalls.

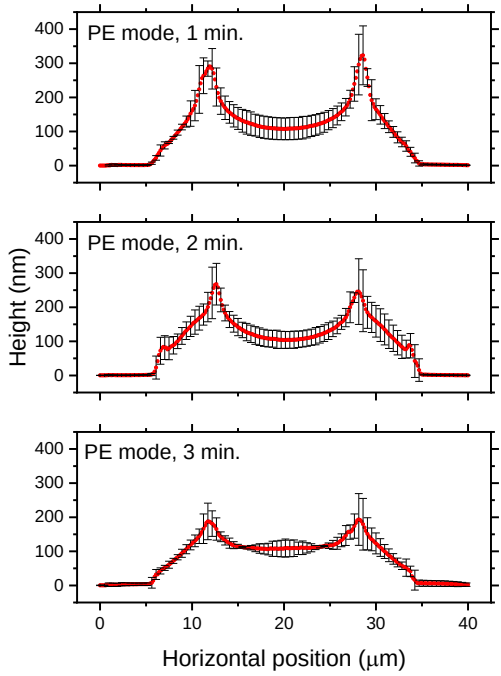

Figure 7: Height profiles of the patterned PEDOT:PSS lines made by plasma-treating the photoresist in plasma etching (PE) mode before spin-coating PEDOT:PSS. The error bars show the maximum and minimum values at each position.

Therefore, the hydrophilicity increases on the entire surface of the patterned photoresist, including the sidewalls, so the U-shaped profiles become more pronounced. Meanwhile, the films become thinner, with less variability at the center of each patterned line and a higher peak at the edge.

In subsequent experiments, to avoid developing U-shaped cross-sectional profiles in the PEDOT:PSS patterns, we performed the O_2 plasma treatment for 3 min in PE mode before spin-coating PEDOT:PSS for the following step, i.e., lifting off the photoresist.

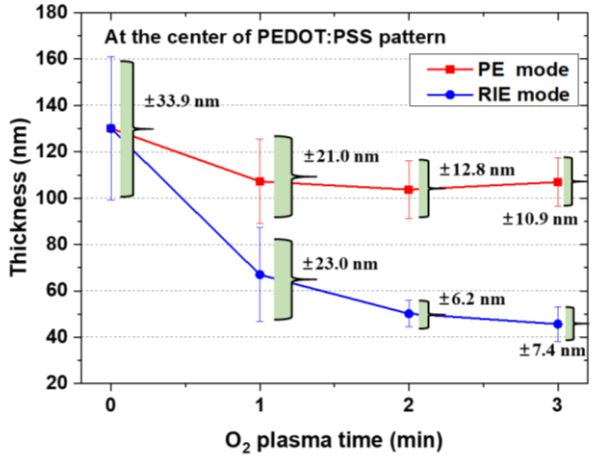

Figure 8: Changes in thickness and its variability at the center of the PEDOT:PSS patterns as a function of O_2 plasma exposure time using PE and RIE modes.

Adding an O_2 Plasma Treatment before Lifting Off the Photoresist

The next step introduces another difficulty that disturbs the uniformity of the patterns. Undesirable patterns, a type of defect, are often observed when lifting off the photoresist. Figure 9 shows an image of typical undesirable patterns remaining on the surface of the patterned PEDOT:PSS, which we assume are related to the PEDOT:PSS covering the top of the photoresist via conformal coverage [30]. Presumably, when the photoresist patterns are lifted off, the PEDOT:PSS anchored to the surface of the photoresist mechanically causes this problem. Further, brush-like wrinkles often appear around the boundaries after spin-coating PEDOT:PSS onto the patterned photoresist, as shown in Figure 10b, which prompts us to consider the effects of conformal coverage. During the spin-coating process, PEDOT:PSS spreads over the entire patterned photoresist surface, meaning that PEDOT:PSS can spread not only in the gaps between the strip patterns but also on top of the patterned lines. Therefore, removing such PEDOT:PSS covering the photoresist before lifting it off would help reduce these defects.

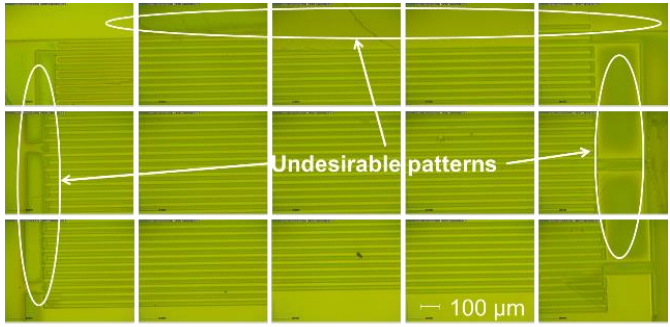

Figure 9: Typical undesirable patterns remaining on the surface of the patterned PEDOT:PSS observed using an optical microscope.

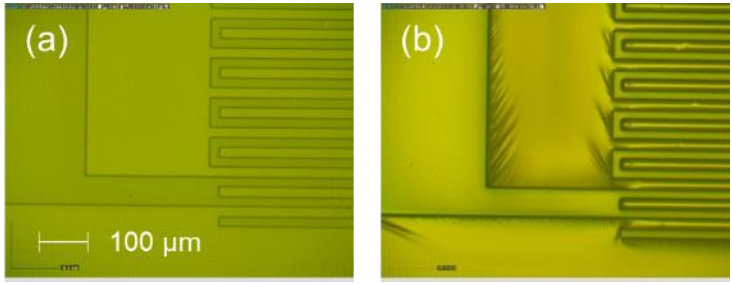

Figure 10: Photoresist patterns (**a**) before and (**b**) after spin-coating PEDOT:PSS observed using an optical microscope.

Thus, to remove the PEDOT:PSS from the top of the photoresist caused by conformal coverage, we introduce another O_2 plasma process before lifting off the photoresist patterns. As expected, applying this additional O_2 plasma treatment at this stage reduces the undesirable patterns and defects in the resulting PEDOT:PSS when the photoresist is finally removed with acetone, as shown in Figure 11. Obviously, however, a longer plasma treatment at this stage also reduces the thickness of PEDOT:PSS itself or even damages the patterns. As an extreme case in which we plasma-treated the PEDOT:PSS pattern for 120 s, its thickness decreased to one-fifth of its designed value, and its linewidths became two-thirds narrower. Further, we observed jagged line patterns, which are side effects of O_2 plasma exposure at this stage. Therefore, the operating time of O_2 plasma has a trade-off

relationship between mitigating these undesirable patterns and maintaining the quality of the PEDOT:PSS patterns.

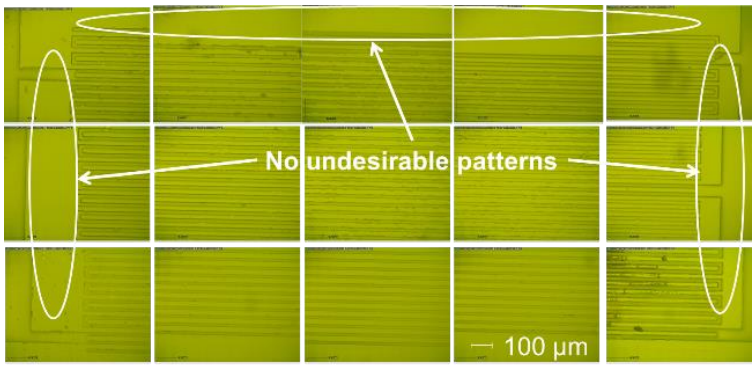

Figure 11: Microscopic image of undesirable patterns being removed when adding O_2 plasma in RIE mode for 15 s.

Nevertheless, adding an O_2 plasma treatment at this stage enables the removal of the unfavorable PEDOT:PSS covering the photoresist, suggesting that it is crucial to remove such PEDOT:PSS from the top of the photoresist or avoid conformal coverage. In order to remove this PEDOT:PSS without affecting the film thickness or damaging the film, O_2 plasma etching with masking would be more reliable.

Combination of the Added O_2 Plasma Treatments

Naturally, we are also interested in how combining the two added O_2 plasma processes eventually improves the quality of the PEDOT:PSS patterns. We thus optimized the plasma treatment operation time in PE mode to be 3 min before spin-coating PEDOT:PSS and that before lifting off the photoresist in RIE mode to be 1 s. Our investigation reveals that even 1 s of O_2 plasma in the RIE mode assists with removing undesirable PEDOT:PSS, thereby promoting the lift-off process while avoiding defects. Figure 12 shows microscopic images and height profiles of the PEDOT:PSS patterns when both O_2 plasma treatments are added to the process. Applying both treatments enables fabricating more uniform, defect-free PEDOT:PSS finger-type patterns with a deviation in the thickness of ±10.6 nm

at the center of the cross-section. The bottom of the lines is still beyond the designed value, thus requiring further optimization; however, avoiding conformal coverage would be crucial to improving microfabrication using photolithography.

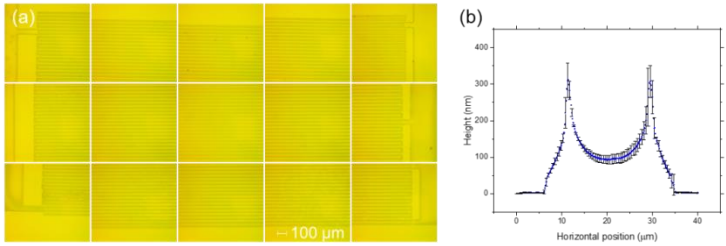

Figure 12: (**a**) Microscopic images and (**b**) height profiles of the PEDOT:PSS patterns made by adding both O_2 plasma treatments to traditional photolithography.

Conclusions

We fabricated finger-type PEDOT:PSS electrodes using conventional photolithographic patterning techniques, during which the cross-sectional U-shaped profiles of the PEDOT:PSS patterns were found instead of rectangular cross-sections. The fragility of the PEDOT:PSS patterns was improved by adding 0.2 wt % GOPS to the PEDOT:PSS suspensions. Using the strengthened PEDOT:PSS patterns, we investigated the effects of adding O_2 plasma treatments to the traditional photolithography process for patterning PEDOT:PSS, expecting to observe how this treatment improved the uniformity of the patterns and how it changed the thickness and U-shaped profiles of the patterns. One O_2 plasma treatment was introduced before spin-coating PEDOT:PSS onto the patterned photoresist layer, and the other was employed before the lift-off process for removing the photoresist layer. The former improved the wettability of the patterned photoresist surface, including that of its sidewalls, and the latter helped partially remove the spin-coated PEDOT:PSS that impeded the lift-off process. In the former O_2 plasma treatment, the uniformity of the thickness at the center of the lines became more uniform, with an improved deviation from several tens of nanometers to several nanometers; however, the

U-shaped patterns became more pronounced when the sidewalls of the patterned photoresist were exposed to the plasma in RIE mode, which could be avoided using more gentle plasma in PE mode. The latter O_2 plasma treatment eventually facilitated the lift-off process while preventing defects, uniformly reducing the entire thickness of the PEDOT:PSS patterns while removing the PEDOT:PSS covering the photoresist. Our findings suggest that the most important factor is how to remove PEDOT:PSS from the top of the photoresist or avoid its conformal coverage. Applying these two additional processes enabled fabricating more uniform, defect-free PEDOT:PSS patterns. Realizing a real THz device using the investigated techniques requires considerable effort to optimize the entire procedure, which would involve many factors, such as the cross-sectional shape of the patterned lines, defects, conductivity, and anchoring strength.

References

1. Zhang XC, Xu J. Introduction to THz Wave Photonics. New York: Springer US. 2010.
2. Shi JW, Huang CB, Pan CL. Millimeter-wave photonic wireless links for very high data rate communication. NPG Asia Mater. 2011; 3: 41–48.
3. Chen CY, Hsieh CF, Lin YF, Pan RP, Pan CL. Magnetically tunable room-temperature 2π liquid crystal terahertz phase shifter. Opt. Express. 2004; 12: 2625–2630.
4. Wu HY, Hsieh CF, Tang TT, Pan RP, Pan CL. Electrically tunable room-temperature 2π liquid crystal terahertz phase shifter. IEEE Photon. Technol. Lett. 2006; 18: 1488–1490.
5. Lin Xw, Wu Jb, Hu W, Zheng Zg, Wu Zj, et al. Self-polarizing terahertz liquid crystal phase shifter. AIP Adv. 2011; 1: 032133.
6. Yang CS, Tang TT, Chen PH, Pan RP, Yu P, et al. Voltage-controlled liquid-crystal terahertz phase shifter with indium–tin–oxide nanowhiskers as transparent electrodes. Opt. Lett. 2014; 39: 2511.
7. Yang CS, Tang TT, Pan RP, Yu P, Pan CL. Liquid crystal terahertz phase shifters with functional indium-tin-oxide nanostructures for biasing and alignment. Appl. Phys. Lett. 2014; 104: 141106.
8. Yang CS, Kuo C, Chen PH, Wu WT, Pan RP, et al. High-

transmittance 2π electrically tunable terahertz phase shifter with CMOS-compatible driving voltage enabled by liquid crystals. Appl. Sci. 2019; 9: 271.
9. Chiang YJ, Yang CS, Yang YH, Pan CL, Yen TJ. An ultrabroad terahertz bandpass filter based on multiple-resonance excitation of a composite metamaterial. Appl. Phys. Lett. 2011; 99: 191909.
10. Chatzakis I, Tassin P, Luo L, Shen NH, Zhang L, et al. One- and two-dimensional photo-imprinted diffraction gratings for manipulating terahertz waves. Appl. Phys. Lett. 2013; 103: 043101.
11. Hsieh CF, Lai YC, Pan RP, Pan CL. Polarizing terahertz waves with nematic liquid crystals. Opt. Lett. 2008; 33: 1174.
12. Sahoo AK, Yang CS, Wada O, Pan CL. Twisted nematic liquid crystal based terahertz phase shifter with crossed indium tin oxide finger type electrodes. IEEE Trans. Terahertz Sci. Technol. 2019; 9: 399–408.
13. Yang CS, Kuo C, Tang CC, Chen JC, Pan RP, et al. Liquid-crystal terahertz quarter-wave plate using chemical-vapor-deposited graphene electrodes. IEEE Photon. J. 2015; 7: 2200808.
14. Kim N, Kee S, Lee SH, Lee BH, Kahng YH, et al. . Highly conductive PEDOT:PSS nanofibrils induced by solution-processed crystallization. Adv. Mater. 2014; 26: 2268–2272.
15. Sun K, Zhang S, Li P, Xia Y, Zhang X, et al. Review on application of PEDOTs and PEDOT:PSS in energy conversion and storage devices. J. Mater. Sci. Mater. Electron. 2015; 26: 4438–4462.
16. Ouyang S, Xie Y, Wang D, Zhu D, Xu X, et al. Surface patterning of PEDOT:PSS by photolithography for organic electronic devices. J. Nanomater. 2015; 2015: 603148.
17. Sun Y, Yang S, Du P, Yan F, Qu J, et al. Investigate the effects of EG doping PEDOT/PSS on transmission and anti-reflection properties using terahertz pulsed spectroscopy. Opt. Express. 2017; 25: 1723.
18. Rwei SP, Lee YH, Shiu JW, Sasikumar R, Shyr UT. Characterization of solvent-treated PEDOT:PSS thin films with enhanced conductivities. Polymers. 2019; 11: 134.
19. Huseynova G, Hyun Kim Y, Lee JH, Lee J. Rising advancements in the application of PEDOT:PSS as a prosperous transparent and flexible electrode material for solution-processed organic electronics. J. Inf. Disp. 2020;

21: 71–91.
20. Ling H, Liu S, Zheng Z, Yan F. Organic flexible electronics. Small Methods. 2018; 2: 1800070.
21. Fan X, Nie W, Tsai H, Wang N, Huang H, et al. PEDOT:PSS for flexible and stretchable electronics: Modifications, strategies, and applications. Adv. Sci. 2019; 6: 1900813.
22. Hwang HS, Zakhidov AA, Lee JK, André X, Defranco JA, et al. Dry photolithographic patterning process for organic electronic devices using supercritical carbon dioxide as a solvent. J. Mater. Chem. 2008; 18: 3087–3090.
23. Lee JK, Taylor PG, Zakhidov AA, Fong HH, Hwang HS, et al. Orthogonal processing: A novel photolithographic patterning method for organic electronics. J. Photopolym. Sci. Technol. 2009; 22: 565–569.
24. Khong SH, Sivaramakrishnan S, Png RQ, Wong LY, Chia PJ, et al. General photo-patterning of polyelectrolyte thin films via efficient ionic bis(fluorinated phenyl azide) photo-crosslinkers and their post-deposition modification. Adv. Funct. Mater. 2007; 17: 2490–2499.
25. Winroth G, Latini G, Credgington D, Wong LY, Chua LL, et al. Polyfluorene-based light-emitting diodes with an azide photocross-linked poly(3,4-ethylene dioxythiophene):(polystyrene sulfonic acid) hole-injecting layer. Appl. Phys. Lett. 2008; 92: 103308.
26. Fenwick O, Oliver K, Cacialli F. Cross-linking of a poly(3,4-ethylene dioxythiophene):(polystyrene sulfonic acid) hole injection layer with a bis-azide salt and the effect of atmospheric processing conditions on device properties. Appl. Phys. Lett. 2012; 100: 053309.
27. Yoshida S, Hagiwara K, Hasebe T, Hotta A. Surface modification of polymers by plasma treatments for the enhancement of biocompatibility and controlled drug release. Surf. Coatings Technol. 2013; 233: 99–107.
28. Håkansson A, Han S, Wang S, Lu J, Braun S, et al. Effect of (3-glycidyloxypropyl)trimethoxysilane (GOPS) on the electrical properties of PEDOT:PSS films. J. Polym. Sci. Part B Polym. Phys. 2017; 55: 814–820.
29. He J, Wan Y, Gao P, Tang J, Ye J. Over 16.7% efficiency organic-silicon heterojunction solar cells with solution-processed dopant-free contacts for both polarities. Adv. Funct. Mater. 2018; 28: 1802192.
30. Chan JR, Huang XQ, Song AM. Nondestructive

photolithography of conducting polymer structures. J. Appl. Phys. 2006; 99: 023710.
31. Athreya S, Venkatesh YD. Application of Taguchi method for optimization of process parameters in improving the surface roughness of lathe facing operation. Int. Ref. J. Eng. Sci. 2012; 1: 13–19.
32. Yoon SS, Khang DY. Roles of nonionic surfactant additives in PEDOT:PSS thin films. J. Phys. Chem. C 2016; 120: 29525–29532.
33. Wang X, Östblom M, Johansson T, Inganäs O. PEDOT surface energy pattern controls fluorescent polymer deposition by dewetting. Thin Solid Films. 2004; 449: 125–132.
34. Charlot B, Sassine G, Garraud A, Sorli B, Giani A, et al. Micropatterning PEDOT:PSS layers. Microsyst. Technol. 2013; 19: 895–903.
35. Deegan RD, Bakajin O, Dupont TF, Huber G, Nagel SR, et al. Capillary flow as the cause of ring stains from dried liquid drops. Nature. 1997; 389: 827–829.
36. Deegan RD, Bakajin O, Dupont TF, Huber G, Nagel SR, et al. Contact line deposits in an evaporating drop. Phys. Rev. E Stat. Phys. Plasmas Fluids Relat. Interdiscip. Top. 2000; 62: 756–765.

Book Chapter

Carbon Dots as a Sustainable New Platform for Organic Light Emitting Diode

Paola Lagonegro, Umberto Giovanella* and Mariacecilia Pasini*

Istituto di Scienze e Tecnologie Chimiche "Giulio Natta" (SCITEC), Consiglio Nazionale delle Ricerche (CNR), Italy

***Corresponding Authors:** Umberto Giovanella, Istituto di Scienze e Tecnologie Chimiche "Giulio Natta" (SCITEC), Consiglio Nazionale delle Ricerche (CNR), via A. Corti 12, 20133 Milano, Italy

Mariacecilia Pasini, Istituto di Scienze e Tecnologie Chimiche "Giulio Natta" (SCITEC), Consiglio Nazionale delle Ricerche (CNR), via A. Corti 12, 20133 Milano, Italy

Published **May 31, 2021**

This Book Chapter is a republication of an article published by Mariacecilia Pasini, et al. at Coatings in December 2020. (Lagonegro, P.; Giovanella, U.; Pasini, M. Carbon Dots as a Sustainable New Platform for Organic Light Emitting Diode. Coatings 2021, 11, 5. https://doi.org/10.3390/coatings11010005)

How to cite this book chapter: Paola Lagonegro, Umberto Giovanella, Mariacecilia Pasini. Carbon Dots as a Sustainable New Platform for Organic Light Emitting Diode. In: Alessio Bosio, editor. Surfaces, Interfaces and Coatings Technology. Hyderabad, India: Vide Leaf. 2021.

Author Contributions: Conceptualization, U.G. and M.P.; writing—original draft preparation, P.L.; writing—review and editing, M.P. and U.G.; funding acquisition, M.P. and U.G. All authors have read and agreed to the published version of the manuscript.

Funding: This work was carried out with the financial support of Regione Lombardia Project "Piattaforma tecnologica per lo sviluppo di sonde innovative in ambito biomedicale" (ID 244356). U.G. thanks the MIUR-PRIN project Prot. 20172M3K5N.

Conflicts of Interest: The authors declare no conflict of interest.

Abstract

Over the past 10 years, carbon dots (CDs) synthesized from renewable raw materials have received considerable attention in several fields for their unique photoluminescent properties. Moreover, the synthesis of CDs fully responds to the principles of circular chemistry and the concept of safe-by-design. This review will focus on the different strategies for incorporation of CDs in organic light-emitting devices (OLEDs) and on the study of the impact of CDs properties on OLED performance. The main current research outcomes and highlights are summarized to guide users towards full exploitation of these materials in optoelectronic applications.

Keywords

Carbon Dots; Organic Light-Emitting Diode; Photoluminescence

Introduction

The growing demand for electronic devices for an ever-increasing number of applications means that green and

sustainable electronics are no longer just a dream but a pressing need [1].
In this context, the electronics and optoelectronics based on organic semiconductors showed, in the last few years, significant growth in many areas dominated by traditional electronics [2]. The foremost advantage of organic materials is that they are cheap, lightweight, easy to be processed, and flexible [3]. However, the synthetic techniques currently used for production of organic semiconductors [4] suffer from toxicity and environmental problems that can seriously prevent their large-scale production. In this regard, application of the principles of green chemistry for development of synthetic sustainable methods for the synthesis of semiconductors is essential to support the development of organic electronics, thus moving towards increasingly sustainable electronic devices [5].

In fact, the use of organic materials to build electronic devices [6] holds the promise that future electronic manufacturing methods will rely on safer and more abundant raw materials [7]. The vision is for resource-efficient synthetic methodologies, whereby both devices themselves and manufacturing of those devices use less materials and more safe materials.

The first pillar on which the new sustainable industrial revolution is based on is inevitably the development of new materials that are possibly safe and sustainable by design [8].

Among the emerging classes of materials able to meet these needs, carbon dots (CDs) are attracting considerable interest. They are part of the nanocarbon family, and differently from the best known carbon nanotube [9], they include quasi-spherical nanoparticles with sizes around 10 nm. Since their first discovery in 2006, CDs [10,11] have gained ever-increasing attention due to their fascinating properties like distinctive optical behavior, tunable emission, different functional groups, good biocompatibility, chemical and photo-stability, low toxicity, and low-cost production. More importantly, CDs properties can be changed by controlling their size, shape, and heteroatom doping and by modifying the surfaces, thanks to the quantum confinement effect (QCE)[12] (Figure 1). They are considered

promising green alternatives to fluorescent dyes [13–15] and generally to toxic metallic colloidal semiconductor nanocrystals and have been proposed for optoelectronic applications in general [12,16–19] (Figure 1), such as sensing, bioimaging, fingerprint detection, gene delivery, solar cells, or printing inks.

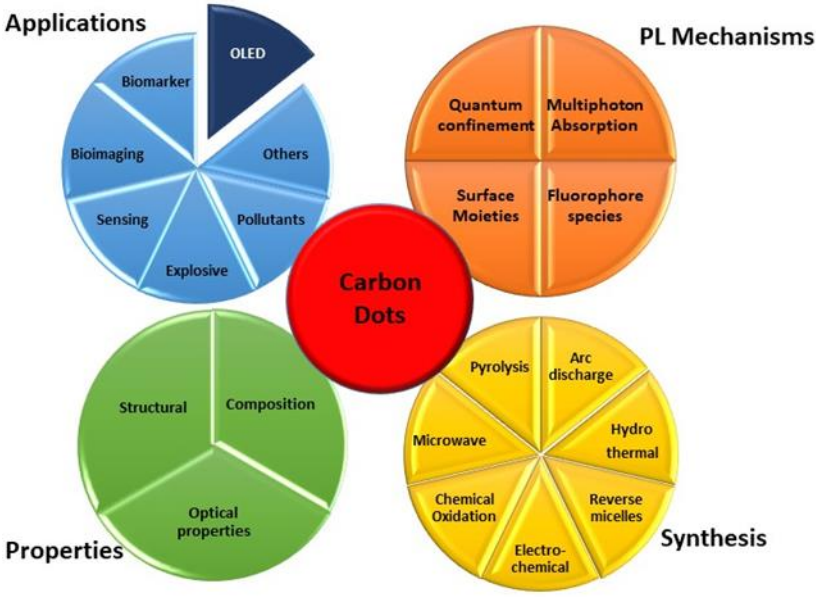

Figure 1: Carbon dots general overview.

In general, CD preparation methods can be grouped into two main approaches: top-down and bottom-up. The first strategy [20–27] involves the use of techniques such as arc discharge, laser ablation, chemical oxidation in strong acid, and electrochemical synthesis to break down carbon sources such as graphite, carbon nanotubes, and nanodiamonds to form fluorescent CDs. In contrast, in the bottom-up approach [28–34], CDs are synthesized from organic molecules by applying hydrothermal solvothermal methods, ultrasonic or microwave treatments, or simple thermal combustion.

Although CDs have been synthesized from different starting materials with a great variety of techniques, there is a huge effort

to develop sustainable synthetic paths which adhere to the principles of green chemistry. It has been demonstrated that CDs can be obtained from any carbon-based materials. This, in particular, guarantees that most by-products of the food supply chain can be reused to produce CDs. Agriculture products contain a myriad of natural molecules that can make up a diverse source of surface functional groups in CD formation.

A relevant feature for CD sustainability has to do with synthetic methodologies for their fabrication. CDs can be produced hydrothermally, that is, by heating the starting materials in water under atmosphere or elevated pressure [28–31,34,35]. Consequently, the cost of production is low, and the operation is easy, relatively safe, and free from organic solvents (Figure 2). Furthermore, shorter processing time and lower energy consumption for CD manufacture can be obtained when microwaves are used as the heating source [36,37].

Toxicity studies of the CDs were performed with both plants and animals (mice), revealing good biocompatibility [38–40], and opened the way not only to their bio-application but also to biodegradable electronics [19,40].

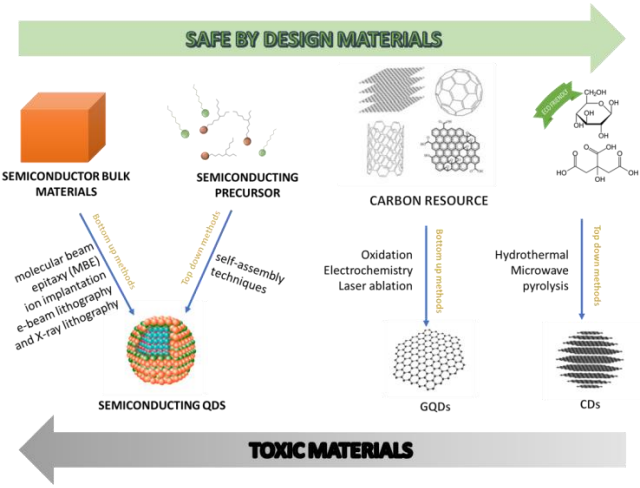

Figure 2: Schematic representation of carbon dots' main characteristics: adapted with permission from [14], copyright 2019 American chemical society, and adapted with permission from [41], copyright 2017 Elsevier.

With this perspective, in the present review, we will discuss CDs obtained with a bottom-up approach as it is the one that best adheres to the principles of green chemistry. They can be obtained from renewable sources or waste such as citric acid or agricultural waste [37]. The synthetic methodologies are simple and inexpensive, and they do not require the use of metal catalysts or chlorinated solvents. We will focalize on CDs as a sustainable new platform for organic light-emitting device (OLED) technology [42,43] without deepening the methods of synthesis on which relevant works have already been written [28–37,44]. In fact, among the various interesting applications of organic electronics, OLEDs are certainly those that have already carved out a slice of the market [42], and for this reason, the development of sustainable active materials and green technologies can already help the economy make a green turn.

In the next Section 2, we will make a brief introduction on the type and optical properties of these luminescent carbon materials. Section 3 will cover the different applications in electroluminescence devices as active layers or as charge regulating layers. In the last section, we will give some perspectives for the use of CDs including potential applications and possible development in particular as a safe-by-design material. We hope that this review will provide new insights to develop new knowledge on CDs, from the point of view of both sustainable synthesis and multiple applications, so that their potential in the optoelectronics area can be consolidated.

Definition of Carbon Dots and Optical Properties

Since their fortuitous discovery in 2004 by Xu et al. [10] and subsequently by Sun et al. in 2006 [11], CDs attracted a great deal of attention. Generally, CDs are 0-dimension nanocarbons with a typical size of less than 10 nm, although approximately 60-nm-size CDs have also been reported. CDs are quasispherical nanoparticles consisting of amorphous and crystalline parts, mainly composed of carbon with a fringe spacing of 0.34 nm, which corresponds to the (002) interlayer spacing of graphite

[12–14]. CDs are often confused, or associated, with graphene quantum dots (GQDs) [15], which are always part of the family of carbon-based nanomaterials but have different characteristics and origins. In fact, GQDs are nanofragments of graphene exhibiting a graphene structure inside the dots with a typical fringe spacing of 0.24 nm associated with the (100) in-plane lattice spacing of graphene. They have only one or a few layers of graphene with variable thickness between 2 and 10 nm and with usually 100 nm in lateral dimension, and they are generally produced by converting graphene or graphene oxide via top-down approaches [14].

Over the last 15 years, CDs have been synthesized with different approaches (i.e., top-down and bottom-up). However, only recently, sustainable precursors and methodologies have been deeply investigated for their production [45,46]. These approaches look for sustainable materials which are low-cost, scalable, industrially and economically attractive, and based on renewable and highly abundant resources. This means that CD synthesis can meet the requirements of circular chemistry. Interestingly, CDs after synthesis can be further functionalized with various surface groups. In particular, oxygen-based functional groups, such as carboxyl and hydroxyl, give excellent solubility in water and are suitable for surface passivation and derivatization with various organic materials. Surface functionalization modifies both the physical properties of CDs such as their solubility in aqueous and non-aqueous solvents and their optical properties. For example, after surface passivation, the fluorescence properties of CDs can be improved [47,48]. In addition, the large conjugated structure endows CDs with some important characteristics, like good photostability, high surface area, and robust surface grafting [49]. Their electronic structures can be tuned by their size, shape, surface functional groups, and heteroatom doping, as theoretically investigated and experimentally confirmed by several groups [50–54]. The tunability of optoelectronic properties by modifying synthetic parameters and precursor strictly resembled the conjugated polymer features [55].

As mentioned above, the CD emission properties are their most amazing characteristics [41] and significant advances have been made in the last years, reaching photoluminescence (PL) quantum yields (PLQYs) up to 80% in CDs produced from citric acid as a renewable precursor or bright and stable PLQYs of 26% converting toxic cigarette butts [28,54].

Mostly, CDs are blue emitters, but emissions from ultraviolet to near-infrared [55–58] as well as white light emission [59] were reported. In general, their PL spectra are symmetrical and broad, with large Stokes shifts (mainly due to the CD size distribution), and usually have an excitation-dependent behavior, with the emission peak varying with the excitation wavelength [22,58].

The emission mechanism of CDs is a longstanding debate, and several hypotheses have been proposed [41] (see Figure 3) such as (i) size-dependent emission, (ii) surface state-derived luminescence, and iii) embedded molecular luminophore [60]. Regardless of the type of mechanism, it has been shown that CD emissions could be regulated by controlling their size (mainly referring to sp_2 carbon domains), their surface passivation and/or functionalization, and their doping due to the presence of heteroatom [61–63].

The first hypothesis proposed is based on the size of CDs [60]. Yuan and coworkers synthetized multicolor-emitting CDs with different dimensions from citric acid (CA) and diaminonaphthalene (DAN) by controlling the process parameters. CDs showed average sizes of about 1.95, 2.41, 3.78, 4.90, and 6.68 nm (Figure 4A), with corresponding tunable absorption (Figure 4B) blue (430 nm), green (513 nm), yellow (535 nm), orange (565 nm), and red (565 nm) emissions, respectively (Figure 4C). In accordance with the results, they deduced that, by increasing the size of CDs and consequently the conjugated π-domain, the bandgap decreases (Figure 4D,E) [65].

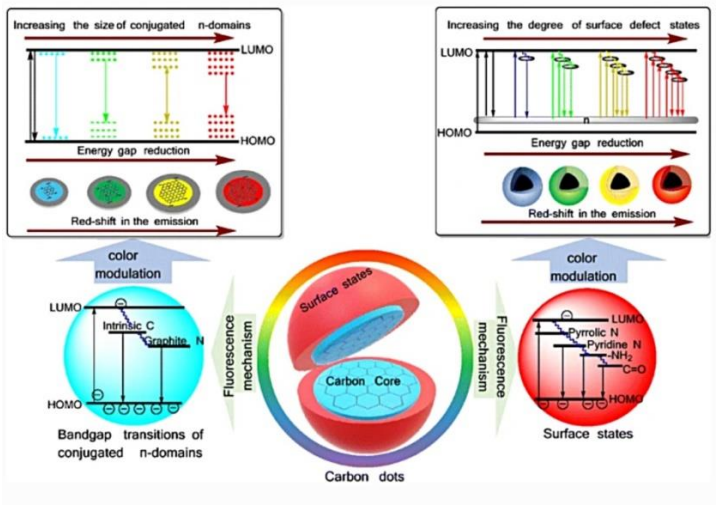

Figure 3: Different hypotheses for carbon dot (CD) emission mechanism: reprinted with permission from [64], copyright 2019 Springer Nature.

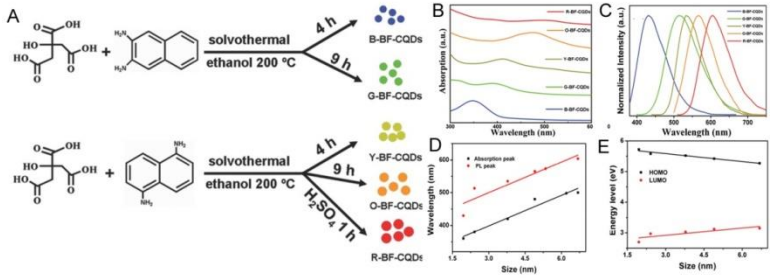

Figure 4: Preparation of bright multicolor bandgap fluorescent (BF) CDs by solvothermal treatment of citric acid (CA) and diaminonaphthalene (DAN) (**A**) from blue to red (**B**–**E**): (**A**) reprinted with permission from [14], copyright 2019 American Chemical Society, and (**B**–**E**) reprinted with permission from [65], copyright 2016 WILEY-VCH Verlag GmbH & Co. KGaA, Weinheim.

A second hypothesis is related to the surface states of CDs. Ding et al. [66] synthetized tunable photoluminescent CDs by one-pot hydrothermal synthesis (Figure 5A). Noteworthy, these CDs had comparable particle size and carbon core but variable degree of oxidation of the surface state. Therefore, a gradual reduction in their band gaps and a red shift in their emission peaks from 440

to 625 nm (Figure 5B,C) was observed by increasing the incorporation of oxygen species into their surface structures (Figure 5D) [66].

Also, Miao et al. [67] hypothesized a similar mechanism. They modulated the CD emission from 430 to 630 nm by controlling the degree of graphitization and the number of surface –COOH groups by changing the molar ratios of CA to urea at different temperatures (Figure 6). The increasing number of –COOH groups on the surface increases the electronic delocalization, and the emission wavelength is consequently red-shifted [64].

Another relevant hypothesis to explain CD emission is molecular luminophore-derived emission or molecular state emission. Small molecules or oligomeric luminophores could be produced during CD synthesis, and these luminophores could be attached to the surface of CD backbones, allowing CDs to have bright emission properties [68]. Song. et al. [69] studied the chemical structure and PL mechanism of CDs from CA and ethylenediamine (EDA). They proved the presence of a type of bright blue fluorophore and that CD emission was a result of small molecules, polymer clusters, and carbon cores. Indeed, the fluorophore may be attached to the carbon core, that may strongly affect the PL properties of the CDs.

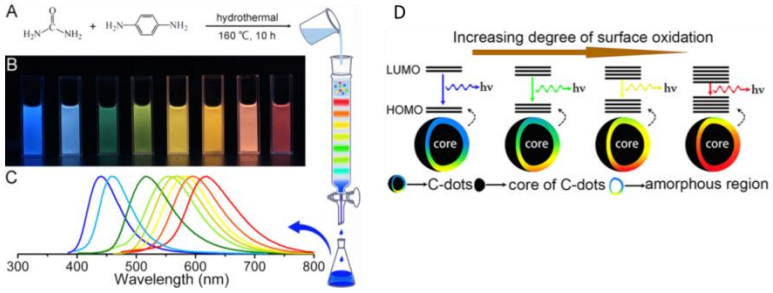

Figure 5: (**A**) One-pot synthesis and purification route for CDs with distinct photoluminescence (PL) characteristics, (**B**) eight CD samples under 365 nm UV light, (C) corresponding PL emission spectra, and (**D**) model for the tunable PL of CDs with different degrees of oxidation: reprinted with permission from [70], copyright 2016 American chemical society.

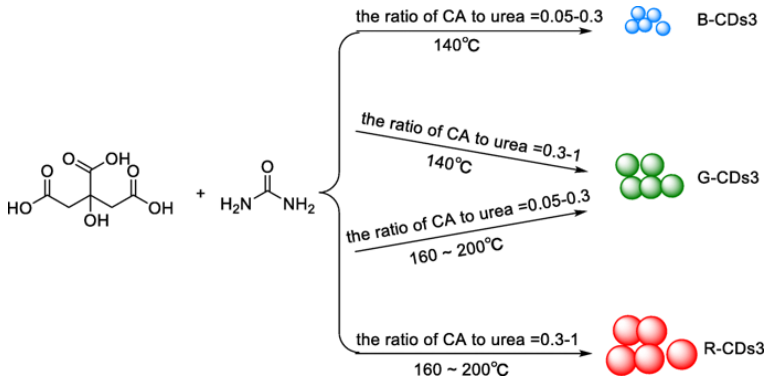

Figure 6: Multicolor-emitting CDs (called as CDs3) by using different molar ratios of CA to urea at different temperatures: the emission of CDs3 can be adjusted from 430 to 630 nm. The photoluminescence quantum yields (PLQYs) of the three CDs3 in blue, green, and red were 52.6%, 35.1%, and 12.9%, respectively. Reprinted with permission from [64], copyright (2019) Springer-Verlag.

OLED-Based Carbon Dots

CDs with amazing properties such as optical characteristics and carbon's intrinsic merits of high stability, low-cost, and environment-friendliness *find natural and* practical *applications* as components in OLED technology.

In the last decade, the interest in OLED based on CDs (hereafter CD-OLEDs) has been growth, and an increasing number of research groups have started to investigate in this field.

We want to provide a recent overview on CD-OLEDs, illustrating the dual employment of CDs as emitter, both as neat layer or as a guest in host–guest systems, and as a charge regulating interlayer (Table 1 and Figure 7). Particular attention will be devoted to the strategies used to prevent aggregation-induced quenching in the solid-state and to tune the emission color. It is also important to underline, although beyond the scope of this collection, that many groups used CDs also as a remote emitter, endowing blue commercial LEDs with a color converting filter based on CDs embedded in poly(methyl-

methacrylate) (PMMA) or other matrices. The blue LED emission was tuned from blue to red by altering the film thickness of the filter or the doping concentration of CDs [68–72].

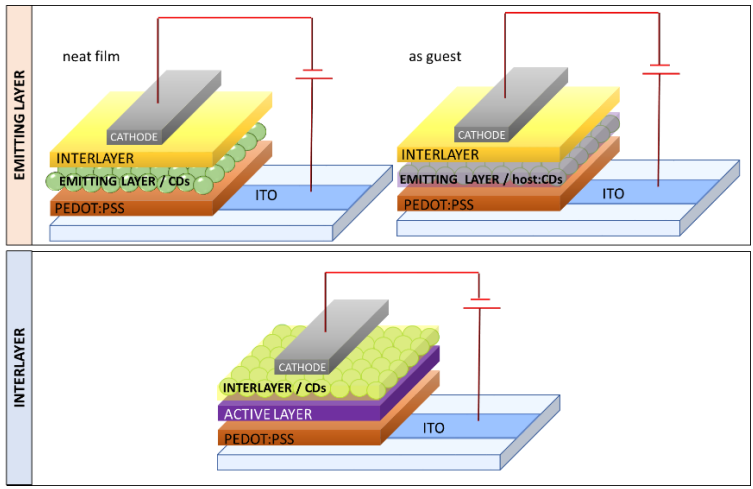

Figure 7: Scheme of the possible device architectures that incorporate CD as an emitter or as an interlayer.

Table 1: Summary of organic light-emitting devices (OLEDs) incorporating a CD layer.

Starting Materials	**Dimension (nm)/Shape**	**EL_{PEAK} (nm)**	**L_{MAX} (cd/m^2)**	**η_c (Cd/A)**	**Ref**
CDs as neat emitter	-	-	-	-	-
Citric acid with 2,3-diaminonaphthalene	1.95 nm	455	136	0.084	[65]
	2.41 nm	536	93	0.045	
	3.78 nm	555	60	0.02	
	4.9 nm	585	65	0.027	
	6.68 nm	628	12	0.0028	
ethylenediamine and phthalic acid	5.53 nm	455	4.97	-	[66]
citric acid + octadecene + 1-hexadecylamine	Spherical 5 nm	550-670	35	0.022	[73]
1-octadecene 1-hexadecylamine	6 ± 1.9 nm	460	21	0.06	[74]
1-hexadecylamine and anhydrous citric acid	3.3 nm	426	24	0.018	[75]
1-hexadecylamine and anhydrous citric acid		426, 452, 588	61		
1-hexadecylamine and anhydrous citric acid + ZnO nps		426, 452, 588	90		
anhydrous citric acid and hexadecylamine	Spherical 2.0–2.5 nm lattice spacing 0.22	554	5.7		[76]
CDs as guest emitter	-	-	-	-	-
citric acid and diaminonaphthalene.	quasi-spherical 2.4 lattice spacing 0.21 nm	450	5240	2.6	[77]
Phloroglucinol	triangular 1.9 nm	476	1882	1.22	[78]
	2.4 nm	510	4762	5.11	
	3 nm	540	2784	2.31	
	3.9 nm	602	2344	1.73	
Citric acid with 2,3-diaminonaphthalene	2.41 nm	536	2050	1.1	[65]
human hair	2D array of CDs 2–6 nm	498	350	0.22	[79]
			700	0.2	
N,N-dimethyl-, N,N-diethyl-, and N,N-dipropyl-p-phenylenediamine	quasi-spherical 2.2 ± 0.31. 2.3 ± 0.28. 2.3 ± 0.26 nm lattice spacing 0.21 nm	605/434 612/435 616/435	5248–5909	3.65 3.85	[80]
anhydrous citric acid and hexadecylamine	spherical_2.0–2.5 nm lattice spacing 0.22	558-550	339.5–455.2	-	[73]
anhydrous citric acid and hexadecylamine	-	474	569.8	-	[81]
CDs as interlayer	-	-	-	-	-
ethylenediamine and citric acid	-	532	30 730	93.8	[82]
banana leaves	4–6 nm (quasi-spherical)	486	-	-	[83]
Ethanolamine	-	622	3500	0.63	[84]

CDs as Emitter

In 2011, Wang et al. [73] demonstrated the first white OLED (WOLED) originating from a single CD component film. CDs, obtained by thermal carbonization of CA in hot octadecene with 1-hexadecylamine (HDA) as the passivation agent (Figure 8a), with a PLQY as high as 60% were incorporated as an emitting layer in WOLEDs with a direct architecture (Figure 8b).

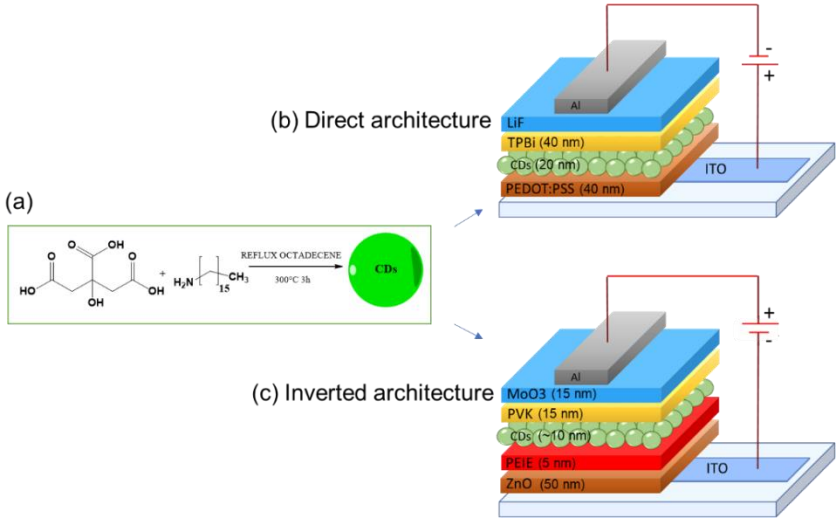

Figure 8: Schematic representation of (**a**) CD synthesis and typical devices architectures: (**b**) direct [74] and (**c**) inverted [73] in which CDs are incorporated as emitters.

Electrically driven WOLED-featured electroluminescence (EL) peaked at 550 nm, with current density (J) of 160 mA/cm^2, a maximum luminance (L_{MAX}) output of 35 cd/m^2 (Figure 9a,b), and a current efficiency (η_c) of 0.022 cd/A. As shown in Figure 9c, the maximum external quantum efficiency (EQE), defined as the ratio between the number of emitted photons and the number of electrons injected into the device, was 0.083% at a J of 5 mA/cm^2.

Wang et al. reported that white light emission was associated with energy transfer among various emitting centers in the CDs, corresponding to different energy transitions.

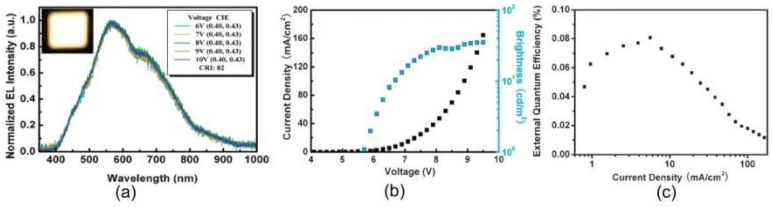

Figure 9: (**a**) Normalized electroluminescence (EL) spectra of direct architecture LEDs at applied bias voltages: the inset is a photograph of a white emission of our device (16 mm^2) operating at 9 V. (**b**) *J–L–V* characteristics of white OLEDs (WOLEDs). (**c**) The dependence of external quantum efficiency (EQE) on J. Reproduced with permission from [73], copyright 2011 The Royal Society of Chemistry.

Paulo-Mirasol et al. [74], in 2019, by using CDs synthesized according to Wang conditions [73], demonstrated that the white light was not due to the charge transfer between the CDs but was the result of different recombination processes within the CDs. Indeed, they proposed two radiative PL mechanisms in the CDs, involving different energies: one originating from the core and a second process that is faster and originates from the surface of CDs. The variation of the current injection controls the activation of the two radiative processes that happen inside the CDs. The combined emission from different energy states results in white light emission at an adequate current injection rate. Differently from Wang and colleagues, Paulo-Mirasol et al. manufactured OLEDs with an inverted architecture ITO/ZnO/PEIE/CDs/PVK/MoO_3/Au (Figure 8c). They modulated the thickness of CDs and polyvinylcarbazole (PVK, well-known and used as a hole transporting layer or HTL) to optimize the performance of devices obtaining WOLEDs with L_{MAX} of 24 cd/m^2 and η_c 0.06 cd/A (Figure 10) comparable to Wang's achievements (L_{MAX} 35 cd/m^2 and η_c of 0.022 cd/A).

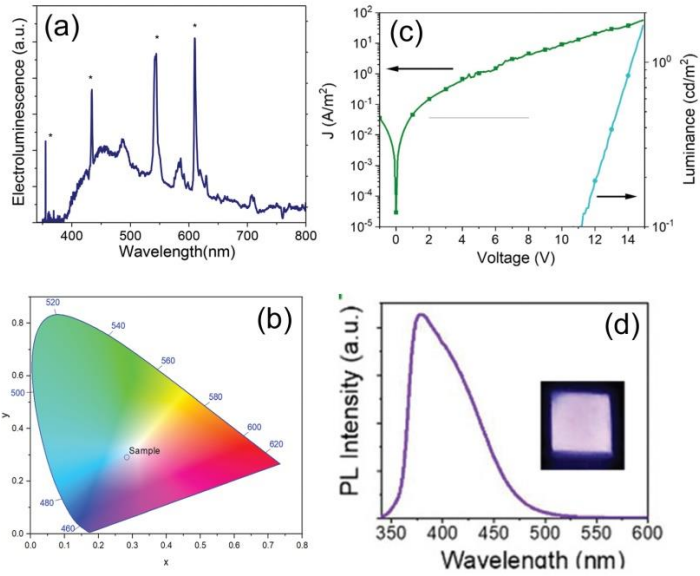

Figure 10: (**a**) The EL spectrum of CD-LED at 8 V (top); (**b**) CIE (Commission Internationale de l'Eclairage) color coordinates of LEDs with CDs as the single emitter, (**c**) J-L versus applied voltage of the LED made without CDs; (**d**) digital picture of the device using polyvinylcarbazole (PVK) as the emissive layer at 12 V and the photoluminescent emission spectra of the device after excitation at 340 nm: reproduced with permission from Reference [74], copyright 2019 The Royal Society of Chemistry.

Ding and colleagues [66] proposed short-chain passivated CDs; in fact, the use of short chains allows for closer CDs, which probably facilitates the injection of carriers into CDs. Their CDs were synthesized via a one-step hydrothermal approach using phthalic acid and ethylenediamine. The resulting CD aqueous solution featured a PLQY of 29.3% and good film-forming ability. CD-OLEDs were fabricated by a solution processing method, and the devices exhibited a stable blue EL peak at 410 nm at 6–9 V. Despite improvement of the carrier transfer ability of CDs achieved by short-chain modification, the lower PLQY compared with that of long-chain passivated CDs and the not optimal device architecture (see the energy barrier at the anode interface in Figure 11a) were the most probable explanation for the lower performance observed in the devices (Figure 11b–d).

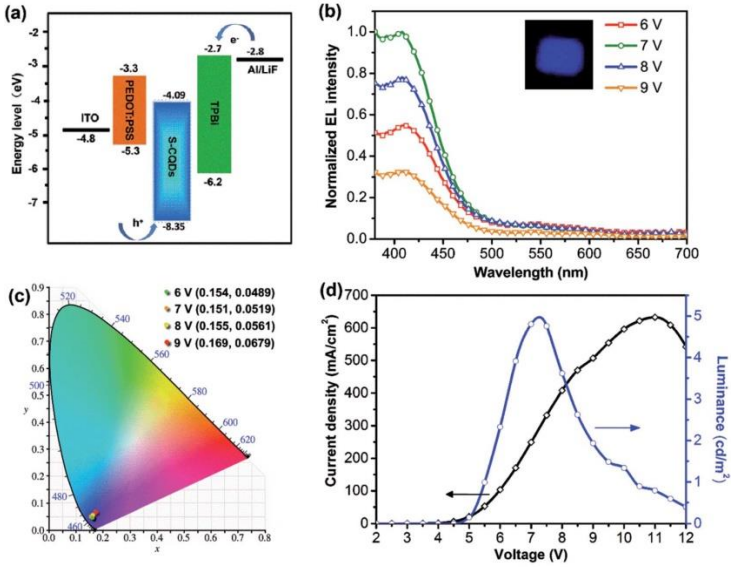

Figure 11: (**a**) The schematic energy level diagram of the CD-LEDs, (**b**) emission spectra at different working voltages (the inset is a photograph of CD-LEDs at 7 V), (**c**) the CIE 1931 chromaticity coordinates of CD-LEDs at different working voltages, and (**d**) *J*–*L*–V characteristics of CD-LEDs: Reproduced with permission from [66], copyright 2017 The Royal Society of Chemistry.

Zhang at al. in 2013 [75] observed for the first time, a multi-colored (bright blue, cyan, magenta, and white) EL from CDs of the same size (3.3 nm). Such a switchable EL behavior had not been previously observed in single nanomaterial emitting layer OLEDs. This all-solution processed device consisted of a CD emissive layer sandwiched between an organic HTL and an organic or inorganic ETL (electron transporting layer, EIL) with typical architecture ITO/PEDOT:PSS/PolyTPD/CDs/TPBI (where poly-TPD was poly-(N,N'-bis(4-butylphenyl)-N,N'-bis(phenyl) benzidine and TPBI 1,3,5-tris(N-phenylbenzimidazol-2-yl) benzene)) or ZnO/LiF/Al (Figure 12A). The devices structure was adjusted to control J and, therefore, the EL spectra. By increasing LiF thickness from 1 at 5 nm or by replacing LiF and TPBi with ZnO, the emitted color changed with the applied voltage from blue, cyan, and magenta and to white from the same carbon dots (Figure 12B-D).

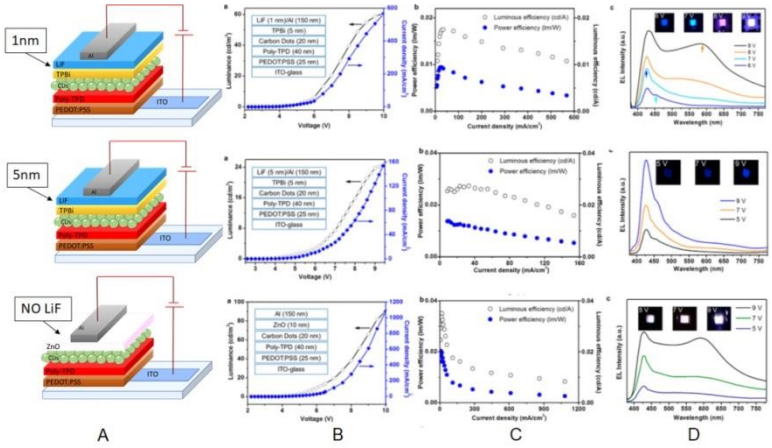

Figure 12: (**a**) Schematic representation of the CD-LED architectures together with (**b**) J and L versus V, (**c**) η_c and power efficiencies vs. J, and (**d**) EL spectra and images of the operating CD-LEDs at different applied voltage: Reproduced with permission from [73], copyright 2013 American Chemical Society.

The L_{MAX} obtained was 24 cd/m^2 for the blue-emitting OLED at low current injection. The L_{MAX} observed in devices incorporating ZnO nanoparticles was higher (90 cd/m^2) thanks to the higher electron mobility of ZnO with respect to organic ETLs.

To solve the problem of aggregation quenching of CDs, a host–guest approach [85,86] has been proposed since 2017, with CDs as guest component and, usually, the PVK as a host matrix.

Yuan et al. [65] compared the performance of a neat CD film to those of CDs dispersed in PVK. They used bright multicolor blue-to-red fluorescent CDs (called MCBF-CDs) with PLQY up to 75%, synthesized through a facile solvothermal method. Their CDs were N-doped, highly surface passivated with a high degree of crystallinity. CDs were firstly employed as an active layer for monochromatic OLEDs with a basic architecture ITO/PEDOT:PSS/CDs/TPBI/Ca/Al (Figure 13a). Monochrome OLEDs featured blue (B), green (G), yellow (Y), orange (O), and red (R) ELs with peaks at 455, 536, 555, 585, and 628 nm and

CIE coordinates (0.19, 0.20), (0.31, 0.47), (0.37, 0.52), (0.46, 0.48), and (0.55, 0.41), respectively. The EL spectra showed voltage-independent behavior as well as no temporal degradation that are of great significance for display technology. In the B-OLEDs, L_{MAX} reached 136 cd/m^2 with η_c of 0.084 cd/A (Figure 13b-d).

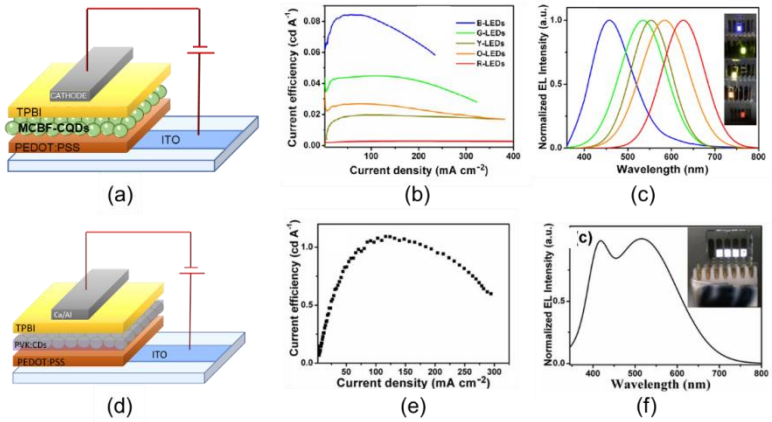

Figure 13: (**a**) Schematic representation of the multicolor blue-to-red fluorescent CD (MCBF-CD)-based device architectures, (**b**) η_c vs. J of MCBF-CD-based monochrome electroluminescent OLEDs from blue to red, (**c**) normalized EL spectra (in the inset is a picture of the working devices), (**d**) schematic representation of the PVK:MCBF-CD–based device architectures, (**e**) η_c vs. J of PVK:MCBF-CD-based monochrome electroluminescent OLEDs from blue to red, (**f**) normalized white EL spectra (in the inset is a picture of the working devices), (**b**,**c**) reproduced with permission from Reference [65], copyright 2016 Wiley-VCH, and (**e**,**f**) reproduced with permission from [14], copyright 2019 American Chemical Society.

In the devices incorporating a blend of green-emitting CD into a PVK polymer matrix (5 wt.% ratio), with ITO/PEDOT:PSS/PVK:MCBF-CDs/TPBI/Ca/Al architecture (Figure 13d), Yuan et al. [65] reached a L_{MAX} and η_c as high as 2050 cd/m^2 and 1.1 cd/A with a low turn on voltage (V_{ON} = 3.9 V) (Figure 13e). In the broad EL spectrum, two peaks were identified, centered at 410 and 517 nm and assigned to PVK and green MCBF-CD emission, respectively (Figure 13f). The CIE coordinate (0.30, 0.33), very close to ideal white, resulted from both the energy transfer from PVK to CD and the direct charge trapping on CD.

In 2018, Xu et al. [76] synthesized oleophilic CDs with a PLQY of 41% by the one-pot microwave carbonization method (Figure 14a) to study the impact of CD aggregation as a limiting factor for the brightness of the CD-LEDs.

They fabricated CD-OLEDs, incorporating a neat CD active layer, with the simple architecture ITO/PEDOT:PSS/CD/TPBI/LiF/Al (Figure 14b). The devices featured modest performance (Figure 14c-f), with yellow emission peaked at 554 nm, L_{MAX} of 5.7 cd/m^2 at 10 V, and CIE coordinates od (0.36, 0.42), most probably because of aggregation of the CDs.

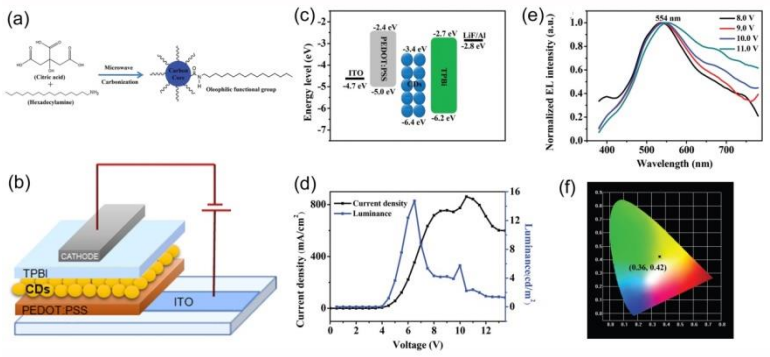

Figure 14: (**a**) Illustration of the route for the synthesis of CDs, (**b**) schematic representation of the device architectures, (**c**) energy level diagram of the CD-LED, (**d**) *J–L–V* characteristics curve of the CD-LED, (**e**) normalized EL spectra of the CD-LED at different driving voltages, (**c**) current density–voltage–luminance (*J–L-V*) characteristics curve of the CD-LED, and (**f**) CIE coordinates of the CD-LED at the working voltage of 10.0 V: reproduced with permission from [76], copyright 2018 The Royal Society of Chemistry.

The impact of CD aggregation on the brightness of CD-OLEDs was studied by Xu et al. also by blending the CDs in PVK. Yellow and white ELs were observed by tuning the doping concentration of the active layer. The yellow EL, mainly derived from direct carrier trapping, reached L_{MAX} of 339.5 cd/m^2 with excellent color stability. The white CD-OLEDs exhibited a Color Rendering Index (CRI) value of 83 with CIE coordinates of (0.29, 0.33) and high L_{MAX} of 544.2 cd/m^2. The

white EL resulted from contemporary emission from PVK and CDs, and the good brightness was attributed to a suitable balance between holes and electrons in the emitting layer (Figure 15) [76].

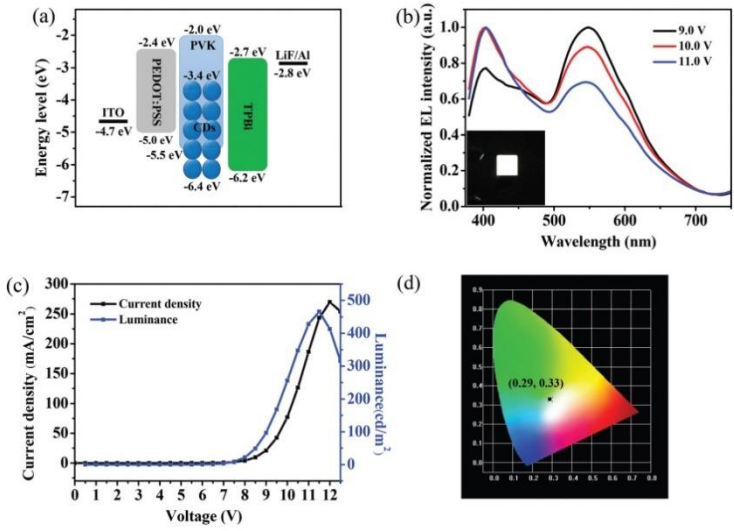

Figure 15: (**a**) The energy level diagram of the white CD-LED, (**b**) normalized EL spectra of the white CD-LED at different voltages (in the inset is a photograph of the working device), (**c**) *J*–*L*-*V* characteristics curve of the white CD-LED, and (**d**) CIE coordinates at a driving voltage of 11 V: reproduced with permission from [76], copyright 2018 The Royal Society of Chemistry.

In the last 3 years, the research on LEDs based on CDs has increased and focalized, almost exclusively, on CDs dispersed in PVK as an emitting layer. The next two articles discussed below showed that amination could be exploited to improve the performance of devices.

Yuan et al. [77] presented deep-blue light-emitting materials and devices based on CDs that outperform also deep-blue emitting LEDs based on Cd^{2+}/Pb^{2+} materials at that time. CDs were synthesized by solvothermal treatment using CA and DAN as precursors. To enable efficient high-color purity, an additional surface amination step using ammonia liquor and hydrazine hydrate under high temperature was performed. This second

step, decreasing the number of defects of CDs and thus suppressing non-radiative pathways, increases the PLQY up to 70%.

CD-OLEDs were manufactured with the architecture ITO/PEDOT:PSS/TFB/PVK:CDs/TPBI/LiF/Al (Figure 16a). The corresponding energy level diagram (Figure 16b) shows a mitigation of energy barrier for both electrons and hole injections thanks to the suitable selection of the different functional layers. Atomic force microscope (AFM) measurements confirmed the small roughness of CDs blended PVK film (Figure 16c). The EL spectra remained centered at 440 nm across the range of voltage explored and are in good agreement with the corresponding PL emission peaks, indicating that an efficient energy transfer from PVK to CDs takes place. *L* and EQE as functions of *V* and *J*, respectively, are shown in Figure 16d,e. L_{MAX}, η_c, and EQE reached remarkable values of 5240 cd/m^2, 2.6 cd/A, and 4%, respectively.

After operating continuously for 3 h at 1000 cd/m^2, the OLED retained 50% of initial luminance (Figure 16f) without evident changes in the EL spectrum.

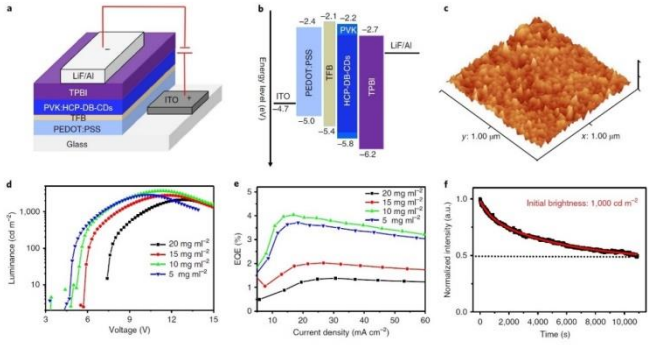

Figure 16: (**a**) PVK:CD-based device structure, (**b**) the energy level diagram, (**c**) the AFM height image of PVK:CD films, (**d**) the L-V curves, (**e**) the EQE–J characteristics, and (**f**) the device stability: Reproduced with permission from [77], copyright 2020 Springer Nature group.

At the same time, Jia and coworkers [80] demonstrated the effectiveness of the electron-donating group passivation strategy to impart in CD finely tuned properties for their application as emitters in CD-OLEDs. Specifically, they developed three efficient red-emissive CDs based on the N,N–dimethyl–(NMe_2), N,N-diethyl–(NEt_2), and N,N-dipropyl–(–NPr_2) p-phenylenediamine derivatives and obtaining CD-NMe_2, –NEt_2, and –NPr_2, respectively (Figure 17a), with the aim to fabricate warm-light WOLEDs.

Thanks to theoretical investigations, they revealed that CD emission originated from the rigid π-conjugated skeleton structure, while –NR_2 passivation played a key role in inducing charge transfer excited state in the π-conjugated structure to afford high PLQY (up to 86%).

Moreover, the polar –NR_2 groups are responsible for the good solubility of CDs in organic solvent and then processability by low-cost spin-coating technique.

Solution-processed OLEDs were fabricated with 9 wt.% CDs–NMe_2 (WOLEDs 1), –NEt_2 (WOLEDs 2), and –NPr_2 (WOLEDs 3) blended in PVK as an emitting layer and the simple architecture ITO/PEDOT:PSS/PolyTPD/blend/TPBI/Ca/Al (Figure 17b). The WOLEDs generated warm-light with two main peaks (434/605, 435/612, and 453/616 nm for WLEDs 1, 2, and 3, respectively, Figure 17c) attributed to emission from PVK and CDs. The corresponding CIE coordinates and correlated color temperatures were (0.379, 0.314)/3365 K, (0.383, 0.311)/3168 K, and (0.388, 0.309)/2987 K. Finally, WOLEDs 1, 2, and 3 displayed voltage-stable EL spectra with a L_{MAX} in the range of 5248–5909 cd/m^2 and a η_c of 3.65-3.85 cd/A (Figure 17d-f).

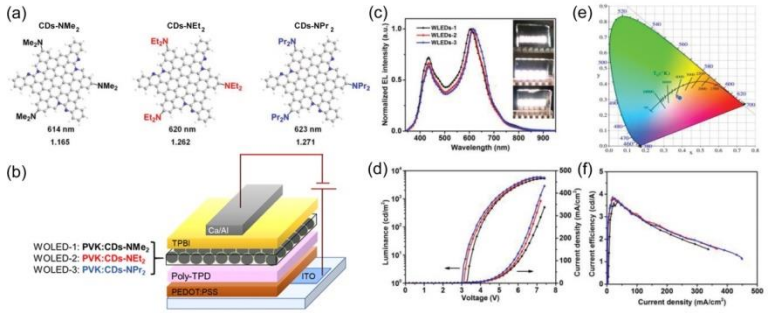

Figure 17: (**a**) CD structures; (**b**) architecture of CD-WLEDs; (**c**) EL spectra of WLEDs 1, 2, and 3 under 7.0 V, (inset, WOLEDs photographs); (**d**) *J–L-V* characteristics; (**e**) CIE coordinates; and (**f**) η_c of WLEDs 1 (black), 2 (red), and 3 (blue): Reproduced with permission from [80], copyright 2019 Wiley-VCH Verlag GmbH & Co.

Yuan et al. [78] recently addressed the issue of broad emission, usually observed in CDs, which limits their application in displays.

They obtained multi-colored narrow bandwidth emission from triangular CDs (T-CDs) synthetized starting from phloroglucinol (PG) (Figure18A). They demonstrated that the molecular purity and high crystallinity of the triangular CDs are indispensable to obtain high color-purity. The triangular structure and the narrow bandwidth emission allowed for dramatic reduction in electron-phonon coupling.

The simple structure ITO/PEDOT:PSS/active layer/TPBI/Ca/Al (Figure 18B) was used for fabrication of OLEDs emitting from blue to red with the T-CDs blended in PVK as an active emission layer. The good match between HOMO/LUMO energy levels of T-CDs and PVK ensured the efficient transfer of both electrons and holes from PVK to T-CDs emitter. The multi-colored OLEDs based on the T-CDs demonstrated high color-purity (FWHM of 30–39 nm) peaked at 476, 510, 540, and 602 nm for B-, G-, Y-, and R-LEDs, respectively, a η_c of 1.22–5.11 cd/A , and L_{MAX} of 1882–4762 cd/m^2, rivalling the well-developed inorganic QD-based LEDs. Finally, the LEDs exhibited outstanding stability, which is of great significance for display technology. See Figure 18 B-I

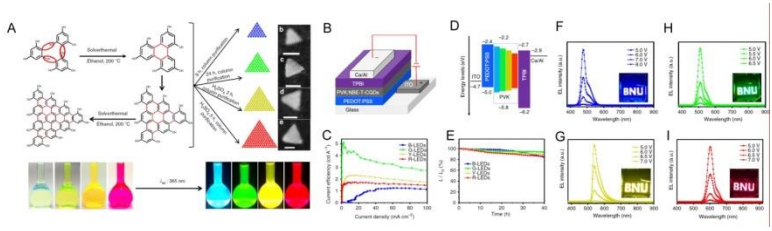

Figure 18: (**a**) Synthesis route of the T-CQDs by solvothermal treatment of PG triangulogen, with photographs of the T-CQD ethanol solution under daylight (left) and fluorescence images under UV light (excited at 365 nm) (right) included; (**b**) the device structure; (**c**) the current efficiency versus current density; (**d**) the energy level diagram of the T-CQD-based LEDs; and (**e**) the stability plots of the B-, G-, Y-, and R-LED. EL spectra of the B- (**f**), G- (**h**), Y- (**g**), and R-LEDs (**i**) at different bias voltage, respectively (the insets are the operation photographs of the B-, G-, Y-, and R-LEDs with the logo of BNU). Reproduced with permission from Reference [78], copyright 2019 Springer Nature group.

Singh and colleagues [79] fabricated the first flexible OLED (Figure 19a,b) based on CDs employing self-assembled 2D array of CDs embedded in a PVK emission layer. The flexible device was switched on at 4.3 V and exhibited a blue/cyan emission peaked at about 500 nm (comparable to PL emission, Figure 19c) with L_{MAX} of 350 cd/m^2 and η_c of 0.22 cd/A (Figure 19d,e), whereas the corresponding OLED device based on the rigid glass substrate featured a L_{MAX} of 700 cd/m^2 and η_c of 0.27 cd/A. Figure 19f shows the CD 2D island in the emitter layer.

The host–guest energy transfer as the main mechanism for CD emission was exploited by Xu et al. [81] for the fabrication of solution-processed blue CD-LEDs with ultrahigh brightness. Oleophylic CDs with a PLQY of 41% were obtained using an anhydrous citric acid as carbon precursor and hexadecylamine as passivation agent by the one-step microwave carbonization method. CDs with different doping concentrations were blended with PVK and incorporated into a simple and PEDOT-free device architecture ITO/PVK:CDs/TPBI/LiF/Al (Figure 20a). The EL spectra of devices were dominated by the 474 nm CD emission peak with a contribution from a PVK at around 410 nm. When the doping concentration was higher than 25 wt.%, a progressive weakening of the PVK contribution in favor of an enhanced CD emission was observed. For the 30 wt.% doping

ratio, the L_{MAX} reached 569.8 cd/m^2 at a driving voltage of 12.5 V, with CIE coordinated at (0.22, 0.27) located in the blue light region (Figure 20b). Also, in this case, the long-chain passivating ligands on the oleophylic CD surfaces were responsible for the unideal transporting performance that limited the device efficiencies. However, it should also be considered that the devices do not contain the commonly employed PEDOT:PSS layer.

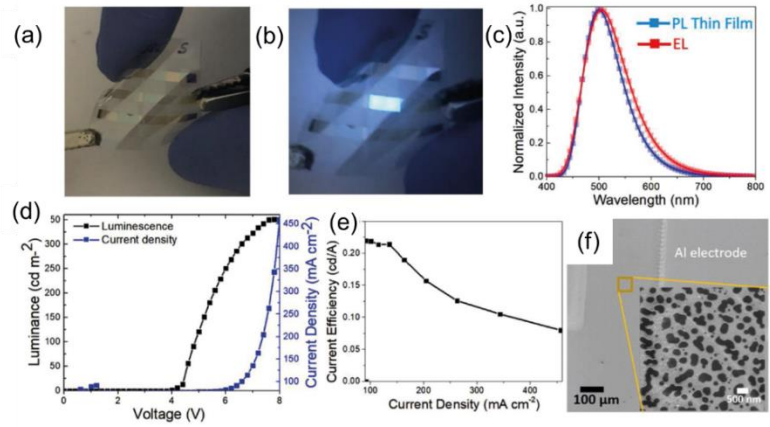

Figure 19: Picture of a flexible device: (**a**) off mode and (**b**) on mode; (**c**) the normalized EL spectra of the device and solid-state PL of a thin film; (**d**) *J-L-V* characteristic of the device; (**e**) current efficiency versus current density; and (**f**) CD 2D islands in the emitter layer: Reproduced with permission from [79], copyright 2020 Wiley-VCH Verlag GmbH & Co.

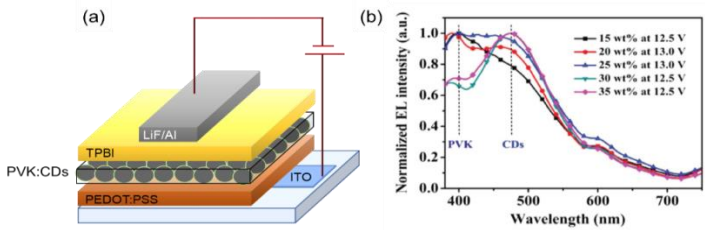

Figure 20: (**a**) Device architecture and (**b**) normalized EL spectra for different CD-doped devices: Reproduced with permission from [81], copyright 2020 Wiley-VCH Verlag GmbH & Co.

CDs as Charge Regulating Interlayer

The possibility to tune the CD's energy levels and intrinsic charge carrier transport enables an alternative use of CD besides incorporation as an emitting layer. In fact, the following paragraph demonstrates that CDs, employed as an interlayer at the electrode interface (for this reason, they are called interfacial layers or charge regulating layers) in devices based on different class of emitters, may improve the overall performance of LEDs. We report examples in which the CD layer was incorporated both as ETL and HTL in either direct or inverted LED architectures (Figure 7).

In 2017, Park et al. [84] explored the possibility to enhance the performance of nanocrystal LEDs (NC-LEDS) based on quantum dot active layers. NC-LEDs typically take advantage of the incorporation of organic or inorganic interfacial layers as charge regulators to ensure charge balancing and high performance [87]. They investigated the role played by CD N-doped interlayers inserted by spin-coating between the PVK (used as HTL) and the core/shell CdSe/CdS quantum dots (QDs)-based emitting layer [88,89]. In fact, QD-LEDs basically consisted of a multilayer architecture ITO/PEDOT:PSS/PVK/with or without N-CD/QD/ZnO/Al (types A and B, Figure 21a). They showed that CD HTL decreased the barrier height for hole injection, thus leading to more charge carrier balance within the emitting layer. Moreover, they demonstrated that the CD interlayer acted as a resonant energy donor layer to the QD layer.

Both type A and B devices exhibited good electrical rectification, but the leakage current of type A QD-LEDs was significantly suppressed by inserting the N-CD layer (see lower J for type A devices with respect to type B ones in the ohmic range below 0.5 V in Figure 21b,c). Noteworthily, the L_{MAX} observed in LED incorporating CDs outperformed type B LEDs, showing 3500 and 20 cd/m^2, and the η_c were 0.63 and 0.044 cd/A, respectively (Figure 21d,e). The EL of both types of LEDs was dominated by the emission peak at 622 nm under applied

voltage >4 V (Figure 21f) with CIE coordinates (0.66, 0.33) corresponding to the highly pure red emission (Figure 21g).

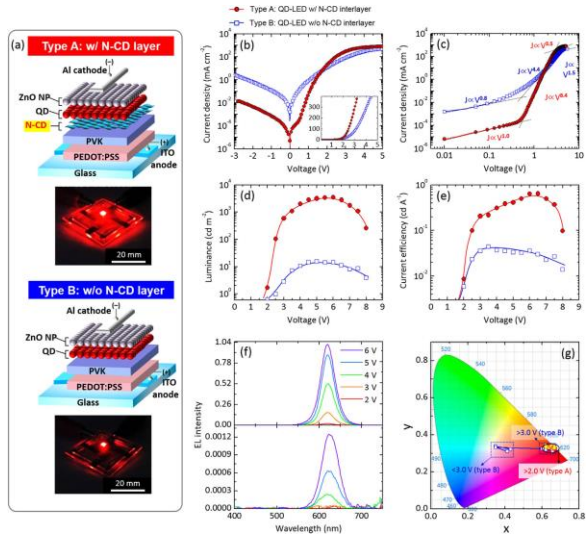

Figure 21: (**a**) Structures of solution-processed quantum dots (QD)-LEDs, with photographs of red emission from both types of QD-LEDs reported; (**b**) *J–V* characteristic curves, with an inset plotted in a linear scale at forward applied voltages; (**c**) *J–V* characteristic curves plotted on double-logarithmic axes; (**d**) luminance and (**e**) current efficiency plotted as a function of applied voltage; (**f**) EL spectra of the N-CD-inserted QD-LED (upper panel) and the control QD-LED (lower panel) at diverse applied voltages; and (**g**) CIE coordinates of EL emission colors measured at various applied bias voltages of 2.0–8.0 V: Reproduced with permission from [84], copyright 2019 Springer Nature group.

In a very recently publication, Paulo-Mirasol et al. [90] described the use CDs as HTL but in an inverted LED architecture. They synthetized four N-doped CDs by citric acid as a precursor of carbon skeleton and p-phenylenediamine, EDA, urea, and HDA as precursors of a capping ligand and showed that the nature of the capping ligand influences directly the optoelectronic properties of CDs (Table 2). The architecture of the device consisted of a ZnO nanoparticle layer directly deposited on the ITO of an emissive conjugated polymer, the well-known and commercially available poly (9,9-dioctylfluorene-alt- benzothiazole or F8BT, and of the CDs (Figure 22A) as HTL. The devices were completed by Au anode.

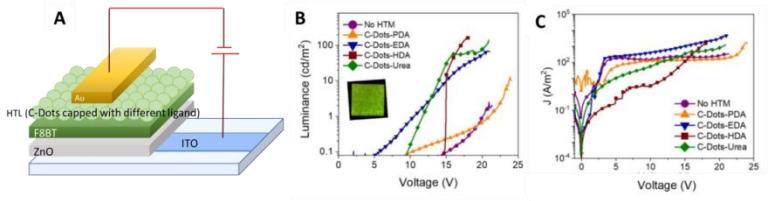

Figure 22: (**A**) Device architecture, (**B**) luminance vs. applied bias (the inset shows a picture of a working device), and (**C**) current density versus applied bias for the inverted LEDs prepared using the CDs in the selective contact for holes: reproduced with permission from Reference [90], copyright 2019 American Chemical Society.

Table 2: Summary of the most relevant parameters of devices from Reference [90], including values obtained for a control device without hole transporting layer (HTL).

Hole Transport Materials	**Capping Ligand Hole Mobility** [a)]	L_{MAX} **(cd/m²)**	η_c **(cd/A)**
C-Dots-EDA	2.41 ± 0.60	70	2×10^{-3}
C-Dots-PDA	1.5 ± 0.47	13	9×10^{-4}
C-Dots-HDA	85.4 ± 1.7	174	8×10^{-4}
C-Dots-Urea	2.92 ± 0.32	146	2×10^{-3}
No HTM (control)	-	2	5×10^{-4}

a) space charge limited current hole mobility measured in hole-only devices.

The LEDs displayed moderate L values but were always clearly superior to the control CD-free device (Figure 22B,C). In the case of EDA capping, the V_{ON} was very low, which indicates the existence of an excellent charge injection capability. On the other hand, devices prepared with urea and HDA CDs showed the highest L, as summarized in Table 2.

Alam et al. [83] reported the use of CDs synthesized with a one-step hydrothermal process using the banana leaf precursor as the ETL in direct architecture LEDs with polyfluorene derivative as the emitting layer (Figure 23a,b). The introduction of CD as the ETL reduces the energy barrier for electron injection, which in turn lowered the V_{ON}. The EL spectra showed dominant peaks typical of PFO but slightly red-shifted compared to that in the literature.

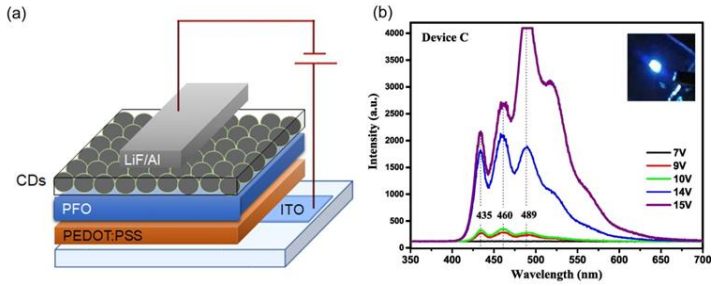

Figure 23: (**a**) Scheme of the device architecture and (**b**) EL spectra as a function of operating voltage: Reproduced with permission from [83], copyright 2019 Wiley-VCH Verlag GmbH & Co.

Zang et al. [82] demonstrated that stable, abundant, and easy-to-synthesize CDs are suitable as solution processable thin transparent films, serving as the cathode surface modifier in inverted LED architecture. This CD ETL minimized the charge injection/extraction energy barrier, improved the interface contact property, and smoothed the electron transport pathways in various optoelectronic devices such as perovskite solar cells and QD-LEDs. A series of CDs with varying content of either amine or carboxyl groups at their surface were synthesized using varying ratios of common precursors CA and EDA. Thanks to a film consisting in a blend of CDs in ZnO, the work-function (WF) of commonly used ITO substrates was modified over a broad range to become suitable as electron injection electrode in the inverted device architecture (Figure 24a,b). Specifically, CD modifiers with abundant amine groups reduced the ITO's WF from 4.64 to 3.42 eV, while those with abundant carboxyl groups increased it to 4.99 eV. They manufactured the inverted QD-LED architecture based on $CsPbI_3$ emitters. The EQE increased from 4.8% to 10.3% and the L_{MAX} increased from 951 to 1605 cd/m^2 thanks to incorporation of the CD layer and in the same way, the EQE of CdSe/ZnS QD-LEDs increased from 8.1% to 21.9% and η_c increased from 34.7 at 93.8 cd/A (Figure 24c-f).

The proposed approach may hold true for CDs with other surface functional groups, which guides us toward more ideal interface materials, offering chances to lower the production costs of

various solution-processed optoelectronic devices with an improved performance.

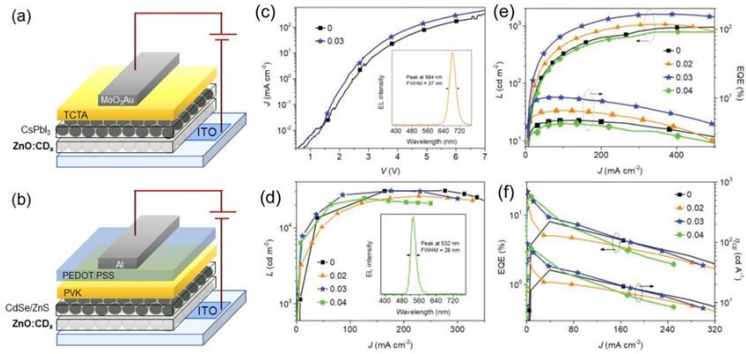

Figure 24: (**a**) $CsPbI_3$ and (**b**) CdSe/ZnS QD-LED device architectures; (**c**) J-V of $CsPbI_3$ QD-LEDs with or without CDs (concentration 0.03 mg/mL in ZnO and CD_x being molar ratios of the CA and EDA precursors) interface modifier, with the EL spectrum of the LED employing the CD (0.03 mg/mL) modifier given as an inset; (**d**) L-J of CdSe/ZnS QD-LEDs modified with different concentrations of CDs as given on the frame (in mg/mL), with the EL spectrum of the LED employing the CDs (concentration 0.03 mg/mL) modifier given as an inset; (**e**) L and EQE versus J of $CsPbI_3$ QD-LEDs modified with different concentrations of $CD_{0.33}$ as given on the frame (in mg/mL); and (**f**) EQE and η_c versus J of CdSe/ZnS QD-LEDs with or without CD modifiers introduced at different concentrations (in mg/mL) provided on the frame: Reproduced with permission from [82], copyright 2019 WILEY-VCH Verlag GmbH & Co.

Summary and Outlook

CDs are materials with a great potential from multiple points of view. In fact, despite being relatively young materials, the discovery of which is placed between 2004 and 2006, their development has already led to particularly encouraging results in many disciplines including biosensing, photonics, and optoelectronics.

The interest in this class of materials is both academic and applicative. In fact, numerous efforts have been made to understand and modulate their chemical and physical properties, and although different mechanisms have been highlighted, much remains to be done, especially in reproducibility and in the deep

understanding of their size, shape, and composition/doping property dependence.

With regard to their application in OLEDs, as reported here, they have been used both as active layers and as charge regulation layers.

CDs have been used as active layers both dispersed in the matrix to avoid aggregation quenching and as a neat film, leading to increasingly encouraging results mostly when their surface was passivated by a hexadecylamine (HDA) agent [71,79].

Recently, CDs have been tested as a charge regulating layer (both for holes and for electrons), in either direct or inverted device's architectures, highlighting their great versatility linked to the huge number of possible modifications, which, as we have pointed out, are related to composition, shape, size, and surface groups. Importantly, CDs used as ETLs in OLED with direct architecture were synthetized with the one-step hydrothermal process using banana leaves as raw material.

In our opinion, the importance of these materials consists in the possibility of declining them for the concept of safe-by-design, which is substantially at the basis of circular economy.

To promote sustainability in the electronics industry, a paradigm shift needs to occur in economic practices from linear to circular. According to the Ellen McArthur Foundation, new electronics must be designed for sustainability from the get-go [91].

Technical performance is the driving force for not only the design but also the use of sustainable precursor (from waste or renewable materials); biodegradability, toxicity, synthetic methodology, and production of toxic waste are only some of the key parameters to be taken into consideration.

In this perspective, although CDs are currently still very far from the performance of other active materials commonly used in LED and OLED such as metallic quantum dots or organic

semiconductors, in a circular perspective, they are already able to meet some fundamental requirements.

For this reason, we hope that this review can offer a contribution and be a source of inspiration for the transition towards "circular organic electronics".

References

1. Baldé CP, Forti V, Gray V, Kuehr R, Stegmann P. International Telecommunication Union, United Nations University, International Solid Waste Association. The Global E-Waste Monitor 2017: Quantities, Flows, and Resources, United Nations University: Tokyo, Japan, International Telecommunication Union: Geneva, Switzerland. Rotterdam: International Solid Waste Association. 2017.
2. Ostroverkhova O. Organic Optoelectronic Materials: Mechanisms and Applications. Chem. Rev. 2016; 116: 13279–13412.
3. Forrest SR, Thompson ME. Introduction: Organic electronics and optoelectronics. Chem. Rev. 2007; 107: 923–925.
4. Hadziioannou G, Malliaras GGM. In: Hadziioannou G, Malliaras GGM, editors. Semiconducting Polymers: Chemistry, Physics and Engineering, 2nd Edition, Two-Volume Set. Hoboken: Wiley. 2006.
5. Zvezdin A, Di Mauro E, Rho D, Santato C, Khalil M. En route toward sustainable organic electronics. MRS Energy Sustain. 2020; 7.
6. Giovanella U, Betti P, Bolognesi A, Destri S, Melucci M, et al. Core-type polyfluorene-based copolymers for low-cost light-emitting technologies. Org. Electron. 2010; 11: 2012–2018.
7. Irimia-Vladu M. "Green" electronics: Biodegradable and biocompatible materials and devices for sustainable future. Chem. Soc. Rev. 2014; 43: 588–610.
8. Yan L, Zhao F, Wang J, Zu Y, Gu Z, et al. A Safe-by-Design Strategy towards Safer Nanomaterials in Nanomedicines. Adv. Mater. 2019; 31: 1805391.

9. Gomulya W, Derenskyi V, Kozma E, Pasini M, Loi MA. Polyazines and polyazomethines with didodecylthiophene units for selective dispersion of semiconducting single-walled carbon nanotubes. Adv. Funct. Mater. 2015; 25: 5858–5864.
10. Xu X, Ray R, Gu Y, Ploehn HJ, Gearheart L, et al. Electrophoretic analysis and purification of fluorescent single-walled carbon nanotube fragments. J. Am. Chem. Soc. 2004; 126: 12736–12737.
11. Sun YP, Zhou B, Lin Y, Wang W, Fernando KAS, et al. Quantum-sized carbon dots for bright and colorful photoluminescence. J. Am. Chem. Soc. 2006; 128: 7756–7757.
12. Xiao L, Sun H. Novel properties and applications of carbon nanodots. Nanoscale Horiz. 2018; 3: 565–597.
13. Li X, Rui M, Song J, Shen Z, Zeng H. Carbon and graphene quantum dots for optoelectronic and energy devices: A review. Adv. Funct. Mater. 2015; 25: 4929–4947.
14. Semeniuk M, Yi Z, Poursorkhabi V, Tjong J, Jaffer S, et al. Future perspectives and review on organic carbon dots in electronic applications. ACS Nano. 2019; 13: 6224–6255.
15. Campuzano S, Yáñez-Sedeño P, Pingarrón JM. Carbon dots and graphene quantum dots in electrochemical biosensing. Nanomaterials. 2019; 9: 634.
16. Liu ML, Chen B Bin, Li CM, Huang CZ. Carbon dots: Synthesis, formation mechanism, fluorescence origin and sensing applications. Green Chem. 2019; 21: 449–471.
17. Wang Y, Hu A. Carbon quantum dots: Synthesis, properties and applications. J. Mater. Chem. C 2014; 2: 6921–6939.
18. Gayen B, Palchoudhury S, Chowdhury J. Carbon dots: A mystic star in the world of nanoscience. J. Nanomater. 2019; 2019: 3451307.
19. Chan KK, Yap SHK, Yong KT. Biogreen synthesis of carbon dots for biotechnology and nanomedicine applications. Nano-Micro Lett. 2018; 10: 72.
20. Zuo J, Jiang T, Zhao X, Xiong X, Xiao S, et al. Preparation and application of fluorescent carbon dots. J. Nanomater. 2015; 2015.

21. Pal A, Sk MP, Chattopadhyay A. Recent advances in crystalline carbon dots for superior application potential. Mater. Adv. 2020; 1: 525–553.
22. Wang L, Li W, Yin L, Liu Y, Guo H, et al. Full-color fluorescent carbon quantum dots. Sci. Adv. 2020; 6: eabb6772.
23. Li X, Wang H, Shimizu Y, Pyatenko A, Kawaguchi K, et al. Preparation of carbon quantum dots with tunable photoluminescence by rapid laser passivation in ordinary organic solvents. Chem. Commun. 2011; 47: 932–934.
24. Yang ZC, Wang M, Yong AM, Wong SY, Zhang XH, et al. Intrinsically fluorescent carbon dots with tunable emission derived from hydrothermal treatment of glucose in the presence of monopotassium phosphate. Chem. Commun. 2011; 47: 11615–11617.
25. Hu S, Liu J, Yang J, Wang Y, Cao S. Laser synthesis and size tailor of carbon quantum dots. J. Nanoparticle Res. 2011; 13: 7247–7252.
26. Tarasenka N, Stupak A, Tarasenko N, Chakrabarti S, Mariotti D. Structure and optical properties of carbon nanoparticles generated by laser treatment of graphite in liquids. ChemPhysChem. 2017; 18: 1074–1083.
27. De B, Karak N. A green and facile approach for the synthesis of water soluble fluorescent carbon dots from banana juice. RSC Adv. 2013; 3: 8286–8290.
28. Zhu S, Meng Q, Wang L, Zhang J, Song Y, et al. Highly photoluminescent carbon dots for multicolor patterning, sensors, and bioimaging. Angew. Chemie Int. Ed. 2013; 52: 3953–3957.
29. Dong Y, Pang H, Yang H Bin, Guo C, Shao J, et al. Carbon-based dots co-doped with nitrogen and sulfur for high quantum yield and excitation-independent emission. Angew. Chemie Int. Ed. 2013; 52: 7800–7804.
30. Chen Y, Lian H, Wei Y, He X, Chen Y, et al. Concentration-induced multi-colored emissions in carbon dots: Origination from triple fluorescent centers. Nanoscale. 2018; 10: 6734–6743.
31. Ehrat F, Bhattacharyya S, Schneider J, Löf A, Wyrwich R, et al. Tracking the source of carbon dot photoluminescence:

aromatic domains versus molecular fluorophores. Nano Lett. 2017; 17: 7710–7716.
32. Bao L, Liu C, Zhang ZL, Pang DW. Photoluminescence-tunable carbon nanodots: Surface-state energy-gap tuning. Adv. Mater. 2015; 27: 1663–1667.
33. Zhang J, Su ZC, Cui Y, Hu G, Tang YL, et al. The roles of self-absorption and radiative energy transfer in photoluminescence of N-doped carbon nanodots in solution. AIP Adv. 2019; 9: 035135.
34. Khan S, Gupta A, Verma NC, Nandi CK. Time-resolved emission reveals ensemble of emissive states as the origin of multicolor fluorescence in carbon dots. Nano Lett. 2015; 15: 8300–8305.
35. Zhu S, Zhang J, Liu X, Li B, Wang X, et al. Graphene quantum dots with controllable surface oxidation, tunable fluorescence and up-conversion emission. RSC Adv. 2012; 2: 2717.
36. Wang X, Qu K, Xu B, Ren J, Qu X. Microwave assisted one-step green synthesis of cell-permeable multicolor photoluminescent carbon dots without surface passivation reagents. J. Mater. Chem. 2011; 21: 2445.
37. Yang ST, Wang X, Wang H, Lu F, Luo PG, et al. Carbon dots as nontoxic and high-performance fluorescence imaging agents. J. Phys. Chem. C 2009; 113: 18110–18114.
38. Wang K, Gao Z, Gao G, Wo Y, Wang Y, et al. Systematic safety evaluation on photoluminescent carbon dots. Nanoscale Res. Lett. 2013; 8: 1–9.
39. Dias C, Vasimalai N, P Sárria M, Pinheiro I, Vilas-Boas V, et al. Biocompatibility and bioimaging potential of fruit-based carbon dots. Nanomaterials. 2019; 9: 199.
40. Sendão R, Yuso M del VM de, Algarra M, Esteves da Silva JCG, Pinto da Silva L. Comparative life cycle assessment of bottom-up synthesis routes for carbon dots derived from citric acid and urea. J. Clean. Prod. 2020; 254.
41. Zhu S, Song Y, Zhao X, Shao J, Zhang J, et al. The photoluminescence mechanism in carbon dots (graphene quantum dots, carbon nanodots, and polymer dots): Current state and future perspective. Nano Res. 2015; 8: 355–381.

42. Giovanella U, Pasini M, Botta C. Organic Light-Emitting Diodes (OLEDs): Working Principles and Device Technology. Cham: Springer. 2016; 145–196.
43. Squeo BM, Pasini M. BODIPY platform: A tunable tool for green to NIR OLEDs. Supramol. Chem. 2020; 32: 56–70.
44. De Medeiros TV, Manioudakis J, Noun F, Macairan JR, Victoria F, et al. Microwave-assisted synthesis of carbon dots and their applications. J. Mater. Chem. C 2019; 7: 7175–7195.
45. Huang CC, Hung YS, Weng YM, Chen W, Lai YS. Sustainable development of carbon nanodots technology: Natural products as a carbon source and applications to food safety. Trends Food Sci. Technol. 2019; 86: 144–152.
46. Ludmerczki R, Mura S, Carbonaro CM, Mandity IM, Carraro M, et al. Carbon dots from citric acid and its intermediates formed by thermal decomposition. Chem. A Eur. J. 2019; 25: 11963–11974.
47. Yuan F, Li S, Fan Z, Meng X, Fan L, et al. Shining carbon dots: Synthesis and biomedical and optoelectronic applications. Nano Today. 2016; 11.
48. Li X, Zhang S, Kulinich SA, Liu Y, Zeng H. Engineering surface states of carbon dots to achieve controllable luminescence for solid-luminescent composites and sensitive Be^{2+} detection. Sci. Rep. 2014; 4: 1–8.
49. Kandasamy G. Recent advancements in doped/co-doped carbon quantum dots for multi-potential applications. C J. Carbon Res. 2019; 5: 24.
50. Mandal B, Sarkar S, Sarkar P. Exploring the electronic structure of graphene quantum dots. J. Nanoparticle Res. 2012; 14.
51. Li Y, Shu H, Niu X, Wang J. Electronic and optical properties of edge-functionalized graphene quantum dots and the underlying mechanism. J. Phys. Chem. C 2015; 119: 24950–24957.
52. Yamijala SS, Bandyopadhyay A, Pati SK. Structural stability, electronic, magnetic, and optical properties of rectangular graphene and boron nitride quantum dots: Effects of size, substitution, and electric field. J. Phys. Chem. C 2013; 117: 23295–23304.

53. Güttinger J, Stampfer C, Frey T, Ihn T, Ensslin K. Graphene quantum dots in perpendicular magnetic fields. Phys. status solidi. 2009; 246: 2553–2557.
54. Li X, Lau SP, Tang L, Ji R, Yang P. Sulphur doping: A facile approach to tune the electronic structure and optical properties of graphene quantum dots. Nanoscale. 2014; 6: 5323–5328.
55. Tao S, Zhu S, Feng T, Xia C, Song Y, et al. The polymeric characteristics and photoluminescence mechanism in polymer carbon dots: A review. Mater. Today Chem. 2017; 6.
56. Guo W, Luo Y, Wei K, Gao X. A cellular level biocompatibility and biosafety evaluation of mesoporous SiO_2-based nanocomposite with lanthanum species. J. Mater. Sci. 2011; 47: 1514–1521.
57. Ge J, Lan M, Zhou B, Liu W, Guo L, et al. A graphene quantum dot photodynamic therapy agent with high singlet oxygen generation. Nat. Commun. 2014; 5: 1–8.
58. Tang L, Ji R, Li X, Bai G, Liu CP, et al. Deep ultraviolet to near-infrared emission and photoresponse in layered n-doped graphene quantum dots. ACS Nano. 2014; 8: 6312–6320.
59. Shamsipur M, Barati A, Karami S. Long-wavelength, multicolor, and white-light emitting carbon-based dots: Achievements made, challenges remaining, and applications. Carbon N. Y. 2017; 124.
60. Song Y, Zhu S, Zhang S, Fu Y, Wang L, et al. Investigation from chemical structure to photoluminescent mechanism: A type of carbon dots from the pyrolysis of citric acid and an amine. J. Mater. Chem. C 2015; 3: 5976–5984.
61. Wang Y, Li Y, Yan Y, Xu J, Guan B, et al. Luminescent carbon dots in a new magnesium aluminophosphate zeolite. Chem. Commun. 2013; 49: 9006–9008.
62. Xu Q, Kuang T, Liu Y, Cai L, Peng X, et al. Heteroatom-doped carbon dots: Synthesis, characterization, properties, photoluminescence mechanism and biological applications. J. Mater. Chem. B 2016; 4: 7204–7219.
63. Li L, Dong T. Photoluminescence tuning in carbon dots: Surface passivation or/and functionalization, heteroatom doping. J. Mater. Chem. C 2018; 6: 7944–7970.

64. Yan F, Sun Z, Zhang H, Sun X, Jiang Y, et al. The fluorescence mechanism of carbon dots, and methods for tuning their emission color: A review. Microchim. Acta 2019; 186: 583.
65. Yuan F, Wang Z, Li X, Li Y, Tan Z, et al. Bright multicolor bandgap fluorescent carbon quantum dots for electroluminescent light-emitting diodes. Adv. Mater. 2017; 29.
66. Ding Y, Zhang F, Xu J, Miao Y, Yang Y, et al. Synthesis of short-chain passivated carbon quantum dots as the light emitting layer towards electroluminescence. RSC Adv. 2017; 7: 28754–28762.
67. Miao X, Qu D, Yang D, Nie B, Zhao Y, et al. Synthesis of carbon dots with multiple color emission by controlled graphitization and surface functionalization. Adv. Mater. 2018; 30: 1704740.
68. Shi L, Yang JH, Zeng HB, Chen YM, Yang SC, et al. Carbon dots with high fluorescence quantum yield: The fluorescence originates from organic fluorophores. Nanoscale. 2016; 8: 14374–14378.
69. Song Y, Zhu S, Yang B. Bioimaging based on fluorescent carbon dots. RSC Adv. 2014; 4: 27184–27200.
70. Ding H, Yu SB, Wei JS, Xiong HM. Full-color light-emitting carbon dots with a surface-state-controlled luminescence mechanism. ACS Nano. 2016; 10: 484–491.
71. Zheng X, Wang H, Gong Q, Zhang L, Cui G, et al. Highly luminescent carbon nanoparticles as yellow emission conversion phosphors. Mater. Lett. 2015; 143.
72. Joseph J, Anappara AA. White-light-emitting carbon dots prepared by the electrochemical exfoliation of graphite. ChemPhysChem. 2017; 18: 292–298.
73. Wang F, Chen Y, Liu C, Ma D. White light-emitting devices based on carbon dots' electroluminescence. Chem. Commun. 2011; 47: 3502.
74. Paulo-Mirasol S, Martínez-Ferrero E, Palomares E. Direct white light emission from carbon nanodots (C-dots) in solution processed light emitting diodes. Nanoscale. 2019; 11: 11315–11321.

75. Zhang X, Zhang Y, Wang Y, Kalytchuk S, Kershaw SV, et al. Color-switchable electroluminescence of carbon dot light-emitting diodes. ACS Nano. 2013; 7: 11234–11241.
76. Xu J, Miao Y, Zheng J, Wang H, Yang Y, et al. Carbon dot-based white and yellow electroluminescent light emitting diodes with a record-breaking brightness. Nanoscale. 2018; 10: 11211–11221.
77. Yuan F, Wang YK, Sharma G, Dong Y, Zheng X, et al. Bright high-colour-purity deep-blue carbon dot light-emitting diodes via efficient edge amination. Nat. Photonics. 2020; 14.
78. Yuan F, Yuan T, Sui L, Wang Z, Xi Z, et al. Engineering triangular carbon quantum dots with unprecedented narrow bandwidth emission for multicolored LEDs. Nat. Commun. 2018; 9: 1–11.
79. Singh A, Wolff A, Yambem SD, Esmaeili M, Riches JD, et al. Biowaste-derived, self-organized arrays of high-performance 2d carbon emitters for organic light-emitting diodes. Adv. Mater. 2020; 32: 1906176.
80. Jia H, Wang Z, Yuan T, Yuan F, Li X, et al. Electroluminescent warm white light-emitting diodes based on passivation enabled bright red bandgap emission carbon quantum dots. Adv. Sci. 2019; 6: 1900397.
81. Xu J, Miao Y, Zheng J, Yang Y, Liu X. Ultrahigh brightness carbon dot–based blue electroluminescent leds by host–guest energy transfer emission mechanism. Adv. Opt. Mater. 2018; 6: 1800181.
82. Zhang X, Zeng Q, Xiong Y, Ji T, Wang C, et al. Energy level modification with carbon dot interlayers enables efficient perovskite solar cells and quantum dot based light-emitting diodes. Adv. Funct. Mater. 2020; 30: 1910530.
83. Alam MB, Yadav K, Shukla D, Srivastava R, Lahiri J, et al. Carbon quantum dot as electron transporting layer in organic light emitting diode. Chemistry Select. 2019; 4: 7450–7454.
84. Park YR, Jeong HY, Seo YS, Choi WK, Hong YJ. Quantum-dot light-emitting diodes with nitrogen-doped carbon nanodot hole transport and electronic energy transfer layer. Sci. Rep. 2017; 7: 1–13.
85. Cappelli A, Villafiorita-Monteleone F, Grisci G, Paolino M, Razzano V, et al. Highly emissive supramolecular

assemblies based on π-stacked polybenzofulvene hosts and a benzothiadiazole guest. J. Mater. Chem. C 2014; 2: 7897–7905.
86. Botta C, Betti P, Pasini M. Organic nanostructured host-guest materials for luminescent solar concentrators. J. Mater. Chem. A 2013; 1: 510–514.
87. Giovanella U, Pasini M, Lorenzon M, Galeotti F, Lucchi C, et al. Efficient solution-processed nanoplatelet-based light-emitting diodes with high operational stability in air. Nano Lett. 2018; 18: 3441–3448.
88. Castelli A, Meinardi F, Pasini M, Galeotti F, Pinchetti V, et al. High-efficiency all-solution-processed light-emitting diodes based on anisotropic colloidal heterostructures with polar polymer injecting layers. Nano Lett. 2015; 15: 5455–5464.
89. Pasini M, Giovanella U, Betti P, Bolognesi A, Botta C, et al. The role of triphenylamine in the stabilization of highly efficient polyfluorene-based OLEDs: A model oligomers study. ChemPhysChem. 2009; 10: 2143–2149.
90. Paulo-Mirasol S, Gené-Marimon S, Martínez-Ferrero E, Palomares E. Inverted hybrid light-emitting diodes using carbon dots as selective contacts: the effect of surface ligands. ACS Appl. Electron. Mater. 2020; 2: 1388–1394.
91. Meloni M, Souchet F, Sturges D. Circular-Consumer-Electronics-2704: An Initial Exploration. Ellen MacArthur Foundation. UK. 2018.

Book Chapter

Fabrication of Co-Ni based Superhydrophobic Coating and its Wear Resistance, Durability and Corrosion Resistance

Yanpeng Xue* and Shuqiang Wang

National Center for Materials Service Safety, University of Science and Technology Beijing, China

***Corresponding Author:** Yanpeng Xue, National Center for Materials Service Safety, University of Science and Technology Beijing, Xueyuan Road 30, 100083 Beijing, China

Published **June 16, 2021**

How to cite this book chapter: Yanpeng Xue, Shuqiang Wang. Fabrication of Co-Ni based Superhydrophobic Coating and its Wear Resistance, Durability and Corrosion Resistance. In: Alessio Bosio, editor. Surfaces, Interfaces and Coatings Technology. Hyderabad, India: Vide Leaf. 2021.

Acknowledgement: The authors thank the support from Fundamental Research Funds for the Central Universities China (Project ID: FRF-TP-20-049A2). And the project was also supported by the Tribology Science Fund of State Key Laboratory of Tribology.

Introduction

Super-hydrophobic surfaces inspired by biological species have been extensively concerned due to their potential applications in corrosion protection [1,2], anti-icing [3,4], water/oil separation [5] and drag reduction [6]. Techniques to make superhydrophobic surfaces can be simply divided into two categories: making a rough surface from a low surface energy material or modifying a rough surface with a material of low surface energy [7,8]. Many methods have been developed to produce rough surfaces, including plasma etching [9], chemical vapor deposition [10], solgel method [11], and electrodeposition [12]. Most of these methods involved multi-step procedures and harsh conditions, or require specialized reagents and equipment. In contrast, electrodeposition has been used as a one step, simple and economic method to fabricate superhydrophobic surface on different substrates. Up to now, a few papers have been published on superhydrophobic nickel films produced by electrodeposition without applying low surface energy materials [13,14]. These researches have usually studied the morphology and wetting behavior of the coatings. Ni coatings prepared by electrochemical deposition have been studied extensively, which exhibit excellent corrosion protection [15].

S. Esmailzadeh et al. [1] fabricated hierarchical nickel films on copper substrate by two-step electrodeposition process. In this work, the corrosion resistant and superhydrophobic nickel films with a hierarchical structure were synthesized by directional electrodeposition process. The relationship between the wettability and surface morphology was studied under different deposition current densities.

However, only limited studies were concerned about the Ni-Co alloy coatings with micro-nanostructures. Silva et al. [16] deposited Ni-Co surfaces with a 3D hierarchical open porous structure by applying a square current wave form on austenitic stainless steel substrates. Xue et al. [17] prepared bimetallic Ni-Co coating with novel hierarchical micro-spherical structures on carbon steel substrate. The properties including surface morphologies, structures, chemical compositions, wetting

properties, as well as the growth mechanism of the electrodeposited hierarchical structure were observed. However, one of the major drawbacks to overcome for practical applications of super-hydrophobic coating, is its mechanical durability due to its fragile micro-nano structures, which is behind the surface super-hydrophobic property [18,19].

In our works, to improve the mechanical durability of the Ni-Co superhydrophobic coating, many attempts have been made such as increasing the cobalt content and adding the second particle WC and CeO_2 on the electrolyte solutions.

Preparation of Co-Ni based Superhydrophobic Coating

Co-Ni Superhydrophobic Coating

A new low-cost process preparation for super-hydrophobic Co-Ni coating was prepared on carbon steel substrate via an electrodeposition route [20]. The Co-Ni coatings were deposited at a constant potential of −1.0, −1.4 and −1.7 V for 3000 s at room temperature in mixed solution $CoCl_2$ 0.1 mol/L + $NiCl_2$ 0.03 mol/L + H_3BO_3 0.1 mol/L. For the bare carbon steel, the polished surface displayed lots of scratches (Figure 1a). After electrochemical deposition under the applied potential at −1.0 V for 3000 s in the above-mentioned solution, the carbon steel surface was covered by uniform granular structures containing average size of sub-micrometer in diameter and the as-polished scratches were covered completely (Figure 1b). As shown in the cross-section view, the thickness of the coating is around 26 μm for the deposition time of 3000 s, and the EDS result showed that the cobalt content is around 93.8%, which is higher than that of the initial electrolyte (77%, $CoCl_2$ 0.1 mol/L $NiCl_2$ 0.03 mol/L). After the deposition at −1.4 V for 3000 s, the coating surface evidenced lots of spherical humps with an average size of 33 μm and a large number of cracks (Figure 1c), which may be attributed to the internal stress generated during the electrochemical deposition process. The cross-section image revealed that the thickness of the coating was around 40 μm and the large spherical humps grew from the thin layer composed of small irregular crystals. Increasing the applied potential to −1.7

V, the cauliflower-shaped micro-nano structures with multiscale fractal nature were obtained (Figure 1d). The EDS result shows that the cobalt content decreased to around 77.7% as presented in Table 1, which is similar to that of the initial electrolyte (77%). The anomalous Co–Ni deposition behavior can be attributed to the formation of Co hydroxyl precipitate, which could hinder the subsequent Ni deposition at the solid/electrolyte interface. Under thermodynamic and kinetic conditions, increasing the over-potential can favor the development of protrusions in the direction of increasing concentration, therefore leading to the formation of cauliflower-shaped micro-nano structures.

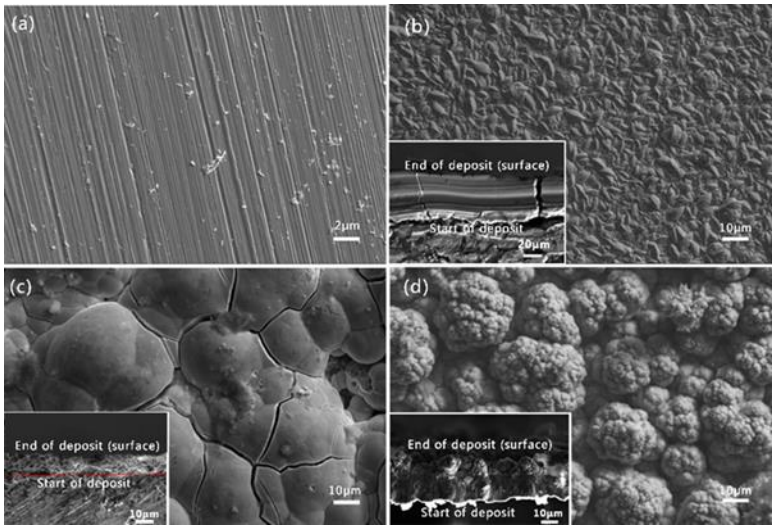

Figure 1: SEM images of (a) the bare carbon steel and the Co–Ni coatings under the applied potential of (b) −1.0 V, (c) −1.4 V, and (d) −1.7 V for 3000 s in the mixed solution at room temperature. The insets show the corresponding cross section.

After electrochemical deposition, the as-prepared samples were treated with 5 wt.% 1H,1H,2H,2H-Perfluorooctyltrichlorosilane (PFTEOS) ethanol solution for 1 h at room temperature, then rinsed and dried for investigations. Figure 2 depicts the contact angle variations of the Co–Ni coatings with the applied potentials before and after modification by PFTEOS in ethanol solution. For bare carbon steel substrate after polishing, and Co–Ni coating deposited at the applied potential of −1.0 V, the

contact angles were around 20°. After modification by PFTEOS, the water contact angle reached 95° and the surfaces displayed a hydrophobic property. After electrodeposition at the applied potentials ranging from −1.4 to −1.7 V, the water contact angles of the Co–Ni coatings with spherical humps structures and cauliflower-shaped micro-nano structures decreased to almost zero, showing the super-wetting properties of deposited Co–Ni coatings. However, after modification by 5 wt.% PFTEOS in ethanol solution for 1 h at room temperature, the water contact angle increases drastically to 140° for the sample with spherical humps structures, and to 161° for the sample with cauliflower-shaped micro-nano structures deposited at −1.7 V, respectively. The above results indicate that the wetting properties of the deposited hierarchical Co–Ni coating with cauliflower-shaped micro-nano structures converted from super-wetting to super-hydrophobic behaviors during the PFTEOS modification process. The super-hydrophobic behavior on Co–Ni coating with cauliflower-shaped micro-nano structures was endowed with a high surface roughness and low surface energy materials achieved by the combination of electrodeposition process at higher overpotential and surface modification by PFTEOS.

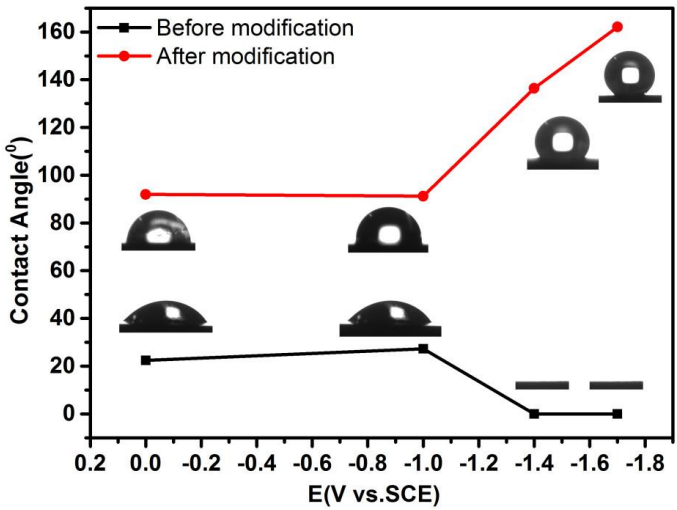

Figure 2: The water contact angles of the samples deposited at different potentials before and after modification by PFTEOS.

Co-Ni/WC Superhydrophobic Coating

In order to further improve the mechanical durability of the Co-Ni coating, robust super-hydrophobic cobalt-nickel coatings reinforced by micro-nano tungsten carbide (WC) particles were achieved on carbon steel substrate by electrochemical deposition from the mixed solution [21]. In order to prepare Co-Ni/WC composite coating by co-electrochemical deposition method, micro-nano WC particles were added into the deposition solution. Figure. 3 shows the SEM images of the as-received micro-nano WC particles with low and high magnification. It can be observed that the particles have irregular shape and a given size distribution varying from a few hundred nanometers up to a few micrometers.

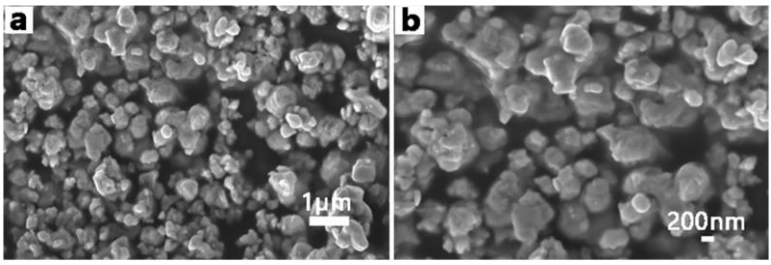

Figure 3: SEM images of micro-nano WC particles (a) low magnification and (b) high magnification.

And the electrodeposition was achieved under the constant current density of 65mA/cm^2 and the deposition time of 3000 s. The Co-Ni electrodeposits were obtained using the mixed solution of $CoCl_2 \cdot 6H_2O$ (0.1 mol/L), $NiCl_2 \cdot 6H_2O$ (0.03 mol/L) and H_3BO_3 (0.1 mol/L). Figure 4 presents the typical surface topographies of Co-Ni coating and Co-Ni/WC composite coatings electrodeposited in a mixed solutions of different concentrations of micro-nano WC particles, around 1.96, 3.92, and 5.88 g/L. The Co-Ni coating electrodeposited in the mixed solution under the applied current density of −65 mA/cm^2 for 3000 s, displays cauliflower shaped micro-nano structures (Figure 4a). These structures are similar to our previous Co-Ni coating obtained at the constant potential of−1.7 V for 3000 s in the same electrolyte [22].

Based on the mixed solution, different contents of micro-nano WC particles were added to prepare Co-Ni/WC composite coating. In the mixed solution containing 1.96 g/L WC particles, the micro-nano particles were entrapped in the Co-Ni coating during the co- electrodeposition process (Figure 4b). It can be observed that micro-nano WC particles are trapped in the electrodeposited Co-Ni coating, and that large cobalt‑nickel grains grow without being hindered by WC particles. Further increasing of the micro-nano WC particles to 3.92 g/L, Co-Ni/WC composite coating with micro-nano cauliflower structures was realized on the substrate. By increasing the micro-nano WC particles added amount to 5.88 g/L, the agglomeration takes place during the co-electrodeposition process and some colonies with the size of tens micrometers could be seen on the substrate (Figure 4d). Indicated by the cross section images, the thickness of the Co-Ni coating and Co-Ni/WC composite coating deposited in the mixed solution with micro-nano WC particles contents of 1.96 g/L and 3.92 g/L was determined to be around 40 μm. While, the thickness of Co-Ni/WC composite coating with micro-nano WC particles content of 5.88 g/L was determined to be around 50 μm under the same deposition conditions. The EDS mappings of the Co-Ni/WC composite coatings show homogeneous distribution of micro-nano WC particles within the composite coatings when the WC particles content is below 3.92 g/L. When the WC content increased to 5.88 g/L, the micro-nano WC particles aggregated together, resulting in the uneven distribution of micro-nano structures. As indicated by the EDS results, the WC contents in the corresponding Co-Ni/WC composite coatings were around 5.3 wt.% (Figure 4b), 9.8 wt.% (Figure 4c) and 19.1 wt.% (Figure 4d), respectively.

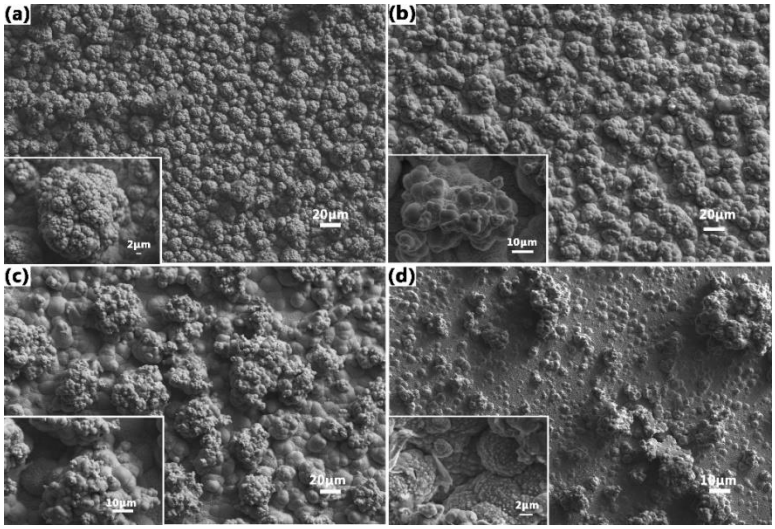

Figure 4: SEM images of (a) the Co-Ni coating in the mixed solution and Co-Ni/WC composite coatings in the mixed solution by adding WC particles: (b) 1.96 g/L; (c) 3.92 g/L; (d) 5.88 g/L under the applied current density of -65 mA/cm^2 for 3000 s at room temperature. The inset shows corresponding high magnification.

For the surface modification, the as-deposited samples were maintained in 20 mL 5 wt.% PFTEOS ethanol solution for a period of 1 h around 30 °C. After modification, the samples were cleaned for observation. Figure 5 shows the transition of wetting properties during the modification process by PFTEOS in ethanol solution. It can be observed that all the electro-deposited Co-Ni alloy coating and Co-Ni/WC composite coatings exhibited super-hydrophilicity before the modification process (Figure 5b). However, after the modification process by PFTEOS in ethanol solution, the electro-deposited Co-Ni alloy coating and Co-Ni/WC composite coatings with the WC content around 5.3 wt.% and 9.8 wt.% displayed the contact angle above 150° and became super-hydrophobic surfaces (Figure 5a). Meanwhile, low WSA values were obtained after the PFTEOS modification process (2° for the electrodeposited Co-Ni coating and 5° for the Co-Ni/WC composite coatings with the WC content around 5.3 wt.% and 9.8 wt.%) (Figure 5c). For example, when the micro-nano WC particles with concentration of about 3.92 g/L were added in the mixed solution, the as-prepared Co-

Ni/WC composite coating with WC content of around 9.8 wt.% display excellent super-hydrophobicity with WCA of 162° and WSA of 3°, which could be attributed to the homogeneous distribution of micro-nano cauliflower structures and fluorinated solution treatment. However, when the concentration of micro-nano WC particles in the mixed solution was increased to 5.88 g/L, the WC particles content of the Co-Ni/WC composite coating is increased to 19.1 wt.%. A great quantity of WC particles induces the formation of particle aggregates in-homogeneously distributed in the coatings, which explain the lower measured WCA (around 145°) and higher WSA (around 16°) values of the composite coating. These results demonstrated that the super-hydrophobicity of the as-electrodeposited Co-Ni/WC composite coatings was influenced by the surface topography variations which were induced by the micro-nano WC particles content added in the electrolyte solution.

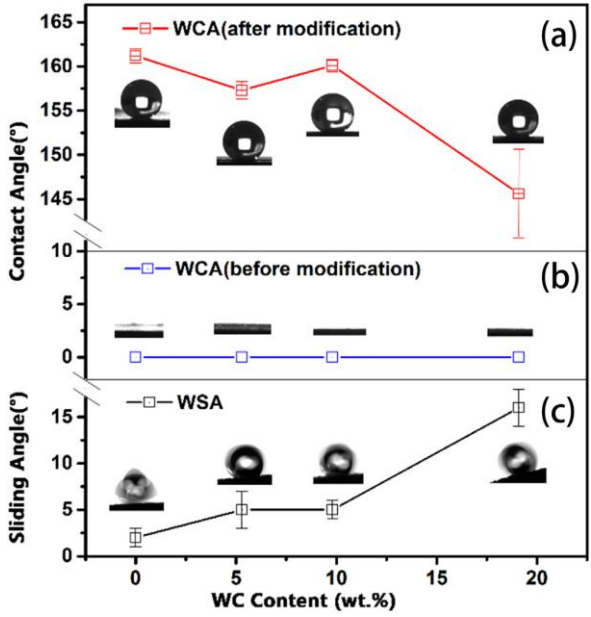

Figure 5: (a) and (b) The water contact angle (WCA) variations with WC particles of Co-Ni/WC composite coating before and after PFTEOS modification. (c) The water sliding angles (WSA) of the CoeNi/WC composite coatings after PFTEOS. The WC particles were 0, 5.3 wt%, 9.8 wt% and 19.1 wt%, respectively.

Co-Ni/CeO_2 Superhydrophobic Coating

Up to now, Rare-earth oxides (REOs) as a second phase particles received less attention on the preparation of super-hydrophobic coatings. Metal atoms in REOs have a lower tendency to exchange electrons and form a hydrogen bond with interfacial water molecules, which is an effective way to build super-hydrophobic surfaces. Because of their unique electronic structure, Rare-earth oxides (REOs) have been proven to be intrinsically hydrophobic [23]. Herein, cerium oxide particles (CeO_2) are added to the coating by co-electrodeposition. The Co-Ni/CeO_2 composite coatings are obtained in the mixed solution with $CoCl_2 \cdot 6H_2O$ (0.1 mol/L), $NiCl_2 \cdot 6H_2O$ (0.03 mol/L), H_3BO_3 (0.1 mol/L) and different amounts of CeO_2 particles in the solution [24]. To ensure uniform distribution of micro-nano CeO_2 particles in the coating, the magnetic stirrer (Model SH-2, Input 220 V 50/60 HZ) is used and adjusted to approximately 800 rpm. At first, the morphologies of the used CeO_2 particles were characterized. By the low magnification SEM image (Figure 6a), the CeO_2 ceramic particles are irregular in shape with the sizes ranged from a few micrometers to a few tens micrometers. From the high magnification SEM image (Figure6b), it is noted that the large particles are loose with the surfaces attached with a great amount of nano-sized CeO_2 particles.

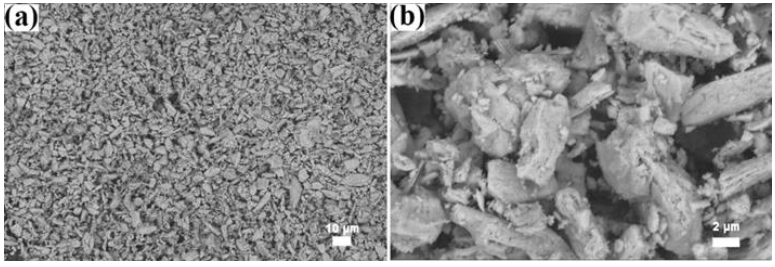

Figure 6: Surface morphology of CeO_2 particles (a) low enlargement and (b) high enlargement.

Figure 7 illustrated the surface topography variation of Co-Ni/CeO_2 composite coatings electrodeposited at constant current density of -65 mA/cm^2 with different contents of CeO_2 particles

added in the above-mentioned mixed solution. When the content of CeO_2 particles in the electrolyte solution was 1.72 g/L, irregular diamond-like structures having a diameter of about several micrometers were aggregated to form a larger-sized irregular structure, and distributed uniformly over the entire surface (Figure7a and 7d). After doubling the CeO_2 content to 3.44 g/L, parts of the diamond structures were replaced by the flaky fish scale structures, and further aggregated into the flower-like micro/nano hierarchical structures (Figure 7b and 7e). With the CeO_2 content rose to 6.88 g/L in the mixed solution, the flower-like micro/nano hierarchical structures were replaced by locally aggregated CeO_2 clusters, which were distributed inhomogeneously on the surface (Figure 7c and 7f). According to the cross section images, the thickness of the composite coating electrodeposited in the mixed solution containing CeO_2 particles of 1.72 g/L was around 15 μm after the deposition time of 2000 s. With the increase of the CeO_2 particles to 3.44 g/L, the thickness of the electrodeposited composite coating increased to 20 μm. However, by adding the CeO_2 particles to 6.88 g/L, the electrodeposited coating's thickness decreased to 16 μm, which could be attributed to the difficulty of co-electrodeposition due to the large amount of CeO_2 particles. According to the EDS analysis, the CeO_2 contents were around 12.4 wt.% (Figure7a), 15.6 wt.% (Figure7b) and 19.1 wt.% (Figure7c) in the corresponding Co-Ni/CeO_2 composite coatings respectively. Under the same deposition conditions, the CeO_2 content in the coatings gradually increased while the nickel in the composite deposits content decreased.

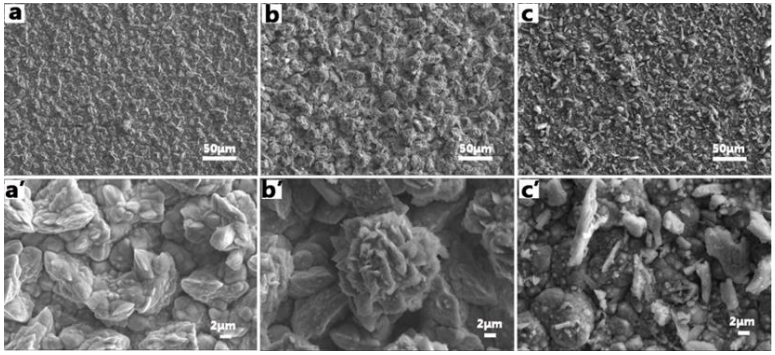

Figure 7: SEM images of Co-Ni/CeO_2 composite coatings in the mixed solution by adding CeO_2 particles: a) 1.72 g/L; b) 3.44 g/L; c) 6.88 g/L under the applied current density of -65 mA/cm^2 for 2000 s at room temperature. a',b',c') Corresponding high magnification.

In order to obtain super-hydrophobicity, PFTEOS ($C_{48}H_4Cl_3F_{13}Si$) was used to decrease the surface energy and the variation of the wetting properties was displayed in Figure 8. After modification, the self-assembled film was formed due to the reaction of PFTEOS molecules with the -OH groups on the composite coating surface, which reduce the polar sites, leading to its super-hydrophobicity [25]. As can be seen in Figure 8, the Co-Ni/CeO_2 coating electrodeposited in the electroplating solution with the 3.44 g/L CeO_2 particles exhibits a better super-hydrophobicity (WCA=160.7°, WSA=2°), revealing that the flower-like hierarchical micro/nano structures could lead to a better super-hydrophobicity.

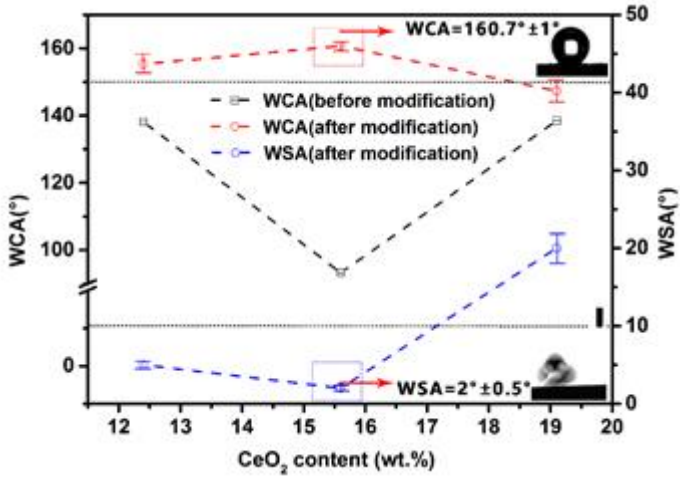

Figure 8: The WCA and WSA variations with CeO_2 contents before and after modification by PFTEOS molecules.

Mechanical Durability

Due to the special features (such as dual micro-nano structures and modification by low surface energy materials) which is essential for fabricating super-hydrophobic surfaces, such surfaces are susceptible to mechanical abrasion. At present, to enhance the abrasion resistance of super-hydrophobic coatings has become the main concern for their practical applications [26,27]. Recently, Ras et al. [28] suggested that linear abrasion should be adopted to assess the mechanical durability of the super-hydrophobic coating because this wear-test method is accessible to most lab researches, applicable in most industrial production, and able to generate a large uniformly surface suitable for wetting measurements. Therefore, in the work the linear abrasion test was conducted, which is shown in Figure 9. The 800 grit SiC sandpaper was placed face up and used as abrasion surface. The super-hydrophobic Co–Ni coating was tested under the applied pressure of 5 kPa at a speed of 5 mm/s.

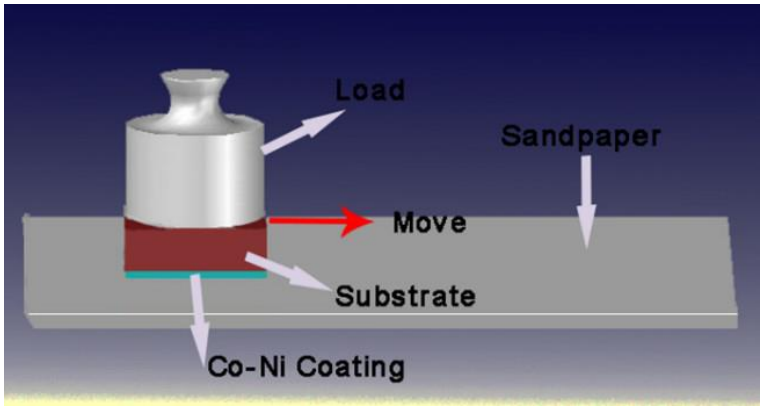

Figure 9: A scheme for linear abrasion test.

Figure 10 depicts the SEM images for the super-hydrophobic Co-Ni coating deposited at −1.7 V before and after linear abrasion tests and the relationship between contact angles and abrasion distance. As shown in Figure 10a, the Co-Ni coating with cauliflower-shaped micro-nano structures shows contact angle of 161° and water sliding angle of 1° before linear abrasion tests, exhibiting greater super-hydrophobicity. After abrasion distance of 1.5 m under the applied pressure of 5 kPa, few prominent cauliflower-shaped micro-nano structures were worn and obvious scratches appeared on the top of these structures (Figure10b). It is obvious that the cauliflower-shaped micro-nano structures were well preserved and the water contact angle maintained around 160° with water sliding angle of 2°. After increasing the abrasion distance to 6 m, large cauliflower-shaped structures were worn more seriously, and the water contact angle dropped to 158° and the water sliding angle increased to 5° (Figure10c). When abrasion distance reaching 12 m, all the large cauliflower-shaped microstructures appeared different degrees of wear and the water contact angle dropped dramatically to near 150° (Figure10d). With the increase of abrasion distance, the water sliding angle increases to 8° after 12 m of abrasion. When the abrasion distance increased to 24 m, the large cauliflower-shaped microstructures were almost completely worn away. The water contact angle dropped to near 143° and the sliding angle increased to 12° (Figure10f). With the increase of abrasion distance, the wetting properties of deposited hierarchical Co-Ni

coating with cauliflower-shaped micro-nano structures transited from super-hydrophobic behaviors to hydrophobic behaviors.

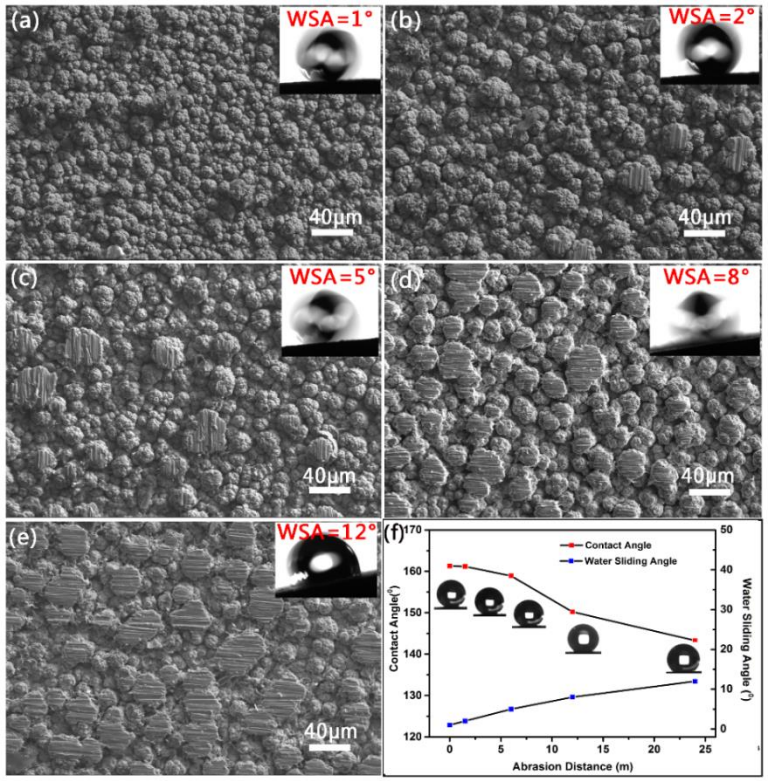

Figure 10: SEM images for (a) super-hydrophobic Co–Ni coating before abrasion and after abrasion under the applied pressure of 5 kPa for (b) 1.5 m, (c) 6 m, (d) 12 m, and (e) 24 m; (f) The water contact angle and water sliding angle variations on these surface with the abrasion distance. The insert images in (a) to (e) are the profiles of a water droplet sliding on the Co–Ni coating with different water sliding angles.

The Co-Ni/WC composite coating with 9.8 wt.% WC particles content was selected for linear abrasion test. The SEM images in Figure 11a displays the typical surface morphologies with cauliflower-like structures of the Co-Ni/WC composite coating with different abrasion distances. Before the abrasion test, the electro- deposited Co-Ni/WC composite coating exhibit a super-hydrophobic behavior with WCA over 162° and WSA around 3°

(Figure11a). In the linear abrasion test, localized friction loss was produced on the cauliflower-like structures by choosing the abrasion distance of 3 m (Figure 11b). When the abrasion distance is increased to 9 m and 32 m (Figure 11c and 11d), the composite coating surface loses some of cauliflower-like structures, but most of undamaged micro-nano structures with small sizes were maintained. As a result, the WCA value decreased and WSA value increased slightly, and the composite coating surface is still exhibiting the super-hydrophobic behavior. However, when the abrasion distance is continually increased to 41 m (Figure 11e), more scratches were found and the small size cauliflower-like structures were removed partially. As a result, the WCA is decreased to 148° and WSA is increased to 18°, and therefore, the as-prepared composite coating can't maintain its super-hydrophobic behavior. From Figure 11f, it can be observed that the linear reduction of WCA and the increase of WSA take place with the increase of the abrasion distance. From the obtained results, it can be observed that the critical value of the abrasion distance from which the loss of super-hydrophobicity takes place is approximately 34 m. Meanwhile, it can be noted that the WSA rose sharply when the abrasion distance is over 30 m. Moreover, the Co-Ni/WC composite coatings with 9.8 wt.% WC particles were scratched by the knife. After the strong knife-scratch process for 10 times, the average contact angle of the Co-Ni/WC composite coating was around 160.5°, which further demonstrated its great mechanical durability.

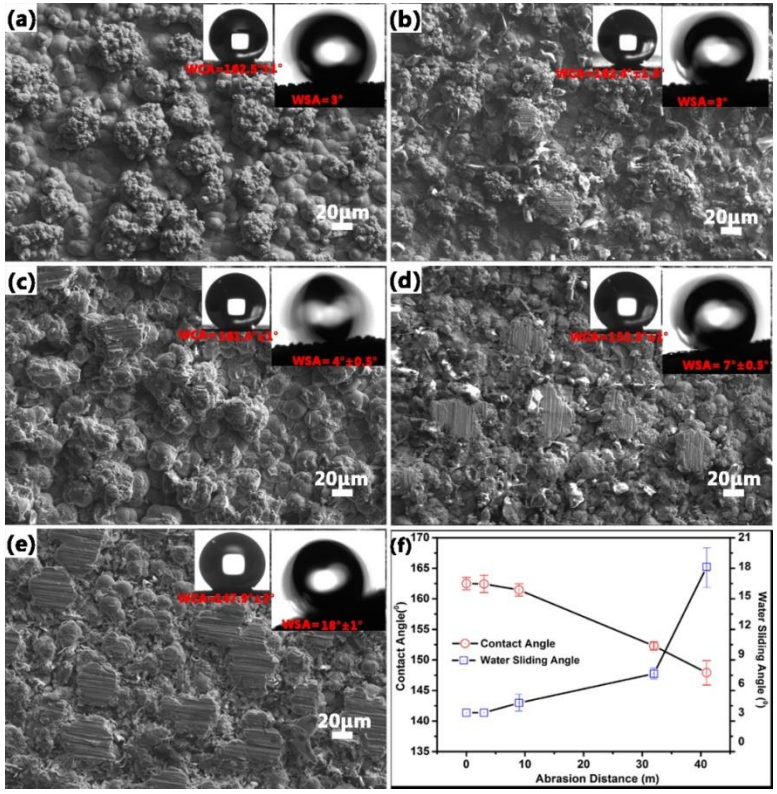

Figure 11: SEM images of the super-hydrophobic Co-Ni/WC composite coating with 9.8 wt% WC under the load pressure of 5 kPa after abrasion for (a) 0 m, (b) 3 m, (c) 9 m, (d) 32 m, (e) 41 m and (f) WCA and WSA variations with the abrasion distances. The insert images are profiles of water contact angles and water sliding angles on the coating surface.

Figure 12 showed the loss of the hierarchical structures on the superhydrophobic Co-Ni/CeO_2 coating surface during the linear abrasion test, in which the super-hydrophobic property degraded gradually with the decrease in WCA and the increase in WSA. When the abrasion distance was within 1.5 m (Figure12b), very few flaky fish scale structures were worn out due to the existence of convex structures and most hierarchical structures were preserved during the abrasion test, which explained the fact that the super-hydrophobic nature of our coating was hardly affected. Those air cushions trapped among the gaps prevented the droplets from permeation. When the abrasion distance increased

to 18 m, large area flaky fish scale structures were worn out by about half but the second level structures were still preserved (Figure12c). The preserved micro-nano structures were still capable of trapping air within the flaky fish scale structures. As a result, the WCA reduced by about 7 degrees and the WSA increased by 6 degrees. The super-hydrophobic behavior was still maintained. With the increase of the abrasion distance to 30 m, the hierarchical structures were worn out (Figure12d). The WCA decreased to around 150° and the WSA increased to 19°, indicating the loss of super-hydrophobicity. From Figure 12e, it could be noted that WCA decreased and WSA increased linearly with the increase of the abrasion distances. Towards the loss of super-hydrophobic property, the critical abrasion distance was around 22.5 m. Meanwhile, the surface roughness was measured to characterize the surface wear loss during the linear abrasion test (Figure12f). The surface roughness decreased linearly with the abrasion distance and the Ra value was close to 5 μm when the abrasion distance was 22.5 m. In comparison to the initial value before the linear abrasion test, the surface roughness value decreased by 5.4.

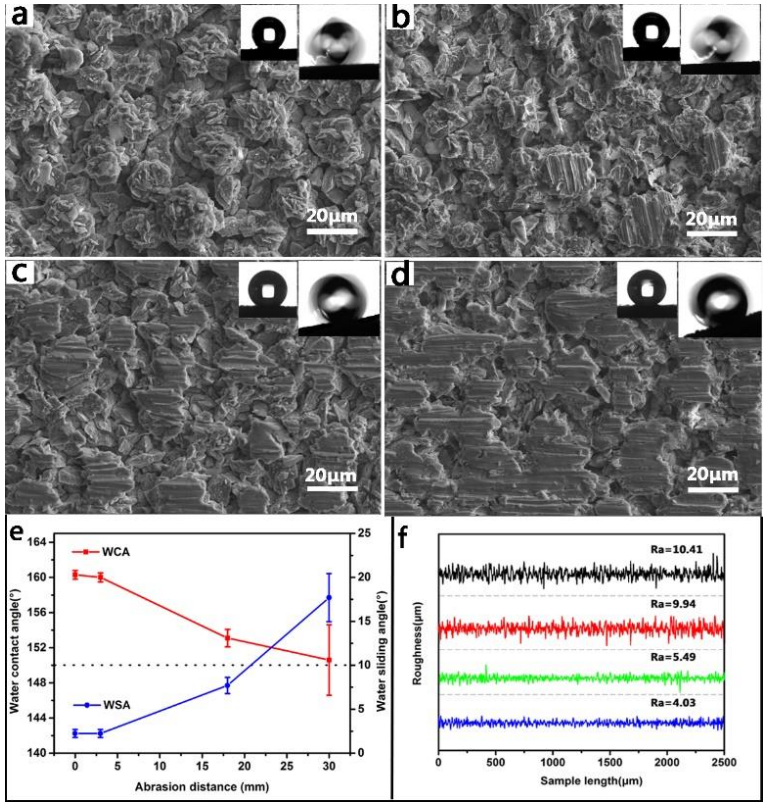

Figure 12: (a-d) SEM images for the abrasion test and the responding WCA and WSA; a) as-deposited super-hydrophobic Co-Ni/CeO2 composite coating and after abrasion under the applied pressure of 5 kPa for b) 1.5 m, WCA=160°, WSA=2°; c) 18 m, WCA=153.1°, WSA=8°; d) 30 m, WCA=150.6°, WSA=19°; e) the different abrasion distance to the variations of: e) WCA and WSA; f) the roughness after the abration test.

Evaluated by the linear abrasion methods, the super-hydrophobic Co-Ni coating can maintain super-hydrophobicity after abrasion distance of 12 m under the applied pressure of 5 kPa, which was attributed to the high cobalt content of the Co-Ni coating. Adding the WC particles, the linear abrasion test indicated that the as-prepared super-hydrophobic Co-Ni/WC composite coating with 9.8 wt% WC content, displayed excellent wear resistance with super-hydrophobic property for abrasion distance up to 34 m. The Co-Ni/CeO_2 composite coating from the electrolyte containing 3.44 g/L possesses a flower-like hierarchical

structures, displaying a super-hydrophobic behavior after the modification by PFTEOS. More importantly, excellent mechanical durability with critical abrasion distance of 22.5 m is achieved under a 5 kPa fixed normal pressure in the liner abrasion test before the loss of super-hydrophobicity. We have found that some features were of vital importance for the wear resistance of superhydrophobic coatings, such as the micro–nano hierarchical structures and microhardness. As indicated by the results, microhardness and roughness showed a positive correlation with the abrasion distance of the superhydrophobic composite coatings. To improve the wear resistance of the superhydrophobic coating, its microhardness was improved by adding second-phase particles, which was proved effective through our works.

Table 1: Abrasion distances leading to the loss of super-hydrophobic properties. Abrasive medium: 800 grit SiC sandpaper.

Materials	Pressure (kPa)	Abrasion Length (m)	Initial WCA (°)	Final WCA (°)	Initial WSA (°)	Final WSA (°)
Co–Ni coating	5.0	12.0	161	150	1	8
Co–Ni/WC coating	5.0	34.0	163	150	3	10
Co–Ni/CeO_2 coating	5.0	30.0	160	150.6	2	19

Corrosion Protection

The potentiodynamic polarization curves of the bare carbon steel, as-prepared super-hydrophobic Co–Ni coating, super-hydrophobic Co-Ni/WC composite coatings with different WC contents and super-hydrophobic coating with different CeO_2 contents were measured at a scan rate of 0.5 mV/s in 3.5 wt.% NaCl solution, and shown in Figure 13.

The carbon steel substrate displayed negative corrosion potential (E_{corr} = −459 mV vs. SCE) with high corrosion current density (I_{corr} = 1.45 ×10^{-5} A/cm^2). The corrosion potential of Co-Ni coating deposited at −1.4 V shifted 100 mV toward positive

direction compared with carbon steel with lower corrosion current density of 1.50×10^{-6} A/cm^2. For the super-hydrophobic Co–Ni coating deposited at −1.7 V, the corrosion potential and corrosion current density are −303 mV and 5.87×10^{-7}A/cm^2 respectively. The corrosion current density of as-prepared super-hydrophobic Co-Ni coating was 20 times lower than that of bare carbon steel substrate, demonstrating the significantly improved anti-corrosion performance of the super-hydrophobic Co-Ni coating with cauliflower-shaped micro-nano structures.

Generally, the positive shift of the corrosion potential and the low corrosion current density are a signature of a better corrosion resistance. As shown in Figure 13b, the Co-Ni/WC composite coatings show a better corrosion resistance compared both to the carbon steel substrate and the super-hydrophobic Co-Ni coating according to these characteristics. The anodic polarization current density measured for super-hydrophobic Co-Ni/WC composite coating with the WC particles content of 9.8 wt.% ($I_{corr}=1.29\times10^{-7}$ A/cm^2) decreases by about two orders of magnitude compared to bare carbon steel ($I_{corr}=1.45\times10^{-5}$ A/cm^2). In addition, although the composite coating with the WC particles content of 19.1 wt.% exhibits hydrophobic property with WCA of 145º, its corrosion current density ($I_{corr}=1.78\times10^{-6}$ A/cm^2) was one order of magnitude lower than that of the bare carbon steel. Compared with the carbon steel substrate, both the anodic and cathodic branches of the as-prepared coatings show lower current density, indicating that the as-prepared super-hydrophobic Co-Ni/WC composite coating provides great corrosion protection performance.

As shown in Figure 13c, for the super-hydrophobic Co-Ni/CeO_2 composite coating (1.72 g/L CeO_2 and 3.44 g/L CeO_2), the corrosion potentials shift positively about 109 mV and 142 mV respectively. Due to the adding of CeO_2 particles, the corrosion probability of the as-prepared super-hydrophobic coatings decreases. The as-prepared super-hydrophobic coatings electrodeposited with the CeO_2 particles of 1.72 g/L and 3.44 g/L exhibited a two orders of magnitude reduction in corrosion rate, which could be attributed to their super-hydrophobicity that the trapped air as a barrier decreased the solution/solid contact area

effectively. However, with the increasing of micro-nano CeO_2 particles to 6.88 g/L, corrosion potential shift negatively a little and the corrosion current density (i_{corr}) was smaller than those of the aforementioned composite coatings, which could be attributed to the formation of holes based on the difficulty of co-electrodeposition under the deposition conditions of large amount of CeO_2 particles in the mixed solution.

These results clearly show that the as-prepared super-hydrophobic Co-Ni coating, super-hydrophobic Co-Ni/WC composite coatings and super-hydrophobic Co-Ni/CeO_2 composite coatings exhibit higher corrosion resistance than carbon steel substrate. The air entrapped in the cauliflower like structures can prevent the super-hydrophobic composite coating from being wetted by the corrosion medium through the limited solid contact area, endowing the coating larger charge transfer resistance and lower corrosion rate, and then better corrosion protection performance [29].

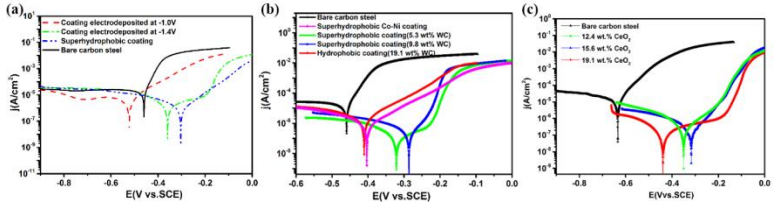

Figure 13: Potentiodynamic polarization curves of (a) Super-hydrophobic Co–Ni coating, (b) Super-hydrophobic Co-Ni/WC composite coatings with different WC contents and (c) Super-hydrophobic coating with different CeO_2 contents in 3.5 wt% NaCl aqueous solution at the scan rate of 0.5 mV/s.

Table 2: Derived results from the potentiodynamic polarization measurements.

Sample	E_{corr} (mV)	I_{corr} (A/cm^2)	Corrosion rate(mm/a)
Bare carbon steel	-459.4	1.45×10^{-5}	0.162
Superhydrophobic Co-Ni coating	-303.3	5.87×10^{-7}	0.0066
Superhydrophobic Co-Ni/WC coating	-286.3	2.48×10^{-9}	0.000028
Superhydrophobic Co-Ni/CeO_2 coating	-316.9	1.24×10^{-7}	0.0014

Long-Term Durability

The long-term durability for two kinds Co-Ni based robust coatings, Co-Ni super-hydrophobic coating and Co-Ni/WC super-hydrophobic coating, was analyzed by immersion test in 3.5 wt.% NaCl solution. The immersion test displayed that two kinds of robust super-hydrophobic coatings have long-term durability, where the Co-Ni super-hydrophobic coating loses super-hydrophobicity after immersion for 20 days and the critical immersion time of Co-Ni/WC super-hydrophobic coating was 12 days, respectively. The loss of super-hydrophobicity could be attributed to the corrosion damage of the micro-nanostructures on the coating and the decomposition of low surface energy materials. In the early stage of immersion, the decomposition of hydrophobic groups occurred firstly. In the later stage, it appeared as corrosion damage of micro-nano structures on the coatings.

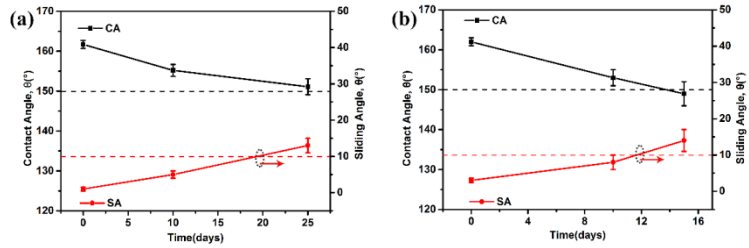

Figure 14: Wettability variations (WCA, WSA) with immersion time of (a) Co-Ni superhydrophobic coating and (b) Co-Ni/WCsuperhydrophobic composite coating.

Conclusion

The Co-Ni based composite coatings were prepared on carbon steel by the co-electrochemical deposition process by adding different micro-nano particles in the mixed solution. During the modification process, the PFTEOS molecules can induce the transit from super-hydrophilicity to super-hydrophobicity of the as-prepared composite coatings. The linear abrasion test revealed that the super-hydrophobic Co-Ni based composite coatings

displayed excellent mechanical durability at 5 kPa load pressure and Co-Ni, Co-Ni/WC, Co-Ni/CeO_2 superhydrophobic coating can keep their super-hydrophobicity for the abrasion distance of 12 m, 34 m, 22.5 m, respectively. The higher abrasion resistance of the deposited Co-Ni based composite coating was attributed to the combination of micro-nano particles addition with high cobalt content inside the coating. Moreover, the corrosion current density of the super-hydrophobic Co-Ni based coating was decreased by more than two orders of magnitude compared to that of bare carbon steel, exhibiting great corrosion protection. With the robust mechanical durability, the as-prepared super-hydrophobic Co-Ni based composite coating could be excellent alternative technique for real applications in the future.

References

1. S Esmailzadeh, S Khorsand, K Raeissi, F Ashrafizadeh. Microstructural evolution and corrosion resistance of super-hydrophobic electrodeposited nickel films. Surf. Coatings Technol. 2015; 283: 337–346.
2. D Zhang, L Wang, H Qian, X Li. Superhydrophobic surfaces for corrosion protection: a review of recent progresses and future directions. J. Coatings Technol. Res. 2016; 13: 11–29.
3. P Eberle, MK Tiwari, T Maitra, D Poulikakos. Rational nanostructuring of surfaces for extraordinary icephobicity. Nanoscale. 2014; 6: 4874–4881.
4. T Maitra, MK Tiwari, C Antonini, P Schoch, S Jung, et al. On the nanoengineering of superhydrophobic and impalement resistant surface textures below the freezing temperature. Nano Lett. 2014; 14: 172–182.
5. Q Ma, H Cheng, AG Fane, R Wang, H Zhang. Recent Development of Advanced Materials with Special Wettability for Selective Oil/Water Separation. Small. 2016; 12: 2186–2202.
6. X Yao, Y Song, L Jiang. Applications of bio-inspired special wettable surfaces, Adv. Mater. 2011; 23: 719–734.
7. X Yanpeng, A Taleb, P Jegou. Electrodeposition of cobalt films with an oriented fir tree-like morphology with adjustable wetting properties using a self-assembled gold nanoparticle modified HOPG electrode. J. Mater. Chem. A.

2013; 1: 11580–11588.
8. C Peng, Z Chen, MK Tiwari. All-organic superhydrophobic coatings with mechanochemical robustness and liquid impalement resistance. Nat. Mater. 2018; 17: 355–360.
9. HC Barshilia, N Gupta. Superhydrophobic polytetrafluoroethylene surfaces with leaf-like micro-protrusions through Ar + O2 plasma etching process. Vacuum. 2014; 99: 42–48.
10. S Rezaei, I Manoucheri, R Moradian, B Pourabbas. One-step chemical vapor deposition and modification of silica nanoparticles at the lowest possible temperature and superhydrophobic surface fabrication. Chem. Eng. J. 2014; 252: 11–16.
11. WH Huang, CS Lin. Robust superhydrophobic transparent coatings fabricated by a low-temperature sol-gel process. Appl. Surf. Sci. 2014; 305: 702–709.
12. W Xi, Z Qiao, C Zhu, A Jia, M Li. The preparation of lotus-like super-hydrophobic copper surfaces by electroplating. Appl. Surf. Sci. 2009; 255: 4836–4839.
13. F Su, K Yao. Facile fabrication of superhydrophobic surface with excellent mechanical abrasion and corrosion resistance on copper substrate by a novel method. ACS Appl. Mater. Interfaces. 2014; 6: 8762–8770.
14. G Zhao, Y Xue, Y Huang, Y Ye, FC Walsh, et al. One-step electrodeposition of a self-cleaning and corrosion resistant Ni/WS2 superhydrophobic surface, RSC Adv. 2016; 6: 59104–59112.
15. J Zhou, G Zhao, J Li, J Chen, S Zhang, et al. Electroplating of non-fluorinated superhydrophobic Ni/WC/WS2 composite coatings with high abrasive resistance. Appl. Surf. Sci. 2019; 487: 1329–1340.
16. RP Silva, S Eugénio, TM Silva, MJ Carmezim, MF Montemor. Fabrication of three-dimensional dendritic Ni-Co films by electrodeposition on stainless steel substrates. J. Phys. Chem. C. 2012; 116: 22425–22431.
17. Y Xue, S Wang, G Zhao, A Taleb, Y Jin. Fabrication of Ni-Co coating by electrochemical deposition with high super-hydrophobic properties for corrosion protection. Surf. Coat. Technol. 2019; 363: 352–361.
18. T Verho, C Bower, P Andrew, S Franssila, O Ikkala, et al.

Mechanically Durable Superhydrophobic Surfaces. Adv. Mater. 2011; 23: 673–678.
19. D Wang, Q Sun, MJ Hokkanen, C Zhang, FY Lin, et al. Design of robust superhydrophobic surfaces. Nature. 2020; 582: 55–59.
20. Y Xue, S Wang, P Bi, G Zhao, Y Jin. Super-hydrophobic Co-Ni coating with high abrasion resistance prepared by electrodeposition. Coatings. 2019; 9: 1–14.
21. S Wang, Y Xue, C Ban, Y Xue, A Taleb, et al. Fabrication of robust tungsten carbide particles reinforced Co–Ni super-hydrophobic composite coating by electrochemical deposition, Surf. Coatings Technol. 2020; 385: 125390.
22. Y Xue, S Wang, P Bi, G Zhao, Y Jin. Super-hydrophobic Co-Ni coating with high abrasion resistance prepared by electrodeposition. Coatings. 2019; 9.
23. G Azimi, R Dhiman, HM Kwon, AT Paxson, KK Varanasi. Hydrophobicity of rare-earth oxide ceramics. Nat. Mater. 2013; 12: 315–320.
24. Y Xue, S Wang, Y Xue, L Cao, M Nie, et al. Robust Self-Cleaning and Marine Anticorrosion Super-Hydrophobic Co–Ni/CeO2 Composite Coatings. Adv. Eng. Mater. 2020; 22.
25. C Jeong, CH Choi. Single-step direct fabrication of pillar-on-pore hybrid nanostructures in anodizing aluminum for superior superhydrophobic efficiency. ACS Appl. Mater. Interfaces. 2012; 4: 842–848.
26. T Darmanin, E Taffi, D Givenchy, S Amigoni, F Guittard. Superhydrophobic Surfaces by Electrochemical Processes. Adv. Mater. 2013; 25: 1378–1394.
27. Y Tian, B Su, L Jiang. Interfacial Material System Exhibiting Superwettability. Adv. Mater. 2014; 26: 6872–6897.
28. X Tian, T Verho, RHA Ras. Moving superhydrophobic surfaces toward real-world applications, Science (80-). 2016; 352: 142–143.
29. P Bi, H Li, G Zhao, M Ran, L Cao, et al. Robust super-hydrophobic coating prepared by electrochemical surface engineering for corrosion protection. Coatings. 2019; 9.

Book Chapter

Eco-Friendly Coatings Containing Microcapsules with Fire-Resistant Properties

Andrés Felipe Jaramillo[1]*, Andrés Díaz-Gómez[2], Jesús Ramirez[2], María Elizabeth Berrio[2], Vanessa Cornejo[2], David Rojas[2], Luis Felipe Montoya[2], Adriana Mera[3] and Manuel Francisco Melendrez[2,4]*

[1]Departament of Mechanical Engineering, Universidad de La Frontera, Chile
[2]Interdisciplinary Group of Applied Nanotechnology (GINA), Hybrid Materials Laboratory (HML), Department of Materials Engineering (DIMAT), Faculty of Engineering, University of Concepcion, Chile
[3]Instituto de Investigación Multidisplinario en Ciencia y Tecnología, Universidad de La Serena, Chile
[4]Unidad de Desarrollo Tecnológico, Chile

***Corresponding Author:** Manuel Francisco Melendrez, Interdisciplinary Group of Applied Nanotechnology (GINA), Hybrid Materials Laboratory (HML), Department of Materials Engineering (DIMAT), Faculty of Engineering, University of Concepcion, 270 Edmundo Larenas, Box 160-C, Concepcion 4070409, Chile

Published **July 08, 2021**

This book chapter is a fuller and more detailed publication of the article published by Manuel Francisco Melendrez, et al. at Coatings in February 2021. (Jaramillo, A.F.; Díaz-Gómez, A.; Ramirez, J.; Berrio, M.E.; Cornejo, V.; Rojas, D.; Montoya, L.F.; Mera, A.; Melendrez, M.F. Eco-Friendly Fire-Resistant Coatings Containing Dihydrogen Ammonium Phosphate Microcapsules and Tannins. Coatings 2021, 11, 280. https://doi.org/10.3390/coatings11030280)

How to cite this book chapter: Andrés Felipe Jaramillo, Andrés Díaz-Gómez, Jesús Ramirez, María Elizabeth Berrio, Vanessa Cornejo, David Rojas, Luis Felipe Montoya, Adriana Mera, Manuel Francisco Melendrez. Eco-Friendly Coatings Containing Microcapsules with Fire-Resistant Properties. In: Alessio Bosio, editor. Surfaces, Interfaces and Coatings Technology. Hyderabad, India: Vide Leaf. 2021.

Author Contributions: A.D.G and M.E.B: Carried out the tannin extraction and its complete characterization. J.R and V.C: Designed the fire-resistance and intumescence experiments. L.F.M, A.F.J and M.E.B: Carried out the fireproof and intumescent formulations and the dual scheme. A.C.M, M.F.M: Analyzed the results and wrote the manuscript. A.D.G and J.R: Developed the field tests and consolidated the formulations obtained. All authors reviewed the manuscript and contributed to its consolidation. All authors have read and agreed to the published version of the manuscript.

Funding: This work was funded by ANID FONDEQUIP Project N°EQM150139, PIA/APOYO CCTE AFB170007, FONDECYT Initiation 11190358 and project FONDEF IDEA ID17i10333.

Acknowledgments: The authors would like to thank to the Interdisciplinary Group of Advanced Nanocomposites (Grupo Interdisciplinario de Nanocompuestos Avanzados, GINA) of the Department of Engineering Materials (DIMAT, according to its Spanish acronym), Engineering School of the University of Concepción, for its laboratory of nanospectroscopy (LAB-NANOSPECT). AFJ would like to thank the University of La Frontera. National Agency for Research and Development of Chile (ANID) by project: FONDEQUIP Project N°EQM150139, PIA/APOYO CCTE AFB170007, FONDECYT Initiation

11190358 and project FONDEF IDEA ID17i10333. MFM would like to thank Valentina Lamilla for her enormous support.

Conflicts of Interest: The authors declare no conflict of interest.

Graphical Abstract

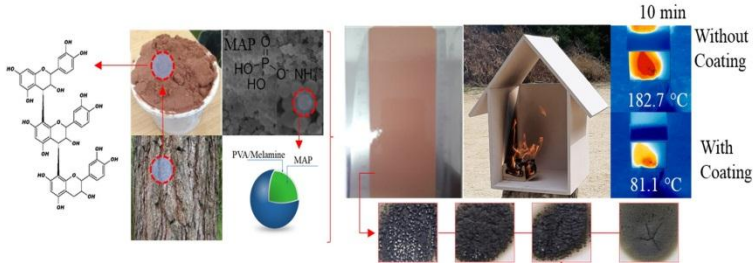

Abstract

The effect of microencapsulation of dihydrogen ammonium phosphate (MAP) in the generation of fire-resistant coatings was studied in the presence of tannins extracted from *Pinus radiata*. MAP was encapsulated to avoid interaction with sodium carbonate (Na_2CO_3), which upon contact with fire, generates unwanted gases. Thus, a fireproof (or intumescent) protective film was produced in the presence of the tannins. Microcapsules were polymerized with melamine and characterized by FTIR, TGA, SEM-EDS. The microcapsules were spherical with a diameter between 0.7 and 1 µm. The as-produced microcapsules were mixed with tannin extract and the properties of their film were evaluated on wood and structural steel substrates; their fire resistance on medium density fiberboard was also evaluated. Flame resistance tests showed a carbonization index of 26.86% using microcapsules (3% w/w); this is better than commercial coatings. The film properties were similar to commercial coatings, but the adherence was slightly decreased, due to agglomeration and also films flexibility.

Keywords

Fire Resistant Coating; Tannin; Eco-Friendly; Microencapsulation; Dihydrogen Ammonium Phosphate

Introduction

Structural steel has been widely used in the construction industry due to properties such as high strength/weight ratio, high ductility, among others. However, its mechanical resistance decreases if the temperature exceeds 500 °C during a fire. Therefore, enhancing this property is a concern for the construction industry; also, technological solutions focused mainly on the development of foams and coatings have been proposed [1]. Fire-resistant coatings (fire retardant and intumescent) have been widely used to protect metal structures and even wood substrates. These types of fire-resistant coatings are composed of a carbon forming material, a mineral acid catalyst, a blowing agent, and a binder resin. During the combustion process, these components operate synergistically to form a honeycomb carbon structure that thermally isolates the coated steel substrate and establishes a protective barrier blocking heat transfer to the steel; while in wood, acts chemically to release less pyrolysis gasses and contain more of the fuel as thermally insulating char [2,3]. The mechanism of protection in fireproof coatings includes retarding the advance of flames on the substrate. On the other hand, in intumescent coatings, the acidic source can release NH_3 and organic acids during the combustion process; this initiates an esterification reaction with the carbonaceous agent. The carbonaceous agent is carbonized by dehydration, and finally, the blowing agent forms an intumescent foam or layer on the surface of the polymeric material [1,4]. These coatings have numerous disadvantages: the carbon protective layer is vulnerable to high temperatures, the coating is prone to aging, and in water-based coatings, the coating displays poor adhesion to substrates [5,6].

To achieve suitable fire resistance, coatings are generally formulated with a high content of solid fillers; these impair the mechanical properties and durability of the film. Moreover, a

major disadvantage of additives is their poor compatibility with the coating resin; this significantly reduces the protection capacity in a fire. There has been limited use of microencapsulation technology in fire retardants and intumescent coatings. Almost no research has been conducted on the durability and fire resistance of the flame-retardant coating after the static immersion test. To overcome these problems, the use of microencapsulated dihydrogen ammonium or monoammonium phosphate (MAP) (acid source) as a fire-resistant additive has been an effective strategy [7,8].

For the scientific and industry communities, the development of ecological and sustainable fire-resistant coating systems has become an urgent challenge. Recently, the study of products from natural sources as potential additives has garnered considerable attention. Their characteristics allow the generation of an insulating carbon layer on substrate surfaces. They provide efficient fire resistance functionality and are therefore promising alternatives to halogen-based chemicals. Almost all renewable resource-based additive approaches to form fire-resistant coatings can impart these beneficial properties [9,10]. Modifying the additive properties through microencapsulation with water or insoluble polymers is an effective method to improve water resistance and polarity. Wu et al. [11] studied flame retardation in microencapsulated ammonium polyphosphate and demonstrated a decrease in particle size upon encapsulation and low water absorption. This result is of great interest since the particle size influences the mechanical properties of the coatings. To solve the aforementioned problems, and to investigate lower toxicity coatings, the microencapsulation of dihydrogen phosphate (MAP) as an acid source and low molecular weight tannins as a carbonaceous agent is proposed.

Tannins extracted from Pinus radiata are mixtures of simple phenols such as gallic acid and sugar esters (primarily glucose and gallic/digallic acids). The presence of gallic acid in hydrolyzable tannins makes them ideal raw materials for preparing the coatings [12,13]. Likewise, the presence of hydroxyl groups in tannins, together with their high reactivity compared to resorcinol and phenol, make them ideal candidates

to produce fire-resistant coatings [14]. Tannins have been used in the production of rigid foams, presenting similar fire-retardant properties to formulations that incorporate specialized additives such as boric acid (H_3BO_3) or phosphoric acid (H_3PO_4). Tannins are obtained from waste bark making them a renewable material, and, once extracted, the bark does not lose its calorific capacity and can be used in industrial boilers.

With increasing focus on sustainability in the construction industry, multi-story timber buildings are becoming increasingly popular. the fire issue becomes important since both the wooden claddings and the building construction itself may get involved in the combustion. In this study, the effect of MAP microencapsulation for the generation of a fire-resistant coating, in the presence of tannins (extracted from Pinus radiata as a carbon source), was examined [15]. The mechanical properties of the obtained coatings were compared and their fire resistance was evaluated. The fire-retardant properties of the coatings were evaluated according to ASTM D1360-90a standard methods; this allowed for an indication of the carbonization index and the weight loss of the substrate. The morphologies of the microcapsules were revealed by scanning electron microscopy (SEM) and the changes in the chemical structure were recorded using Fourier Transform Infrared Spectroscopy (FTIR). The mechanical film properties were determined using ISO and ASTM standard methodologies.

Materials and Methods

The reagents used for the microencapsulation of dihydrogen ammonium phosphate or monoammonium phosphate (MAP) were as follows: 2,4,6-triamine-1,3,5-triazine (melamine), polyvinyl alcohol (PVA), ethanol (96% v/v), monoammonium phosphate (MAP), formaldehyde (37% v/v), sodium carbonate (Na_2CO_3), and acetic acid. These were analytical grade and supplied by Merck SA. Pinus radiata tannins were extracted according to the procedure described by Fernández et al. [16] and were used as a carbon source. The bark of Pinus radiata was added to a pilot reactor, and extraction with a mixture of ethanol/water was performed under reduced pressure. The

extract was subsequently dried in an oven at 40 °C under reduced pressure until a fine tannin powder was obtained. The appropriate amount of tannin extract or low molecular weight tannins (L-MWT) was dissolved in water to make up the fractions used in this study.

Synthesis of the Prepolymer and Preparation of the MAP Microcapsules

The prepolymer was synthesized using a modified version of the method reported by Wu et al. [11]. 2 g of PVA and 2 g of melanin were added to a 500 mL round bottom flask, followed by 100 mL of distilled water. After the dissolution of the solids, the pH of the solution was adjusted to 4-5 using acetic acid and was then heated at 90 °C in an oil bath for 1.5 hours with constant stirring. Subsequently, the pH of the solution was adjusted to between 8 and 9 using a 10% (w/v) Na_2CO_3 solution, and another 2 g of melanin was added first, followed by the 5 mL of formaldehyde 37% (v/v). Finally, the obtained mixture was heated at 90 °C for 1 hour to obtain the prepolymer. MAP microcapsules were prepared as follows: 10 g of MAP was dispersed in 25 mL of ethanol by stirring at 1000 rpm for 5 min. Afterward, this solution was added to the prepolymer obtained previously and the pH of the mixture was adjusted to between 4-5 using a 10% (v/v) H_2SO_4 solution. The resultant solution was heated to 80 °C with constant stirring at 400 rpm for 3 hours. The solution was then centrifuged at 9000 rpm for 15 min. The obtained microcapsules were filtered and washed with distilled water and dried in an oven at 70 °C for 24 hours. The obtained solid was denoted as microcapsules of monoammonium phosphate (McMAP).

Coating Formulation, Surface Preparation, and Application Onto Substrates

Three coatings were produced, each with a different formulation, to determine the effect of the incorporation of microcapsules in active additives on the fire resistance. A water-based acrylic coating was created as a control sample. Microcapsules of MAP (McMAP) were added to this coating at 3 and 9% w/w ratios.

The coatings were formulated with λ values between 1.37 and 1.51, where λ is the relationship between the pigment volume concentrations (PVC) (50 to 65%) and the critical pigment volume concentration (CPVC) (36 to 43%) [17,18]. Table 1 shows the compositions of the coating components. The preparation of the coatings was achieved with a mechanical stirrer and a Cowles-type dispersion propeller operated at speeds of 550-700 rpm. The components were added into a 1 L plastic container and were constantly agitated by varying the speed of the rotor. Zirconia grinding balls were used to ensure adequate dispersion and to reduce the particle size to a value of 5 Hegman (35 - 40 μm). The surface of the metal substrates (Steel ASTM A36) was prepared according to the established standards of the SSPC (Steel Structures Painting Council. Pittsburgh, USA), applying section SP1 (Solvent Cleaning: removal of all visible oil, grease, soil, drawing and cutting compounds, and other soluble contaminants from steel surfaces with solvent, vapor, cleaning compound, alkali, emulsifying agent, or steam) and SP5 (Metal blast cleaning: when viewed without magnification, the surface shall be free of all visible oil, grease, dust, dirt, mill scale, rust, coating, oxides, corrosion products and other foreign matter).

The wood substrate was dried in an oven at 30 °C for 48 h and the adhered powders were superficially cleaned. Due to their high solid content, the formulated coatings were applied onto the substrates using a brush. The thickness of the films was between 150-200 μm. The formulated coatings were denoted as: F-Blank (acrylic water-based formulation); F-3% McMAP (parent formulation + 3% w/w McMAP); and F-9% McMAP (blank + 9% w/w McMAP). In addition, two commercial coatings were tested for comparison. Intumescent FireWall 200 commercial paint; Tricolor (C-INT), and Ignifuga Retardant 77 commercial paint; Chilcorrofin (C-IGN) were used.

Table 1: Specifications of the experimental materials in the blank formulation, F3, and F9. All formulations were prepared in (w/w).
3 and 9 indicate the percentage of McMAP used.

Formulations Components	F-Blank	F-3% McMAP	F-9% McMAP
Water	27.80	27.74	27.80
Caolín (Opacit)	5.12	4.75	4.75
Calcium carbonate (Hifill)	13.33	12.35	3.01
L-MWT	15.50	15.00	15.00
McMAP	0.00	3.01	9.03
Foamaster MO 2134	0.16	0.14	0.14
Acronal S716 1.09	31.00	26.00	26.00

Characterization and Fire Behavior Tests

Chemical, Morphological, and Structural Characterization of Microcapsules

The obtained microcapsules were characterized by Attenuated Total Reflection Fourier Transform Infrared Spectroscopy (ATR-FTIR) using a Spectrum Two kit (Perkin Elmer). Each spectrum was obtained by consecutive scanning at a resolution of 1 cm^{-1} over the range 4000-500 cm^{-1}. The morphological characteristics of the microcapsules were revealed by Scanning Electron Microscopy (SEM) using a Jeol JSM 6380 LY operated at an acceleration voltage of 20 kV. Before SEM analysis, the samples were coated with 50 nm of gold. Elements present in the microcapsule were qualitatively determined by Energy-Dispersive X-ray Spectroscopy (EDS).

Thermogravimetric Analysis (TGA)

TGA was performed using a Pyris TGA kit (TG 209 F3 Tarsus). Further, 5 mg of the microcapsules was placed in an aluminum crucible and subjected to a heating cycle over the range 25-600 °C. The heating rate was 10 °C/min. The system was purged with nitrogen at a flow rate of 50 mL/min.

Evaluation of the Properties of the Coatings

A range of mechanical assessments was conducted on the coated substrates and the commercial coatings according to standard ASTM and ISO testing methodologies. The dynamic viscosity of the coating was measured using a Krebs viscometer in accordance with ASTM D562, while the dry film thickness was measured according to ASTM 6132 using an Elcometer 456 kit. To determine the hydrophobicity of the coating, the contact angle (CA) formed between the coating and a drop of deionized water was determined. The change of the angle over numerous periods of 10 seconds, in static conditions, was evaluated with a Kruss Goniometer model DSA25S controlled by software. The average CA value was obtained by measuring the same sample in different positions. Mechanical properties were evaluated on metallic substrates with dimensions of 10 x 10 x 0.3 cm for cupping, adhesion, and abrasion tests. Flexibility tests were completed on substrates with dimensions of 15 x 6 x 0.3 cm. The standards applied for these tests were as follows: adherence (ASTM D4541 using a PosiTest AT-A kit), abrasion (ASTM D4060 using a Taber Abraser model 5135 kit with a load of 1000 kg and type CS-10 abrasion wheels), flexibility (ISO 1519 using a BYK cylinder mandrel 5710), and cupping (ISO 1520 using a BYK PF-5405 cupping machine).

Fire Behavior of the Coating

The fire resistance of the coatings was evaluated using an adapted version of ASTM D1360-90a. A constant flame was applied by a torch, at an inclination of 45° to the sample, for 180 seconds, taking temperature measurements of the area every 15 seconds. The tests were carried out in triplicates for each formulation. In addition, the weight, width, length, and initial and final thickness of each specimen were recorded throughout the test. Thus, the carbonization index, weight loss, and resistance to temperature increases were evaluated.

Results and Discussions

Chemical, Morphological, and Structural Characterization of Microcapsules

The FTIR spectra of the encapsulating materials (melamine and PVA) are shown in Figure 1a, while the spectra of the additive to be encapsulated (MAP) and the obtained microcapsules (McMAP) are presented in Figure 1b. Table 2 summarizes the characteristic vibrational bonding signals of the samples. Based on these results, the formation of the McMAPs is evidenced by the disappearance of the stretching bands of the primary amine from the melamine (3500 and 3440 cm^{-1}). This indicates that the reaction with polyvinyl alcohol to form the prepolymer was successful. The appearance of the vinylidene stretching signal at 1664 cm^{-1} originating from the PVA, as well as the characteristic stretching signal at 3200 cm^{-1} related to alcohol groups that did not react, confirm the formation of the encapsulating polymer. The encapsulated MAP signals observed at 1256 and 880 cm^{-1} are ascribed to P=O stretching and P-O asymmetric stretching vibrations, respectively [11,19].

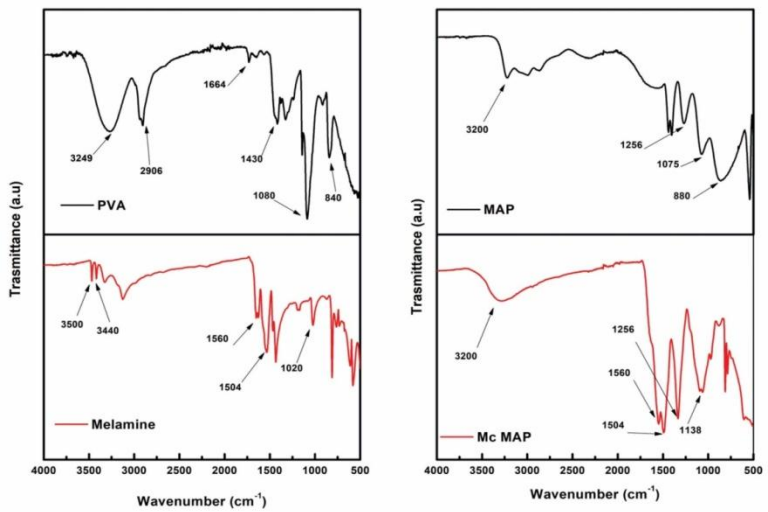

Figure 1: FTIR spectra of the MAP microencapsulation materials.

Table 2: Infrared vibration signals from reagents and microcapsules.

Vibration signal	Melamine	PVA	MAP	McMAP
	Wavenumber (cm^{-1})			
N-H Stretching Primary Amine	3500 3440			
N=C Stretching	1630			
N-H Bending Primary Amine	1560			1560
N-C Stretching	1020			1138
O-H Stretching Alcohol		3249		3200
C-H Stretching sp2 sp3		2936 2906		
C=C Stretching alkene		1664		1664
C-H Bending alkane		1430		
O-H Bending		1330		
C=C Bending alkene		840		
NH4+			3200	
P=O Stretching			1256	1256
P-O Symmetric Stretching			1075	
P-O Asymmetric Stretching			880	880

Figure 2 shows the surface morphology, particle diameter, and EDS analysis of the McMAPs. Perfectly spherical microcapsules are observed, with uniform size and no irregularities. The particle size distribution varied between 0.7 - 1 µm with an average diameter of 0.98 µm (Figure 2a, 2c). The diameter of the obtained microcapsules was smaller than that reported by Wu et al. [11] (20 µm). Furthermore, compositional analysis by EDS (Figure 2b) showed characteristic signals for C, N, P, and O; these results confirm the MAP encapsulation. The compositional mapping of the McMAPs is illustrated in Figure 3; a homogeneous distribution of each element was seen throughout the microcapsule. The presence of carbon is attributed to the fact that the microcapsule is an organic polymer formed from PVA, melamine, and formaldehyde. The presence of nitrogen results from the incorporation of melamine in the polymer matrix while the observed phosphorus signal is due to

monoammonium phosphate existing both inside the microcapsule and in its wall.

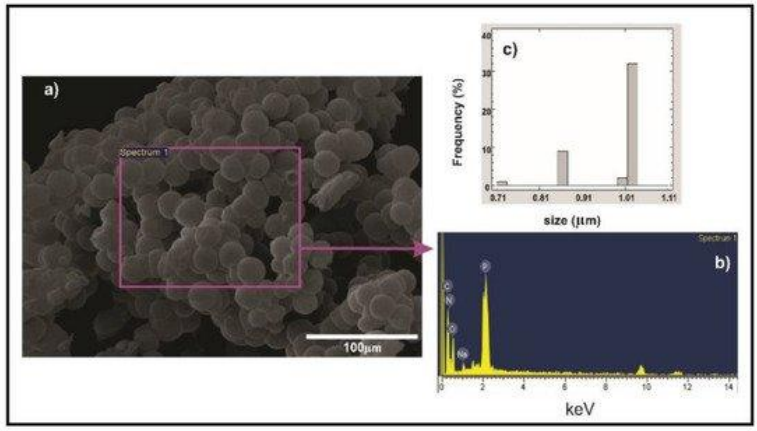

Figure 2: a) SEM micrographs of the McMAP and b) size distribution histogram for the microcapsules. c) EDS analysis.

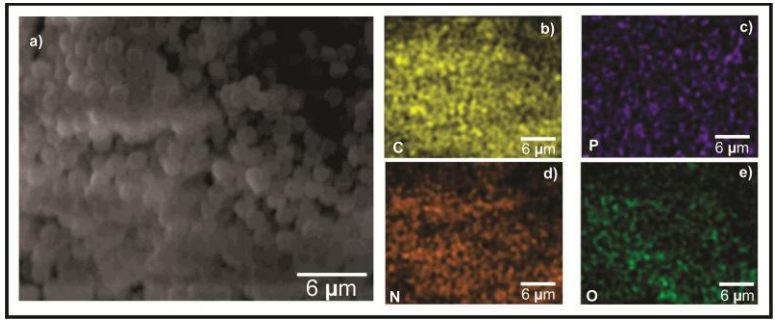

Figure 3: a) McMAP EDS mapping image and distributions of the various elements that make up the microcapsules: b) carbon (C), c) phosphorus (P), d) nitrogen (N), and e) oxygen (O).

Thermogravimetric Analysis (TGA)

The thermogravimetric analysis (TGA) curve and Differential Thermogravimetric Analysis (DTG) for the McMAPs are shown in Figure 4 and the decomposition temperatures are reported in Table 3. Only 26.51% of the initial mass was retained at 600 °C as revealed in the TGA curve. The observed loss of mass

corresponds to the thermal degradation of the microcapsules. Upon determining the first derivative DTG of the TGA curve, three clear decomposition processes are identified for McMAP: 40-190 °C, 200-430 °C, and 430-600 °C. The maximum temperatures of each stage are 103.4 °C, 337.2 °C, and 468.2 °C. The first stage of degradation corresponds to the decomposition of PVA and is attributed to the breakdown of ester bonds, the release of non-flammable gases due to the decomposition of melamine, and the evaporation of absorbed water [20,21]. The loss of mass in the second stage is caused by the elimination of NH_3 from the melamine units [22]. The final stage of thermal degradation is a result of MAP decomposition in the microcapsules, which generates phosphoric acid and metaphosphoric acid, followed by their dehydration to form phosphorous oxides (P_4O_{10}) [21,23].

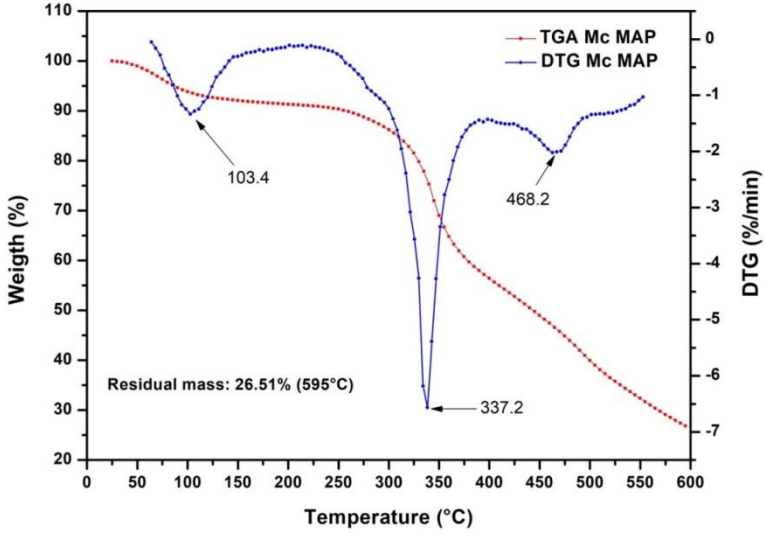

Figure 4: TGA and DTG analysis of the McMAP.

Table 3: Result of decomposition temperature and residual mass of McMAP microcapsules.

Sample	T5%	Tmax1	Tmax2	Tmax3	Residual Mass (%)		
					400 °C	500 °C	600 °C
McMAP	90.00 °C	103.40 °C	337.20 °C	468.20 °C	50 %	40 %	27 %

Formulation of Coatings with MAP Microcapsules

The particle sizes for the four formulations described in Table 1 were evaluated using the ASTM D-333 standard. For the reference formulation (F-Blank), a Hegman value of 5 (<38.10 microns) was determined. On the other hand, the formulations that comprised microcapsules (F-3% McMAP and F-9% McMAP) presented Hegman values of 4 (<50.80 microns). These results can be explained by the inferior dispersion of the microcapsules in sub-optimal media causing agglomeration. This is the case for intumescent coating formulations that contain high solid content, where satisfactory dispersion of the microcapsules is difficult to achieve. As previously mentioned, the formulations that include microcapsules were produced with a high-volume content of solids, exhibiting PVC contents between 49.90% and 65.42%, and a λ ratio in the range of 1.37 to 1.51 (Table 4). These high PVC contents produce dull coatings and inhibit blistering, however, the permeability and the risk of substrate corrosion increase. For this reason, when industrially applied on steel, these formulations must be coated with a sealant that protects it from corrosive environments. In this work, the resistance of the coatings to weathering was not evaluated, therefore a sealant was not applied.

Table 4: PVC, CPVC and λ values for the formulations

Formulations	PVC	CPVC	λ
F-Blank	49.90	36.53	1.37
F-3% McMAP	58.70	39.52	1.49
F-9% McMAP	65.42	43.46	1.51

Evaluation of the Mechanical Properties of the Coatings

Visual inspection of the formulated coatings was conducted using opacity drawdown charts. Figure S1 (a-c) shows the results obtained for the F-Blank and F-3% McMAP coatings. The formulations show good opacity and covering power when applied on the substrate, with slight changes in the tonality depending on the amount of inorganic filler and tannins present.

These coatings form a continuous film on the substrate (Figure S1 a, b), however, upon further addition of MAP microcapsules (i.e., F-9% McMAP), agglomerations and cracks were formed on the coating. Results obtained from the dynamic viscosities are shown in Table 5; when the percentage of MAP in the microcapsules increases, the viscosity increases. The F-9% McMAP sample displayed the highest viscosity with a value of 2407 cp. This is because the tannins present in the MAP microcapsules absorb any water in the formulation [11]. This high viscosity is to be expected as the coating has a high solid content, characteristic of intumescent commercial coatings. The high viscosities proved to be problematic for the application of the films onto various substrates, for this reason a brush was used.

Table 5: Evaluation of Film Properties of McMAP Formulations and Commercial Coatings.

Formulations	Viscosity (cp)	Steel Substrate		Wood Substrate		Contact Angles	
		Dry film thickness (µm)	σ	Dry film thickness (µm)	σ	°	σ
F-Blank	381	153.5	15.40	125.1	0.07	44.56	1.10
F-3% McMAP	1743	190.8	27.00	99.1	0.49	45.38	4.78
F-9% McMAP	2402	154.9	13.40	65.55	2.68	60.27	6.02
C-INT	-	256.86	43.35	65.73	1.73	43.42	9.06
C-IGN	-	49.46	5.48	61.65	0.49	70.34	2.77

Table 5 also shows the dry film thicknesses of the formulations on metal substrates. Figure S1 (d-i) shows the coatings applied on a metal substrate. When two successive coatings were applied on the metallic substrate, the thicknesses of the applied coatings (F-Blank, F-3% McMAP, and F-9% McMAP) are between 150 and 190 µm. Two coats of the commercial paints were also applied on the metallic substrate and these exhibited thicknesses of 256 and 49 µm for C-INT and C-IGN, respectively. The difference in thickness is because the commercial intumescent formulation (C-INT) has a high solids content (greater than 65%). while the commercial fire-retardant paint (C-IGN) is a varnish with a solid content lower than 30%. Furthermore, the formulated and commercial coatings were applied to wood to

evaluate fire resistance properties. The thicknesses obtained on wood were lower than those applied on metal. This is most likely due to the absorption of the coating by the open pores of the medium density fiberboard (MDF) wood utilized.

Table 5 shows the contact angle results for the coatings. These results for all evaluated coatings are also shown in Figure 5. The three formulated and the two commercial coatings were hydrophilic in character, presenting contact angle values lower than 90°. The F-9% McMAP coating displayed was slightly less hydrophilic with an angle of 60.27 ° ± 6.02. This performance is attributable to the particle sizes in the McMAPs and the roughness of the coating owing to its high solid content. As the content of microcapsules in the formulations increases, the contact angle also increases. For the F-Blank control coating, the contact angle was 44.56° ± 1.10, due to the water solubility of the added tannins. Similarly, the commercial coatings present values of 43.42° and 70.34° for C-INT and C-IGN, respectively.

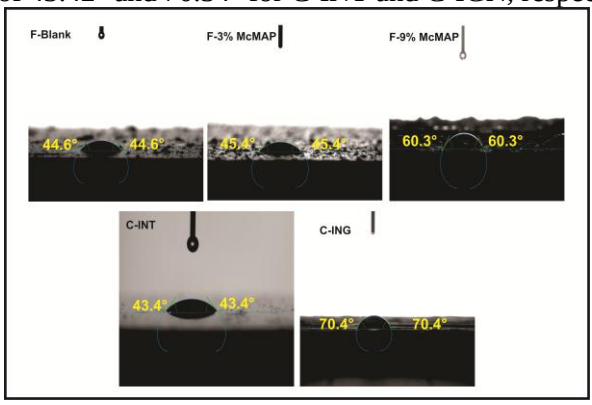

Figure 5: Contact angle of the formulated coatings.

Although the F-9% McMAP formulation presented the best contact angle as previously mentioned, it did not demonstrate suitable film properties. For this reason, it was not possible to determine its mechanical properties. The mechanical properties of the other coatings (formulated and commercial) were evaluated, and the results are summarized in Table 6. The 3% McMAP sample showed a slight improvement in the resistance to abrasion with respect to the F-Blank sample and lower losses from mechanical wear were observed with a value of 179.20 mg obtained.

Table 6: Evaluation of the mechanical properties of coatings.

Formulations	Abrasion	Flexibility	Cupping		Adhesion	
	Wear Index (mg)	Diameter mandrel without fail (mm)	Impact resistence (mm)		Mpa	Type failure
F-Blank	193.40	12	1.00 (± 0.68)		1.77 (± 0.03)	100% cohesive
F-3% McMAP	179.10	12	0.59 (± 0.04)		0.74 (± 0.04)	90% cohesive
F-9% McMAP	-	-	-	-	-	-
C-INT	342.70	16	1.70 (± 0.12)		1.06 (± 0.04)	90% cohesive
C-IGN	274.22	2	8.38 (± 0.04)		3.50 (± 0.69)	98% adhesive

Figure S2 shows the mass loss of the coatings for the abrasion test. The commercial coatings exhibited the greatest losses, with values of 342.70 and 274.22 mg for the C-INT and C-IGN, respectively. Flexibility tests indicate that formulated coatings performed better than the C-INT, and worse than the C-ING (Figure S3). Because the latter is a varnish, it has excellent flexing properties, unlike high solid content coatings where there is a deficiency of resin in the solid volume (Table 6). The moderate behavior revealed for the F-3% McMAP is due to the presence of McMAP particles in the formulation. These results agree with those obtained in the abrasion test. The particle size, degree of packing, and continuity of the film are determining factors for obtaining excellent mechanical film properties. A reduction in the adherence by over 50% was determined; in both formulations the failure mechanism resulted from inadequate cohesion, indicating poor physical interaction within the coating layer. Lower thickness coatings are incomparable with higher thickness coatings in terms of mechanical test

The reference formulation (F-Blank) presented enhanced adhesion to the metallic substrate in comparison to the F-3% McMAP sample, indicating that the incorporation of the microcapsules produces a relatively negligible negative effect on the adherence to the metal. 1.77 ± 0.03 MPa of adhesion was determined for F-Blank, compared to 0.74 ± 0.01 MPa for F-3% McMAP. Figure S4 shows the results of the adhesion and cupping tests. The cupping test showed similar trends to those observed in adherence tests; the commercial coatings perform better than McMAP formulated coatings. The coatings obtained with F-9% McMAP failed to obtain film properties and covering power due to the high amount of McMAP, for this reason it was not possible to evaluate their mechanical properties.

Fire Behavior of the Coating

Fire performance tests for the formulated coatings, were performed on the wood substrate (MDF). Figure 6 shows the specimens after the flame resistance test; a zone of fire advancement is observed on the wood surface. The largest affected area and the highest fire spread rate occurred on

uncoated wood, followed by F-Blank and F-9% McMAP. For the F-3% McMAP formulation, the fire expanded to a lesser degree, behaving similarly to commercial coatings (C-INT and C-IGN). We expected that the fire-retardant effect would be superior with a higher MAP microcapsules content. However, the opposite was seen; this was attributed to the excellent properties of the 3% McMAP film where its components were homogeneously dispersed, and well-integrated with the resin. Likewise, the presence of L-MWT and McMAP play an important role in generating a sufficient fire-retardant effect. As such, tannins are excellent materials for generating a carbonaceous layer that prevents flame propagation. No significant intumescent behavior (foaming or swelling) was observed in any of the formulated coatings. However, a uniform carbonaceous layer was formed on the wood substrate.

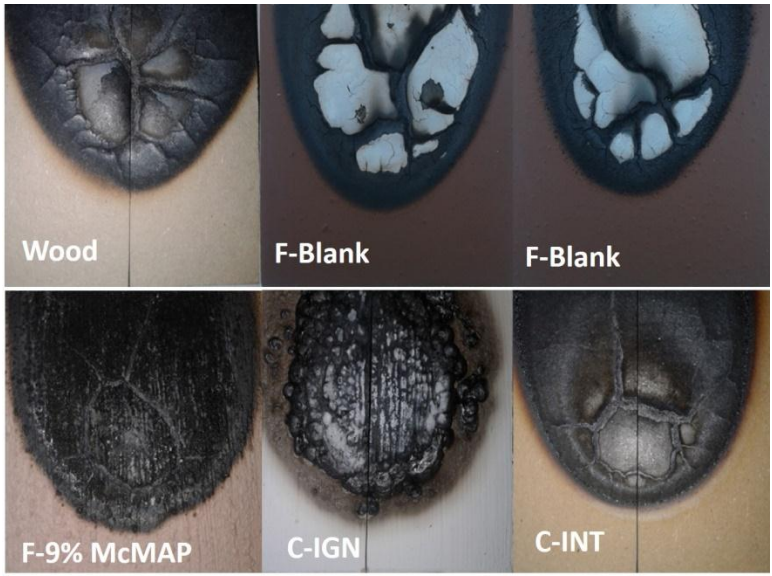

Figure 6: Flame resistance of the formulated coatings.

Figure 7 illustrates the temperature versus time curve of the flame resistance test. This curve represents the increase in temperature of the back of the substrate, where each coating was applied. As can be seen, the flame behavior process occurs in

three stages. The first stage corresponds to the initial interaction of the fire with the coating; a high-temperature gradient does not occur and it is maintained at 0 - 1.5 °C above the initial test temperature, whereas for C-INT, $\Delta T = 0$ °C. In the second stage, a dramatic increase in the temperature gradient occurred from 45 to 90 s, until it reached a maximum, due to the partial loss of the coating from the substrate. The maximum obtained temperature gradients were between 10.40 and 32.80 °C. The highest gradient was obtained for F-9% McMAP, followed by F-3% McMAP. The final stage is the complete degradation of the coating and the advance of the fire on the wood. A decrease in ΔT was observed due to the formation of a superficial carbonaceous layer. This effect was not seen for C-INT, in which only the first two stages were observed. This was due to the formation of foam and/or intumescence of the coating, preventing direct flame propagation and protecting the substrate.

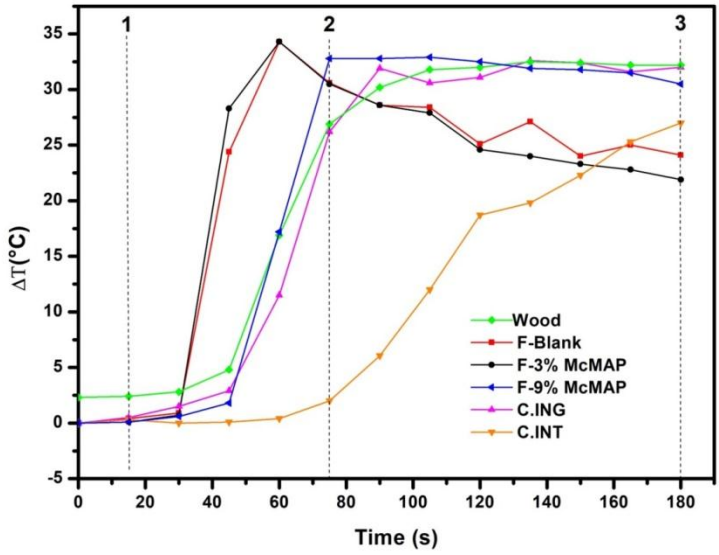

Figure 7: Fire behavior of the formulated coatings.

The results obtained for the carbonization index and the loss of mass in the wood substrate are reported in Table 7 and plotted in Figure 8. These tests were carried out strictly according to the ASTM D1360-90a (1994) standard methodology. The results

were limited to the ASTM D1360-90a test setup, it could maybe be different if tested in, e.g., the ISO 5660 Cone Calorimeter at varying heat fluxes or in the full-scale ISO 9705 Room Corner Test, i.e., tests far outside the focus of the present study. Some materials perform well in small scale tests but fail catastrophically in large- or full-scale situations due to high radiant heat flux levels.

The best carbonization index performance was obtained for the F-3% McMAP coating with a value of 26.86% determined. This result confirms that superior film and mechanical properties are extremely important to enhance the fire-retardant properties. The carbonization index of uncoated wood was 37.44% indicating that coatings that contain tannins and McMAP act as flame retardants as they generate a carbonaceous layer that reduces the mass loss of the wood substrate. The C-INT and C-IGN commercial coatings presented carbonization indices of 32.50% and 39.02%, respectively, demonstrating the superior performance of the F-3% McMAP. Importantly, the F-3% McMAP coating displayed the lowest mass loss percentage (9.05%), better than the other formulated coatings and the uncoated wood. The mass loss of the F-3% McMAP coating is greater in comparison to the C-INT, however, its film behavior is superior. Therefore, fire-retardant properties are present in this film. On the other hand, increasing the McMAP content generates greater flame resistance, however, suitable protection is not observed since the carbonization indices and the mass loss percentage are higher. Excellent film properties are essential, as these directly influence the behavior of the coating toward fire. Non-continuous film coatings that contain fissures or cracks allow the heat transport to pass the coating, reducing the fire resistance properties. Although the 3% formulation was the most efficient, other studies where other percentages of microcapsules are contemplated and tests in Cone calorimetry with different heat fluxes must be carried out, for the complete characterization of the formulas and better understand their resistance against fire.

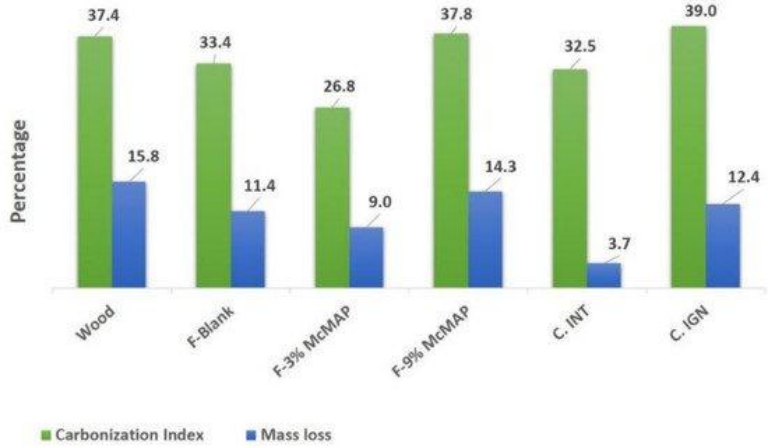

Figure 8: Mass loss and carbonization index of the coatings.

Table 7: Mass Loss and Carbonization Index of Coatings.

Formulations	% Carbonization Index	% Mass Loss
Uncoated wood	37.40	15.80
F-Blank	33.40	11.40
F-3% McMAP	26.80	9.00
F-9% McMAP	37.80	14.30
C-INT	32.50	3.70
C-IGN	39.00	12.40

Conclusions

We obtained MAP microcapsules through a solution-phase polymeric reaction between melamine and polyvinyl alcohol, as confirmed by FTIR and TGA. Agglomerated microspheres of uniform size were generated, with an average size of 0.98 µm and no irregularities. The formulated coatings presented high values of PVC that increased as the incorporation of McMAP increased, affecting the film properties. The three obtained coatings were hydrophilic in character since their contact angles were lower than 90°, however, these angles were higher than those of C-INT and were close to those of C-IGN. The

mechanical properties of the F-Blank and F-3% McMAP formulated coating were similar. Increasing the amount of McMAP did not improve the mechanical properties of the coatings; on the contrary, the properties were diminished although not significantly. The coatings containing McMAP exhibited lower temperature gradients indicating greater resistance to fire. The fire progress and substrate temperature were well controlled by the coatings. The F-3% McMAP coating exhibited superior mechanical and fire resistance properties compared to the F-9% McMAP coating. Based on this, we conclude that the properties of the coatings deteriorate due to agglomeration upon incorporation of higher amounts of McMAP.

References

1. Jimenez M, Duquesne S, Bourbigot S. Intumescent fire protective coating: Toward a better understanding of their mechanism of action. Thermochim. Acta. 2006; 449: 16–26.
2. Puri RG, Khanna AS. Effect of cenospheres on the char formation and fire protective performance of water-based intumescent coatings on structural steel. Prog. Org. Coatings. 2016; 92: 8–15.
3. Han Y, Wu H, Zhang W, Zou D, Liu G, et al. Constitutive equation and dynamic recrystallization behavior of as-cast 254SMO super-austenitic stainless steel. Mater. Des. 2015; 69: 230–240.
4. Laoutid F, Bonnaud L, Alexandre M, Lopez-Cuesta JM, Dubois P. New prospects in flame retardant polymer materials: From fundamentals to nanocomposites. Mater. Sci. Eng. R Reports. 2009; 63: 100–125.
5. Wang ZY, Han EH, Ke W. Fire-resistant effect of nanoclay on intumescent nanocomposite coatings. J. Appl. Polym. Sci. 2007; 103: 1681–1689.
6. Liu Z, Dai M, Zhang Y, Gao X, Zhang Q. Preparation and performances of novel waterborne intumescent fire retardant coatings. Prog. Org. Coatings. 2016; 95: 100–106.
7. Shao ZB, Deng C, Tan Y, Chen MJ, Chen L, et al. Flame retardation of polypropylene via a novel intumescent flame

retardant: Ethylenediamine-modified ammonium polyphosphate. Polym. Degrad. Stab. 2014; 106: 88–96.
8. Cao K, Wu SL, Wang KL, Yao Z. Kinetic study on surface modification of ammonium polyphosphate with melamine. Ind. Eng. Chem. Res. 2011; 50: 8402–8406.
9. Liu Z, Dai M, Hu Q, Liu S, Gao X, et al. Effect of microencapsulated ammonium polyphosphate on the durability and fire resistance of waterborne intumescent fire-retardant coatings. J. Coatings Technol. Res. 2019; 16: 135–145.
10. Yew MC, Ramli Sulong NH. Fire-resistive performance of intumescent flame-retardant coatings for steel. Mater. Des. 2012; 34: 719–724.
11. Wu K, Song L, Wang Z, Hu Y. Microencapsulation of ammonium polyphosphate with PVA-melamine-formaldehyde resin and its flame retardance in polypropylene. Polym. Adv. Technol. 2008; 19: 1914–1921.
12. Montoya LF, Contreras D, Jaramillo AF, Carrasco C, Fernández K, et al. Study of anticorrosive coatings based on high and low molecular weight polyphenols extracted from the Pine radiata bark. Prog. Org. Coatings. 2019; 127.
13. Jaramillo AF, Montoya LF, Prabhakar JM, Sanhueza JP, Fernández K, et al. Formulation of a multifunctional coating based on polyphenols extracted from the Pine radiata bark and functionalized zinc oxide nanoparticles: Evaluation of hydrophobic and anticorrosive properties. Prog. Org. Coatings. 2019; 135: 191–204.
14. Amaral-Labat G, Szczurek A, Fierro V, Stein N, Boulanger C, et al. Pore structure and electrochemical performances of tannin-based carbon cryogels. Biomass and Bioenergy. 2012; 39: 274–282.
15. Celzard A, Fierro V, Amaral-Labat G, Pizzi A, Torero J. Flammability assessment of tannin-based cellular materials. Polym. Degrad. Stab. 2011; 96: 477–482.
16. Bocalandro C, Sanhueza V, Gómez-Caravaca AM, González-Álvarez J, Fernández K, et al. Comparison of the composition of Pinus radiata bark extracts obtained at bench- and pilot-scales. Ind. Crops Prod. 2012; 38: 21–26.
17. Asbeck WK, Loo M. Van Critical Pigment Volume Relationships. Ind. Eng. Chem. 1949; 41: 1470–1475.

18. Rodríguez MT, Gracenea JJ, Saura JJ, Suay JJ. The influence of the critical pigment volume concentration (CPVC) on the properties of an epoxy coating: Part II. Anticorrosion and economic properties. Prog. Org. Coatings. 2004; 50: 68–74.
19. Chupin L, Motillon C, Charrier-El Bouhtoury F, Pizzi A, Charrier B. Characterisation of maritime pine (Pinus pinaster) bark tannins extracted under different conditions by spectroscopic methods, FTIR and HPLC. Ind. Crops Prod. 2013; 49: 897–903.
20. El-Zaher NA, Osiris WG. Thermal and structural properties of poly(vinyl alcohol) doped with hydroxypropyl cellulose. J. Appl. Polym. Sci. 2005; 96: 1914–1923.
21. Giraud S, Bourbigot S, Rochery M, Vroman I, Tighzert L, et al. Microencapsulation of phosphate: Application to flame retarded coated cotton. Polym. Degrad. Stab. 2002; 77: 285–297.
22. Kim JH, Kwon DJ, Shin PS, Baek YM, Park HS, et al. The evaluation of the interfacial and flame retardant properties of glass fiber/unsaturated polyester composites with ammonium dihydrogen phosphate. Compos. Part B Eng. 2019; 167: 221–230.
23. Patrick Lim WK, Mariatti M, Chow WS, Mar KT. Effect of intumescent ammonium polyphosphate (APP) and melamine cyanurate (MC) on the properties of epoxy/glass fiber composites. Compos. Part B Eng. 2012; 43: 124–128.

Supplementary Materials:

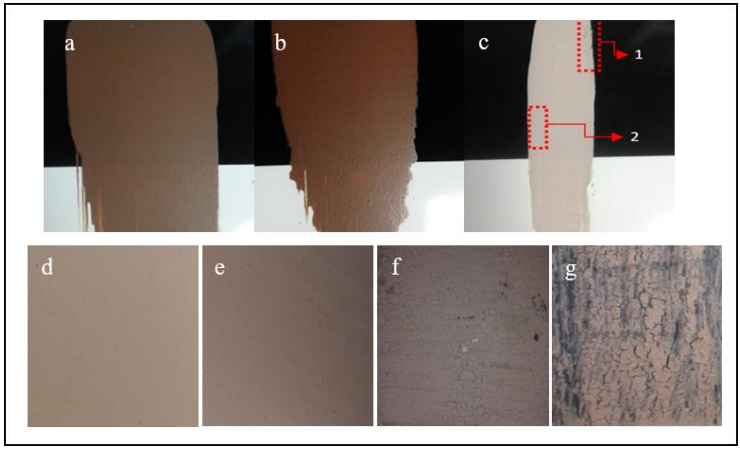

Figure S1: **a-b)** Opacity Tests **a)** F-Blank**, b)** F-3% McMAP, **c)** F-6% McTannin, **d-i)** Application of the coating on metal substrate d**)** F-Blank, **e)** F-3% McMAP, **f)** F-6% McTannin, **g)** F-9% McMAP

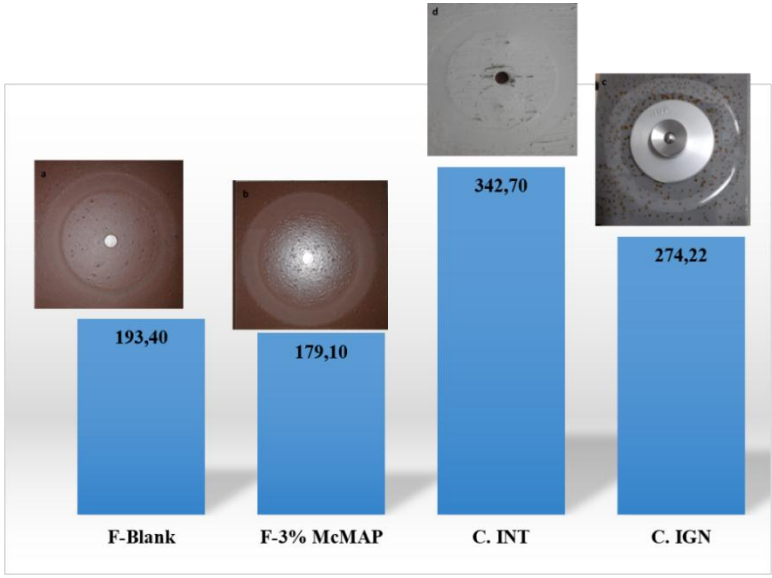

Figure S2: Wear Index **a)** F-Blank, **b)** F-3% McMAP, **c)** C.IGN and **d)** C.INT.

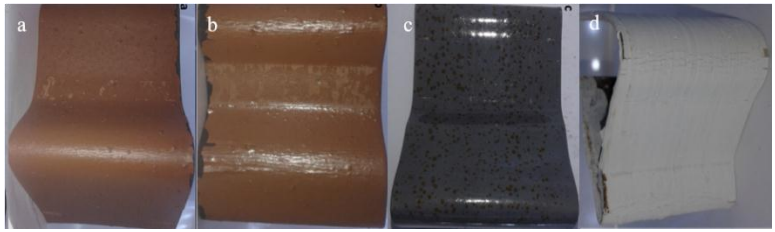

Figure S3: Flexibility test **a)** F-Blank, **b)** F-3% McMAP, **c)** C.IGN and **d)** C.INT.

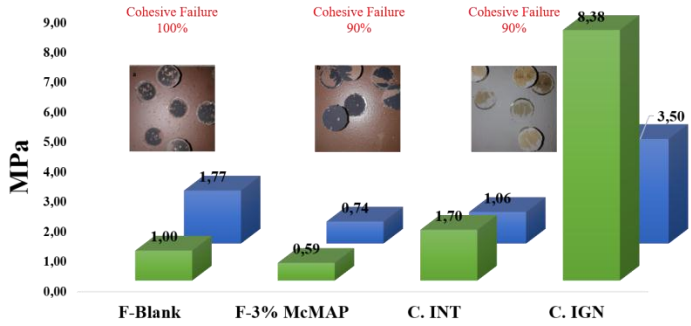

Figure S4: Cupping (green bar) and Pull-off adhesion (blue bar) test on metallic substrate.

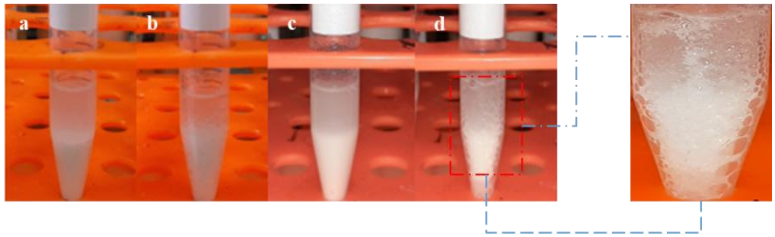

Figure S5. MAP reaction without encapsulation with Na_2CO_3

Book Chapter

Synthesis of Reduced Graphene Oxide Using an Environmentally Friendly Method and its Application to Energy Materials

Ichiro Imae*

Department of Applied Chemistry, Graduate School of Advanced Science and Engineering, Hiroshima University, Japan

***Corresponding Author:** Ichiro Imae, Department of Applied Chemistry, Graduate School of Advanced Science and Engineering, Hiroshima University, 1-4-1 Kagamiyama, Higashi-Hiroshima, Hiroshima 739-8527, Japan

Published **July 15, 2021**

This Book Chapter is a republication of an article published by Ichiro Imae at Coatings in March 2021. (Imae, I. Reduction of Graphene Oxide Using an Environmentally Friendly Method and Its Application to Energy-Related Materials. Coatings 2021, 11, 297. https://doi.org/10.3390/coatings11030297)

How to cite this book chapter: Ichiro Imae. Synthesis of Reduced Graphene Oxide Using an Environmentally Friendly Method and its Application to Energy Materials. In: Alessio Bosio, editor. Surfaces, Interfaces and Coatings Technology. Hyderabad, India: Vide Leaf. 2021.

Funding: This research received no external funding.

Conflicts of Interest: The author declares no conflict of interest.

Abstract

Since graphene oxide can be synthesized in large quantities by oxidation of inexpensively available natural graphite and can be dispersed in water, it can be coated onto a variety of substrates by solution processes. Graphene oxide can also be reduced to yield reduced graphene oxide, which has similar electronic features to graphene. This review introduces the environmentally friendly methods for the synthesis of reduced graphene oxide utilizing electrochemical and thermal methods and summarizes our recent research results on their application to energy-related materials such as electric double-layer capacitors, thermoelectric devices, transparent conductive films, and lithium-ion secondary batteries.

Keywords

Graphene Oxide; Reduced Graphene Oxide; Environmentally Friendly Methods; Sol–Gel Method; Electric Double-Layer Capacitors; Thermoelectric Devices; Transparent Conductive Films; Lithium-Ion Secondary Batteries

Introduction

Graphene is a single layer of carbon atoms lined up in a hexagonal lattice, and graphite is composed of these multiple layers. Until the 2000s, graphene was difficult to obtain, and research in this area was slow for many years. However, in 2004, Andre Geim and Konstantin Novoselov succeeded in obtaining graphene by attaching a piece of graphite to cellophane tape (Scotch tape) and peeling it off, and since then, graphene has attracted attention as a new electronic functional material due to its unique electrical properties [1]. Graphene can be obtained not only by direct exfoliation from graphite by tape (as described above) but also by the chemical vapor deposition (CVD) method. However, the former is

inefficient and the latter requires large equipment, so both are not suitable for industrial use. On the other hand, the synthesis of graphene via graphene oxide, which is obtained from the oxidation of graphite, has recently attracted much interest due to its suitability for mass-scale synthesis (Figure 1). In this method, graphite oxide is first synthesized by chemical oxidation of graphite. Graphite oxide has many hydrophilic oxygen functional groups inserted between the graphite layers, which weakens the interaction between the layers, and can be easily exfoliated into a monolayer by sonication in water to produce graphene oxide (GO), which is uniformly dispersed in water. Finally, the GO can be reduced to obtain a material with electrical properties similar to graphene. Strictly speaking, however, it is difficult to obtain perfect graphene from this method, so the material obtained from this method is often called "reduced graphene oxide" (rGO).

There are three main methods of GO reduction: (1) chemical reduction, (2) electrochemical reduction, and (3) thermal reduction. Among them, chemical reduction is the most frequently used method to synthesize rGO by the chemical reduction of oxygen functional groups such as epoxy groups in GO using a reducing agent such as hydrazine [2]. However, due to the high toxicity of hydrazine, reduction using hydrazine is not a preferred method from an industrial viewpoint. Recently, reduction using hydrogen iodide has also been attempted [3], but this method is also industrially undesirable because hydrogen iodide is highly corrosive. In addition, a unique reduction method using food-derived substances such as vitamin C [4], glucose [5], and xylitol [6] has been reported, but their reaction efficiency is not very high. More recently, reduction methods of GO using Joule heat and microwaves have also been reported [7].

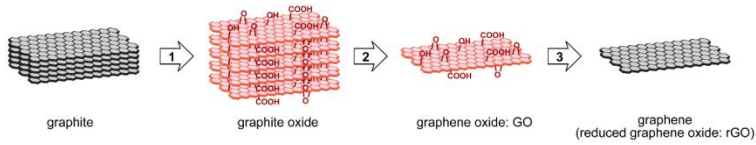

Figure 1: Synthetic route of graphene (reduced graphene oxide) through graphene oxide from graphite (**1**: oxidation, **2**: exfoliation, **3**: reduction).

In contrast, electrochemical reduction is a method of reducing oxygen groups by electrode reaction and is therefore more environmentally friendly than chemical reduction methods in that it does not use toxic reagents. Another feature is that the electronic state of the resulting graphene can be easily manipulated by controlling the reduction level through electrolysis conditions. The thermal reduction method is not exactly a reduction reaction but rather a simple thermal decomposition which removes the oxygen functional groups (hydroxyl, epoxy, carboxyl groups, etc.) in GO. This method can synthesize rGO on a mass scale as long as there is an electric furnace that can provide heat in an inert atmosphere, making it suitable for industrial-scale production processes in addition to being environmentally friendly.

In this review, the electrochemical and thermal reduction methods that we adopted for the synthesis of rGO are introduced, and examples of our efforts to develop highperformance energy-related materials using each method are presented. Since this review summarizes the GO-related research we have been working on, it is recommended that the readers refer to the recent review by Prof. M. Mercedes Velázquez et al. on the myriad of GO-related research that has been carried out [8].

Synthesis of Graphene Oxide

There are three main methods used for the synthesis of GO: Brodie [9], Staudenmaier [10], and Hummers [11] methods. Among these methods, the Brodie and Staudenmaier methods use potassium chlorate as the oxidizing agent, while the Hummers method uses potassium permanganate as the oxidizing agent to reduce the risk of explosion, which was a concern in the former two methods. However, in the Hummers method, only the surface of the graphite is oxidized, leaving an incompletely oxidized graphite core, which tends to produce oxidized graphite with insufficient exfoliation. Therefore, the Modified Hummers [12] and Improved Hummers [13] methods were developed to improve the synthesis efficiency of GO by pre-oxidation of graphite. Details on the characteristics of these GO synthesis

methods are provided in the review by Prof. M. Mercedes Velázquez et al. [8]. In our study, the Modified Hummers method was employed and GO aqueous dispersions were synthesized by the following procedure.

The natural graphite powder (2.0 g) was put into a solution of concentrated H_2SO_4 (8 mL), $K_2S_2O_8$ (1.0 g), and P_2O_5 (1.0 g), and stirred at 80 ºC for 5 h. The mixture was cooled to room temperature, and 200 mL of deionized water was slowly added and left to stand overnight. The solution was filtered through a Buchner funnel, washed until the filtrate was neutral, and dried spontaneously at room temperature to obtain a pre-oxidized graphite powder. The pre-oxidized graphite was then subjected to oxidation by the Hummers method. The pre-oxidized graphite powder (2.0 g) was put into cold (0 ºC) concentrated H_2SO_4 (50 mL). $KMnO_4$ (7.0 g) was added gradually with stirring and cooling for 1 h. The mixture was then stirred at 35 ºC for 2 h, and distilled water (110 mL) was added at 0 ºC. Hydrogen peroxide solution was added until no gas was generated from the reaction solution, after which the color of the mixture changed to bright brown. Using a Buchner funnel, the mixture was filtered and washed with 9 vol % HCl solution (500 mL) in order to remove metal ions. The GO product was suspended in distilled water to give a viscous dispersion, which was subjected to dialysis using a standard regenerated cellulose dialysis membrane (Spectra/Por® 1, Repligen Corp. (formerly Spectrum Laboratories, Inc.), Rancho Dominguez, CA, USA) to completely remove metal ions and acids. This process was carried out for one week while changing the distilled water. The GO was then dispersed in water by sonication for 1 h. GO was dispersed in water by sonication for 1 h and then centrifuged to remove the few remaining impurities (this process was carried out twice). The concentration of the final GO aqueous dispersion was determined by vacuum drying 1.0 mL of the GO aqueous dispersion and measuring the weight of the resulting GO powder.

Electrochemical Reduction

Electrochemical Reduction of GO in Organic Solvents

The electrochemical reduction of GO is generally carried out in aqueous electrolyte solutions, but since GO is water dispersible, it is necessary to immobilize GO on the electrode by prior chemical treatment [14]. We carried out the electrochemical reduction of GO in organic solvents, taking advantage of the fact that GO does not detach from the electrode in organic solvents as compared to aqueous systems [15]. For the electrochemical reduction of GO, platinum and indium–tin oxide (ITO) could be used as working electrodes, but the reduction reaction proceeded more effectively when fluorine-doped tin oxide (FTO), which can be applied in a wide potential window, was used. Figure 2 shows the linear sweep voltammetry (LSV) of the system using propylene carbonate (PC) as the organic solvent, tetraethylammonium tetrafluoroborate (Et_4NBF_4) as the supporting electrolyte, and FTO coated with a drop-cast film of GO as the working electrode. For comparison, the LSV data using only FTO without GO coating (bare FTO) as the working electrode are also shown. The reduction current flowed from around 0.5 V vs. Fc/Fc^+, indicating that electrochemical reduction of GO is possible. When the applied potential became more negative than 1.0 V at LSV, the color of the film changed from brown to black, suggesting that GO was changing to rGO (Figure 3). Electrochemically reduced GO is henceforth referred to as “erGO”.

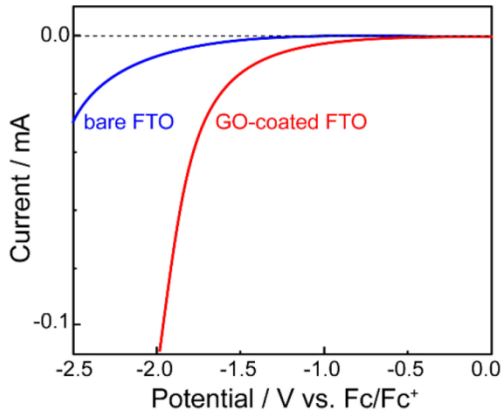

Figure 2: Linear sweep voltammogram of GO (red) (supporting electrolyte: 0.5 M Et_4NBF_4 in propylene carbonate). As a reference, the LSV curve of bare FTO is shown (blue).

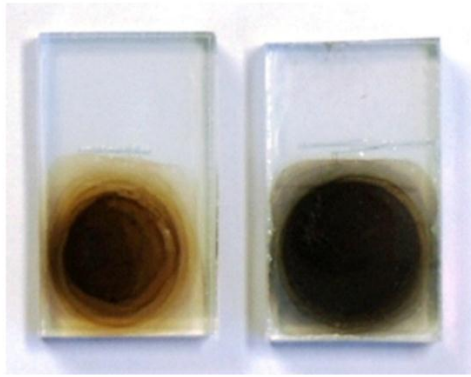

Figure 3: Photo-images of GO (left) and erGO (right).

Fourier Transform Infrared (FT-IR) and X-ray photoelectron spectroscopy (XPS) were measured to identify the chemical structure of erGO (Figure 4). Although no significant absorption bands were observed in the raw graphite, absorption bands originating from C=O stretching vibration of the carbonyl group, angular vibration of the carboxyl group, and C–OH stretching vibration of the hydroxyl group were observed in GO powder at 1740, 1370, and 1220 cm^{-1}, respectively. However, after the electrochemical reduction of

GO, the characteristic absorption bands were no longer observed in the spectrum of the films as in graphite, suggesting that most of the oxygen-containing groups were removed by the electrochemical reduction. In addition, the C1s spectra in XPS showed that the signal derived from oxidized species in GO almost completely disappeared by electrochemical reduction. In order to investigate the electrical properties of erGO, the electrical conductivity of erGO films was measured by the four-probe method and found to be about 3 S cm^{-1}, which is comparable to that of rGO obtained by chemical reduction with hydrazine.

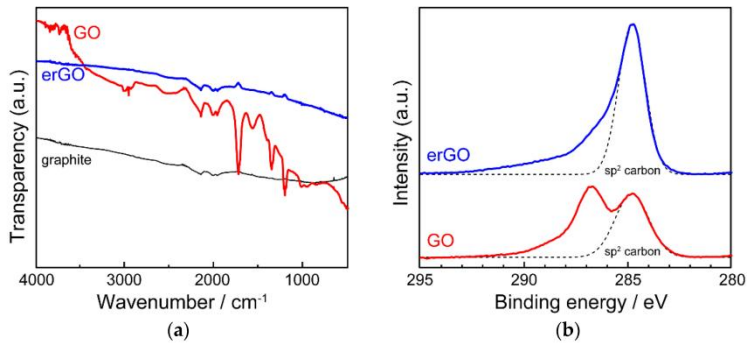

Figure 4: (**a**) FT-IR and (**b**) XPS spectra of erGO.

In addition to its high electrical conductivity, graphene has a large specific surface area of 2600 m^2 g^{-1}, which makes it promising as an electrode material for electric double-layer capacitors (EDLCs). EDLC is one of the electronic components used in a wide range of industries as a backup power source for integrated circuit (IC) and large-scale integration (LSI) memories and actuators. The sweep rate dependence of the specific capacity of EDLC prepared using erGO obtained by electrochemical reduction in propylene carbonate (PC) is shown in Figure 5. Although the rate of decrease in specific capacitance was about 20% compared to that at 10 mV s^{-1}, it was found that the specific capacitance was maintained to some extent.

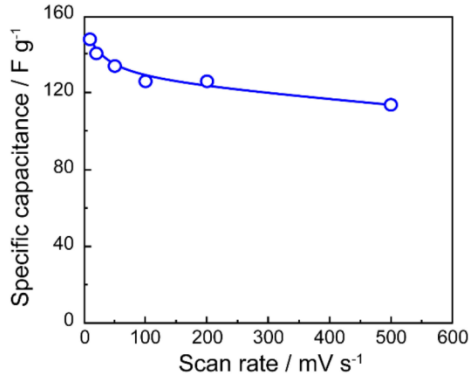

Figure 5: Specific capacitances of erGO/FTO in Et_4NBF_4 (0.5 M) in propylene carbonate plottedagainst the scan rate.

Preparation of Alternating Layer Films with Conducting Polymers

In erGO, many oxygen groups are removed after reduction, and the graphene-like π-conjugated structure is reconstructed, resulting in stronger π-plane interactions. Therefore, erGO single component films do not provide as high a surface area as expected because they tend to stack similar to graphite. One of the promising methods to increase capacitance is to add pseudo-capacitance based on redox reaction, and conducting polymers are attracting attention as a material to be used for providing pseudo-capacitance [16,17]. However, because it has been difficult to find an efficient way to composite graphene with conducting polymers, the conventional method suffers from degradation due to swelling and disintegration during repeated redox reactions, resulting in a decrease in the cycle life.

We have developed an easy method to fabricate alternating layered films of rGO and conducting polymers by taking advantage of the fact that conducting polymers can be easily synthesized by electrochemical oxidative polymerization and that the resulting polymer films are deposited on the electrode surface [18,19]. We focused on the fact that among conducting polymers, polyaniline (PAn) and polypyrrole (PPy) can be

synthesized using relatively inexpensive and water-soluble aniline (An) and pyrrole (Py) as starting materials, and we developed an efficient method to fabricate alternating layered films by the following method using a two-electrode cell. GO aqueous dispersion containing sulfuric acid and An was cast on the FTO electrode and then sandwiched through the spacer (Figure 6a). In order to obtain PAn by electrochemical oxidative polymerization of An, the monomer An must be oxidized to generate cation radicals. However, if the resulting PAn is subjected to a high oxidation state (peroxidation state), it will degrade due to oxidative decay [20,21], so the applied voltage should be as low as possible. Therefore, optimization of the voltage applied to the cell was carried out. As a result, it was found that the lowest voltage at which PAn could be obtained was 1.4 V, so a voltage of -1.4 V~ +1.4 V was applied between the two electrodes. On the other hand, GO is sufficiently electrolytically reduced at -1.4 V to produce erGO, but once GO is reduced to yield erGO, erGO is not re-oxidized back to GO at a voltage of about +1.4 V. Therefore, if a voltage of +1.4 V and -1.4 V is applied to both electrodes alternately, erGO and PAn are generated alternately on both electrodes, and two composite films are produced simultaneously (Figure 6b). It is also possible to fabricate composite films in which erGO and PAn are uniformly dispersed across each other by applying voltage in a scanning manner in this system. When PAn is oxidized, it incorporates the anionic moiety of the electrolyte in solution (doping), and when it is reduced, it releases the anion (de-doping). When the voltage is scanned, the doping/de-doping process smoothly takes place and the molecular chains of PAn can easily form a stable network. It can also be expected that the specific surface area of erGO will increase as PAn inserts between each layer of erGO sheets and props up each sheet.

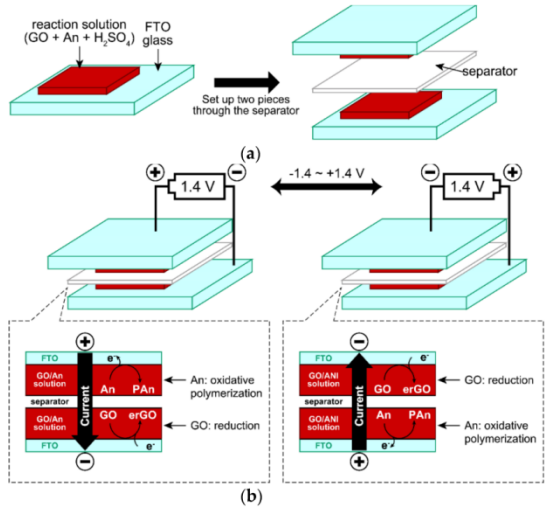

Figure 6: Illustration of a two-electrode cell for electrochemical conversion of GO/An to the erGO/PAn composite: (**a**) Set-up of the cell, (**b**) Redox reaction occurring at both electrodes.

An example of the cyclic voltammogram (CV) of the erGO/PAn composite film obtained by this method is shown in Figure 7. The current flowing from around ± 1.1 V is the oxidation current of An. The peak current at around ±0.26 V seen immediately after the start of the voltage scan is thought to be due to the redox reaction of quinone/hydroquinone groups, which is also seen in other carbon materials [22,23]. This peak current disappears after 50 voltage scans, suggesting that GO has been completely reduced and converted to erGO. The large peak current at around 0 V is the redox wave of PAn that continues to be generated on the electrode. The behavior of the CV curves indicates that the electrochemical oxidation of An acts as well as the electrode reaction of the counter electrode when GO is electrochemically reduced to produce erGO. When voltage was applied to the solution containing only GO without An, almost no current was observed and the electrochemical reduction of GO did not proceed.

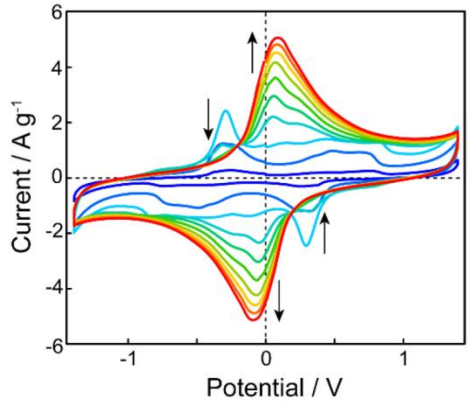

Figure 7: CV curves of a two-electrode cell of the mixture (GO + An + H_2SO_4) at 100 mV s^{-1}.

The brittleness of the resulting erGO/PAn composite film was reduced due to the uniform dispersion of PAn between the erGO sheets, and the film was easily peeled off from the FTO electrode to obtain a self-standing film. The film was flexible and could be bent or folded at sharp angles (Figure 8). It can also be cut out into any desired shape. These characteristics are beneficial properties when considering practical applications (especially wearable devices). The electrical conductivity of the composite film was 70 S cm^{-1}, which is significantly higher than that of erGO film (3 S cm^{-1}) and PAn nanofiber film (2 S cm^{-1}) [24].

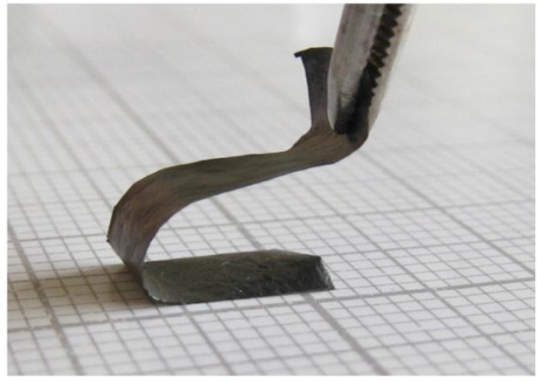

Figure 8: Photo-image of the erGO/PAn composite film.

The capacitance of EDLC with the obtained erGO/PAn composite film was significantly affected by the mass ratio of GO and An in the reaction solution (GO:An ratio), and the highest capacitance of 205 F g^{-1} was obtained when the GO:An ratio was 4:1 (H_2SO_4 concentration: 2.0 mol dm^{-3}). EDLCs using erGO/PAn composite films obtained from the reaction solutions with different GO:An ratios (2:1, 4:1, and 16:1), denoted as erGO/PAn-2:1, erGO/PAn-4:1, and erGO-PAn-16:1, respectively, were repeatedly charged and discharged under the same voltage scanning conditions as in Figure 7, and their cycle life was investigated (Figure 9). At the beginning of the cycle, their capacities were 159 F g^{-1} for erGO/PAn-2:1, 206 F g^{-1} for erGO/PAn-4:1, and 193 F g^{-1} for erGO/PAn-16:1. The capacities of all of them decreased slightly by repetition of charging and discharging. Further charge–discharge cycles were repeated, and when the number of cycles exceeded 3000, the capacity became constant regardless of the number of cycles. Even after 20,000 cycles, the capacities of erGO/PAn-2:1, erGO/PAn-4:1, and erGO/PAn-16:1 remained at 95 F g^{-1}, 141 F g^{-1}, and 160 F g^{-1}, respectively, all showing a good cycle life.

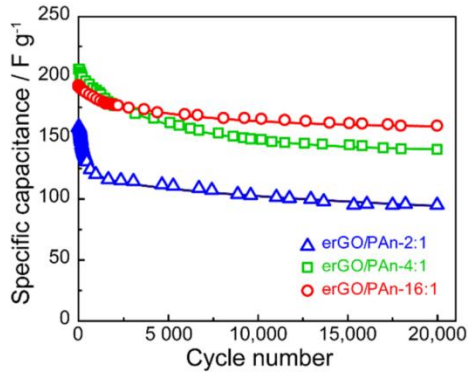

Figure 9: Changes in specific capacitance cycle number for composite films of erGO/PAn.

As a new application of the resulting rGO/conducting polymer composite films, we also investigated their thermoelectric properties. Thermoelectric devices, which can

directly convert thermal energy into electrical energy, have long been used as power sources, such as space probes (such as "Voyager") in faraway places where sunlight cannot reach, and are coming back into the limelight as a technology to recover unused heat. Organic thermoelectric materials using conducting polymers (polythiophene and polyaniline) and nanocarbon compounds (carbon nanotubes and graphene) have been attracting attention for their application to the recovery of unused heat. We have also been working on the development of thermoelectric materials based on polythiophenes with various molecular structures [25–31] and their composites with carbon nanotubes [32]. As part of these studies, we also investigated the thermoelectric properties of the erGO/PAn composite film prepared by the method shown above.
The performance of thermoelectric materials is evaluated to be excellent when the *ZT* value shown in Equation (1) is large.

$$ZT = \frac{S^2\sigma}{\kappa}T = \frac{PF}{\kappa}T \quad (1)$$

where σ is the electrical conductivity, S is the Seebeck coefficient, κ is the thermal conductivity, T is the operating environment temperature, and PF is the power factor ($PF = S^2\sigma$). In this study, we investigated the effect of the fabrication conditions of the composite film on the *ZT* value.

Two methods of fabricating composite films were investigated: (1) the potential scanning method, where a voltage is applied in a triangular wave in the range of ±1.4 V and (2) the potential stepping method, where two potentials of +1.4 V and -1.4 V are applied alternately. Two types of substrates, FTO and stainless steel (SUS), were investigated for the working electrode. It was found that the thermoelectric properties of the resulting composite films were significantly affected by the combination of these factors. Among them, the composite film prepared by the potential step method using an SUS plate as the working electrode showed the highest thermoelectric performance. The thermoelectric properties of the composite films were also found to be affected by the electrolysis treatment time, and the electrical

conductivity started to increase rapidly after 5 h of treatment and reached its highest value after about 10 h (Figure 10). However, when the electrolytic treatment time exceeded 15 h, the electrical conductivity began to decrease. This was attributed to the peroxidation of PAn caused by the prolonged electrolytic treatment. On the other hand, the Seebeck coefficient did not change significantly with the electrolysis time. As a result, the power factor was also affected by the large change in electrical conductivity and showed the highest value around 10 h of electrolysis treatment time. In general, the thermal conductivity of graphene alone is very high, 3000 W m^{-1} K^{-1}, which works as a disadvantage to reduce the *ZT* value. However, by compositing with PAn, which has a relatively low thermal conductivity of 0.1 ~ 0.3 W m^{-1} K^{-1}, the thermal conductivity of the composite films could be reduced to 0.05 ~ 0.85 W m^{-1} K^{-1}, resulting in a maximum *ZT* value of 0.024 for the composite films.

In our research, we have been concentrating on compositing rGO with conducting polymers, but electrochemical methods are very useful, not only for organic materials, but also for compositing with inorganic materials such as nickel [33–35].

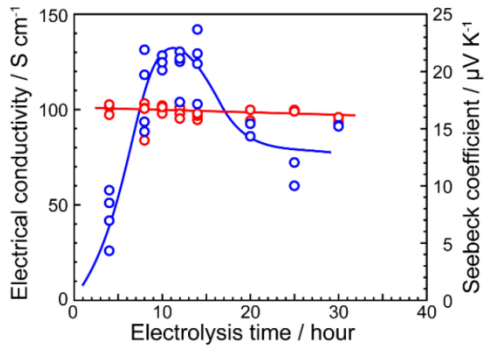

Figure 10: Thermoelectric properties of erGO/PAn composites prepared by various electrolysis times.

Thermal Reduction

Application to Transparent Conductive Films with High Mechanical Strength by Combination with Silica

When extremely thin graphene films are applied to glass substrates, transparent conductive films can be produced due to the excellent electrical conductivity and transparency of graphene. However, graphene is brittle and does not adhere well to the glass substrate, which causes the problem of graphene detaching from the glass substrate after long-term use. We have previously reported that when tetraethyl orthosilicate (TEOS) is added to an aqueous dispersion of a commercially available conducting polymer, a composite of poly(3,4-ethylenedioxythiophene) and poly(4-styrenesulfonic acid) (PEDOT:PSS, Figure 11), the water and acid (sulfonic acid in PSS) cause a sol–gel reaction of TEOS to form a composite of PEDOT:PSS and silica. The resulting silica can adhere to the surface of the glass substrate through chemical bonds (Figure 12), and we have succeeded in developing transparent conductive films with excellent mechanical properties such as scratch hardness and adhesion strength [36]. In addition, while this film has excellent transparency in the visible light range, it has high absorption of near-infrared light. Therefore, it is highly expected that this feature can be used to make this film applicable to heat-shielding materials [37].

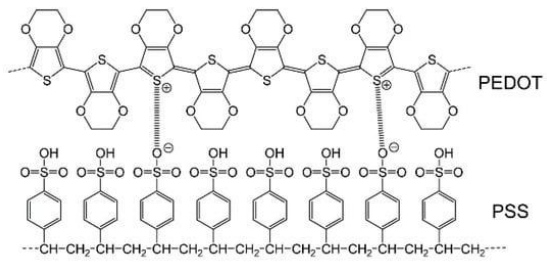

Figure 11: Chemical structure of PEDOT:PSS.

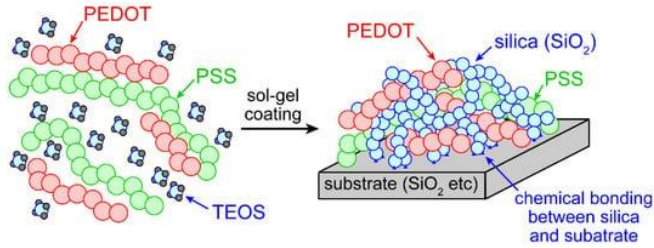

Figure 12: Synthesis of the PEDOT:PSS/silica composite using sol–gel reaction.

The sol–gel reaction used here is a reaction in which organometallic and inorganic compounds (such as TEOS and tetrachlorosilane) containing the target metal are hydrolyzed and polycondensed in the presence of an acid or basic catalyst and water to produce metal oxides [38,39]. For example, multifunctional alkoxysilanes and halosilanes can easily yield silicon dioxide (silica, SiO_2) by sol–gel reaction (Figure 13). This technique has been applied in various fields as a simple method to fabricate metal oxide thin films. Silica-like polymers (polysilsesquioxane), in which one of the substituents on the silicon atom is replaced by an organic group, can also be synthesized by the same method, and various functions can be introduced by the organic substituents [40–47].

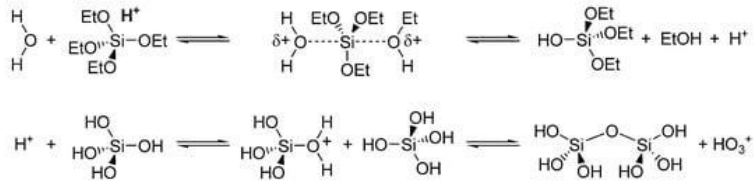

Figure 13: Mechanism of the sol–gel reaction.

Since GO is obtained by oxidizing graphite under acidic conditions and exfoliating it in water and the product contains many acidic functional groups such as hydroxyl and carboxyl groups, the aqueous dispersion of GO can be obtained in an acidic state. Hence, it is expected that the GO acidic aqueous dispersion with these characteristics can be used to achieve

the following: when TEOS is added to the GO acidic aqueous dispersion, the sol–gel reaction proceeds simply by mixing, and the GO/silica composite film can be obtained by coating the resulting solution on a substrate. Finally, the GO/silica film is annealed in air or a vacuum to produce the graphene/silica composite film (Figure 14). If the substrate is a metal oxide such as silica glass or ITO, the graphene/silica composite film can be strongly fixed to the substrate via chemical bonding due to the dehydration condensation between the hydroxyl groups on the substrate surface and the silanol at the end of the molecular chain of silica in the film. Based on this idea, graphene/silica composite films were synthesized by the following method [48,49]: TEOS was added to the GO acidic aqueous dispersion in the proportions shown in Table 1 and stirred for 12 h at room temperature. A phase separation between TEOS and GO aqueous dispersion was observed immediately after TEOS was added to the GO acidic aqueous dispersion. However, the solution became homogeneous (sol state) as the reaction progressed and hydrophilic silanols were formed. The resulting mixed solution was spin-coated onto a glass or quartz substrate and subjected to thermal reduction (reduction conditions: 300 ºC in air, 300 ºC in a vacuum, 500 ºC in a vacuum, and 800 ºC in a vacuum) to produce a composite film of thermally reduced GO (“trGO”) and silica. Among the films prepared by the feed ratios shown in Table 1, GS27 with the highest silica content was visually confirmed to be inhomogeneous, probably due to phase separation between trGO and silica. Therefore, further investigations were performed only for the composite films with a silica content less than 23 mol % (trGO ~ GS23).

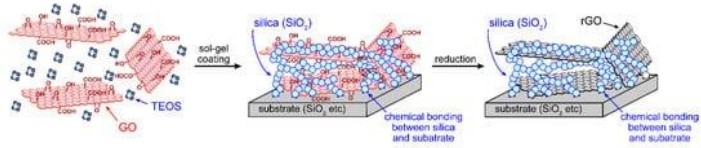

Figure 14: Conceptual diagram of the synthesis of rGO/silica composite films using sol–gel reaction.

Table 1: Feed ratio of GO and TEOS and the theoretical content of silica in the resulting films.

Films	Feed Ratio of GO/TEOS (Volume Ratio)	SiO_2 Contents in Composite Films (mol %)
trGO	1000/0	0.0
GS07	996/4	6.8
GS13	992/8	12.8
GS18	988/12	18.2
GS23	984/16	22.9
GS27	980/ 20	27.2

First, we investigated the effect of the concentration of GO water dispersion on the transparency of the films (Figure 15). As a result, the transmittance of the film prepared using the solution with a GO concentration of 5 mg mL^{-1} was maintained at about 80% of that of the glass substrate alone, indicating that the film had relatively high transparency. Next, the effect of the silica concentration in the films was investigated, and it was found that the transmittance of the films was not significantly affected by changes in the composite ratio of trGO to silica (Figure 16). The mechanical strength of the films was evaluated using a pencil scratch hardness tester [50], and it was confirmed that the films of trGO alone peeled off when scratched with pencils of all harnesses in the range of 6B~6H. On the other hand, the strength of the trGO/silica composite film increased as the silica content and the annealing temperature of the film increased, and GS23 fabricated at 800 ºC in a vacuum showed no damage to the film even when scratched with a 3H hardness pencil (Figure 17). The electrical conductivity of the films was evaluated, and it was found that the electrical conductivity tended to decrease as the silica content in the film increased, while it tended to increase as the heat treatment temperature of the film increased (Figure 18). The correlation between the strength of the films and the electrical conductivities was investigated and it was found that the optimum relationship between the strength and the electrical conductivity was established in the case where the scratching strength of the film was F and the electrical conductivity was 32 S cm^{-1} (Figure 19).

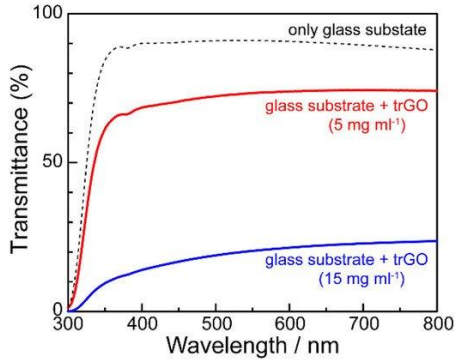

Figure 15: Transmission spectra of trGO films on slide glasses prepared with GO solutions of 5 mg mL^{-1} (red) and 15 mg mL^{-1} (blue). The dotted line denotes the transmission spectrum of the slide glass itself.

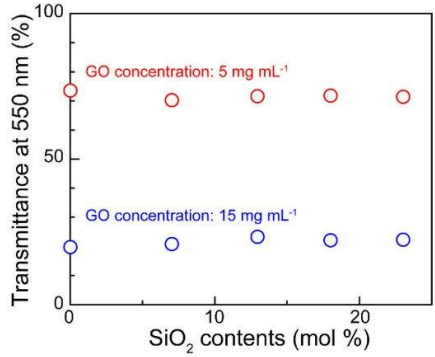

Figure 16: Transmittances of trGO/SiO_2 films at 550 nm plotted against silica contents forGO = 5 mg mL^{-1} (red) and 15 mg mL^{-1} (blue).

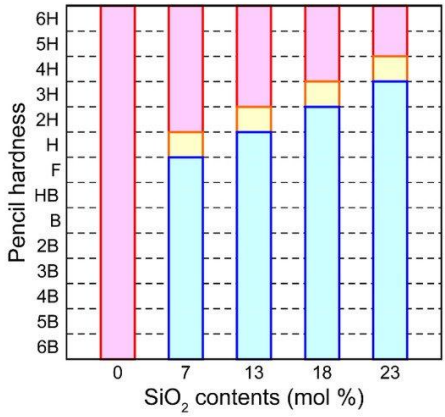

Figure 17: Pencil hardness test of trGO and trGO/SiO_2 films prepared at 800 ºC. (Red: cohesive fracture, Yellow: plastic deformation, and Blue: no damage)

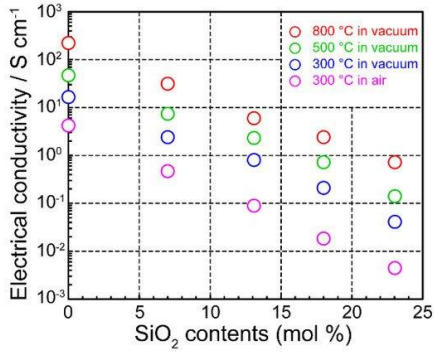

Figure 18: Electrical conductivities of trGO and trGO/SiO_2 films as a function of the silica content.

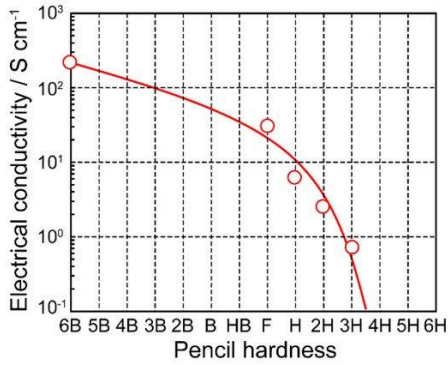

Figure 19: Correlation between pencil hardness and electrical conductivity of trGO/SiO_2 films.

Application to Anode Materials for Lithium-Ion Secondary Batteries with High Capacity and High Durability

In 2019, Goodenough, Whittingham, and Yoshino were awarded the Nobel Prize in Chemistry for their achievements in research and development on lithium-ion batteries (LIBs). Rechargeable batteries, which can be used repeatedly by recharging, have already been put to practical use as a power source for mobile phones and laptop computers and are also expected to be further developed as a power source for electric vehicles in the future [51–54]. Among rechargeable batteries, LIBs have attracted the most interest because of their high energy density, light weight, and high output voltage. Yoshino is the first person in the world to devise and manufacture a prototype rechargeable battery of today's LIBs, using graphite as the anode and lithium cobalt oxide ($LiCoO_2$) as the cathode. He also developed the basic LIB technology of using aluminum (Al) as the positive electrode current collector, as well as the electrode, battery, and peripheral technologies necessary for practical use, resulting in the commercialization of the LIB, a new type of compact and lightweight rechargeable battery.

In LIBs using graphite as anode materials, lithium ions are intercalated and deintercalated between the layers of graphite

during charging and discharging (Equation (2)).

$$6C + Li^+ + e^- \rightleftarrows C_6Li \quad (2)$$

From this equation, the theoretical capacity of carbon materials such as graphite as the anode material is 372 mAh g^{-1}. Currently developed LIBs have already achieved values close to this theoretical capacity, and the development of new materials with higher capacity is eagerly awaited in order to expand their applications to large devices such as electric vehicles and energy storage systems. Silicon (Si) is an anode material that is currently attracting attention from this viewpoint [55–58]. The use of Si can be expected to provide a high theoretical capacity (4198 mAh g^{-1}) based on Equation (3).

$$Si + 4.4\ Li^+ + 4.4e^- \rightleftarrows Li_{4.4}Si \quad (3)$$

However, when Si is changed to $Li_{4.4}Si$, the volume expands 3.8 times, and the stress of expansion and shrinkage of the material due to charging and discharging causes the Si to collapse and pulverize and to detach from the electrode (Figure 20). With the aim of overcoming this problem, we applied our previously developed technology for the synthesis of graphene/silica composites to synthesize graphene/Si composites [59].

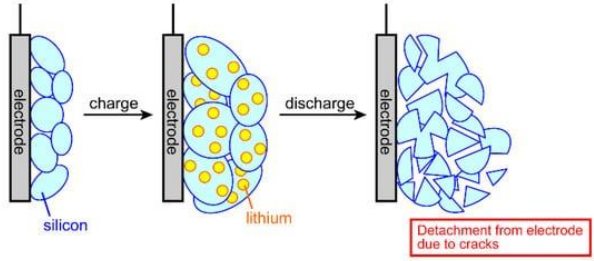

Figure 20: Collapse, pulverization, and detachment of silicon due to repeated charging and discharging.

While GO can be reduced to graphene (trGO) only by heat treatment at about 1000 ºC, silica cannot be reduced only by heat treatment at this temperature because of its high thermal stability.

Commercially, silicon has been produced in the order of hundreds of thousands of tons by reacting silica with carbon at 3000 ºC in an electric furnace (Equation (4)) [60].

$$SiO_2 + 2\ C \rightarrow Si + 2\ CO \quad (4)$$

However, since the graphene/silica composite is used as the starting material in this study, if this composite is heated as is, the carbon component in the composite will be used to reduce the silica, as shown in Equation (4). Heat treatment at temperatures as high as 3000 ºC is also industrially costly. In order to proceed the reduction of silica under mild heating conditions without consuming the graphene in the composite, we applied a reduction method using magnesium metal (Mg) (magnesiothermic reduction) [61].

The synthesis method is as follows; TEOS was added to the GO aqueous dispersion (5 mg mL^{-1}) and stirred for 24 h. Mg powder was added to the obtained GO/silica composite, dispersed by sonication, and dried at 80 ºC. After the dried samples were heat-treated (800 ºC, vacuum), the graphene/Si composites were prepared by removing the byproducts of Mg-based compounds (MgO, Mg_2Si, etc.) with hydrochloric acid and the remaining silica with hydrofluoric acid.

In order to evaluate the structure of the obtained product, Raman spectroscopy was performed (Figure 21). In the spectrum of the sample before heat treatment, the D band derived from structural defects around 1350 cm^{-1} and the G band derived from the sixmembered ring structure around 1600 cm^{-1}, which are observed in graphite and graphene, were observed. On the other hand, in the spectrum of the product annealed in the presence of Mg, a sharp peak derived from Si was newly observed at around 520 cm^{-1}. These results suggest that silica in the GO/silica composite can be reduced to Si by heat treatment in the presence of Mg.

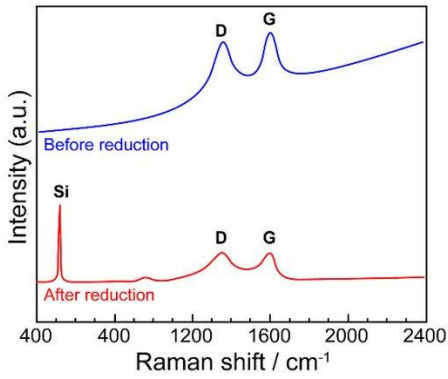

Figure 21: Raman spectra of composites before (blue) and after (red) magnesiothermic reduction.

XPS measurements were also performed to analyze the composition of the composite (Figure 22). The C1s spectra showed that the signals derived from sp^3 carbon (285 eV) and the oxygen group (286 ~ 288 eV) in GO almost disappeared, and the signal intensity derived from sp^2 carbon (284.3 eV) increased in the composite obtained by annealing in the presence of Mg. The Si2p spectrum showed that only one signal derived from silica was observed around 103.5 eV in the GO/silica spectrum, but when the composite was heated in the presence of Mg, the intensity of this signal was greatly reduced and new signals derived from Si (99.5 ~ 99.8 eV) and partially oxidized silicon (SiOx, $0 < x < 2$, 100.1 ~ 102.0 eV) were observed. These results indicate that both GO and silica could be reduced by heat treatment in the presence of magnesium, although not completely. The composite obtained by the magnesiothermic reduction is hereafter referred to as "mrGO/Si".

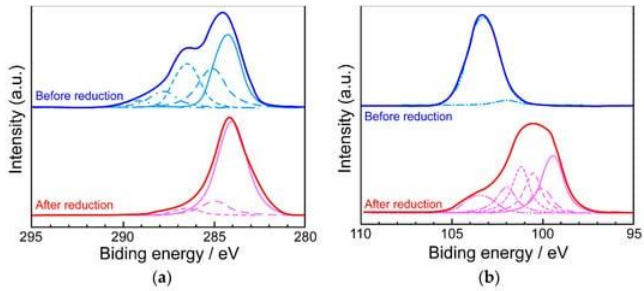

Figure 22: (**a**) C1s and (**b**) Si2p XPS spectra of composites before (blue) and after (red) magnesiothermic reduction.

A battery using the obtained mrGO/Si composite as the anode material was fabricated and its charge–discharge characteristics were investigated. The initial capacity of the LIB fabricated with the mrGO/Si composite film was lower than that of the battery fabricated with silicon alone, but about four times higher than that of the battery fabricated with graphite. We also found that the cycle stability of LIB with mrGO/Si composite was superior to that of LIB with silicon (Figure 23).

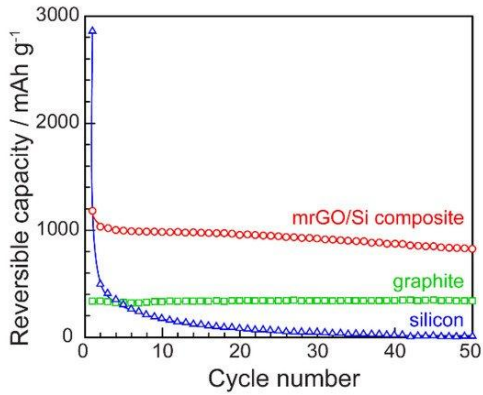

Figure 23: Cyclability of LIBs using the mrGO/Si composite (red), silicon (blue), and graphite (green)as anodes.

Summary and Perspectives

In this review, our recent topics on the synthetic method of reduced graphene oxide (rGO) using graphene oxide by electrochemical or thermal reduction were presented. It was found that the rGO synthesized in this way can be used as important electrode materials in energy storage devices such as electric double-layer capacitors and lithium-ion batteries, transparent conductive films that allow electricity to flow while being transparent, and thermoelectric conversion devices that can recover electric energy from unused and discarded thermal energy. Since there is no need to use highly toxic reagents and the reaction is clean in that it uses water as the solvent, this method has a low environmental impact from the perspective of industrialization, which is in line with the "Sustainable Development Goals (SDGs)".

As mentioned earlier, graphene oxide can also be chemically reduced by food-related materials such as vitamin C. The disadvantage of this method is its low reaction efficiency, but it is very attractive from the perspective of environmental friendliness. This method, in combination with electrochemical or thermal reduction techniques, may lead to the synthesis of graphene-like compounds with even higher efficiency and environmental friendliness. It is also very interesting to introduce microwaves. A novel GO reduction method combining these two methods is currently under investigation.

References

1. Rashid bin Mohd Yusoff A. Graphene-Based Energy Devices. Weinheim: Wiley-VCH. 2015.
2. Stankovich S, Dikin DA, Piner RD, Kohlhaas KA, Kleinhammes A, et al. Synthesis of graphene-based nanosheets via chemical reduction of exfoliated graphite oxide. Carbon. 2007; 45: 1558–1565.
3. Pei S, Zhao J, Du Z, Ren W, Cheng HN. Direct reduction of graphene oxide films into highlyconductive and flexible graphene films by hydrohalic acids. Carbon. 2010; 48:

4466–4474.
4. Chen W, Yan L. In situ self-assembly of mild chemical reduction graphene for three-dimensional architectures. Nanoscale. 2011; 3: 3132–3137.
5. Xu YL, Qi JM, Sun FF, Ma N. Carbocatalysis: Reduced graphene oxide-catalyzed Boc protection of hydroxyls and graphite oxide-catalyzed deprotection. Tetrahedron Lett. 2015; 56: 2744–2748.
6. Liu Y, Feng J. An attempt towards fabricating reduced graphene oxide composites with traditional polymer processing techniques by adding chemical reduction agents. Comp. Sci. Technol. 2017; 140: 16–22.
7. Dong L, Yang J, Chhowalla M, Loh KP. Synthesis and reduction of large sized graphene oxide sheets. Chem. Soc. Rev. 2017; 46: 7306–7316.
8. López-Diaz D, Merchán MD, Velázquez MM. The behavior of graphene oxide trapped at the air water interface. Adv. Colloid Int. Surf. 2020; 286: 102312.
9. Brodie BC. Researches on the atomic weight of graphite. Quart. J. Chem. Soc. Lond. 1860; 12: 261–268.
10. Staudenmaier L. Verfahren zur Darstellung der Graphitsäure (Method for the preparation of graphitic acid). Ber. Dtsch. Chem. Ges. 1898; 31: 1481–1487.
11. Hummers WS, Jr, Offeman RE. Preparation of graphitic oxide. J. Am. Chem. Soc. 1958; 80: 1339.
12. Kovtyukhova NI, Ollivier PJ, Martin BR, Mallouk TE, Chizhik SA, et al. Layer-by-layer assembly of ultrathin composite films from micron-sized graphite oxide sheets and polycations. Chem. Mater. 1999; 11: 771–778.
13. Marcano DC, Kosynkin DV, Berlin JM, Sinitskii A, Sun Z, et al. Improved synthesis of graphene oxide. ACS Nano. 2010; 4: 4806–4814.
14. Shao Y, Wang J, Engelhard M, Wang C, Lin Y. Facile and controllable electrochemical reduction of graphene oxide and its applications. J. Mater. Chem. 2010; 20: 743–748.
15. Harima Y, Setodoi S, Imae I, Komaguchi K, Ooyama Y, et al. Electrochemical reduction of graphene oxide in organic solvents. Electrochim. Acta. 2011; 56: 5363–5368.
16. Kötz R, Carlen M. Principles and applications of electrochemical capacitors. Electrochim. Acta. 2000; 45:

2483–2498.
17. Snook GA, Kao P, Best AS. Conducting-polymer-based supercapacitor devices and electrodes. J. Power Sources. 2011; 196: 1–12.
18. Jiang X, Setodoi S, Fukumoto S, Imae I, Komaguchi K, et al. An easy one-step electrosynthesis of graphene/polyaniline composites and electrochemical capacitor. Carbon. 2014; 67: 662–672.
19. Imae I, Fujimoto D, Zhang L, Harima Y. Electrosynthesis of a multilayer film stacked alternately by poly (3,4ethylenedioxythiophene) and reduced graphene oxide from aqueous solution. Electrochem. Commun. 2017; 81: 65–69.
20. Kobayashi T, Yoneyama H, Tamura H. Oxidative degradation pathway of polyaniline film electrodes. J. Electroanal. Chem. Int. Electrochem. 1984; 177: 293–297.
21. Kabumoto A, Shinozaki K, Watanabe K, Nishikawa N. Electrochemical degradation of polyaniline. Synth. Metals. 1988; 26: 349–355.
22. Shao Y, Yin G, Zhang J, Gao Y. Comparative investigation of the resistance to electrochemical oxidation ofcarbon black and carbon nanotubes in aqueous sulfuric acid solution. Electrochim. Acta. 2006; 51: 5853–5857.
23. Wang G, Yang J, Park J, Gou X, Wang B, et al. Facile synthesis and characterization of graphene nanosheets. J. Phys. Chem. C 2008; 112: 8192–8195.
24. Zhang Y, Jiang X, Zhang R, Sun P, Zhou Y. Influence of the nanostructure on charge transport in polyaniline films. Electrochim. Acta. 2011; 56: 3264–3269.
25. Zhang L, Goto T, Imae I, Sakurai Y, Harima Y. Thermoelectric properties of PEDOT films prepared by electrochemical polymerization. J. Polym. Sci. Part B Polym. Phys. 2017; 55: 524–531.
26. Imae I, Akazawa R, Harima Y. Seebeck coefficients of regioregular poly(3-hexylthiophene) correlated with doping levels. Phys. Chem. Chem. Phys. 2018; 20: 738–741.
27. Imae I, Koumoto T, Harima Y. Thermoelectric properties of polythiophenes partially substituted by ethylenedioxy groups. Polymer. 2018; 144: 43–50.

28. Imae I, Shi M, Ooyama Y, Harima Y. Seebeck coefficients of poly(3,4-ethylenedioxythiophene):poly(styrene sulfonate) correlated with oxidation levels. J. Phys. Chem. C 2019; 123: 4002–4006.
29. Imae I, Kataoka H, Harima Y. Flexible thermoelectric materials based on conducting polymers doped with silicone polymer electrolyte. Mol. Cryst. Liquid Cryst. 2019; 685: 100–106.
30. Imae I, Goto T, Ooyama Y, Harima Y. Thermoelectric properties of poly(3,4-thylenedioxythiophene) with fluorine-containing polyanion as dopant. Polymer. 2020; 199: 122538.
31. Imae I, Akazawa R, Ooyama Y, Harima Y. Investigation of organic thermoelectric materials using potential-step chronocoulometry: Effect of polymerization methods on thermoelectric properties of poly(3-hexylthiophene. J. Polym. Sci. 2020; 58: 3004–3008.
32. Zhang L, Harima Y, Imae I. Highly improved thermoelectric performances of PEDOT:PSS/SWCNT composites by solvent treatment. Org. Electron. 2017; 51: 304–307.
33. Tseluikin VN, Vasilenko EA. Electrodeposition and properties of composite coating based on nickel. Russ. J. Appl. Chem. 2011; 84: 1920–1922.
34. Jabbar A, Yasin G, Khan WQ, Anwar MY, Korai RM, et al. Electrochemical deposition of nickel graphene composite coatings: Effect of deposition temperature on its surface morphology and corrosion resistance. RSC Adv. 2017; 7: 31100–31109.
35. Gajewska-Midziałek A. Composite coatings with nickel matrix and graphene as dispersed phase. Pol. J. Chem. Technol. 2018; 20: 54–59.
36. Imae I, Nakamura Y, Komaguchi K, Ooyama Y, Ohshita J, et al. Development of a simple method for fabrication of transparent conductive films with high mechanical strength. Sci. Technol. Adv. Mater. 2012; 13: 045005.
37. Tsukada S, Nakanishi Y, Kai H, Ishimoto T, Okada K, et al. NIR-shielding films based on PEDOT-PSS/polysiloxane and polysilsesquioxane hybrid. J. Appl. Polym. Sci. 2020; 137: 48367.

38. Wright JD, Sommerdijk NAJM. Sol-Gel Materials: Chemistry and Applications. Singapore: Gordon and Breach Science Publishers. 2000.
39. Schubert U. Chemistry and fundamentals of the sol–gel process. In: Levy D, Zayat M, editors. The Sol-Gel Handbook. Weinheim: Wiley-VCH. 2015; 1: 3–27.
40. Imae I, Kawakami Y. Unique photoluminescence property of a novel perfectly carbazole-substituted POSS. J. Mater. Chem. 2005; 15: 4581–4583.
41. Imae I, Kawakami Y, Ooyama Y, Harima Y. Solid state photoluminescence property of a novel POSS-based material having carbazole. Macromol. Symp. 2007; 249–250: 50–55.
42. Kawakami Y, Lee DW, Pakjamsai C, Seino M, Takano A, et al. Formation and functionalization of aryl-substituted silsesquioxanes. ACS Symp. Ser. 2007; 954: 301–312.
43. Imae I, Takenaka Y, Tokita D, Ooyama Y, Komaguchi K, et al. Drastic enhancement of cycle lifetime of electrochromic devices using polysilsesquioxane as an anchoring agent. Chem. Lett. 2008; 37: 964–965.
44. Imae I, Takayama S, Tokita D, Ooyama Y, Komaguchi K, et al. Development of anchored oligothiophenes on substrates for the application to the tunable transparent conductive films. Polymer. 2009; 50: 6198–6201.
45. Imae I, Tokita D, Ooyama Y, Komaguchi K, Ohshita J, et al. Charge transport properties of polymer films comprising oligothiophene in silsesquioxane network. Polym. Chem. 2011; 2: 868–872.
46. Imae I, Tokita D, Ooyama Y, Komaguchi K, Ohshita J, et al. Oligothiophenes incorporated in a polysilsesquioxane network: Application to tunable transparent conductive films. J. Mater. Chem. 2012; 22: 16407–16415.
47. Imae I, Takayama S, Tokita D, Ooyama Y, Komaguchi K, et al. Synthesis of a novel family of polysilsesquioxanes having oligothiophenes with well-defined structures. Int. J. Polym. Sci. 2012; 2012: 484523.
48. Imae I, Oonishi T, Isaak IS, Yamamoto S, Harima Y. Facile fabrication of transparent conductive graphene/silica composite films with high mechanical strength. Synth. Met. 2017; 224: 33–35.

49. Imae I, Harima Y. Method for Producing Graphene/Silica Composite. Japanese Patent No. 6437825, 22 November 2018. ASTM D3363-92 Test Method for Film Hardness by Pencil Test. West Conshohocken: ASTM. 1992.
50. Ozawa K. Lithium Ion Rechargeable Batteries. Weinheim: Wiley-VCH. 2009.
51. Scrosati B, Abraham KM, Schalkwijk WV, Hassoun J. Lithium Batteries: Advanced Technologies and Applications. Hoboken: John Wiley & Sons. 2013.
52. Glaize C, Geniès SJ. Lithium Batteries and Other Electrochemical Storage Systems. Surrey: John Wiley & Sons. 2013.
53. Aifantis KE, Hackney SA, Kumar RV. High Energy Density Lithium Batteries: Materials, Engineering, Applications. Weinheim: Wiley-VCH. 2013.
54. Casimir A, Zhang H, Ogoke O, Amine JC, Lu J, et al. Silicon-based anodes for lithium-ion batteries: Effectiveness of materials synthesis and electrode preparation. Nano Energy. 2016; 27: 359–376.
55. Zuo X, Zhu J, Müller-Buschbaum P, Cheng YJ. Silicon based lithium-ion battery anodes: A chronicle perspective review. Nano Energy. 2017; 31: 113–143.
56. Zhu B, Wang X, Yao P, Li J, Zhu J. Towards high energy density lithium battery anodes: Silicon and lithium. Chem. Sci. 2019; 10: 7132–7148.
57. Zhao X, Lehto VP. Challenges and prospects of nanosized silicon anodes in lithium-ion batteries. Nanotechnology. 2021; 32: 042002.
58. Imae I, Yukinaga K, Kimura Y. Manufacturing Method of Graphene-Si Composite. Japanese Kokai Tokkyo Koho (Published Unexamined Patent Application) Publication No. 2020033244. 2020.
59. Rochow EG. Silicon and Silicones: About Stone-Age Tools, Antique Pottery, Modern Ceramics, Computers, Space Materials and How They All Got That Way. Berlin: Springer. 1987.
60. Entwistle J, Rennie A, Patwardhan S. A review of magnesiothermic reduction of silica to porous silicon for lithium-ion battery applications and beyond. J. Mater. Chem. A 2018; 6: 18344–18356.

Book Chapter

Copper Nitride: An Emerging Earth-Abundant Light Absorber for Next Generation Photovoltaic Technology

María Isabel Rodríguez-Tapiador[1,2]* and Susana Fernández[1]*

[1]Departamento de Energías Renovables, Centro de Investigaciones Energéticas, Medioambientales y Tecnológicas (CIEMAT), Spain
[2]Universidad Rey Juan Carlos, Área de Ciencia e Ingeniería de Materiales, Tulipán, Spain

***Corresponding Authors:** María Isabel Rodríguez-Tapiador, Departamento de Energías Renovables, Centro de Investigaciones Energéticas, Medioambientales y Tecnológicas (CIEMAT), Madrid 28040, Spain

Susana Fernández, Departamento de Energías Renovables, Centro de Investigaciones Energéticas, Medioambientales y Tecnológicas (CIEMAT), Madrid 28040, Spain

Published **October 10, 2023**

This Book Chapter is an excerpt of articles published by S Fernández, et al. at Coatings and Materials in June 2023 and February 2023 respectively. (Rodríguez-Tapiador, M.I.; Asensi, J.M.; Roldán, M.; Merino, J.; Bertomeu, J.; Fernández, S. Copper Nitride: A Versatile Semiconductor with Great Potential for Next-Generation Photovoltaics. Coatings 2023, 13, 1094. https://doi.org/10.3390/coatings13061094) (Rodríguez-Tapiador, M.I.; Merino, J.; Jawhari, T.; Muñoz-Rosas, A.L.; Bertomeu, J.; Fernández, S. Impact of the RF Power on the Copper Nitride Films Deposited in a Pure Nitrogen Environment for Applications as Eco-Friendly Solar Absorber. Materials 2023, 16, 1508. https://doi.org/10.3390/ma16041508)

How to cite this book chapter: María Isabel Rodríguez-Tapiador, Susana Fernández. Copper Nitride: An Emerging Earth-Abundant Light Absorber for Next Generation Photovoltaic Technology. In: Alessio Bosio, editor. Surfaces, Interfaces and Coatings Technology. Hyderabad, India: Vide Leaf. 2023.

Conflicts of Interest: The authors declare no conflict of interest.

Author Contributions: Conceptualization, M.I.R.-T. and S.F, methodology, M.I.R.-T. and S.F, software, M.I.R.-T; validation, M.I.R.-T, formal analysis, M.I.R.-T, investigation, M.I.R.-T. and S.F, resources, S.F, data curation, M.I.R.-T,; writing—original draft preparation, M.I.R.-T. and S.F, writing—review and editing, S.F, visualization, M.I.R.-T, supervision, S.F, project administration, S.F, funding acquisition, S.F. All authors have read and agreed to the published version of the manuscript.

Funding: This research was funded by MCIN/AEI/10.13039/501100011033, grant number PID2019-109215RB-C42. M.I.R.-T. also acknowledges partial funding from MEDIDA C17.I2G: CIEMAT. Nuevas tecnologías renovables híbridas, Ministerio de Ciencia e Innovación, Componente 17 “Reforma Institucional y Fortalecimiento de las Capacidades del Sistema Nacional de Ciencia e Innovación”. Medidas del plan de inversiones y reformas para la recuperación económica funded by the European Union—NextGenerationEU.

Acknowledgments: The authors would like to thank A. Soubrié from Centro de Microscopía Electrónica “Luis Bru” for her help and advice in the AFM measurements; Dr. M. Roldán, from National Fusion Laboratory (CIEMAT), for his support in the SEM/EDS measurements; J. Merino, from Technology Support

Center (CAT) of University Rey Juan Carlos, for his advice in XRD measurements; and Dr. J.M. Asensi and Dr. J. Bertomeu, from Departament de Física Aplicada of Universitat de Barcelona for his help and support in the PDS measurements.

Abstract

Copper nitride (Cu_3N) is attracting a great interest in several application fields, highlighting its use as a solar absorber material for flexible and lightweight thin film solar cells. This growing attention is because this metastable semiconductor is non-toxic, composed of earth-abundant elements, and its band gap energy can be easily tuneable according to manufacturing conditions and deposition methods used.

Due to such interest, this work presents a summary about the optimization of the Cu_3N with the aim of demonstrating its suitability to be considered, in a near future, as a good choice as a light absorber. The Cu_3N thin films were fabricated by reactive radio-frequency (RF) magnetron sputtering at room temperature (RT), at RF power (RFP) values ranged from 25 to 200 W, in two controlled environments (pure N_2 and a mixture of Ar/N_2 gases) at different total pressures, ranged from 1.0 to 5.0 Pa. All the thin films were deposited on both glass substrates and silicon wafers. In the first section, the study is focused on determining the best sputtering environment for the thin film fabrication; meanwhile, in the second one, the work shows the influence of the RFP on the thin film properties.

The structural, morphology and chemical properties were determined using X-ray Diffraction (XRD), Raman and Fourier Transform Infrared (FTIR) spectroscopies, Atomic Force Microscopy (AFM), and Scanning Electron Microscopy (SEM) equipped with Energy-dispersive X-ray spectroscopy (EDS) analysis. The results revealed that the Cu_3N films exhibited a polycrystalline structure, with the preferred orientation varying from (100) to (111) depending on the deposition conditions used. Raman spectroscopy confirmed the presence of Cu-N bonds in characteristic peaks observed in the 618–627 cm^{-1} range, while SEM and AFM images confirmed the presence of uniform and

smooth surface morphologies. The optical properties, investigated by UV-VIS-NIR and photothermal deflection (PDS) spectroscopies, revealed suitable band gap, refractive index, and Urbach energy values, indicating the interesting potential of Cu_3N as solar absorber for photovoltaic technology.

This study highlights the favourable properties of Cu_3N films deposited using the RF sputtering method, paving the way for their implementation in the next-generation of thin-film photovoltaic technologies. These findings contribute to the progress and optimisation of Cu_3N-based materials for efficient solar energy conversion. The values obtained demonstrated the capability of Cu_3N for solar energy conversion applications.

Introduction

Transition metal nitride materials, such as copper nitride (Cu_3N), are attracting increasing interest because of their outstanding optical, electrical and energy storage properties [1,2], which have allowed this material to be used in a wide variety of application fields, as pictured Figure 1. Among these application fields, it can be highlighted integrated circuits, photodetectors, optoelectronics, energy conversion applications and other related technologies [3–5].

This material is a metastable non-toxic semiconductor that is composed of earth-abundant elements, which makes it an eco-friendly material, and with a band gap energy that can be easily tuneable depending on both the manufacturing conditions and the deposition methods.

Cu_3N has been investigated as a potential material for energy storage applications, such as batteries and other energy storage devices, due to its thermal and chemical stability [6]. Recent works have reported that Cu_3N can be used as electrode material in lithium-ion batteries, exhibiting excellent performance in capacity and cycle stability [7]. Moreover, Cu_3N has demonstrated high electrochemical and catalytic activities for various important reactions, making it a promising material in this sector [8-10]. Nowadays, Cu_3N is attracting great interest as a new solar absorber material for flexible and lightweight thin

film solar cell technology [11], considering its possible incorporation into novel designs. This would be really useful to open new doors for a future generation of cost-effective photovoltaic devices.

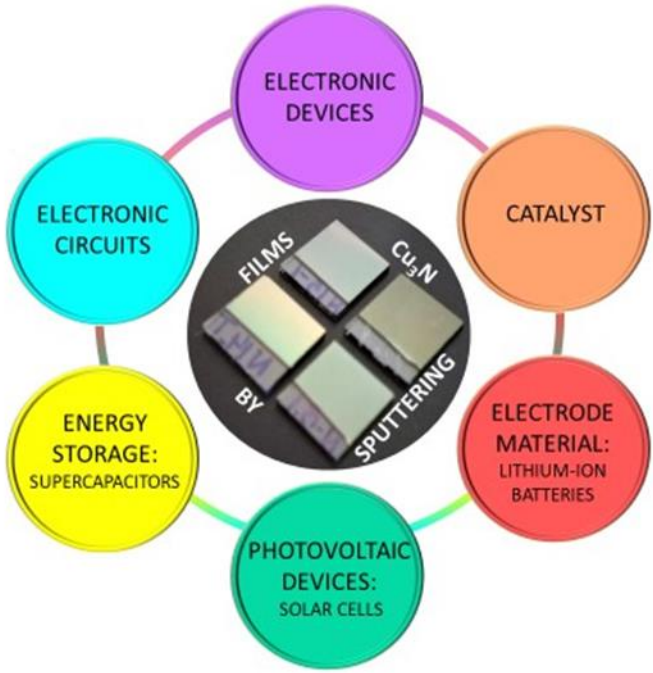

Figure 1: Several applications of Cu_3N thin films in different technological fields.

Regarding its crystal structure at room temperature (RT), Cu_3N is a binary compound that displays a cubic anti-ReO_3 crystal system (space group Pm3m) made up of nitrogen (N) atoms at the corners of the unit cell and the copper (Cu) atoms, located at the centre of the cubic edges (see Figure 2). Because of that, this crystal structure is extremely favourable to insert metal atoms at the interstitial body centre site (½,½,½) [12], a fact that could lead to different chemical interactions between Cu and N atoms, affecting the electronic structure of the material. Among the most common elements used to be inserted in that position, alkali metals (Li) [13], transition metals (Ti, Pb, Ni, Zn, Cr, Fe, Mn, Al and Sc) [14–16] and/or non-metals (H and O) can be found [17,18].

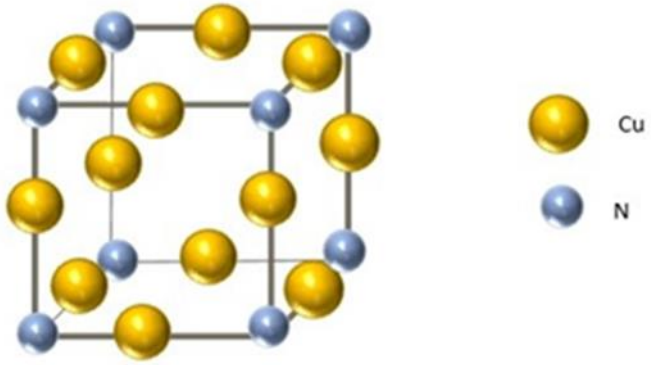

Figure 2: Picture of the anti-ReO_3 crystal structure of the Cu_3N compound. The copper atoms are represented by the yellow balls and the nitrogen, by the grey balls.

The bond angle of Cu-N-Cu reported is approximately 180 degrees, and the lattice parameter and density are 3.817 Å and 6.1 g/cm^3, respectively [19]. This material exhibits thermal stability up to close to 250°C [20]. Depending on its chemical composition, the Cu-N compound family can offer a wide variety of optoelectronic properties, i.e, the Cu-rich Cu_4N films that shows a metallic behaviour, the Cu-rich, N-rich and stoichiometric Cu_3N films that present a semiconducting performance [21]. Hence, it is clear that there is a strong relationship, between its chemical bonds and its electronic properties. This fact is mainly attributed to the hybridization effect between the Cu 3d-N 2p bands and the Cu (4s, 4p) conduction bands, which gives rise to the desired covalent bonding effect [22]. In addition, Cu_3N displays insulator-to-conductor transition behaviour, with electrical conductivity values ranging between 10^{-3}-10^{-2} Scm^{-1} [23]. Moreover, its electrical properties can be modified by doping them with metal or non-metal elements resulting in either p-type or n-type behaviour [24]. To switch between these electric characters, doping concentration, synthesis conditions, surface modifications, and interface engineering can be adjusted to alter charge carriers, crystal structure, defect density, and electrical properties. By controlling these factors, copper nitride's resistivity can be fine-tuned to achieve the desired conductivity

[25-27]. This approach can potentially enhance and broaden the scope of applications for Cu_3N films. Because of this, it is a promising candidate for future technological advancements, developments, and innovations in various fields, including electronic devices such as thin-film transistors (TFTs) and complementary metal-oxide-semiconductor (CMOS) circuits [28].

From the optical point of view, experimental studies have shown that this material presents indirect and direct band gap values, ranged from 1.17 to 1.69 eV and 1.72 to 2.38 eV, respectively [29,30]. Taking these values in mind, Cu_3N can be also considered a promising light absorber eco-friendly material, potential candidate to replace the silicon in solar cells. As it was explained before, its crystal structure and chemical composition can be optimised by controlling the parameters during its preparation, resulting in an optimised optical bandgap to reach a maximum photovoltaic voltage [23,31,32]. In fact, the development of p-type and n-type Cu_3N thin films and the adjustment of Cu/N chemical composition through reasonable control methods, can be easily performed to achieve materials and structures ready to be used in photovoltaic thanks to their excellent indirect bandgap values. This approach could significantly increase the conversion efficiency of solar energy [23,33].

There are several chemical and physical methods to prepare Cu_3N thin films. Among the chemical fabrication techniques, both chemical vapour deposition (CVD) and atomic layer deposition (ALD) are commonly used to fabricate it in a gas phase. These methods involve the use of precursors such as Cu(hfac)2 and [Cu(sBu-Me-amd)]2 [34] to determine its resulting phase composition, its morphology and to establish the growth rate [35,36]. Ammonolysis reactions can also be used to prepare bulk Cu_3N powder samples [37], as well as thin films [38]. In addition, recent works have shown that Cu_3N nanowire arrays can be synthesised by an ammonolysis reaction from copper (II) oxide precursors grown on copper surfaces deposited by electro or PVD in an ammonia solution [39, 40].

Regarding the physical ones, sputtering is one of the most popular physical vapour deposition (PVD) methods used to fabricate films of metals, alloys, oxides, and nitrides [41-44]. Since the pioneering work of Terada et al. (1989) on epitaxial growth of copper nitride [45], reactive RF magnetron sputtering has become the most widely used mode for the fabrication of the binary nitride. This method involves using a vacuum chamber in which a copper (Cu) target is bombarded with high-energy ions, causing Cu atoms to be ejected from the target, and finally deposited onto a substrate to form a thin film. By introducing nitrogen gas, with or without argon (Ar) gas, into the chamber during this process, Cu_3N can be grown on a substrate. This method's ease, simplicity, low cost, reproducibility and sustainability make it a very attractive choice for the growth of Cu_3N thin films. Previous studies have already reported that by modifying the bias voltage [46], the type of substrate [45], the working pressure [47], and the RF power [48], the film properties can be adjusted, allowing the variation in optical, electrical, structural, and morphological features to suit them to the desired ones depending on the application field.

Nowadays, the design of desired functional material properties by controlling deposition parameters is a key technological topic. For this reason, in this chapter, we show the impacts of (i) the process gas and its working pressure, and (ii) both the RFP and the gas pressure on the properties of Cu_3N thin film, prepared by reactive RF magnetron sputtering, with the purpose of adjusting them to the device requirements. In the first case, two different atmospheres were studied: an environment based on the mixture of N_2 and Ar gases, and another one, based on a pure N_2 gas. The working pressures were ranged from 1.0 to 5.0 Pa. Whereas in the second one, the choice of the gas atmosphere was an Ar-free environment using pressures of 3.5 and 5 Pa, and RFPs from 25 to 200 W. In all cases, the thin films were fabricated at RT, which means significant energy savings for the manufacturing process. The changes in crystalline nature, chemical composition, morphology, and electrical and optical properties of the thin films were examined in depth. The aim is to determine what sputtering deposition conditions give rise to a material with the most suitable optoelectronic properties and

with the highest absorption coefficient that allow it to be considered as a candidate for absorber material. Thanks to the possibility of such tuning, an ad-hoc material could be fabricated and used as a potential substitute absorber of silicon in PV devices.

Materials and Methods

Cu_3N Thin Films Fabrication with Physical Techniques

Cu_3N thin films were deposited on different substrates, <100> polished n-type floating zone crystalline silicon (c-Si) wafers and 1737F Corning glass (Corning Inc, New York, USA), by reactive RF magnetron sputtering in a commercial MVSystem LLC (Golden Colorado, USA) mono-chamber sputtering system (see Figure 3). The 3-inch diameter Cu target, with a purity of 99.99%, was from Lesker company (St. Leonards-on-Sea, East Sussex, UK). Before the sputtering deposition, the substrate surfaces were carefully treated: the surface of the silicon wafer was prepared by removing the native silicon dioxide layer using a solution of 1% hydrofluoric acid (HF) in a mixture of deionised water and isopropyl alcohol. The wafer was immersed in this solution for 5 min. On the other hand, the glass substrates were subjected to ultrasonic cleaning with ethanol and deionised water for 3 min. Then, they were submerged in isopropyl alcohol. Afterwards, all substrates were dried by blowing nitrogen gas over them.

The sputtering chamber was initially pumped to a base pressure of 2.6×10^{-5} Pa, and the distance between the target and substrate was set to 10 cm. A pre-sputtering process was performed for 5 minutes to clean the target surface. Then, the deposition was conducted for 30 minutes at RT and 50 W of RFP. The process gases used were N_2 (99.9999%) and Ar (99.9999%), with flow rates of 20 sccm and 10 sccm, respectively, controlled by mass flow controllers from MKS Instruments (MKS Instruments, Andover, MA, USA). The total gas pressure varied between 1.0 to 5.0 Pa by adjusting the position of the "butterfly" valve in the magnetron system.

Figure 3: Photography of the physical deposition system used for the Cu_3N thin film fabrication.

Characterization Techniques

The thickness of the films was measured using a Dektak 8 profilometer (Bruker, San José, CA, USA). A tip force of 68.67 µN and a scan size of 2000 µm were used. To determine the crystallinity of the Cu_3N films, XRD was performed using a commercial system (model PW3040/00 X'Pert MPD/MRD) (Malvern Panalytical Ltd, Malvern, UK) with Cu-kα radiation (λ=0.15406 nm). The 2θ range scanned was 10°-60°, with a step size of 0.01° and a time of 20 s per step. The topography was analysed with a multimode nanoscope AFM model IIIA (SPM; Veeco Digital In-strument) in tapping mode using a silicon nitride AFM tip (OTR8, Veeco). The surface roughness was quantified using mean root square (RMS) analysis, and the grain size from the two-dimensional (2D) AFM 1x1 μm^2 images, using the Gwyddion software (Gwyddion software, http://gwyddion.net/). The variation of surface morphology as a function of the gaseous environment used was determined using a JEOL JSM 7600F scanning microscope, equipped with a field emission Schottky electron gun (FESEM), in-lens secondary

electron detector and elemental analysis system for chemical composition EDS. Several surface regions were analysed at an acceleration voltage of 15 kV to determine quantitatively the amount of Cu and N in the thin film.

The molecular structure was determined using a dispersive spectrometer Confocal Raman microscope with capabilities for obtaining XYZ 3D confocal Raman images, equipped with a 532 nm laser, two diffraction gratings (600 and 1800 gr/nm), 3 objectives (5x, 75x and 100x), and option to obtain photocurrent mappings (Horiba LabRam soleil, Longjumeau Cedex, France). This measurement provides valuable information about the sample's vibrational modes and helps characterise its molecular structure. A Perkin Elmer Spectrum 100 FT-IR was also used to complement the information obtained from the Raman measurements. The spectra were measured in the transmittance mode in the wave number, which ranged between 400–4000 cm^{-1}. Electrical properties, such as sheet resistance and resistivity, were obtained with a commercial 4-point probe measurement system (Signatone, EEUU). It was estimated that the errors in the measured parameters were around 2%.

Finally, to determine the suitability of Cu_3N as a solar absorber, the optical transmittance spectra were measured at normal incidence using a UV/VIS/NIR Perkin Elmer Lambda 1050 spectrophotometer. The optical band gap energies (E_g) were calculated from these spectra for indirect and direct transitions. The optical properties of Cu_3N thin films deposited on glass were analysed by UV-VIS-NIR optical spectroscopy and PDS. The Transmittance (T_{opt}) and reflectance (R_{opt}) spectra were obtained with a PerkinElmer Lambda 950 UV-Vis-NIR spectrometer equipped with an integrating sphere. While the transverse PDS setup used to measure weaker absorption consists of a 100 W tungsten halogen lamp, PTI 01-0002 monochromator (spectral range of 400–2000 nm), and Thorlabs MC1000 optical chopper (4 Hz light modulation frequency). A Signal Recovery 7265 lock-in amplifier was connected to a Hamamatsu C10442-02 PSD position-sensitive detector to measure the deflection of a MC6320C 10 mW laser probe beam. Samples were put in a quartz cell filled with Fluorinert TM FC-

40. T_{opt} and R_{opt} measurements allow for determining the optical absorbance ($A_{opt} = 1 - T_{opt} - R_{opt}$) in the strong absorption region. In addition, the interference fringes observed in both spectra can be used to estimate the film thickness and their refractive index (n_{∞}). On the other hand, the PDS measurement is very effective for determining absorbance (APDS) in the weak (and very weak) absorption region. Thus, it is possible to determine the absorbance over a broad-spectrum range by combining optical measurements with PDS. The absorption coefficient (α) is obtained by a fit based on the calculation of absorbance using the transfer matrix method (TMM). These measurements allow the determination of the most suitable sputtering conditions to achieve a more efficient solar absorber material.

Results

In the following subsections, the quality of the Cu_3N films as well as the evaluation of the capability as solar absorber are presented. All the films in the study exhibited excellent physical stability and good adhesion to the respective substrate, even after exposure to ambient air; therefore, no evidence of cracking or peeling off was observed after the deposition process.

Impact of the Type of Process Gas and its Pressure on the Cu_3N Thin Film Properties

In this subsection, the results derived from the type of environment used in the growth process as well as its value are presented. Table 1 details the sputtering deposition conditions and the results from the film thickness measurement.

Table 1: Deposition conditions of Cu_3N films, varying N_2 flow ratios (0.7 and 1.0) and different total pressures.

Total pressure (Pa)	N_2 flux (sccm)	Ar flux (sccm)	N_2 flow ratio	Deposition rate (nm/s)	Thickness (nm)
1.0	20	10	0.7	0.053	95 ± 5
2.0	20	10	0.7	0.054	96±7
3.5	20	10	0.7	0.115	207±18
5.0	20	10	0.7	0.055	98±2
1.0	20	0	1.0	0.091	164±12
2.0	20	0	1.0	0.065	118±20
3.5	20	0	1.0	0.060	109±16
5.0	20	0	1.0	0.058	104±20

The sputtering deposition rate varied depending on the deposition conditions, obtaining close values to those reported by other authors [33,46]. These data reveal that the working pressure can be considered as an essential parameter in thin film fabrication: As the working pressure increased the number of impacts between the sputtered species and gas atoms rose within the process chamber. This effect led to a decrease in the deposition rate due to a reduction of the mean free path of the species of the plasma [20]. This trend was clearly observed for the samples deposited in the N_2 pure atmosphere, as shown in Figure 4. It is well known that there is an abrupt decrease in deposition rate due to the nitridation process that is more favored at high gas pressures [37]. At the same time, the sputtering ratio Cu/N began to be higher when the N_2 gas pressure decreased. This would favor the metallic regime and hence, obtain the gradual increase of the sputtering yield at low working pressures. In addition, this would indicate that, under such values of N_2 gas pressure, the target "poisoning" effect would not have started yet; hence, a gradual decrease of the deposition rate with the gas pressure was achieved.

On the other hand, it can be noticed that the films prepared under the N_2/Ar gas mixture environment presented lower deposition rates than those prepared in N_2 pure atmosphere. In the case where the sputtering process was carried out in a N_2/Ar atmosphere, the decrease in the deposition rate was not so evident, remaining almost constant at 0.055 nm/s (see Figure 4). This could be attributed to a poorer nitridation process occurring on the surface target due to the lower presence of N_2 in the gas mixture. It should be pointed out that a significant increase was observed in the deposition rate at 3.5 Pa, reaching a value of 0.115 nm/s. This was attributed to the change in the preferred crystal structure orientation, specifically to the (111) plane, a plane of lower density that would lead to a rougher film with a lower refractive index, as will be shown later [20].

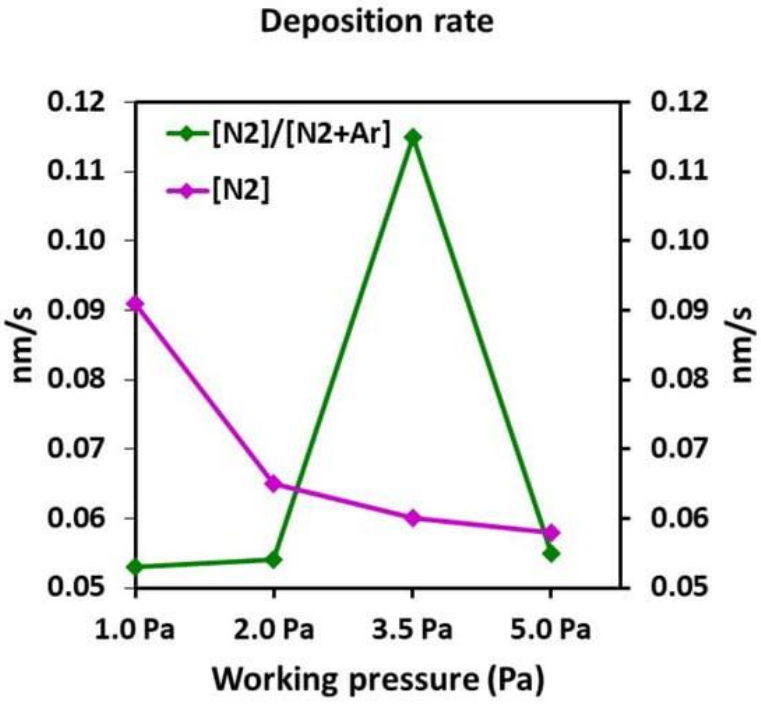

Figure 4: Deposition rate to different N_2 flow ratios of 0.7 and 1.0, and different total working pressure. Rest of the deposition conditions of Cu_3N films: RT and RFP =50W.

Figure 5 illustrates the XRD patterns of the Cu_3N deposited at the pressure range of 1.0–5.0 Pa in the different environments: the N_2 pure atmosphere (Figure 5a)) and the gas mixture of N_2/Ar (Figure 5b)). All of the films exhibited a polycrystalline nature, characterized by an anti-ReO_3 crystal structure, typical of cubic Cu_3N (card number 00-047-1088), and hence, dominated with the Cu_3N phase. Regardless of the working gas pressure used, the samples deposited in the N_2 pure atmosphere showed the (100) plane as the preferred orientation (Figure 5 a)).

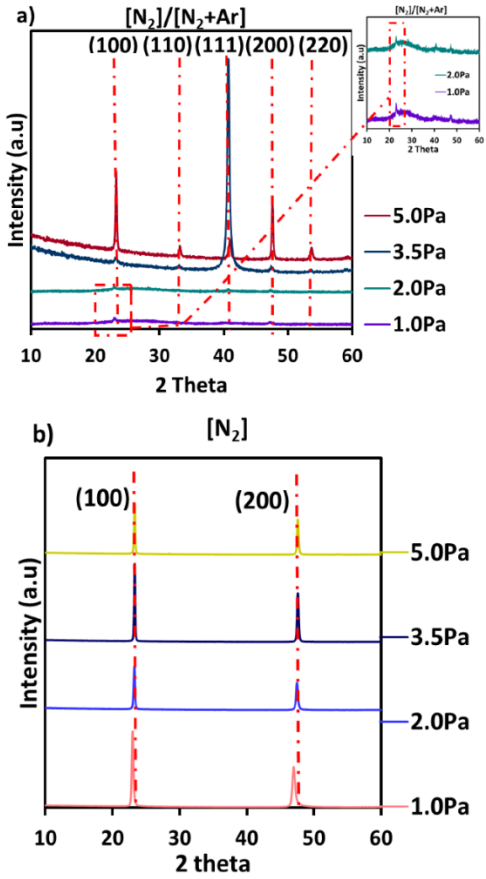

Figure 5: XRD spectra of Cu_3N films at different gas pressures and nitrogen flow ratios (a) $[N_2]/[N_2+ Ar]$ r = 0.7 and (b) $[N_2]$ r = 1.0.

On the other hand, the XRD patterns of the samples deposited in the N_2/Ar gas mixture (Figure 5b)) showed the appearance of (100), (110), (111), (200), and (220) diffraction peaks. In this case, and at the low gas pressures used, a weak (100) peak emerged over an amorphous hump, caused by the glass substrate. At the pressure of 3.5 Pa, the film showed a (111) preferred orientation, while the sample deposited at 5.0 Pa presented the (100) plane as the most intense peak. Other authors previously reported this transition in the preferred orientation. It could be attributed to the higher density of the N atoms that reached the substrate and reacted with the Cu atoms, leading to high-density

Cu-N bonds for the preferential growth along the (100) direction. This can indicate that the nitridation process was more effective when the gas pressure increased and, hence, the growth was favoured along the N-rich planes of Cu_3N [49].

On the other hand, the constant lattice a was determined by calculating the interplanar spacing using Bragg's law [50], expressed as the following Equation (1):

$$d(hkl) = \frac{a}{\sqrt{(h^2+k^2+l^2)}} \quad (1)$$

where d is the interplanar spacing, and h, k and l are the Miller indices. Furthermore, the grain size (τ) was determined using the Debye–Scherrer Equation (2) [51] as follows:

$$\tau = \frac{k\lambda}{\beta \cdot \cos\theta_B} \quad (2)$$

where k is a constant (0.9), λ is the X-ray wavelength (0.154 nm), θ is the diffraction angle, and β is the full width at half maximum (FWHM) of the predominant peak.

Table 2 and Table 3 summarize the FWHM of the main diffraction peak, the lattice constant, the predominant plane, the 2θ value, and the grain sizes derived from the XRD patterns of all the samples, depending on the N_2 flow ratio.

Table 2: XRD data extracted from the XRD spectra of the Cu_3N films fabricated on glass via RF magnetron sputtering in a mixed N_2/Ar atmosphere.

N_2 flow ratio: 0.7				
Working pressure (Pa)	1.0 *	2.0 *	3.5	5.0
2θ (°)	23.03	22.97	40.73	23.23
Predominant direction	-	-	(111)	(100)
Lattice parameter a (nm)	0.3858	0.3872	0.3813	0.3814
FWHM (°)	0.24	0.24	0.53	0.31
Grain size (nm)	34	34	16	27

* Poor crystalline quality. Preferential orientation is not easy to identify.

Table 3: XRD data extracted from the XRD spectra of the Cu_3N films fabricated on glass via RF magnetron sputtering in a pure N_2 atmosphere.

N_2 Flow ratio: 1.0				
Working pressure (Pa)	1.0	2.0	3.5	5.0
2θ (°)	22.77	23.17	23.29	23.28
Predominant direction	(100)	(100)	(100)	(100)
Lattice parameter a (nm)	0.3903	0.3840	0.3810	0.3813
FWHM (°)	0.20	0.15	0.21	0.21
Grain size (nm)	40	55	39	40

It can be observed that the FWHM values for the samples deposited in the N_2/Ar gas mixed atmosphere were superior to those for the samples deposited in the pure N_2 atmosphere, indicating an improved quality for these last films. The same trend was obtained for the grain size, reaching values as high as 55 nm when the samples were fabricated in a pure N_2 atmosphere. Concerning the lattice parameter, at the low pressures of 1.0 and 2.0 Pa, greater values than the theoretical one (0.3817 nm) were achieved, regardless of the N_2 flow ratio used. This fact could indicate a move away from the stoichiometry condition for such samples [52].

Figure 6 pictures the plan-view FESEM and AFM 1×1 μm^2 2D micrographs of the Cu_3N thin films deposited in N_2/Ar gas mixed atmosphere (Figure 6 a)) and pure N_2 environment (Figure 6b)). FESEM analysis revealed the presence of smooth and uniform surfaces, composed mainly of columnar grains, which are characteristic of the sputtering method [45,53,54]. These findings align with the results obtained from the AFM analysis [47,55,56], as shown in Figure 6.

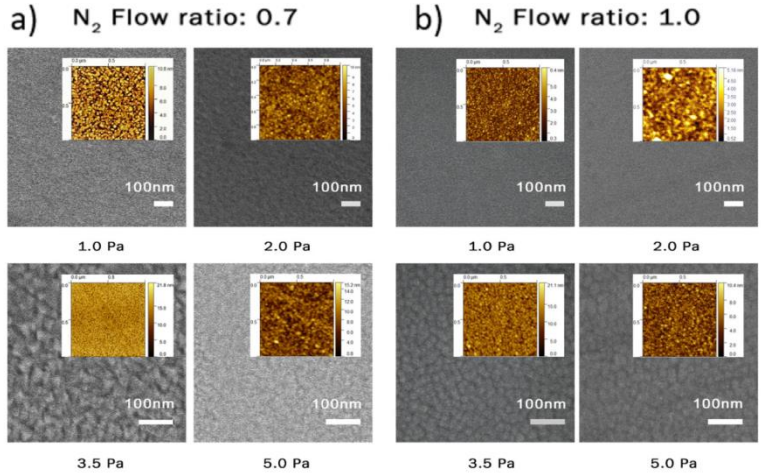

Figure 6: Top view FESEM images: Magn. 90,000×; 100 nm, and AFM 1×1 μm^2 2D of the samples deposited at flow nitrogen ratios of. (a) $[N_2]/[N_2+ Ar]$ r = 0.7 and (b) $[N_2]$ r = 1.0.

The grain size was influenced by both the environment and the total pressure applied during the deposition process. It was observed that lower working pressures resulted in larger grain sizes. This phenomenon was attributed to the formation of Cu_3N crystallites and the adhesion of tiny copper crystals, possibly caused by a decrease in N_2 density. These observations were supported by grain size calculations performed with the commercial software Gwyddion from AFM measurements (Tables 4 and 5), these results reinforced the values obtained using the Debye–Scherrer equation (see Tables 2 and 3).

Table 4 and Table 5 summarize the grain size and surface roughness RMS of the Cu_3N films, calculated from the 2D AFM micrographs, as function of the N_2 flow ratio.

Table 4: Surface roughness RMS and grain size calculated from AFM 1×1 μm^2 images of the Cu_3N films fabricated on glass, via reactive RF magnetron sputtering, in a mixed N_2/Ar atmosphere.

N_2 Flow ratio: 0.7				
Working pressure (Pa)	1.0	2.0	3.5	5.0
RMS (nm)	1.39± 0.15	1.26 ± 0.14	2.77 ± 0.23	1.77 ± 0.21
Grain size (nm)	19 ± 2	22 ± 3	17 ± 3	34 ± 3

Table 5: Surface roughness RMS and grain size calculated from AFM 1×1 μm^2 images of the Cu_3N films fabricated on glass via reactive magnetron sputtering in a pure N_2 atmosphere.

N_2 Flow ratio: 1.0				
Working pressure (Pa)	1.0	2.0	3.5	5.0
RMS (nm)	0.90 ± 0.15	1.15 ± 0.50	2.21 ± 0.27	1.34 ± 0.12
Grain size (nm)	19 ± 2	32 ± 2	33 ± 2	35 ± 2

Based on these results, it can be concluded that regardless of both the total working pressure and N_2 flow ratio used, the surfaces were very flat, with RMS values not exceeding of 3 nm. In this sense, it can be noticed that even though the RMS was very low, there was a difference between the films deposited using pure N_2 gas and those deposited in the N_2/Ar gas mixture, obtaining slightly smoother surfaces in the first case. On the other hand, the grain size varied depending on the process parameters: larger sizes as working pressure increased. Specifically, the larger grain sizes obtained for the films deposited at 1.0 Pa and 2.0 Pa in a mixture of N_2/Ar gases may be due to the formation of small agglomerates, due to the amorphous character seen in XRD. It should be pointed out that the grain size values estimated from XRD patterns were slightly higher than the obtained from AFM measurements. This can be explained because the first ones were an average value of a larger area analysed, while the second ones were calculated in a small area at a specific point.

The chemical composition of the samples was determined qualitatively using EDS data (Table 6). The analysis revealed a Cu/N ratio below three, indicating the non-stoichiometry of the

deposited material. Interestingly, an increased Cu/N ratio was observed at higher working pressures. This phenomenon was attributed to the increased energy of the nitrogen atoms at higher working pressures, enhancing the formation of bonds with the Cu ones. Moreover, all Cu_3N films exhibited the presence of trace amounts of oxygen. This observation may be associated with exposure to ambient oxygen, as observed in the Raman analysis but not detected in the XRD patterns.

Table 6: The EDS analysis provided insights into the qualitatively composition of the examined films.

Working pressure (Pa)	1.0	2.0	3.5	5.0
Cu/N ratio $[N_2]/[N_2+Ar]$ r= 0.7	1.79	2.08	2.10	2.17
Cu/N ratio $[N_2]$ r= 1.0	1.87	1.88	2.07	2.13

Figure 7 displays the Raman spectra of the Cu_3N films deposited at different working pressures and N_2 flow ratios of 0.7 (Figure 7a)) and 1.0 (Figure 7b)). Cu_3N has a crystal structure belonging to the Pm-3m space group where the unit cell contains one formula unit. As a result, no first-order Raman signal is expected for a perfect cubic Cu_3N. Although theoretical calculations suggest the absence of active Raman modes, the possibility of modes arising due to the breakdown of the selection rule cannot be ruled out. This is due to $Cu_xN_{(1-x)}$'s highly non-stoichiometric nature and the breakdown in crystal symmetry caused by defects in the structure. The prominent Raman peak around 619–627 cm^{-1} in Figure 7 corresponds to the stretching of the Cu-N bond, characteristic of Cu_3N [52, 55, 56]. A slight shift of that Raman peak was observed as the working pressure varied, while the Raman shift value tends to move to lower ones when using the N_2/Ar gas mixture compared to using the pure N_2 gas in the deposition process.

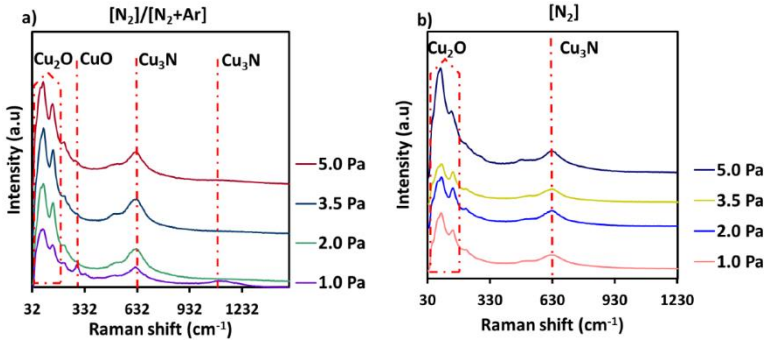

Figure 7: Raman spectra for Cu_3N films deposited at different pressures on glass and the nitrogen flow ratios of (a) $[N_2]/[N_2+Ar]$ r = 0.7 and (b) $[N_2]$ *r*= 1.0.

Furthermore, the Raman shifts of CuO_2 and CuO also appeared in the spectra at 94 cm^{-1}, 150 cm^{-1}, and 295 cm^{-1}, respectively. The samples prepared in the N_2/Ar gas mixture showed a higher presence of different copper oxides that may have formed on the film surface upon contact with atmospheric air and/or within the crystal structure. In order to analyse the Raman signal derived from the presence of these types of oxides, these measurements were complemented with the XRD data. As a result, it was confirmed that the characteristic 2θ peaks of CuO_2 and CuO at 36.5° and 35.5°, respectively [57], did not appear in any diffraction patterns, reinforcing the idea that the oxidation process would be happening due to environmental causes. However, the role of oxygen impurities cannot be ignored, as oxygen always remains an unintentional impurity in nitride-based materials [19]. Therefore, a more detailed theoretical analysis is required to interpret and assign the active Raman peak appropriately. Table 7 and Table 8 show the prepared samples' Raman shift values and the FWHM.

Table 7: Raman peak position and full width at half-maximum (FWHM) of the Cu_3N films deposited at different pressures on glass in a mixed N_2/Ar atmosphere.

N_2 Flow ratio: 0.7				
Working pressure (Pa)	1.0	2.0	3.5	5.0
FWHM (cm^{-1})	78.9 ± 2.8	76.8 ± 1.8	82.9 ± 3.4	68.1 ± 2.7
Peak position (cm^{-1})	618.0 ± 1.2	621.0 ± 0.4	619.0 ± 0.6	621.0 ± 0.6

Table 8: Raman peak position and full width at half-maximum (FWHM) of the Cu_3N films deposited at different pressures on glass in a pure N_2 atmosphere.

N_2 Flow ratio: 1.0				
Working pressure (Pa)	1.0	2.0	3.5	5.0
FWHM (cm^{-1})	82.9 ± 1.7	74.9 ± 2.0	68.0 ± 3.6	65.2 ± 1.3
Peak position (cm^{-1})	623.0 ± 0.3	625.0 ± 0.4	626.0 ± 0.5	627.0 ± 0.4

The position of the main peak and the FWHM were calculated by simulating via the OriginLab program (OriginPro 8, OriginLab Corporation, Northampton, MA, USA). As observed, the FWHM value decreased as the working pressure increased, suggesting that the lower the FWHM value, the lower the nitrogen concentration in the sample. There is an exception for the sample prepared in the gas mixture at 3.5 Pa, where the FWHM did not exhibit that tendency, attributed to its structural change to the (111) preferential plane revealed by its XRD pattern. However, this sample does not follow that trend. In summary, the results from XRD and Raman show that the films with superior structural quality were those prepared in the pure N_2 atmosphere and at pressures of 3.5 Pa and 5.0 Pa. Furthermore, these films exhibited a less variety of grain orientations, with a predominant (100) plane and the Raman shift values were closer to the formation of the theoretical bonding structure.

Optical properties were determined from transmittance and reflectance spectra, obtained using UV-Vis-NIR spectroscopy, and shown in Figure 8. The transmittance spectra revealed high transmittance in the NIR region (>700 nm), which gradually decreased in the VIS range (450–700 nm), reaching very low values in the UV range (300–400 nm).

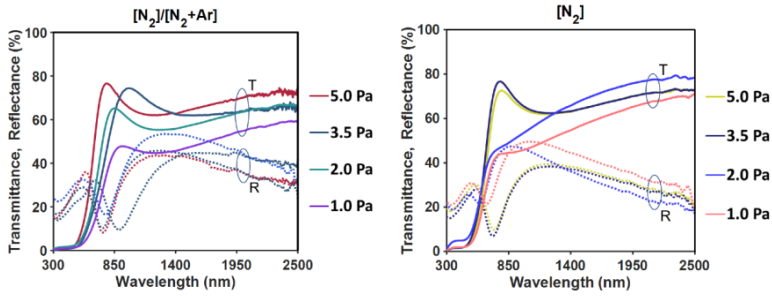

Figure 8: Transmittance and reflectance spectra of Cu_3N films deposited at different pressures and atmospheres.

For most samples, a minimum of transmittance was observed in the transparent region (>700 nm), associated with a maximum in the reflectance spectra. This is an effect of the interferences, produced within the films, from multiple reflections due to the samples' homogeneity and flatness. Thanks to that, the light can maintain its coherence in the internal reflections. It should be noted that the thin film thickness (<200 nm) limits the number of interferences observed in the spectra (in fact, the maximum of transmittance beyond 2500 nm, which should be about 92% according to the refractive index of the glass, is not observed in any case). However, the detection of the minimum of T_{opt} (or a maximum of R_{opt}) is sufficient to determine, by the fit of T_{opt} (or R_{opt}) in the transparent region, the thickness and refractive index (n_∞) of the films.

Table 9 summarizes the optical parameters obtained. It can be observed that the thickness obtained from the adjustments of the optical spectra were slightly superior to the measured with profilometry (see data in Table 1). This disparity in values could be attributed to how this value is determined: profilometry provides direct thickness measurements, whereas PDS relies on indirect one.

Table 9: Obtained values of the optical properties of Cu_3N films deposited on glass analysed via UV-VIS-NIR optical spectroscopy and PDS at different N_2 flow ratios.

N_2 Flow ratio: 0.7				
Working Pressure (Pa)	1.0	2.0	3.5	5.0
Optical fit parameters				
Film thickness (nm)	110	123	173	125
Refractive index n_∞	3.05	2.65	2.44	2.45
Band gap fit parameters				
Transition energy E_2 (eV)	2.18	2.27	2.38	2.46
Direct band gap E_g^d (eV)	1.91	2.02	2.09	2.22
Indirect band gap E_g^i (eV)	1.10	1.28	1.22	1.53
Urbach fit parameters				
Transition energy E_1 (eV)	1.55	1.69	1.64	1.90
Urbach energy E_U (meV)	261	233	243	205
Absorption coefficient at E_1 (cm^{-1})	6.3×10^4	5.1×10^4	4.0×10^4	5.2×10^4
N_2 flow ratio: 1.0				
Working Pressure (Pa)	1.0	2.0	3.5	5.0
Optical fit parameters				
Film thickness (nm)	109	65	126	123
Refractive index n_∞	2.85	2.79	2.43	2.43
Band gap fit parameters				
Transition energy E_2 (eV)	2.30	2.25	2.42	2.37
Direct band gap E_g^d (eV)	2.05	2.06	2.21	2.15
Indirect band gap E_g^i (eV)	1.30	1.48	1.55	1.49
Urbach fit parameters				
Transition energy E_1 (eV)	1.74	1.82	1.96	1.88
Urbach energy E_U (meV)	253	186	229	217
Absorption coefficient at E_1 (cm^{-1})	8.0×10^4	6.5×10^4	6.0×10^4	5.3×10^4

The refractive index values were in the range of 2.4–3.0, which are consistent with the values typically reported for Cu_3N [35]. It can be noticed that higher refractive index values were obtained for the samples deposited at lower total pressures, regardless of the atmosphere used in the film deposition. This phenomenon can be attributed to the higher Cu content in the samples deposited at lower working pressures. This assumption can also be supported by examining the XRD patterns and EDS analysis.
The absorption coefficient (α) in the strong absorption region can be calculated with reasonable accuracy from the absorbance A_{opt}, reflectance R_{opt} and thickness d of the film as follows:

$$\alpha \approx -\frac{1}{d} ln\left(1 - \frac{A_{opt}}{1-R_{opt}}\right) \quad (3)$$

In the weak absorption region, Equation (3) is unsuitable for estimating α because of multiple reflections. However, in this case, assuming that the refractive index is practically constant ($n \approx n_\infty$), it is possible to derive α into a wide range of the spectrum (from about 3.5 eV to 0.5 eV).

Figure 9a) shows the A_{opt} and A_{pds} spectra for the Cu_3N samples deposited at 5.0 Pa and N_2/Ar gas mixture. As can be seen, the determination of A_{opt} at wavelengths longer than 800 nm is unreliable (the error in the measurement of T_{opt} and R_{opt} is of the order of A_{opt}). However, the PDS measurement in this region allows us to obtain the absorbance, Apds. Figure 9b) shows the absorption coefficient spectrum obtained by combining the calculation according to Equation (3) for the intense absorption region ($\alpha > 1/d$) and the TMM model fit for the weak absorption region.

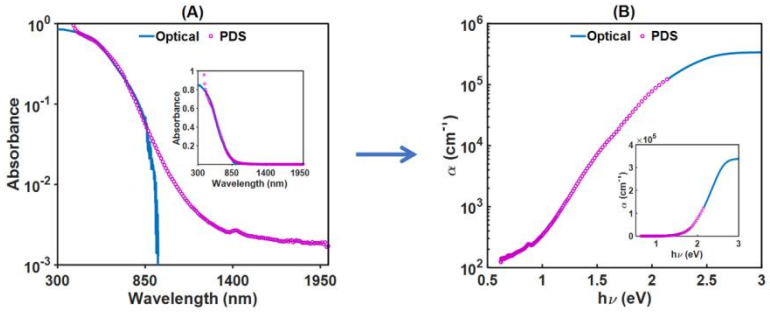

Figure 9: Absorbance obtained from optical measurements and PDS for the Cu_3N film deposited at 5.0 Pa pressure in pure N_2 atmosphere. In (a), the absorbance spectra are shown, and in (b), the absorption coefficient is calculated from the fit based on the transfer matrix method. The insets show the same graphs on a linear scale.

Once α was obtained, the indirect and direct optical band gaps of Cu_3N were calculated using the Tauc plot:

$$(\alpha h\nu)^{1/m} = B\left(h\nu - E_g\right) \tag{4}$$

where $h\nu$ is the photon energy, E_g is the band gap energy, B is a constant, and m is a factor, which depends on the nature of the electron transition (2 for indirectly allowed transitions and 1/2 for direct allowed transitions). Figure 10 shows the Tauc plots with $m = 2$ and $m = 1/2$ of the different Cu_3N samples deposited at different pressures in the two environments. The decrease in total pressure implies a decrease in both band gaps. This effect was more significant in the samples deposited on the N_2/Ar mixture.

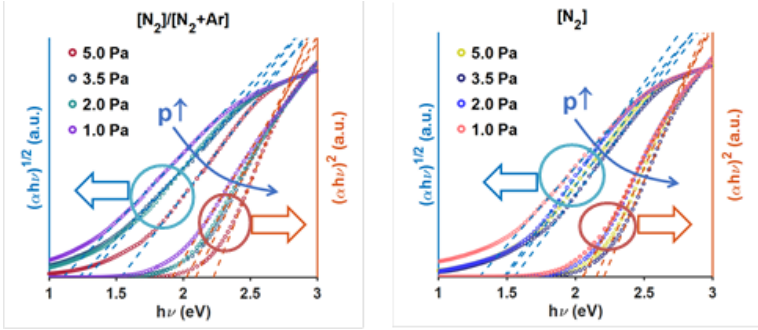

Figure 10: A plot of $(\alpha h\nu)^{1/2}$ and $(\alpha h\nu)^2$ vs photon energy (eV) for the Cu_3N films at different gas pressures and atmospheres. For easy comparison, normalised values of the absorption coefficient are considered.

Trying to further analysis, different energy ranges were distinguished according to the behaviour of α. Thus, the electronic transitions associated with the direct band gap took place for photon energies in a narrow range from 2.1 to 2.4 eV, as a lower limit, to approximately 2.5 eV, as an upper limit. On the other hand, the electronic transitions associated with the indirect gap cover a larger range extending about 0.5 eV toward lower photon energies. In addition, at lower energies, exponential Urbach absorption (α_U) can be observed, which is related to electronic transitions involving the band tails.

To accurately determine the direct and indirect band gaps, we performed a fine least-squares fit of the spectral dependence α according to the following model:

$$\text{At } h\nu < E_1: \quad \alpha_U(h\nu) = \alpha_0 \exp(h\nu/E_U) \tag{5}$$

where E_1 is the transition energy, E_U is the Urbach energy (the slope of the exponential tail), and α_0 is the absorption prefactor.

$$\text{At } h\nu > E_2: \quad \alpha_d(h\nu) = B_d\sqrt{h\nu - E_g^d} \tag{6}$$ (direct Tauc model)

E_2 is the transition energy, B_d is a constant, and E_g^d is the direct band gap energy.

At $E_1 < h\nu < E_2$: $\alpha_i(h\nu) = B_i\left(h\nu - E_g^i\right)^2$ (7) (indirect Tauc model)

B_i is a constant, and $E_g^i$is the indirect band gap energy. On the other hand, it can be observed that α must vary continuously and smoothly through the different regions. This implies imposing continuity conditions for α and its derivative at the two transition energies:

$$\begin{aligned} \alpha_i(E_1) &= \alpha_U(E_1) \quad \frac{d\alpha_i}{dE}(E_1) = \frac{d\alpha_U}{dE}\alpha_U(E_1) \\ \alpha_i(E_2) &= \alpha_d(E_2) \quad \frac{d\alpha_i}{dE}(E_2) = \frac{d\alpha_d}{dE}\alpha_U(E_2) \end{aligned} \tag{8}$$

which reduces the eight parameters of the model described by Equations (5)–(7) to only four independent ones. The graphs in Figure 11 depict the fit of the experimental data with the model described by Equations (5)–(8). A correlation between these energies and total pressure was observed, the effect measurable for the samples deposited in the mixed N_2/Ar atmosphere. The inset in Figure 10 pictures the fit in the sub-gap region at the edge of the indirect band gap at E_1, plotted in a logarithmic scale. This is the region where α is described by the Urbach exponential, related to the states in the band tails. The same was deduced from the Tauc plots in Figure 9, the samples with the narrowest band gap (direct and indirect) were obtained at the lowest total pressures. Therefore, by modifying the deposition parameters, such as total working pressure and N_2 flow ratio, the optical properties of Cu_3N thin films can be tailored to achieve desirable properties, making them promising for applications in optoelectronics and photonics.

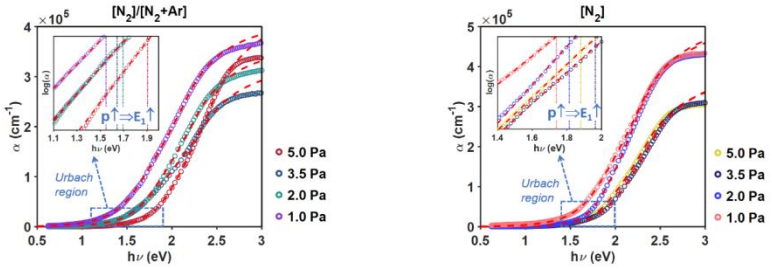

Figure 11: Absorption coefficient spectra of Cu_3N layers at different pressures and atmospheres. The red dashed lines show the fit according to the model equations described (5)–(8). In the logarithmic scale, the insets show the exponential tail of the Urbach region; note the effect of pressure on the transition energy E_1.

Finally, the shaded regions in Figure 12 represent the range of photon energies ($E_1<h\nu<E_2$) associated with the electronic transition by the indirect gap. In general, there is an increasing tendency for the band gap with the total pressure.

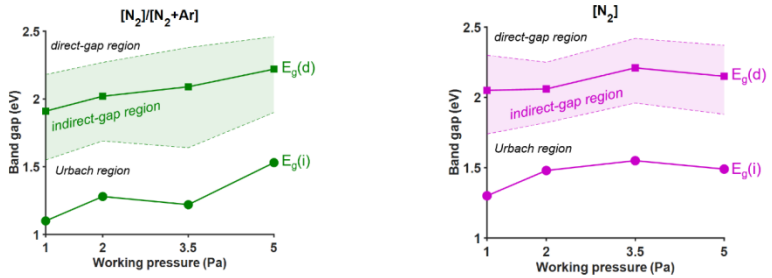

Figure 12: Evolution with a working pressure of the energies of the direct gap $E_g(d)$ and the indirect gap $E_g(i)$ for the two deposition atmospheres. The shaded region indicates the range of photon energies ($E_1<h\nu<E_2$) associated with electronic transitions according to the indirect gap: for higher energies ($h\nu>E_2$), the transitions are associated with the direct gap and for lower energies ($h\nu<E_1$) with the Urbach tail.

Regarding the Urbach energy (E_U), increasing values were obtained as the total pressure decreased. These values were superior to those of other semiconductor materials [34]. It is known that high E_U values indicated a higher internal defect density, while lower E_U ones suggest a lower internal defect density. Hence, the Urbach band tail is related to impurity

adsorption [17, 62]. According to the literature, Cu_3N shows E_U values ranging from 105 to 238 meV [34, 62] depending on the substrate temperature. Therefore, it can be concluded that the samples deposited at higher total pressures feature reasonable band gap energies and E_U values to be used in photovoltaic applications.

Impact of RF Power on the Cu_3N Films Deposited in a pure N_2 Environment

In this section, we present the relevance of RFP on the thin film properties and their optical properties to determine their suitability as solar energy conversion applications. Table 10 describes the sputtering deposition conditions used in this study.

Table 10: Sputtering deposition conditions used to fabricate the Cu_3N films at RT in N_2 pure atmosphere at different RF powers and gas pressures. Film thickness is also included.

Total gas pressure: 3.5 Pa						
RF Power (W)	25	50	75	100	150	200
Film thickness (nm)	45	85	95	100	175	215
Deposition time (s)	1800	1800	900	900	600	420
Total gas pressure: 5.0 Pa						
RF Power (W)	25	50	75	100	150	200
Film thickness (nm)	40	85	90	100	155	210
Deposition time (s)	1800	1800	900	900	600	420

Figure 13 shows the evolution of the deposition rate with the RFP values used. That parameter was calculated from the Cu_3N film thickness, data obtained with the profilometer and the deposition time (see data in Table 10). As expected, the deposition rate increased with the RFP. This tendency is due to the enhancement of the Cu atoms flow obtained as RFP rises at a constant gas pressure. It should be pointed out that a linear trend with two different slopes can be observed as function of the RFP. This indicates that two different growth regimes were taking place, which is expected to have an effect on the film properties. On the other hand, there was almost no difference between the rates measured at the two different gas pressures used in this work. This would mean that the modification of the number of species in the plasma, due to the increase in the gas pressure, was

not great enough to lead to a higher number of collisions between them. Therefore, at a higher pressure of 5.0 Pa, the sputtered Cu atoms still reached the substrate surface by losing a similar amount of energy as that lost at the lower pressure of 3.5 Pa due. Hence, no meaningful increase in collisions were taking place.

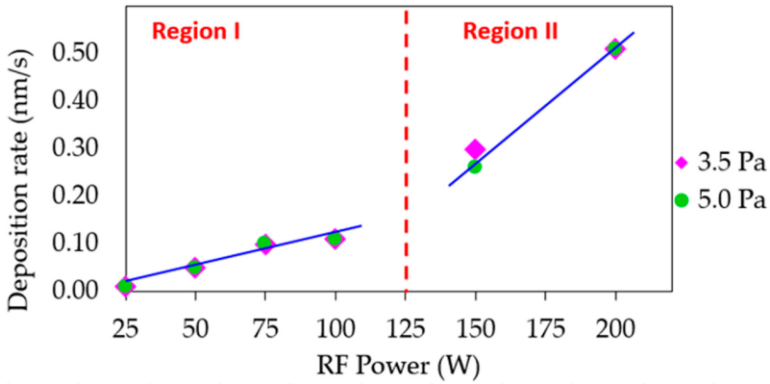

Figure 13: Deposition rate calculated for Cu_3N samples prepared at different RF power values and gas pressures. The line is a visual guide.

Figure 14 shows the XRD patterns of the Cu_3N films deposited on glass at the N_2 gas pressures of 3.5 and 5.0 Pa, and the RFP values of 25 W to 100 W (region I) (Figure 14 a)) and 150 and 200 W (region II) (Figure 14b)). All of them revealed a polycrystalline nature with an anti-ReO_3 structure, typical of the cubic Cu_3N (card n° 00-047-1088), and no evidence for Cu-phase and CuO_x formation were observed. A clear predominant (100) direction was obtained at RFP values up to 150 W. This preferential orientation, referring to the (100) and (200) diffraction planes, are related to an N-rich growth (Figure 14 a)) [63]. This N-rich growth mode was attributed to the low amount of Cu atoms within the plasma at such values of RFP. As the RFP increased, a transition to the dominant (111) plane was observed, which corresponded to a change in the growth mode towards a Cu-rich material (Figure 14 b)) [64-66]. On the other hand, an amorphous matrix around $2\theta \sim 20\text{-}30°$ was observed in samples from region II (samples deposited at the highest values of RFP, 150 and 200 W), being more evident in the case of the

thin film fabricated at 200 W and 5.0 Pa (see Figure 14 b)). In its XRD pattern, the (100), (111) and (200) diffraction planes could be intuited, where the (100) diffraction peak was the most intense. Its amorphous nature can be attributed to a saturation effect of the Cu_3N film that may take place when the gas pressure rises above a certain value, as other authors previously reported [67]. Taking the above results into account, all the Cu_3N films presented in this study would be showing a possible over-stoichiometry, where additional N atoms would be inserted into the lattice, probably as interstitials. This stage would be more evident as the gas pressure increased, due to an enhancement in the number of energetic and ionized N species within the plasma. In addition, the (100)-oriented material seemed to be preferred to the (111)-oriented one. As Z. Cao et al. previously reported [68], the Cu_3N material with the (111) plane as preferred orientation showed Cu atoms agglomerated at the grain boundaries forming nanocrystals. Hence, these samples could give rise to an uncertain factor in determining their optical and electrical properties. In fact, Y. Du et al. [69] also observed a sudden drop in the measured electrical resistivity of the (111)-oriented Cu_3N material due to an additional conductance mechanism, causing the percolation effect to come into play that was not beneficial if the material can be used as a solar absorber. Finally, it should be pointed out that the number of diffraction peaks that appeared in the patterns of the samples fabricated in the N_2 pure environment (see Figure 14) were less than those obtained in our previous work for the samples fabricated in a mixture of Ar and N_2 [48]. This fact can positively contribute to minimizing trapping centres due to the reduction of grain-orientation effects, indicative of a better crystal quality.

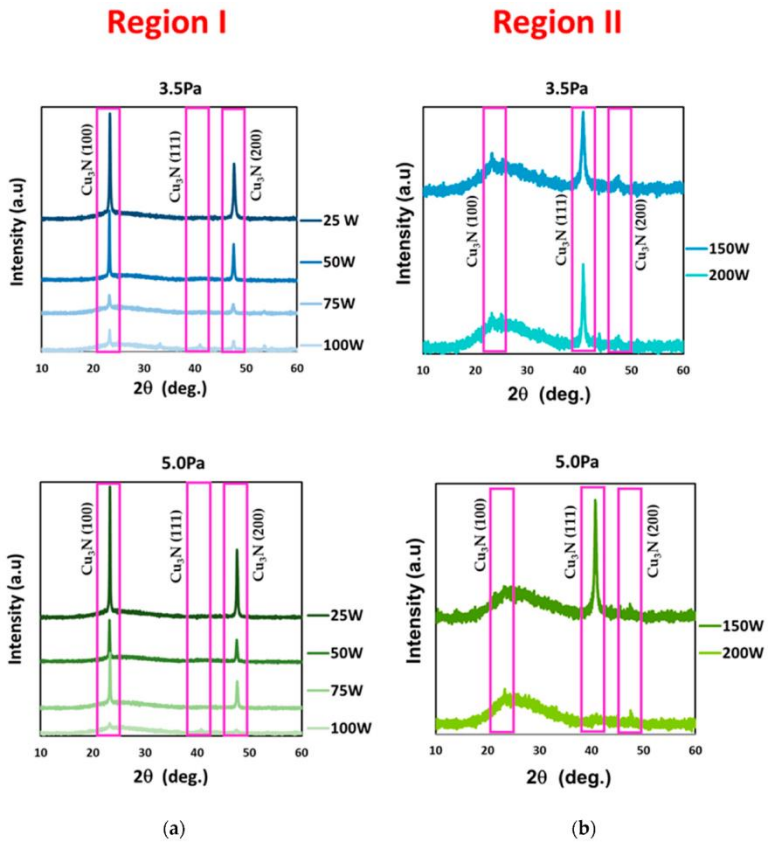

Figure 14: X-ray diffraction spectra of Cu_3N films deposited at gas pressures of 3.5 Pa and 5.0 Pa and the different RF power of (**a**) 25 W to 100 W (region I) and (**b**) 150 W and 250 W (region II).

The FWHM, the grain size and the lattice parameter, extracted from equations (1) and (2), are summarized in Table 11 as function of the RFP.

Table 11: Main XRD data extracted from the XRD spectra of the Cu_3N films fabricated on glass by reactive RF magnetron sputtering in pure N_2 atmosphere.

Total gas pressure: 3.5 Pa						
RF Power (W)	25	50	75	100	150	200
2θ (°)	23.327	23.248	23.203	23.272	40.746	40.748
Predominant direction	(100)	(100)	(100)	(100)	(111)	(111)
Lattice parameter a (nm)	0.3810	0.3826	0.3833	0.3822	0.3836	0.3833
FWHM (°)	0.048	0.138	0.1771	0.1181	0.1771	0.1771
Grain size (nm)	30	31	27	36	30	32
Total gas pressure: 5.0 Pa						
RF Power (W)	25	50	75	100	150	200
2θ (°)	23.297	23.214	23.343	23.251	40.794	23.293
Predominant direction	(100)	(100)	(100)	(100)	(111)	(100)
Lattice parameter a (nm)	0.3818	0.3832	0.3817	0.3826	0.3840	0.3814
FWHM (°)	0.1378	0.0787	0.048	0.2362	0.0787	0.6298
Grain size (nm)	27	36	33	38	27	3

According to data summarized in Table 11, the (100) diffraction peak shifted to lower values of angle 2θ (reference position 2θ = 23.285°) when RFP increased. On the other hand, the lattice parameters calculated were slightly higher than the theoretical one (0.38170 nm). These can demonstrate the over-stoichiometry of the film in terms of N content, as other authors have previously reported [66,70,71]. With regard to the mean grain size calculated, no clear trend was observed, being the values around 27–38 nm, similar to those found in the literature [66,72,73]. A higher grain size was obtained for the samples in region I and hence, a better crystal quality for these samples was expected. This was also confirmed by the FWHM values.

Figure 15 shows the evolution of the FWHM and the lattice parameter as function of the RFP. The region I corresponded to the samples with the (100) plane as preferred orientation, meanwhile the region II was represented by the samples with the (111) diffraction plane as the dominant one. In the region I, the samples deposited at 3.5 Pa showed a minimum FWHM value at 25 W, whereas this minimum shifted to 75 W in those deposited at 5.0 Pa, indicative of an improved structural quality. This displacement of the RFP could be explained by the slight difference in the number of N-species within the plasma at the working gas pressures used. As the RFP increased, a high number of Cu atoms with high energy and enhanced mobility reached the surface, resulting in an improved crystallinity. However, in the case of 3.5 Pa, fewer N atoms would be within the plasma and the number of Cu atoms would increase with the RFP, there being an excess of the latter. In addition, the probability of the formation of defects due to disorder at the Cu and N sites can be more elevated. This is what occurred at 3.5 Pa and RFP above 25 W, where a detriment in the crystal quality was observed as RFP increased. In contrast, at 5.0 Pa, the excess of Cu atoms began to be compensated by the increase of N species within the plasma to form the Cu-N bond. For this reason, the sample with improved crystallinity was deposited at a higher RFP of 75 W. On the other hand, no clear trend was observed for the samples of region II deposited at 3.5 Pa; but a huge increase in FWHM was obtained for the sample deposited at 5.0 Pa and 200 W, attributed to its amorphous character.

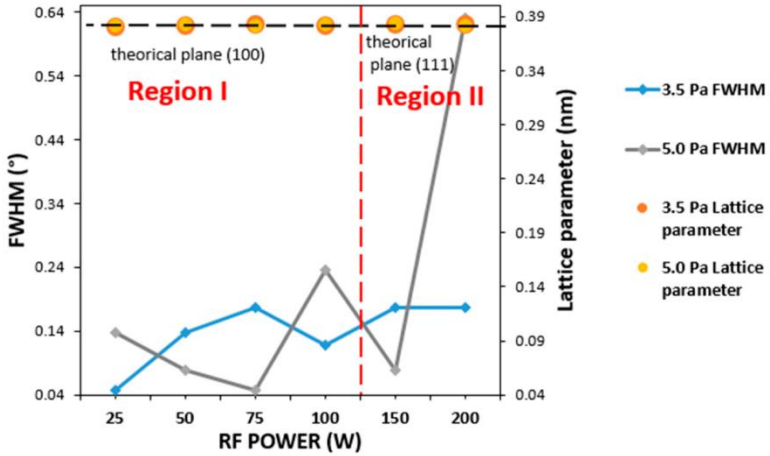

Figure 15: FWHM and lattice parameters extracted from the XRD spectra of Cu_3N films deposited at the gas pressures of 3.5 Pa and 5.0 Pa and the different RF powers of 25 W to 100 W (region I) and 150 W and 250 W (region II).

The surface morphology of the thin films was studied by AFM. Figure 16 depicts the 1×1 μm^2 2D micrographs of the Cu_3N films sputtered at 3.5 Pa (Figure 16 a)), and 5.0 Pa (Figure 16 b)). From these images, the grain size and the surface roughness of the Cu_3N films was obtained, summarized in Table 12. According to these results, all films presented smooth surfaces, with grain sizes not strongly influenced by both the RFP and the N_2 gas pressure. However, it was observed that the grain shapes were slightly different depending on the sputtering conditions used. In this sense, two types of morphologies were achieved, in agreement with the two regions previously defined: pyramidal-cone and nodular-like structures, attributed to both the transition observed in the crystalline orientation and the increase of the deposition rate with the RFP [74]. The films of region I (prepared at 3.5 Pa) showed a conical morphology attributed to the strong (100) preferred orientation [75]. Large polygonal grains with irregular shapes were separated by many voids. As the RFP increased, the grains began to be agglomerated to form a big grain, a fact attributed to their higher number of grain orientations. This agreed with the worsening observed in the crystallinity of such films by XRD, where, in region I, as the intensity of the (100) diffraction peak decreased with increasing

RFP, the (111) peak appeared more intense. On the other hand, the morphology of the samples in region II deposited at 150 and 200 W and presenting the (111) plane as the preferred orientation, showed nodular-like structures [50]. In the case of the samples prepared at 5.0 Pa, a similar trend was observed.

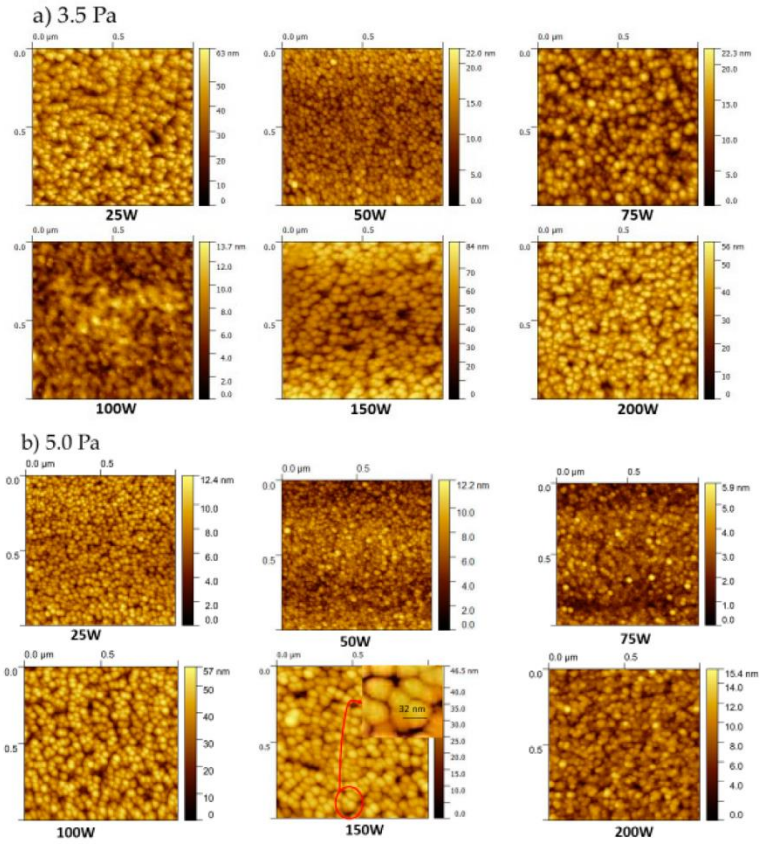

Figure 16: 1×1 μm^2 2D AFM micrographs of the sputtered Cu_3N films deposited at different RFP and at (**a**) 3.5 Pa and (**b**) 5.0 Pa of working pressure.

Table 12: Surface roughness RMS and grain size calculated from AFM 1×1 μm^2 images of the Cu_3N films fabricated on glass by RF magnetron sputtering in a pure nitrogen atmosphere.

Total gas pressure: 3.5 Pa						
RF Power (W)	25	50	75	100	150	200
RMS (nm)	8.50	2.20	3.25	1.77	8.81	7.40
Grain size (nm)	31	31	33	34	36	37
Total gas pressure: 5.0 Pa						
RF Power (W)	25	50	75	100	150	200
RMS (nm)	1.50	1.33	1.50	8.02	5.60	5.70
Grain size (nm)	29	35	33	34	32	33

Data in Table 12 revealed grain sizes ranged from 29 to 37 nm, close to the values obtained from the XRD measurements by using the Debye-Scherrer Equation (2). A different grain morphology was also observed in the (111)-oriented films. Such samples presented small agglomerated grains that led to visibly larger grains, as the corresponding AFM micrographs of pictured in Figure 16. This agglomeration may be attributed to nitrogen loss that is more favourable in the (111) planes. As it was showed before in the XRD patterns, this orientation was obtained as the RFP increased. Finally, a slight reduction in surface roughness RMS by increasing the gas pressure was observed at low RFP. As the working pressure increased, more N_2^+ ions struck the Cu target, leading to a higher energy of the ion bombardment on the substrate, and hence, more atom diffusion. Under this scenario, the density of the films was enhanced and the surfaces were flattened [47]. In addition, the samples deposited at 150 and 200 W (samples in region II) presented higher RMS values than the other samples, which is attributed to the observed changes in morphology and in the preferred orientation, as previously explained. The highest RMS values were shown by the samples deposited at 25 W and 3.5 Pa, and 100 W and 5.0 Pa, which were attributed to the presence of many deep voids on their surfaces. Therefore, the sputtering conditions that led to the smoothest surfaces together with an improved crystallinity were 75 W of RFP and 5.0 Pa of gas pressure.

Chemical composition was qualitatively determined from EDS data collected in Table 13. These data revealed a qualitative ratio of Cu to N lower than 3, confirming the non-stoichiometry of the fabricated material [46, 76]. From these measurements, the samples showed a slight increase in the Cu/N ratio as the RFP increased due to a higher number of Cu atoms; but no significant increase of N in the network was observed with rising gas pressure, as we argued when determining the deposition rate. The samples deposited at 200 W showed the highest presence of Cu in the lattice, as expected.

Table 13: Relative chemical composition of the Cu_3N films in the study, derived from EDS analysis.

RF Power (W)	25	50	75	100	200
Cu/N ratio (3.5 Pa)	1.85	1.94	1.70	2.15	2.33
Cu/N ratio (5.0 Pa)	1.87	2.06	2.36	2.48	2.87

Figure 17 shows the prominent Raman peak at around 613–644 cm^{-1}, characteristic of the formation of the Cu_3N, and which corresponded to the stretching of the Cu–N bond [59]. A Raman shift at a lower frequency was observed as the RFP rose, as well as when increasing the gas pressure. This shift would imply a deviation from the stoichiometric level, as already previously observed. That is, at a high RFP, the presence of Cu in the lattice is more evident. In addition, the shape of the main peak was asymmetric, which was clearer for samples in region II.

Table 14 summarizes the main parameters derived from Raman spectra. A slight shift to lower wavenumber was observed as the RFP increased, regardless of the gas pressure. This could be indicative of a deviation from the stoichiometric level that changed with the RFP parameter [73]. At 3.5 Pa, the main peak was widened as the RFP increased, in agreement with the data extracted from the XRD spectra (see Figure 14). The sample deposited at 25 W showed the narrowest main band, supporting the improved crystalline quality. At 5.0 Pa, the narrowest band was obtained at 75 W, as the XRD data also revealed.

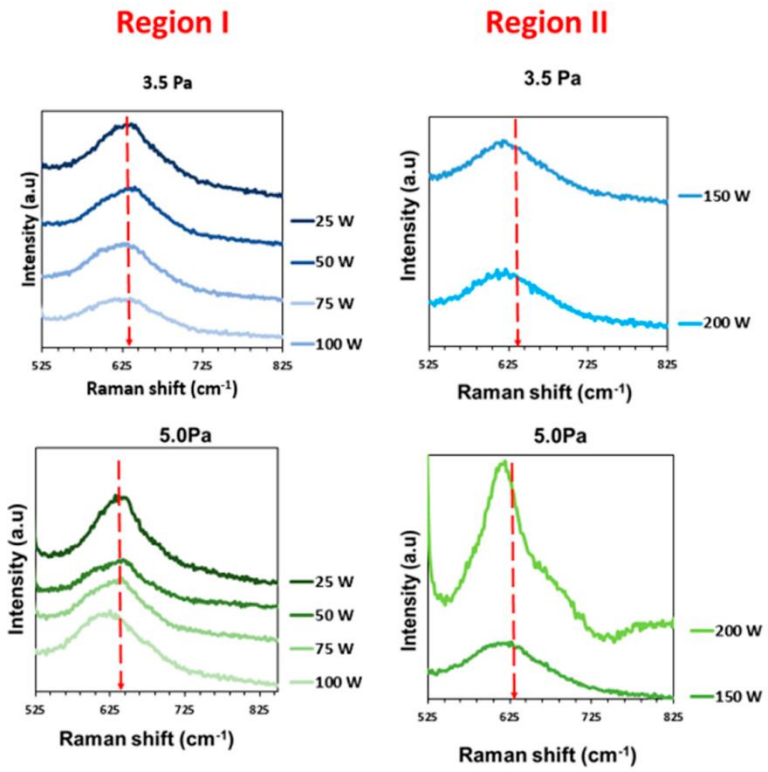

Figure 17: The Raman spectra of Cu_3N films prepared at different RFP and gas pressures of 3.5 Pa and 5.0 Pa. (25–100 W, region I, and 150–200 W, region II).

Table 14: Main parameters of Cu_3N films RFP derived from the Raman spectra.

RF Power (W)	25	50	75	100	150	200
FWHM (cm^{-1})(3.5 Pa)	66	82	105	99	121	114
Raman peak (cm^{-1})	632	637	621	621	616	616
FWHM (cm^{-1})(5.0 Pa)	108	120	107	118	108	77
Raman peak (cm^{-1})	644	640	627	620	616	616

Figure 18 depicts the FTIR spectra of the deposited Cu_3N films. In all cases, a prominent peak around 650 cm^{-1} was observed, which was attributed to the intrinsic vibration of the Cu–N lattice mode [79]. The peak at ≈ 2049 cm^{-1} corresponded to the azide (N_3) stretching vibration, confirming the formation of the Cu_3N

compound [80]. As the RFP increased, the intensity of the azide peak decreased, again related to the fact that, at a higher RFP, the Cu_3N film became more Cu-rich, fact previously observed from the EDS data (see Table 13). In addition, an asymmetric peak with a shoulder at longer wavenumbers was obtained at lower RFP values (region I), which was more evident in the samples deposited at 3.5 Pa. Both the asymmetry and the shoulder began to disappear as both the RFP and the amount of gas were increased. This disappearance could be attributed to a better formation of the Cu-N bond due to the higher presence of Cu atoms as the RFP increased. The asymmetry and the shoulder also appeared in the samples of region II deposited at 5.0 Pa. This effect could be due to a possible imperfection in the formation of the Cu-N bond because of a greater presence within the plasma of both Cu atoms and energetic and ionized N species.

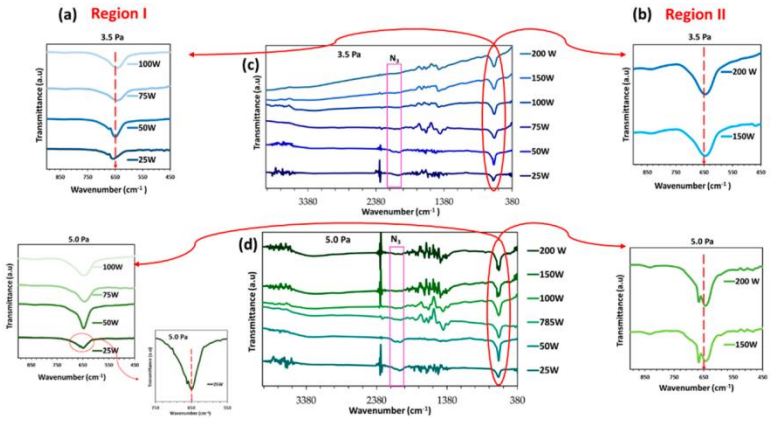

Figure 18: FTIR spectra of Cu_3N films prepared at different RF power and gas pressures of 3.5 Pa and 5.0 Pa for samples in (**a**) region I and (**b**) region II. The whole spectra of the samples are pictured in (**c**,**d**).

The resistivity of the films was measured with the four-point probe system. The results indicated a resistive material in all cases, where the values ranged from 0.2×10^3 to 5.4×10^3 Ω-cm. This electrical performance was consistent with the chemical data and non-stoichiometric structure, richer in N than in Cu, derived from EDS and XRD measurements, respectively. This could be indicative of a p-type Cu_3N material produced by the

Cu^+ vacancies due to the range of N_2 gas pressure used. These values were similar to those found in the literature for Cu_3N films deposited by the same technique [13,56,79,80].

Finally, the optical properties of the Cu_3N thin films deposited on glass substrates were analyzed by UV-VIS-NIR spectroscopy in the range of 300–2500 nm. Figure 19 shows the transmittance spectra of the deposited films. In general, the films showed a high transmittance in the NIR (>700 nm), that gradually decreased in the VIS range (450–700 nm) and turned to very low values in the UV range (300–400 nm). It was also observed that, as the RFP increased, the average transmittance value was drastically affected, obtaining values ranging from 60% to 45%. This could be explained because the films were increasingly richer in Cu as the RFP rose, as previously reported [26, 56]. A relationship between the increase in the thickness of the samples and the decrease in the percentage of transmittance was observed, which was attributed to the absorption of the material. In addition, the transmittance spectra showed a shift of the sharp absorption edge to lower energies as the RFP increased, as a result of the variation in the films composition and the structural change observed [81].

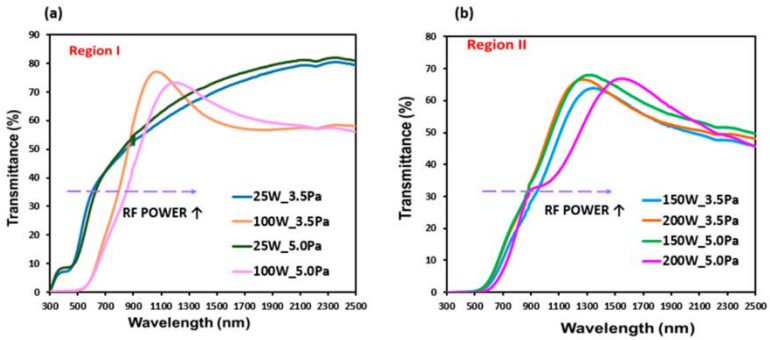

Figure 19: Transmittance spectra of Cu_3N films prepared at different RF powers and working pressures. (**a**) region I; (**b**) region II.

The optical band gap was calculated from the transmittance spectra, using the Tauc Plot Equation (4). The results are summarised in Table 15.

Table 15: Direct and indirect band gap energy values calculated for the Cu_3N films fabricated on glass in a pure N_2 atmosphere at different RF powers.

Total gas pressure: 3.5 Pa						
RF Power (W)	25	50	75	100	150	200
Eg (eV)						
Direct $(\alpha h\nu)^2$	2.30	2.10	2.05	2.05	2.00	1.90
Indirect $(\alpha h\nu)^{1/2}$	1.90	1.80	1.70	1.70	1.60	1.70
Total gas pressure: 5.0 Pa						
RF Power (W)	25	50	75	100	150	200
Eg (eV)						
Direct $(\alpha h\nu)^2$	2.10	2.18	2.05	2.01	2.05	2.10
Indirect $(\alpha h\nu)^{1/2}$	1.80	1.80	1.70	1.70	1.70	1.70

The samples deposited at the lowest pressure of 3.5 Pa presented E_g values for the direct transitions ranging from 1.90 to 2.30 eV, and for the indirect allowed transitions, from 1.6 to 1.9 eV (Figure 20). In the case of the samples deposited at 5.0 Pa, the direct band gap energy ranged from 2.01 to 2.18 eV, and the indirect ranged from 1.70 to 1.80 eV. Therefore, a non-clear tendency with the gas pressure could be established and attributed to the different sample thicknesses. On the other hand, as RF power increased, a narrow band gap energy was obtained. This could be attributed to the increase in the amount of unbonded Cu atoms with RF power that formed electronic transitions from the defect levels to the valence band [82].

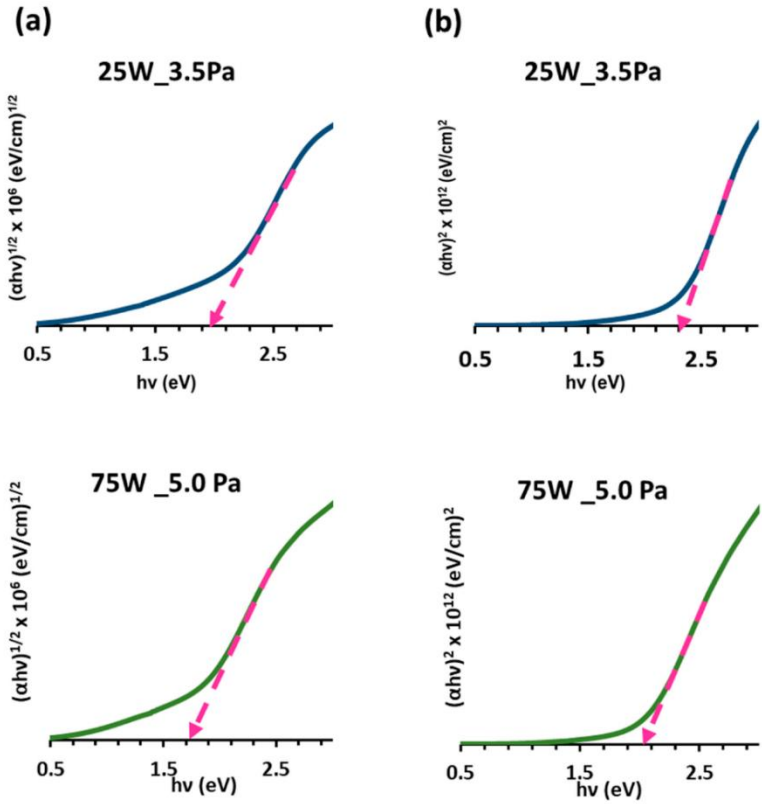

Figure 9: Plot of $(h\nu\alpha)^{1/2}$ and $(h\nu\alpha)^2$ vs $h\nu$ for the optimized samples deposited at (**a**) 25 W and 3.5 Pa, and (**b**) 75 W and 5.0 Pa.

Finally, the values obtained of the direct and indirect band gap could be considered as suitable and within the range required to use this material as a solar absorber.

Conclusions

This work presented how the main properties of Cu_3N thin films deposited by reactive RF magnetron sputtering can be tuned by changing the RFP and the gas pressure.

Firstly, it was evaluated which would be the most favourable environment to obtain Cu_3N thin films with the best performance. In this sense, a RPF of 50W and different N_2 flow

ratios of 0.7 and 1.0 were studied. The results provide valuable insights into these films' optical and structural properties. The analysis of the film structure revealed polycrystallinity, with a preferred growth orientation along the (100) plane when the N_2 flow ratio was r = 1.0. However, an amorphous matrix was observed for an N_2 flow ratio of 0.7 and low total working pressures up to 2.0 Pa; at working pressures above 2.0 Pa, a tendency for growth along the (111) plane was obtained. These findings and the lattice parameter values extracted from the XRD patterns suggest that the films deposited in the N_2/Ar gas mixture tend to have a higher concentration of Cu. Raman characterization confirmed the formation of Cu-N bonds. The presence of oxygen in the Raman spectra and in the EDS analysis was attributed to environmental factors due to no Cu-O bond-related structures were detected in the XRD patterns. The Cu/N ratio demonstrated an increase in the total working pressure. FESEM and AFM analysis showed a film morphology consisting of columnar grains with a very smooth and homogeneous surface. Through a combined analysis of the optical properties using conventional UV-VIS-NIR and PDS spectroscopies, the absorption coefficient over a wide range of photon energies (from 0.5 eV to 3.5 eV) was determined. A model with two band gaps, indirect and direct, and the Urbach exponential tail in the subgap region described the complete absorption coefficient spectrum. Depending on the deposition conditions, the energy of the direct gap varied in the range of 1.1 to 1.5 eV and the direct gap in the range of 1.9–2.2 eV. Generally, as the working pressure decreased, the energies of the two gaps tended to decrease, with the effect being most evident in the layers deposited in the N_2/Ar gas mixture environment. The samples deposited with the lowest working pressure (1 Pa) presented the highest value of the Urbach energy (>250 meV). The minimum value of the Urbach energy of 183 meV was found for the sample deposited at 2 Pa in a pure N_2 atmosphere. Finally, these films exhibited desirable structural, morphological, and optical properties, making them promising candidates as solar absorbers.

Secondly, the effect of the RFP on the thin film properties was also studied. The results revealed as the RFP increased, the deposition rate also rose, showing a linear trend but with two differentiated slopes depending on the power: 25–100 W (labeled as region I) and 150–200 W (labeled as region II). Such a division in regions was also observed in the rest of the film properties. From XRD, the films from region I showed a (100) preferred orientation, related to an N-rich material, that turned to the (111) preferred plane, related to a Cu-richer material, when the samples were deposited at 150 W of RFP (region II). No difference was observed at the two different N_2 pressures used. However, a better crystalline quality was obtained for the samples deposited at 25 W and 3.5 Pa, and at 75 W and 5.0 Pa. AFM measurements also revealed a different morphology in each case, changing from conical (region I) to nodular-like (region II) structures as the RF power increased. In addition, rougher surfaces were obtained for samples of region II, while the smoothest surfaces were achieved at 5.0 Pa. Regarding the chemical composition, qualitative EDS measurements indicated a gradual and slight increase in Cu as the RFP increased. FTIR and Raman confirmed the formation of Cu-N bonds, with a slight displacement to a lower wavenumber as the RFP rose. From the electrical point of view, all of the films showed high resistivity. The band gap energy were ranged from 1.60 to 1.90 eV for the indirect transitions, and 1.90 to 2.30 eV for the direct transitions; suitable ranges for the proposed application.

In summary, this work demonstrated: (i) the feasibility of magnetron sputtering to manufacture a stable Cu_3N material at RT; (ii) how the material properties strongly depend on deposition parameters; and (iii) which sputtering parameters lead to a material useful for use as a solar absorber (i.e, good structural quality, smooth surfaces, large grain size, stable Cu-N bond and adequate bandgap value). All these approaches have an enormous potential to open new horizons to achieve the definitive take-off thin film and flexible solar technologies by using ecofriendly and earth abundant materials.

References

1. Zakutayev A. Design of nitride semiconductors for solar energy conversion. J. Mater. Chem. A 2016; 4: 6742–6754.
2. Borsa DM, Boerma DO. Growth, structural and optical properties of Cu3N films. Surf. Sci. 2004; 548: 95–105.
3. Jiang A, Qi M, Xiao J. Preparation, structure, properties, and application of copper nitride (Cu_3N) thin films: A review. J. Mater. Sci. Technol. 2018; 34: 1467–1473.
4. Bouazza A. Deposition of Thin Films Materials used in Modern Photovoltaic Cells. Int. J. Thin Film Sci. Technol. 2022; 11: 313–320.
5. Paredes P, Rauwel E, Rauwel P. Surveying the Synthesis, Optical Properties and Photocatalytic Activity of Cu_3N Nanomaterials. Nanomaterials. 2022; 12: 2218.
6. Ścigała A, Szłyk E, Dobrzańska L, Gregory DH, Szczęsny R. From binary to multinary copper-based nitrides–Unlocking the potential of new applications. Coord. Chem. Rev. 2021; 436: 213791.
7. Chen W, Zhang H, Yang B, Li B, Li Z. Characterization of Cu_3N/CuO thin films derived from annealed Cu_3N for electrode application in Li-ion batteries. Thin Solid Films. 2019; 672: 157-164.
8. Wu H, Chen W. Copper nitride nanocubes: size-controlled synthesis and application as cathode catalyst in alkaline fuel cells. J Am Chem Soc. 2011; 133: 15236-15239.
9. Lee BS, Yi M, Chu SY, Lee JY, Kwon HR, et al. Copper nitride nanoparticles supported on a superparamagnetic mesoporous microsphere for toxic-free click chemistry. Chemical communications. 2010; 46: 3935-3937.
10. Yin Z, Yu C, Zhao Z, Guo X, Shen M, et al. Cu_3N Nanocubes for Selective Electrochemical Reduction of CO_2 to Ethylene. Nano Lett. 2019; 19: 8658-8663.
11. Tilemachou A, Zervos M, Othonos A, Pavloudis T, Kioseoglou J. p-Type Iodine-Doping of Cu_3N and Its Conversion to γ-CuI for the Fabrication of γ-CuI/Cu_3N pn Heterojunctions. Electron. Mater. 2022; 3: 15–26.
12. Li S, Hao J, Yu S. Mechanical properties of cubic Cu_3N and Cu_4N: A theoretical investigation. Vacuum. 2021; 191: 110366.

13. Yamada N, Maruya K, Yamaguchi Y, Cao X, Ninomiya Y. P-to n-type conversion and nonmetal–metal transition of lithium-inserted Cu_3N Films. Chem. Mater. 2015; 27: 8076–8083.
14. Giubileo F, Di Bartolomeo A, The role of contact resistance in graphene field-effect devices. Prog. Surf. Sci. 2017; 92: 143-175.
15. Jiang A, Xiao J, Gong C, Wang Z, Ma S. Structure and electrical transport properties of Pb-doped copper nitride (Cu_3N: Pb) films. Vacuum. 2019; 164: 53–57.
16. Gao L, Ji A, Zhang W, Cao Z. Insertion of Zn atoms into Cu_3N lattice: Structural distortion and modification of electronic properties. J. Cryst. Growth. 2011; 321: 157–161.
17. Borsa D, Grachev S, Presura C, Boerma D. Growth and properties of Cu 3 N films and Cu_3N/γ′-Fe_4N bilayers. Appl. Phys. Lett. 2002; 80: 1823–1825.
18. Miura A, Takei T, Kumada N. Synthesis of Cu_3N from CuO and $NaNH_2$. J. Asian Ceram. Soc. 2014; 2: 326–328.
19. Zervos M, Othonos A, Pavloudis T, Giaremis S, Kioseoglou J, et al. Impact of Oxygen on the Properties of Cu_3N and $Cu_{3-x}N_{1-x}O_x$. J. Phys. Chem. C 2021; 125: 3680–3688.
20. Zachwieja U, Jacobs H. Ammonothermalsynthese von kupfernitrid, Cu3N. Journal of the Less Common Metals. 1990; 161: 175-184.
21. Yue GH, Yan PX, Liu JZ, Wang MX, Li M, et al. Copper nitride thin film prepared by reactive radio-frequency magnetron sputtering. J. Appl. Phys. 2005; 98: 103506.
22. Hou Z. Effects of Cu, N, and Li intercalation on the structural stability and electronic structure of cubic Cu_3N. Solid State Sci. 2008; 10: 1651–1657.
23. Hahn U, Weber W. Electronic structure and chemical-bonding mechanism of Cu_3 N, Cui_3NPd, and related Cu (I) compounds. Phys. Rev. B 1996; 53: 12684.
24. Matsuzaki K, Okazaki T, Lee YS, Hosono H, Susaki T, Controlled bipolar doping in Cu3N (100) thin films. Appl. Phys. Lett. 2014; 105: 222102.
25. Matsuzaki K, Harada K, Kumagai Y, Koshiya S, Kimoto K, et al. High-Mobility p-Type and n-Type Copper Nitride Semiconductors by Direct Nitriding Synthesis and In Silicon Doping Design. Adv. Mater. 2018; 30: e1801968.

26. Chen SC, Huang SY, Sakalley S, Paliwal A, Chen YH, et al. Optoelectronic properties of Cu_3N thin films deposited by reactive magnetron sputtering and its diode rectification characteristics. J. Alloys Comp. 2019; 789: 428-434.
27. Mukhopadhyay AK, Momin MA, Roy A, Das SC, Majumdar A. Optical and Electronic Structural Properties of Cu_3N Thin Films: A First-Principles Study (LDA + U). ACS Omega. 2020; 5: 31918-31924.
28. Tanveer Z, Mahmood K, Ikram S, Ali A, Amin N. Modulation of thermoelectric properties of thermally evaporated copper nitride thin films by optimising the growth parameters. Phys. B: Condensed Matter. 2021; 605: 412712.
29. Matsuzaki K, Katase T, Kamiya T, Hosono H. Symmetric ambipolar thin-film transistors and high-gain CMOS-like inverters using environmentally friendly copper nitride. ACS Appl. Mater. & Interfaces. 2019; 11: 35132-35137.
30. Ghoohestani M, Karimipour M, Javdani Z. The effect of pressure on the physical properties of Cu_3N. Physica Scripta. 2014; 89: 035801.
31. Sahoo G, Meher S, Jain MK. Room temperature growth of high crystalline quality Cu_3N thin films by modified activated reactive evaporation. Mater. Sci. Eng.: B 2015; 191: 7-14.
32. Noh H, An H, Lee J, Song J, Hong HJ, et al. large enhancement of the photocurrent density in N-doped Cu_3N films through bandgap reduction. J. Korean Ceramic Soc. 2020; 57: 345-351.
33. Rodríguez-Tapiador MI, Merino J, Jawhari T, Muñoz-Rosas AL, Bertomeu J, et al. Power effect on the properties of copper nitride films as solar absorber deposited in pure nitrogen atmosphere. Appl. Res. 2023.
34. Birkett M, Savory CN, Fioretti AN, Thompson P, Muryn CA, et al. Atypically small temperature-dependence of the direct band gap in the metastable semiconductor copper nitride Cu_3N. Phys. Rev. B 2017; 95.
35. Rahmati A, Ghoohestani M, Badehian H, Baizaee M Ab. initio study of the structural, elastic, electronic and optical properties of Cu_3N. Mater. Res. 2014; 17: 303-310.
36. Fallberg A, Ottosson M, Carlsson JO. CVD of Copper (I) Nitride. Chemical Vapor Deposition. 2009.

37. Modin A, Kvashnina KO, Butorin SM, Werme L, Nordgren J, et al. Electronic structure of Cu(3)N films studied by soft x-ray spectroscopy. J. Phys. Condens. Matter. 2008; 20: 235212.
38. Paniconi G, Stoeva Z, Doberstein H, Smith RI, Gallagher BL, et al. Structural chemistry of Cu_3N powders obtained by ammonolysis reactions. Solid State Sciences. 2007; 9: 907-913.
39. Szczesny R, Hoang TKA, Dobrzanska L, Gregory DH. Solution/Ammonolysis Syntheses of Unsupported and Silica-Supported Copper(I) Nitride Nanostructures from Oxidic Precursors. Molecules. 2021; 26.
40. Scigala A, Szlyk E, Rerek T, Wisniewski M, Skowronski L, et al. Copper Nitride Nanowire Arrays-Comparison of Synthetic Approaches. Materials (Basel). 2021; 14.
41. Xia Y, Fan G, Chen K, Chen Y, He Z, et al. Preparation and anti-corrosion performances of grass-like microstructured superhydrophobic surface on copper via solution-immersion. Mater. Let. 2022; 323: 132482.
42. Kashin A, Ananikov V. A SEM study of nanosized metal films and metal nanoparticles obtained by magnetron sputtering. Russ. Chem. Bull. 2011; 60: 2602-2607.
43. Padamata SK, Yasinskiy A, Yanov V, Saevarsdottir G. Magnetron Sputtering High-Entropy Alloy Coatings: A Mini-Review. Metals. 2022; 12: 319.
44. Tadjine R, Houimi A, Alim MM, Oudini N. Oxygen flow rate effect on copper oxide thin films deposited by radio frequency magnetron sputtering. Thin Solid Films. 2022; 741: 139013.
45. Hu DC, Kuo DH, Kao JY, Chen CS, Tsao CC, et al. Fabrication of nitride films by co-sputtering of high-entropy alloys and tungsten. J. Aus Cer. Soc. 2022; 59: 105-115.
46. Islam MM, Georgiev DG, Stable stoichiometric copper nitride thin films via reactive sputtering. App. Phys. A 2022; 128: 579.
47. Kong Q, Ji L, Li H, Liu X, Wang Y, et al. Influence of substrate bias voltage on the microstructure and residual stress of CrN films deposited by medium frequency magnetron sputtering. Mater. Sci. Eng.: B 2011; 176: 850-854.

48. Figueira C, Rosario GD, Pugliese D, Rodríguez-Tapiador M, Fernández S. Effect of Argon on the Properties of Copper Nitride Fabricated by Magnetron Sputtering for the Next Generation of Solar Absorbers. Materials. 2022; 15: 8973.
49. Ghosh S, Singh F, Choudhary D, Avasthi D, Ganesan V, et al. Effect of substrate temperature on the physical properties of copper nitride films by rf reactive sputtering. Surf. Coat. Technol. 2001; 142: 1034-1039.
50. Dorranian D, Dejam L, Sari AH, Hojabri A. Structural and optical properties of copper nitride thin films in a reactive Ar/N_2 magnetron sputtering system. Eur. Phys. J. Appl. Phys. 2010; 50: 20503.
51. Hadian F, Rahmati A, Movla H, Khaksar M. Reactive DC magnetron sputter deposited copper nitride nano-crystalline thin films: Growth and characterization. Vacuum. 2012; 86: 1067–1072.
52. Xiao J, Li Y, Jiang A. Structure, optical property and thermal stability of copper nitride films prepared by reactive radio frequency magnetron sputtering. J. Mater. Sci. Technol. 2011; 27: 403–407.
53. Nowakowska-Langier K, Chodun R, Minikayev R, Okrasa S, Strzelecki GW, et al. Phase composition of copper nitride coatings examined by the use of X-ray diffraction and Raman spectroscopy. J. Mol. Struct. 2018; 1165: 79–83.
54. Alyousef HA, Hassan A, Zakaly HM. Exploring the Impact of Substrate Placement on Cu3N Thin Films as a Solar Cell Window Layer: Structural and Optical Attributes. Mater. Today Commun. 2023; 35: 106183.
55. Paredes P, Rauwel E, Rauwel P. Surveying the Synthesis, Optical Properties and Photocatalytic Activity of Cu3N Nanomaterials. Nanomaterials. 2022; 12: 2218.
56. Chen YH, Lee PI, Sakalley S, Wen CK, Cheng WC, et al. Enhanced Electrical Properties of Copper Nitride Films Deposited via High Power Impulse Magnetron Sputtering. Nanomaterials. 2022; 12: 2814.
57. Sanjana T, Sunil MA, Shaik H, Kumar KN. Studies on DC sputtered cuprous oxide thin films for solar cell absorber 655 layers. Mater. Chem. Phys. 2022; 281: 125922.
58. Kumar K, Kumar A, Devi S, Tyagi S, Kaur D. Relevant photovoltaic effect in N-doped CQDs/MoS2 (0D/2D)

quantum dimensional heterostructure. Ceram. Int. 2022; 48: 14107–14116.
59. Fallberg A, Ottosson M, Carlsson JO. Phase stability and oxygen doping in the Cu–N–O system. J. Cryst. Growth. 2010; 312: 5.
60. Wilczopolska M, Nowakowska-Langier K, Okrasa S, Skowronski L, Minikayev R, et al. Synthesis of copper nitride layers by the pulsed magnetron sputtering method carried out under various operating conditions. Materials. 2021; 14: 2694.
61. Rahmati A, Ghoohestani M, Badehian H, Baizaee MA. initio study of the structural, elastic, electronic and optical properties of Cu_3N. Mater. Res. 2014; 17: 303–310.
62. Xiao J, Qi M, Gong C, Wang Z, Jiang A, et al. Crystal structure and optical properties of silver-doped copper nitride films (Cu_3N: Ag) prepared by magnetron sputtering. J. Phys. D Appl. Phys. 2018; 51: 55305.
63. Wang J, Chen J, Yuan X, Wu Z, Miao B, et al. Copper nitride (Cu3N) thin films deposited by RF magnetron sputtering. J. Cryst. Growth. 2006; 286: 407–412.
64. Nowakowska-Langier K, Chodun R, Minikayev R, Okrasa S, Strzelecki GW, et al. Phase composition of copper nitride coatings examined by the use of X-ray diffraction and Raman spectroscopy. J. Mol. Struct. 2018; 1165: 79–83.
65. Yuan X, Yan P, Liu J. Preparation and characterization of copper nitride films at various nitrogen contents by reactive radio-frequency magnetron sputtering. Mater. Lett. 2006; 60: 1809–1812.
66. Meymian MRZ, Heravi AD, Mehr AK. Influence of bias voltage on optical and structural characteristics of Cu3N films deposited by reactive RF magnetron sputtering in a pure nitrogen atmosphere. Mater. Sci. Semicond. Process. 2020; 112: 104995.
67. Pierson J. Influence of bias voltage on copper nitride films deposited by reactive sputtering. Surf. Eng. 2003; 19: 67–69.
68. Cao Z. Thin Film Growth for Thermally Unstable Noble-Metal Nitrides by Reactive Magnetron Sputtering. In Thin Film Growth. Amsterdam: Elsevier. 2011; 185–210.

69. Du Y, Ji A, Ma L, Wang Y, Cao Z. Electrical conductivity and photoreflectance of nanocrystalline copper nitride thin films deposited at low temperature. J. Cryst. Growth. 2005; 280: 490–494.
70. Sakalley S, Saravanan A, Cheng WC, Chen SC, Sun H, et al. High power impulse magnetron sputtering growth processes for copper nitride thin film and its highly enhanced UV—Visible photodetection properties. J. Alloys Compd. 2022; 896: 162924.
71. Gordillo N, Gonzalez-Arrabal R, Alvarez-Herrero A, Agullo-Lopez F. Free-carrier contribution to the optical response of N-rich Cu_3N thin films. J. Phys. D: Appl. Phys. 2009; 42: 165101.
72. Sahoo G, Meher S, Jain MK. Room temperature growth of high crystalline quality Cu_3N thin films by modified activated reactive evaporation. Mater. Sci. Eng. B 2015; 191: 7–14.
73. Okrasa S, Wilczopolska M, Strzelecki G, Nowakowska-Langier K, Chodun R, et al. The influence of thermal stability on the properties of Cu_3N layers synthesized by pulsed magnetron sputtering method. Thin Solid Film. 2021; 735: 138889.
74. Park H, Seo H, Kim SE. Anti-oxidant copper layer by remote mode N2 plasma for low temperature copper–copper bonding. Sci. Rep. 2020; 10: 21720.
75. Ścigała A, Szłyk E, Dobrzańska L, Gregory DH, Szczęsny R. From binary to multinary copper-based nitrides–Unlocking the potential of new applications. Coord. Chem. Rev. 2021; 436: 213791.
76. Xiao J, Qi M, Cheng Y, Jiang A, Zeng Y, et al. Influences of nitrogen partial pressure on the optical properties of copper nitride films. RSC Adv. 2016; 6: 40895–40899.
77. Yu W, Zhao J, Jin C. Simultaneous softening of Cu_3N phonon modes along the T 2 line under pressure: A first-principles calculation. Phys. Rev. B 2005; 72: 214116.
78. Singh K. Magnetic and spectroscopic studies on cupric azide. Trans. Faraday Soc. 1971; 67: 2436–2444.
79. Fioretti AN, Schwartz CP, Vinson J, Nordlund D, Prendergast D, et al. Understanding and control of bipolar

self-doping in copper nitride. J. Appl. Phys. 2016; 119: 181508.
80. Yuan XM, Li HJ, Wei Y, Zhang Q. Copper Nitride Films Prepared by Reactive Radio-Frequency Magnetron Sputtering. Adv. Mater. Res. 2012; 374–377: 1515–1518.
81. Khalaf MK, Saud N, Muhammed MS. Plasma Diagnostics and Characterizations of Reactive Magnetron Sputtered Copper Nitride Thin Films. In IOP Conference Series: Materials Science and Engineering. Bristol: IOP Publishing. 2020; 072029.
82. Tian X, Tang H, Luo J, Nan H, Shu T, et al. High-Performance Core–Shell Catalyst with Nitride Nanoparticles as a Core: Well-Defined Titanium Copper Nitride Coated with an Atomic Pt Layer for the Oxygen Reduction Reaction. ACS Catal. 2017; 7: 3810–3817.

Book Chapter

Development of Si-Based Anodes for All-Solid-State Li-Ion Batteries

Xuyang Zhao[1,2,3], Yunpeng Rong[1,2,3], Yi Duan[1,2,3], Yanlong Wu[1,2,3], Deyu He[1,2,3], Xiaopeng Qi[1,2,3]* and Jiantao Wang[1,2,3]*

[1]National Power Battery Innovation Center, GRINM Group Corporation Limited, Beijing 100088, China
[2]China Automotive Battery Research Institute Co., Ltd., Beijing 101407, China
[3]General Research Institute for Nonferrous Metals, Beijing 100088, China

***Corresponding Authors:** Xiaopeng Qi, National Power Battery Innovation Center, GRINM Group Corporation Limited, Beijing 100088, China

Jiantao Wang, National Power Battery Innovation Center, GRINM Group Corporation Limited, Beijing 100088, China

Published **September 12, 2024**

This Book Chapter is a republication of an article published by Xiaopeng Qi, et al. at Coatings in May 2024. (Zhao, X.; Rong, Y.; Duan, Y.; Wu, Y.; He, D.; Qi, X.; Wang, J. Development of Si-Based Anodes for All-Solid-State Li-Ion Batteries. Coatings 2024, 14, 608. https://doi.org/10.3390/coatings14050608)

How to cite this book chapter: Xuyang Zhao, Yunpeng Rong, Yi Duan, Yanlong Wu, Deyu He, Xiaopeng Qi, Jiantao Wang. Development of Si-Based Anodes for All-Solid-State Li-Ion Batteries. In: Alessio Bosio, editor. Surfaces, Interfaces, and Coatings Technology. Hyderabad, India: Vide Leaf. 2024.

Funding: This work was supported by the National Natural Science Foundation of China (U21A2080), Beijing Natural Science Foundation (JQ22028), Jilin Province Science and Technology Major Project (20210301021GX), National Key Research and Development Program of China (2022YFE0202400), New Energy Vehicle Power Battery Life Cycle Testing and Verification Public Service Platform Project (2022-235-224).

Conflicts of Interest: The authors declare no conflicts of interest.

Abstract

All-solid-state Li-ion batteries (ASSBs) promise higher safety and energy density than conventional liquid electrolyte-based Li-ion batteries (LIBs). Silicon (Si) is considered one of the most promising anode materials due to its high specific capacity (3590 mAh g^{-1}) but suffers from poor cycling performance because of large volumetric effects leading to particle pulverization, unstable solid electrolyte interphase (SEI), and electric disconnection. In ASSBs, additional issues such as poor solid-solid contacts and interfacial side reactions between Si and solid-state electrolytes (SSEs) are also hindering their practical application. This review first outlines the prospects and recent research achievements of Si-based anodes with special focuses on various Si structures and composite materials, then analyzes the issues of the electrochemical-mechanical effects, and finally summarizes key factors and promising strategies for further improving the Si-based anodes for high-performance ASSBs.

Keywords

Si-Based Anodes; All-Solid-State Batteries; Interface Issues; Electrochemical-Mechanical Coupling Effects;

1. Introduction

Li-ion batteries (LIBs) are widely used in portable electronic products and electric vehicles (EV) because of their merits of high energy density (HED), long cycle life, and low memory effect [1-3]. Traditional LIBs based on organic liquid electrolytes have safety hazards and are approaching their energy density limits. In comparison, all-solid-state batteries (ASSBs) using less flammable solid-state electrolytes (SSEs) and enabling aggressive high-capacity active materials can meet the persistent pursuit of high safety performance, HED from battery manufacturers, and end consumers [4-5].

Apart from the cathode materials, anode materials play a decisive role in the key performance indicators, especially the energy density, of the LIBs [6-7]. Candidates of anode materials for ASSBs include graphite, Li metal, and alloy anode such as Si, etc [8-10]. Graphite is stable, low-cost, and is the dominating anode material in commercial LIBs. However, with a theoretical specific capacity as low as 372 mAh g^{-1}, graphite presents a limit on the energy density of LIBs [11]. Li metal poses an ultra-high specific capacity (3860 mAh g^{-1}) and a low electrochemical potential (−3.04 V vs SHE), and can greatly increase the energy density of the battery can greatly increase the energy density of the battery when matched with high-voltage cathode materials [12]. However, it compromises the inherent safety promise of ASSBs because of their high flammability and high-probability dendrite formation which can lead to internal short circuits (ISCs) in the cell. In contrast, Si also has a high specific capacity (3590 mAh g^{-1}), but is chemically much more stable and environmentally friendly, and thus is also regarded as a promising and practical anode candidate for HED ASSBs, especially in the near-to-medium term. As shown in Figure 1a, compared to Li metal, Si is advantageous with high annual production and low cost [13]. On the other hand, while Li metal can undergo severe chemical reactions with some SSEs (e.g., sulfide SSEs) [14], forming by-products with low ionic conductivities, Si is chemically much more stable and thus compatible with most SSEs [15]. Moreover, Li metal and Si behave differently under high stacking pressures that are

generally required in the ASSBs manufacturing process to realize close solid-solid contacts [16]. At pressures above 25 MPa [17], Li metal may propagate through the SSEs and lead to short circuits with the cathodes, whereas Si can bear much higher pressures because of its high Young's modulus of 130 GPa [18]. In addition, Li metal is very sensitive to ambient environment and must be processed in gloveboxes or dry rooms [19]. Conversely, Si has good air stability and is suitable for large-scale manufacturing.

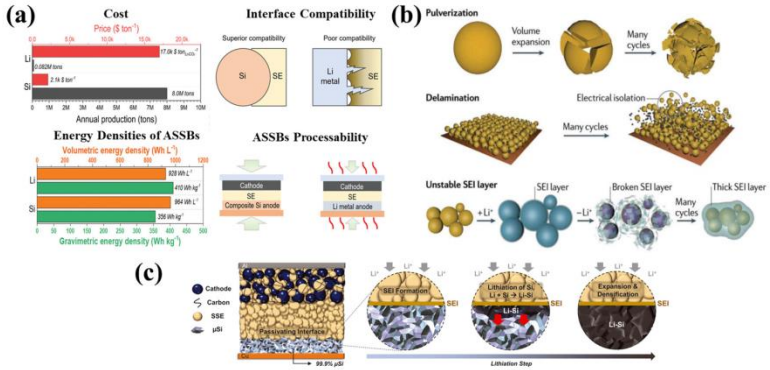

Figure 1: (**a**) General evaluation of the Si-anode and Li-metal anode in ASSBs [19]. "Reproduced with permission from [Cao, Daxian, et al.], [Advanced materials]; published by [WILEY - V C H VERLAG GMBH & CO. KGAA], [2022]" (**b**) Schematic diagram of the bulk effect of Si materials in LIBs [20]. "Reproduced with permission from [Jang Wook Choi et al.], [Nature Reviews Materials]; published by [Springer Nature], [2016]" (**c**) Stabilized SEI between Si anode and electrolyte in ASSBs [21].

Nonetheless, Si has its problems, which mostly originate from the alloying lithiation mechanism and resulting huge volumetric change (up to ≥300%). These problems are illustrated in Figure 1b and include (1) instability in the material level: Si is prone to particle pulverization during the charging and discharging process because of high internal stress; (2) instability in the electrode level: repeated expansion and contraction of the electrode as a whole may lead to electric disconnection and isolation; (3) instability at the interface: the volume effect may cause repeated rupture and excessive growth of surface solid electrolyte interphase (SEI) film, which consumes active Li and increases interfacial impedance. The above three unstable

processes collectively account for the generally observed poor cycling performance of Si anodes. In addition, (4) the rate performance of Si is generally not good because of its low electric conductivity and low Li-ion diffusion coefficient, compared to conventional anode materials such as graphite.

These issues could be intensified or relieved when Si anodes are used in ASSBs. In 2009, Lee et al. first investigated the application of Si nanoparticles in ASSBs with sulfide SSE [22]. In this work, Si nanoparticles demonstrated higher capacity retention in ASSBs than in liquid batteries after the same number of cycles. The volume expansion of Si material during cycling is inevitable. However, sulfide-based SSEs with good mechanical ductility may be beneficial in buffering the volume and stress effects of the Si anodes. Moreover, the cracks formed in the electrodes were reported to be vertical to the current collectors and may not necessarily cause electric connection failure [19, 23]. The problem of the surface instability of Si anode related to excessive SEI growth could also be alleviated in ASSBs. In 2021, Meng's group first reported an ASSB with a carbon-free Si anode that can achieve a capacity of 2800 mAh g−1, a capacity retention of 80% over 500 cycles, and an average columbic efficiency (CE) of > 99.9% at room temperature [21]. As shown in Figure 1c, unlike liquid electrolytes, SSEs do not completely wet the electrode active material, and therefore the excessive growth of SEI and Li-ion consumption during cycling could be largely suppressed by the reduced Si/SSE interface area.

Stimulated by the urgent demand for HED and safe ASSBs, there are some review studies on Si-based anodes for ASSBs from different perspectives. Wang et al. [24] and Pilgun Oh et al. [14] reviewed the developments of HED anodes for ASSBs based on sulfide SSEs. Lewis et al. summarized the progress and promise of alloy anode materials in ASSBs [25]. Hanyu Huo et al. examined the Si-based anodes for ASSBs with different cell and electrode types [26]. Liu et al. discussed the challenges and solutions for Si-based anodes in various LIBs including liquid, quasi-solid, and all-solid batteries [27]. There are also several review reports on Si-based anode for solid-state batteries with a

focus on different SSEs [28-30]. However, only a few reviews mainly focus on the engineering and modification of Si, as well as fundamental issues in Si-based ASSBs.

In this review, we summarize the current development and application of Si anode in ASSBs. The development of Si structures is first introduced, and this includes μm-, nm-, porous Si, thin-film Si, and columnar Si. In addition, we discuss the composition and alloying of Si such as Si/C and Li-Si alloys, etc. Later, we highlight the main factors that could impact the performance of Si in ASSBs, including interface issues and the electrochemical-mechanical coupling effect between Si and SSEs. Finally, we propose some prospects and strategies for the current hindrance that may put forward the research of Si in ASSBs.

2. Si Anodes

2.1. Si anodes with different particle sizes

The size of Si particle anodes is a significant factor influencing their accessible capacities and cycling performances. It has been found that by reducing the size of Si particles to nanometers, the stress concentration caused by volume expansion can be effectively relieved, which can prevent Si from pulverization and powdering. However, the high specific surface area of nm-Si could also bring more side reactions consuming more electrolytes and active Li ions. In addition, large-scale production of nm-Si generally involves complicated processes and demanded equipment, and thus leads to high costs.

In 2018, Dunlap et al. [31] investigated the effect of Si particle sizes on the electrochemical performance of Si/C anode. They found that the Si/C anode prepared with 50 nm Si has a higher first cycle capacity and cycling stability than the Si/C anodes with μm-Si (1-3 μm and 325 mesh Si) because the amorphous carbon matrix was not robust enough for the μm-Si (Figure 2a). Pores and cracks were observed in electrodes with Si/C anode with μm-Si, which could increase the cell impedance. Trevey et al. [32] compared the cycling performances of nm-Si (50-100 nm) and μm-Si (1-5 μm) in ASSBs with sulfide SSE (Figure 2b).

At the same cutoff voltages, the nm-Si anode exhibits a higher discharge capacity and improved cycling performance over the μm-Si anode. Rana et al. [33] investigated the influence of the Si particle size on the rate performance, and found that the rate performance as well as the first cycle capacity of the Si anode improves as the particle size decreases. The surface-to-volume ratio of active materials plays a decisive role in the rate performance. While the larger sizes of μm-Si may be advantageous for achieving higher effective ionic conductivity of the electrodes [34-36], nm-Si with a high surface-area-to-volume ratio can provide more contact sites, more effective reaction interfaces, and thus can achieve higher specific capacity (Figure 2c,d).

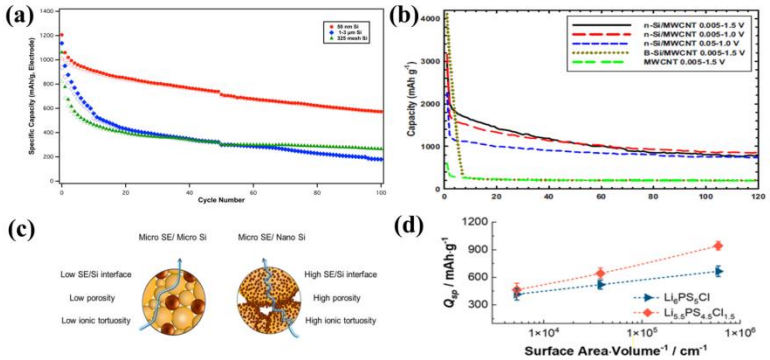

Figure 2: (**a**) Cycling performance of Si-C electrodes[31]. "Reproduced with permission from [Dunlap et al.], [Solid state ionics]; published by [ELSEVIER BV], [2018]" (**b**) Cycling performance of nm-Si and bulk Si under different voltage range [32]. "Reproduced with permission from [Trevey et al.], [Electrochemical and solid state letters]; published by [IOP Publishing], [2010]" (**c**) Schematic showing influence of Si particle size on the performance of the anode composites [33]. (**d**) Dependence of the specific capacity of the composites at a current density of 8 mA·cm−2 on the surface area/volume ratio of the Si particles [33]. "Reproduced with permission from [Moumita Rana et al.], [ACS Energy Letters]; published by [American Chemical Society], [2023]"

Takahashi et al. [23] presented a slurry-mixing method for fabricating Si-75Li2S-25P2S5(LPS) electrodes applicable to the binder-free sheet-type ASSBs. Unlike powder-pressed Si composite anodes, this method is suitable for the current manufacturing process for traditional LIBs and is promising for

large-scale production [26,37-38]. The μm-Si-LPS sheet can deliver a discharge capacity of 3058 mAh g−1 and an initial coulombic efficiency (ICE) of 90%, while the nm-Si-LPS anode using the same preparation method delivers a higher capacity of 3168 mAh g−1 but a lower ICE of 86% (Figure 3a,b). The lower ICE of nm-Si can be ascribed to its higher specific surface area and irreversible side reaction from the surface oxide layer [39]. Jung et al. [38] came to the same conclusion by fabricating sheet-type Si composite anode with a different method of infiltrating electrodes with SSEs in a Li6PS5Cl-ethanol solution (Figure 3c). Both μm-Si and nm-Si anodes showed high first-cycle discharge capacities over 3000 mAh g−1, however, the nm-Si anode delivered a lower ICE than the μm-Si anode. nm-Si demonstrates good electrochemical performances in sulfide-based full-cell ASSBs. In 2022, Zhu et al. [19] designed a high-energy ASSB based on an nm-Si composite anode, a Li2SiOx@S-NMC composite cathode, and a thin sulfide SSE membrane, which shows great potential for industrial applications. The full cell exhibited remarkable cell-level energy densities of 285 and 177 Wh kg−1 at current densities of 0.158 and 3.16 mA cm−2 (Figure 3d). When cycled at C/3, the cell showed good cycling stability for 1000 cycles (Figure 3e). There are also some reports on the performance of full-cell ASSBs using μm-Si. Meng et al. [21] developed an ASSB that utilized a μm-Si anode, a sulfide Li6PS5Cl SSEs, and a LiNi0.8Co0.1Mn0.1O2(NMC811) cathode. The full cell achieved capacity retention of 80% after 500 cycles and an average CE of >99.9% (Figure 3f). A distinctive feature of this battery is that the anode does not contain carbon. Conductive carbon and electrolytes were generally added to ensure good electron and ion transport paths, but they reduced the weight proportion of the active material and the effective electrode loading [31, 40-41]. Eliminating the carbon additives is also favorable in maintaining the stability of the SSE after forming a relatively stable two-dimensional interfacial SEI layer with a limited area. This is in contrast to the uncontrolled growth of the SEI of Si anode during prolonged cycling [42].

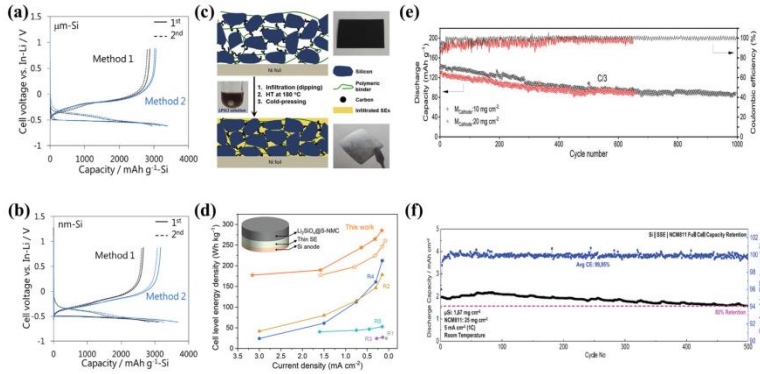

Figure 3: Charge–discharge curves of binder-free (**a**) μm-Si and (**b**) nm-Si half-cells [23]. "Reproduced with permission from [Yamamoto et al.], [Journal of power sources]; published by [ELSEVIER S.A.], [2018]"(**c**) Schematic diagram illustrating the process for infiltration of conventional Si composite electrodes with solution-processable SSEs[38]. "Reproduced with permission from [Kim et al.], [Journal of power sources]; published by [ELSEVIER S.A.], [2019]"(**d**) Cell-level energy density comparison with different ASSBs employing a Si anode[19]. (**e**) Long-term cycling performance of a full cell with an nm-Si composite anode and cathode mass loadings of 10 and 20 mg cm−2[19]. (**f**) Cycle life of μm-Si||SSE||NCM811 cell at room temperature [21].

Although both nm- and μm-Si have shown promise for applications in ASSBs, some problems remain to be addressed. nm-Si may exacerbate the interfacial side reactions with SSEs due to its higher specific surface area, and could also have size-matching issues with micro-sized SSEs, which may result in lower ionic conductivity of the electrode [33]. The electrodes consisting of μm-Si are subject to void formation and porosity change, which affect the cycling performance of the ASSBs [42].

2.2. Si Anodes with Different Structures

2.2.1. Porous Si Anode

Porous materials have many advantages, such as high specific surface area, plenty of active sites, and short ion diffusion distances, which favor good rate performances in LIBs [43]. The porous structure also improves the cycling performance of ASSBs because the connections internal of the porous Si improve the structure integrity and the pores can act as a buffer region accommodating the volume changes during cycling.

Okuno et al. [44-45] investigated the effects of the structure and dispersion method of porous Si on the performances of ASSBs with a sulfide SSE. The nano-porous Si half-cell exhibits an excellent capacity retention of 89% after 50 cycles, with a remaining capacity of approximately 11 times higher than that of the non-porous Si half-cell (Figure 4a) [46]. The improved cycling stability could be because the volume expansion of Si during charging can be accommodated by the nanosized pores and the elastic deformation of the surrounding SSE. Furthermore, Okuno et al. [47] studied the effect of dispersion methods of mechanical milling and hand milling. The highly dispersed nano-porous Si electrodes prepared by mechanical milling enabled capacity retention of 80% up to 150 cycles (Figure 4b). It is believed that the stress generated by the nano-porous Si could be relieved by the elastic deformation of the surrounding electrolyte so that the electrolyte can maintain good contact with the nano-porous Si during the delithiation (Figure 4c). In the case of a low degree of dispersion (prepared by hand milling), the stress generated by the aggregated nano-porous Si may cause the electrolyte to deform plastically, and thus voids can be formed between the nano-porous Si and the electrolyte during delithiation, leading to a reduction in capacity. It should also be noted that the highly dispersed nano-porous Si electrodes (prepared by mechanical milling) exhibited a lower first cycle charge/discharge capacity as well as a lower ICE than that prepared by hand milling. This could be related to the larger contact area between the nano-porous Si and the SSE and the more surface oxide layers of the nano-porous Si prepared by mechanical milling.

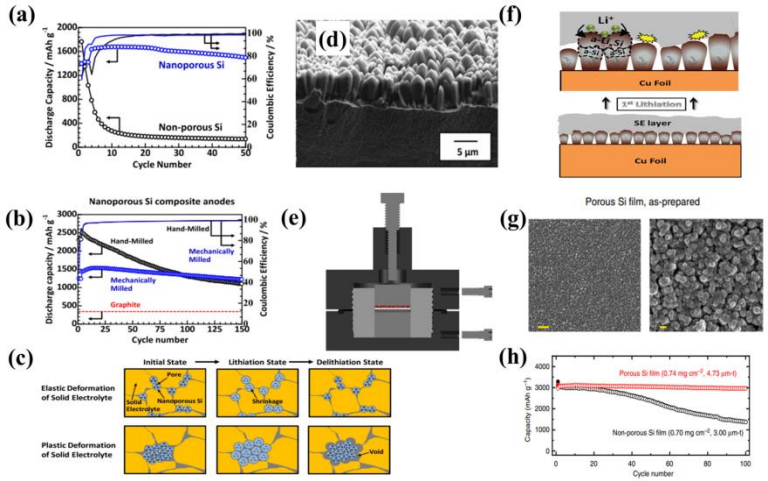

Figure 4: (**a**) Discharge capacity and CE of nanoporous and non-porous Si half-cells [46]. "Reproduced with permission from [Okuno et al.], [Journal of the Electrochemical Society]; published by [IOP Publishing], [2022]" (**b**) Cycle performances of half-cells with mechanically milled and hand-milled nanoporous Si composite anodes [47]. (**c**) Microstructural behavior of mechanically milled and hand-milled nanoporous Si composite anodes [47]. "Reproduced with permission from [Okuno et al.], [Journal of the Electrochemical Society]; published by [IOP Publishing], [2020]" (**d**) SEM image of col-Si as cross-section [48]. "Reproduced with permission from [Cangaz, Sahin, et al.], [Advanced Energy Materials]; published by [WILEY - VCH VERLAG GMBH & CO.], [2020]" (**e**) Illustration of the test cell setup for ASSB cell construction [48]. "Reproduced with permission from [Cangaz, Sahin, et al.], [Advanced Energy Materials]; published by [WILEY - VCH VERLAG GMBH & CO.], [2020]" (**f**)Illustration of morphological and phase changes in col-Si during first lithiation [48]. "Reproduced with permission from [Cangaz, Sahin, et al.], [Advanced Energy Materials]; published by [WILEY - VCH VERLAG GMBH & CO.], [2020]" (**g**) Microscopy images of as-prepared amorphous Si films. [49](**h**) Cycling performances of amorphous Si anode films [49]. "Reproduced with permission from [Junichi Sakabe et al.], [Communications Chemistry]; published by Springer Nature], [2018]"

2.2.2 Columnar Si Anode

Columnar Si is also a promising architecture [50-51]. The low surface area-to-volume ratio of columnar Si favors a high ICE [52]. Cangaz et al. [48] prepared a columnar Si anode (col-Si) by physical vapor deposition process (PVD) and coupled it with a Ni-rich layered oxide cathode to form ASSBs with a Li6PS5Cl SSE. Figure 4d shows the macroscopic structure of col-Si, which

is compactly aligned with each other and vertically connected to the foil. The full-cell delivered a good capacity retention of 82% after 100 cycles. No short circuits were observed even at a relatively high charging rate (1 mA cm−2). The SSE contacts closely with columnar Si but does not penetrate the gaps. This condition facilitates a 2D lateral SEI that can be further stabilized by external pressure (Figure 4e). As shown in Figure 4f, due to the close contacts between Si pillars prohibiting SSE penetration, during the lithiation/delithiation, the volume expansion of col-Si occurs mainly in the longitudinal direction and not inside the anode, which ensures the stability of the SEI during the cycling process. The volumetric effects can also be accommodated by the external pressure.

2.2.3 Film Si Anode

Thin-film Si anodes generally exhibited lower volume expansion than Si particles and also showed promise in ASSBs [53]. Thin film Si anodes have been successively deposited on the surface of the SSEs and show good compatibility[54-56]. Miyazaki et al. [57] reported an amorphous Si(a-Si) film anode for ASSBs with a specific capacity of 2400 mAh g−1 after 100 cycles at 0.1 mA cm−2. To alleviate accumulated stress and enhance cycling performance, Sakabe et al. [49] designed porous amorphous Si films (Figure 4g), which delivered a high capacity of 3128 mAh g−1 and a very low capacity fading rate of 0.06% per cycle even at a high practical areal capacity of 2.3 mAh cm−2 (Figure 4h). Despite its promise, film Si anodes also face limitations and some important factors should be considered. For example, film thickness affects the cycling performance [58], and crystallinity and microstructure affect the ion/electron transport properties.

3. Si-Based Composite Anodes

Compositing Si with other conductive, active, buffering, or coating materials to form Si-based composite anodes is a prevailing strategy to improve the cycling and rate performances of Si towards HED LIBs [59-60]. Herein, the electrochemical performances of Si-based anodes in ASSBs that are mentioned in this section are partly summarized in Table 1.

3.1 Si/C Composite Anodes

Carbon materials in Si/C composite anodes can serve several roles: (1) as coating materials restricting the volume change of Si and preventing the surface side reactions; (2) as conductive substrates/networks improving the conductivity of the electrode; (3) as active material contributing capacity. Following these concepts, many Si/C composite anodes, such as simple Si/C composites [31], core-shell structured Si/C [61], Si/graphene [62], Si/carbon nanofiber (CNF)[63], Si/carbon-nanotube(CNT) [64], have been designed and studied in Si-based anodes in ASSBs.

Poetke et al. [65] prepared Si-C void composites using polyvinyl butyral (PVB) as a void template (Figure 5a,b). The void inside the composite material was designed to provide free space for the volume expansion. And the carbon shell can prevent the Si from direct contact with the electrolyte. As anode in ASSBs, the Si-C void composite exhibited a higher capacity retention and CE compared to it delivered in LIBs with liquid electrolyte because of the inhibited side reactions and suppressed excessive growth of SEI. Han et al. [66] designed a novel μm-Si/SiO2/Li3PO4 (LPO)/C multilayer coated Si composite anode (Figure 5c,d). The SiO2/Li3PO4@C coating layer can provide ionic and electronic fast pathways and improve the integrity of the Si particles. In addition, theoretical calculations suggested that the SiO2 layer could reduce the energy barrier of Li+ transport. The μm-Si/SiO2/LPO/C electrode showed a reversible specific capacity of 2482.1 mAh g−1 with an ICE of 88.7%, and a capacity of 1001.9 mAh g−1 maintained after 200 cycles at 0.5 A g−1. In sharp contrast, the Si@C anode without the SiO2/Li3PO4 interlayer only delivered a capacity of 1130.8 mAh g−1 at 0.2 A g−1 and maintained a capacity of 202 mAh g−1 after 100 cycles (Figure 5e). Recently, a Si@MgO@C monothetic anode electrode was developed by the same group [67], see Figure 5f. The conductive carbon network prepared with a polyacrylonitrile (PAN) backbone facilitated the electron transport and the charge transfer kinetics at the Si/SSEs interfaces. Matched with a poly(ethylene oxide(PEO)/Li1.3Al0.3Ti1.7(PO4)3(LATP) /nano cellulose

(NCF) SSE, the Si@MgO@C electrode exhibited a high capacity of 2576.1 mAh g−1 with a CE of 81.4% during the first cycle, and a remaining capacity of 792.1 mAh g−1 after 200 cycles at a current density of 0.5 A g−1 (Figure 5f,g).

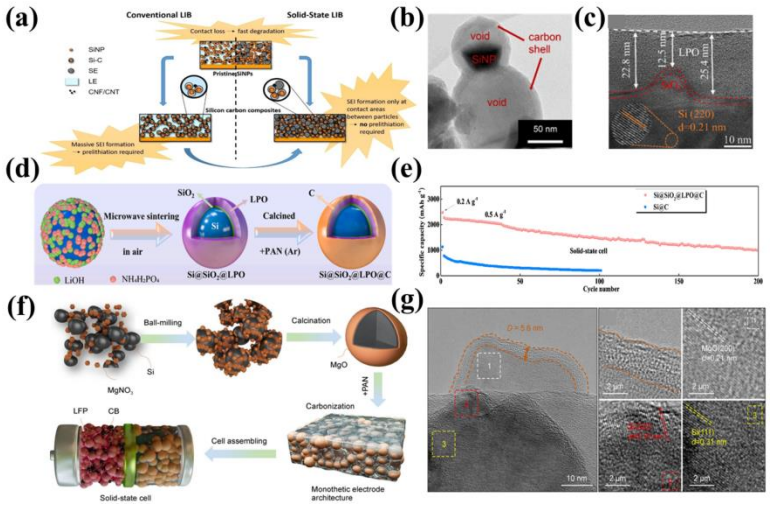

Figure 5: (a) Schematic representation of SiNP and Si-C anode in liquid and solid electrolyte Li-ion batteries [65] (b) TEM images of the Si-C composite [65]. "Reproduced with permission from [Poetke et al.], [BATTERIES JOURNAL]; published by [John Wiley & Sons], [2021]"(c) TEM image of the Si@SiO2@LPO composite material[66]. (d) Schematic illustration of the synthesis processes of Si@SiO2@LPO@C material [66]. (e) The cycling performance of Si@SiO2@LPO@C and Si@C electrodes in a half solid-state cell [66]. "Reproduced with permission from [Gu, Lanhui, et al.], [Energy Storage Materials]; published by [Elsevier], [2022]" (f) Schematic illustration of the synthesis process and potential advantages [67] and (g) TEM image of the Si@MgO particle [67]. "Reproduced with permission from [Xiang Han et al.], [Rare Metals]; published by [Springer Nature], [2023]"

Paik et al. [63] reported Si nanoparticles embedded in carbon nanofiber (CNF) sheathed with Li6PS5Cl (LPSCl) (Si/CNF@LPSCl, Figure 6a) as anode material to achieve high energy density and stable cyclability for sulfide-based ASSBs. The CNF with good mechanical properties and high electronic conductivity [68-69] can build good electronic transport pathways and buffer the volumetric effect of the Si particles. Furthermore, the conformal coating of LPSCl on the fiber enhances the ionic transport and stability at the active

material/SSE interface. The Si/CNF@LPSCl electrode exhibits a capacity retention of 84.3% after 50 cycles at 0.5C in a half cell with a Li-In counter electrode (Figure 6b). Li et al. [70] reported a Si/CNF composite anode electrode with unique vertical 3D architecture, a nanostructured coaxial Si shell coated on vertically aligned carbon nanofibers (VACNFs) (Figure 6c), which act as a good electron intercalation medium. Matched with a good thermal and stable mechanical gel polymer electrolyte, the Si-VACNFs showed a high capacity of 3450 mAh g−1 at 0.36 A g−1 and 1732 mAh g−1 at 3.8 A g−1. Huang et al. [64] designed a Si/CNTs/C anode with a "reinforced concrete" structure (Figure 6d), in which CNT frameworks can prevent disruption of the electron/ion transport pathways, and can mitigate the volume expansion of Si. The Si/CNTs/C@Li6PS5Cl electrode showed a stable capacity of 1226 mA h g−1 after 50 cycles at 50 mA g−1 in a half cell. Kim's group studied the diffusion-dependent [71] electrodes (DDEs) consisting mainly of graphite and Si without SSEs to meet the high power and high energy density requirements of ASSBs [72-73]. Adding high-capacity nm-Si in graphite enabled much thinner coating layers and therefore can shorten the diffusion distance of Li ions in the graphite DDEs and increase the energy density (Figure 6e). Graphite can accommodate the volume change of Si and provide a good electron transport path. The electrode with optimized composition demonstrated high areal and volumetric capacities of 2.76 mAh cm−2 and 935 mAh cm−3 at a high current density of 1.77 mA cm−2. Furthermore, they developed the dry pre-lithiated DDEs (PL-DDEs) by introducing Li metal powder [73], which can supply Li ions to the active materials even in a dry state to enhance the CEs and compensate for the Li loss prolonging the cycling (Figure 6f). In contrast to other methods, this pre-lithiation method is simple and can avoid additional side reactions [74-75]. Compared to the bare DDE, the capacity retention of the ASSBs with the PL-DDE was significantly improved to 85.2% after 200 cycles.

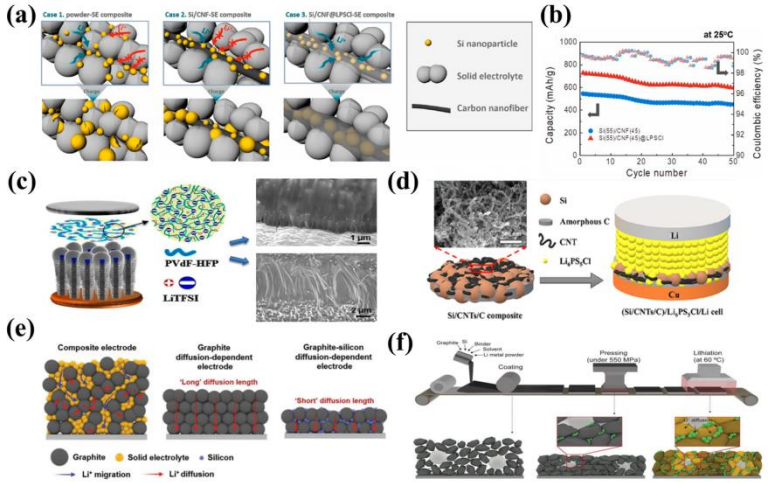

Figure 6: (a)Schematic illustration of the active material and electrolyte composite electrode: Si particle-SSE composite (case 1), Si/CNF-SSE composite (case 2), and Si/CNF@LPSCl-SSE composite (case 3) [63]. (b) Cycling performance of the Si(55)/CNF(45) composite electrode and Si(55)/CNF(45)@LPSCl composite electrode [63]. "Reproduced with permission from [Kim et al.], [Journal of power sources]; published by [ELSEVIER S.A.], [2021]"(c) Schematic illustration of the Si-VACNF half-cell with the gel electrolyte and SEM images of film Si-coated VACNF electrodes after half-cells charge−discharge cycles[70]. "Reproduced with permission from [Gaind P et al.], [Applied Materials]; published by [American Chemical Society], [2015]"(d) Schematic of the Si/CNTs/C composites[64]. "Reproduced with permission from [Liuyi Hu et al.], [ACS Applied Energy Materials]; published by [American Chemical Society], [2022]"(e) Schematic illustration of the structure and Li-ion transport of the composite electrode, the graphite diffusion-dependent electrode, and the graphite–Si diffusion-dependent electrode [72]. "Reproduced with permission from [Kim et al.], [Advanced Energy Materials]; published by [WILEY - VCH VERLAG GMBH & CO.], [2022]"(f) Schematic illustrations of the PL-DDE fabrication process, including the slurry coating, pressing, and dry pre-lithiation process, and the structural and lithiation state changes in each fabrication step[73]. "Reproduced with permission from [Kim et al.], [Advanced Energy Materials]; published by [WILEY - VCH VERLAG GMBH & CO.], [2023]"

3.2 Effects of Carbon Additives for Si anode

Due to the low electronic and ionic conductivity of Si, carbon additives are usually added to the Si anode to ensure electron transport [76-77]. The type and content of carbon additives have a large impact on ASSBs. Okuno et al. [78] systematically

investigated the effects of the content of acetylene black (AB) in the composite anode on the battery performance. They found that a higher content of AB can increase the electronic conductivity and first charging capacity of the anode (Figure 7a), however does not necessarily lead to increased discharge capacity and capacity retention (Figure 7b). Compared to granular AB which is disadvantageous to form a continuous channel, one-dimensional materials like carbon nanotubes (CNTs) and two-dimensional graphene are superior choices for constructing a stable conducting network and are also beneficial for alleviating the volume effects of Si anodes. James et al. [32] compared the effects of multi-walled carbon nanotubes (MWCNTs) and AB on the nm-Si anodes (Figure 7c). After 100 cycles, the capacity of the electrode using MWCNTs was ~100% higher than that using AB (Figure 7d). The reason was ascribed that MWCNTs can provide a higher specific surface area for contact with Si and pose a higher flexibility to adapt to the volume change of Si during the cycling process.

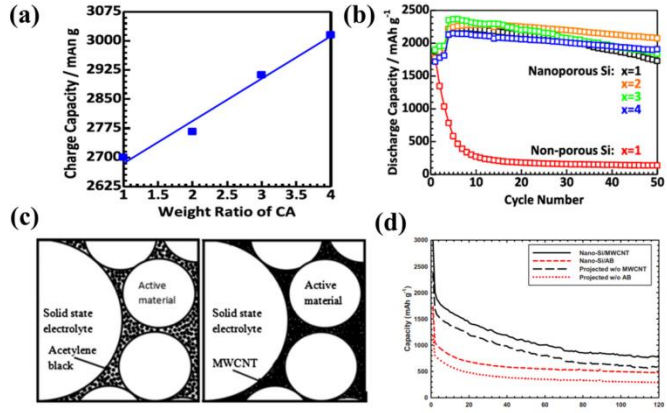

Figure 7: (a) Relationship between carbon additive CA content and initial charge capacity of nanoporous Si half-cells [78]. (b) Cycle performance of nanoporous Si half-cells containing various amounts of CA[78]. "Reproduced with permission from [Okuno, Ryota, et al.], [Electrochemistry communications]; published by [ELSEVIER INC.], [2022]"(c) Different carbon additive in composite anode[32]. (d) Comparison showing superior performance of MWCNT as a conductive additive for ASSBs over AB [32]. "Reproduced with permission from [Trevey et al.], [Electrochemical and solid state letters]; published by [IOP Publishing], [2010]"

3.3 Li-Si Alloy Anode

Compared to pure Si, Li-Si alloys, generally prepared by controlled pre-lithiation of pure Si, pose higher ICE[79-81], improved electronic and ionic conductivity, decreased hardness, and a smaller volume expansion, and therefore can give rise to improved cyclability and rate performances[82-85].

Ji et al. [86] reported a facile lubricant-assisted ball-milling technique [87] using μm-Si powder and Li metal pieces as precursors, and hexane as a solvent, to synthesize an all-electrochem-active pre-lithiated Si and (Figure 8a). The anode was relatively soft, highly conductive, and with a high Li diffusivity, and therefore cannot only enhance the energy density but also prevent electrolyte-related interfacial degradation [21]. As a result, the LixSi–LixSi symmetric cell displayed stable cycling over 320 h at 4 mAh cm−2 (Figure 8b). Zhang et al. [88] tried in situ pre-lithiation by placing the Si in direct contact with the ultra-thin Li foil based on a short-circuiting mechanism under stack pressure. The reversible delithiation capacity and kinetics of the Si anode were improved, which enabled a full cell to achieve a mass-energy density of 402 Wh kg−1 (at a rate of 0.1 C) and stable cycling over a wide temperature range(-30-50°C). Lim's group [89] reported a Li3PS4+Li–Si composite anode for ASSBs to mitigate the short-circuit issues (Figure 8c) caused by Li dendrites and chemo-mechanical failure because of uneven lithiation/delithiation reaction [90]. Non-uniform alloying distribution and Li plating close to the SSE were effectively mitigated by the more pathways for Li ions in the anode (Figure 8d,e). The Li3PS4+Li–Si composite anode exhibited stable cycling performance for 355 cycles without any short-circuit.

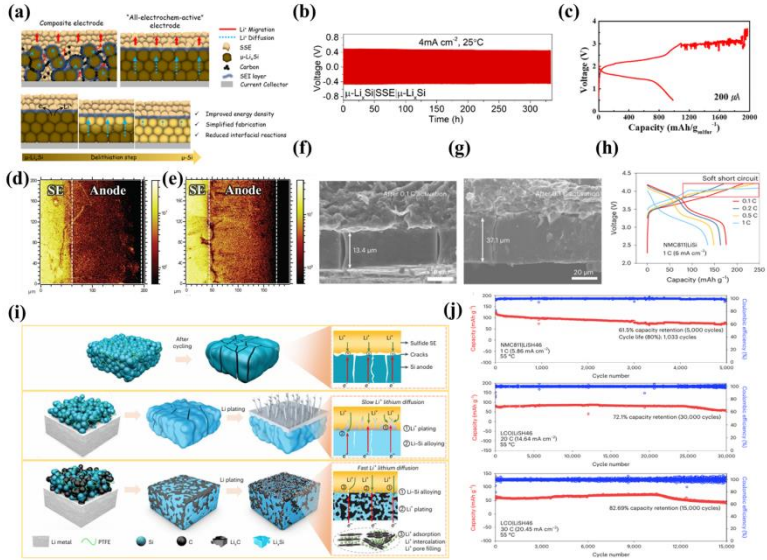

Figure 8: (a) Schematic of a composite electrode design compared with an all-electrochem-active electrode design and the delithiation process of an all-electrochem-active electrode μ-LixSi electrode [86]. (b) The cycling performance of the μ-LixSi|SSE|μ-LixSi symmetric cell [86]. "Reproduced with permission from [Ji, Weixiao, et al.], [Energy Storage Materials]; published by [Elsevier], [2022]"(c) Discharge–charge voltage curves of Li-Si anode[90]. TOF-SIMS data with respect to 7Li+ for Li3PS4+Li–Si alloy cell. (d) after 2.7V charge and (e)after 3.7V charge [89]. "Reproduced with permission from [Kim et al.], [Advanced Science]; published by [Wiley], [2023]" Cross-section SEM image of (f) Si anode (g) Li-Si anode after activation at 0.1 C for 2 cycles[91]. (h) Charge/discharge curves of Li-Si anode at different rates[91](i) Schematic illustration of mechanisms for Si, LiSi, and LiSH46 anodes in ASSBs [91].(j) Long-term cycle of full cells with a LiSH46 anode[91]. "Reproduced with permission from [Wenlin Yan et al.], [Nature Energy]; published by [Springer Nature], [2023]"

Recently, Wu et al. [91] developed a hard carbon stabilized Li-Si alloy anode. Si can form a continuous amorphous film with minimized vacancy and close contact, due to the boundary fusion mechanism during the initial lithiation [92], but is prone to longitudinal cracks after many cycles[93] (Figure 8f). Li-Si alloy was proved effective in suppressing the cracks (Figure 8g), but still subjected to short-circuit issues (Figure 8h). By introducing hard carbon (HC) materials with high disorder, low potential plateaus, and sufficient defects [94], they further restricted the

volume change and cracks in the electrode, as well as the Li dendrite growth. The Li-rich phases Li15Si4 and LiC6 after lithiation formed a three-dimensional conducting network, which can enlarge the active area, and improve the dynamics and structural stability of the electrode (Figure 8i). The hard carbon stabilized Li-Si alloy anode enabled high load and long-cycled sulfide-based ASSBs. Matching with the NMC811 cathode, it delivered a capacity retention of 80% after 1033 cycles, and 61.5% after 5000 cycles (Figure 8j). It can also be cycled at high rates, delivering a capacity retention of 80% after 15,000 cycles at 30 C (Figure 8j). In another study, to avoid Li dendrite growth and short circuits, Huang et al. [95] prepared an all-electrochemically active Si/Li21Si5 composite anode, in which Li21Si5 was uniformly distributed and acted as a continuous soft buffering medium against volume expansion of Si particles. At the same time, it could build excellent ionic/electronic conductive channels in the electrode and therefore can direct Li ions to the Si particles, avoiding the formation of Li dendrites. The LCO/Li3InCl6|SSE|Si/Li21Si5 ASSBs using this composite anode achieved an ICE of 97.8% at 25°C, a first area discharge capacity of 17.9 mAh cm−2 at 55°C, and an anode expansion rate of only 18.1%.

3.4 Other Si-based Composites Anode

Apart from carbon and alloys, many other materials with advantageous properties were also exploited to combine with Si. Among them, conductive polymers [96] and 2D materials with superior mechanical properties than inorganic materials were widely used to stabilize the structure and improve the performances of the Si anodes.

Polyacrylonitrile (PAN) can be made electrically conductive without carbonization by controlling the heat treatment temperature in the appropriate range [97]. Lee et al. [41] utilized PAN as both a binder and conductive additive for Si-rich anodes (70 wt%) and investigated the electrochemical properties of the Si-PAN anode at different cutoff voltages. The Si-PAN half cell delivered a high ICE of around 84% and an initial discharge capacity close to the theoretical capacity of Si (3579 mAh g−1)

in the cutoff voltage range of 5-200 mV, indicating that PAN can effectively mitigate the volume expansion of Si to maintain a stabilized electrode structure. Improved stable cycling can be achieved by increasing the cutoff voltage, which prevents the Si from undergoing large structure changes, although at the cost of capacity loss [32, 98]. After 200 cycles at 60 °C, a cell with a cutoff voltage of 100 mV delivered a capacity retention rate of 77.4%. By adjusting the heat treatment process, PAN can be transformed into amorphous carbon. Using PAN as a precursor, Han et al. [99] prepared a self-integrated Si-N-MXene anode with a Si-N chemical bond between Si and amorphous carbon and an N-MXene chemical bond between MXene and amorphous carbon which can improve the structural stability of the whole electrode. The Si-N-MXene/PEO@LATP/Li half cell delivered an initial capacity of 2305 mAh g−1 with an ICE of 82.02% at a current of 0.2 A g−1. The capacity remained at 881 mAh g−1 after 90 cycles at a current of 0.4 A g−1. For the LiFePO4 (LFP)/PEO@LATP/Si-N-MXene full cell, the first cycle capacity was 1659.2 mAh g−1 at 0.32 A g−1 and no capacity fading was observed after 60 cycles. Zhao et al.[100] developed high-capacity ASSBs using a metal-organic framework(MOF) derived carbon-hosted Si (Si@MOF) anode and a fiber-supported PEO/garnet composite electrolyte. The Si nanoparticles were uniformly encapsulated in a micron-sized MOF carbon skeleton, which could buffer the volume change of Si while providing a conductive channel. Benefiting from this composite strategy, the Si@MOF anode exhibits excellent interfacial stability toward the composite polymer electrolyte and delivers an initial capacity of 1967 mAh g−1 with an ICE of 72.0%. As a comparison, bare Si electrodes showed a low ICE of 50.8%, probably because of a severe interfacial reaction between the unprotected Si and the electrolyte. After 50 cycles, the Si@MOF maintained a reversible capacity of 1442 mAh g−1, which was much higher than that of the bare Si electrode (636 mAh g−1 after 50 cycles).

Table 1: Electrochemical performances of Si-based anodes

Si-based anode	Solid-state electrolytes	Ionic conductivity	Counter electrode and Voltage range	ICE	Current	Cycling performance	Refs
Si-C	Li_6PS_5Cl	/	Li 0.01V-2.00V	73.2%	0.2 mA cm^{-2}	53th: >1000 mAh g^{-1}_{Si-C}	[65]
Si@SiO_2@LPO@C	PEO@LATP	2.86*10^{-5} S cm^{-1} (50°C)	Li 0.005-1.5 V	88.7%	0.5 A g^{-1} (50°C)	200th: 1001.9 mAh g^{-1}	[66]
Si@MgO@C	PEO@LATP@ NCF	1.68*10^{-4} S cm^{-1} (50°C)	Li 0.005-1.5 V	81.4%	0.3 A g^{-1}	100th: 1658.9 mAh g^{-1}	[67]
Si/CNF@LPSCl	Li_6PS_5Cl	/	Li-In 0.05-1.5 V	/	0.5C (25°C)	Capacity retention:83.4%(50 cycles)	[63]
Si-VACNF	Gel Polymer	~2.2*10^{-3} S cm^{-1}	Li 0.05-1.5V	76%	2.6 A g^{-1}	100th: ~1050 mAh g^{-1}	[70]
Si/CNTs/C	Li_6PS_5Cl	2.13*10^{-3} S cm^{-1} (30°C)	Li	59.7%,	50 mA g^{-1}	50th: 1226 mAh g^{-1}	[64]
Si/Graphite	Li_6PS_5Cl	/	Li	/	1.77 mA cm^{-2} (50°C)	Capacity retention:88.8%(100 cycles)	[72]
PL-Si/Graphite	Li_6PS_5Cl	/	Li 0.01-2.0V	~108.9%	0.5C (60°C)	Capacity retention:79.5%(150 cycles)	[73]
LiSH46	Li_6PS_5Cl	/	NCM811 2.5-4.2V	/	1C (55°C)	Capacity retention:61.5%(5000 cycles)	[91]
Si/$Li_{21}Si_5$	Li_6PS_5Cl	/	LCO/Li_3InCl_6 2-4.2 V	97.8%	0.5C (25°C)	Capacity retention:80%(175 cycles)	[95]
Si-PAN	77.5Li_2S-22.5P_2S_5	/	Li-Ln 100mV-1V	~84%	0.1C (60°C)	200th:1606 mAh g^{-1}	[41]
Si-N-MXene	PEO@LATP	3.4*10^{-4} S cm^{-1} (50°C)	Li 0.005-1.5 V	82.02%	0.4 A g^{-1} (50°C)	90th:881 mAh g^{-1}	[99]
Si@MOF	PVDF/PEO/garnet	81*10^{-4} S cm^{-1} (25°C)	Li 0.01-1.5 V	72.0	0.2 A g^{-1} (60°C)	50th:1442 mAh g^{-1}	[100]

4. Key Factors Influencing Performance of Si in ASSBs

4.1. Interface Issues Between Si and SSEs

The interface issues between the Si-based anode and SSEs are a focus of current research. Interfacial issues typically involve chemical/electrochemical stabilities of the SSEs, the surface substances of Si, and side reactions between them. In liquid batteries, the SEI forms on the anode surface due to solvent reduction and may break and re-generate as the Si expands/shrinks in volume, which continuously depletes the Li+ and electrolytes and increases the cell impedance [101]. However, the growth mechanism of SEI in ASSBs also deviates from that in liquid batteries. Unlike the liquid electrolyte, the SSEs will not completely wet the electrode material. By reducing the contact interface between Si and SSEs, the SEI can be limited to a 2D plane, which can be kept relatively stable and inhibit excessive side reactions and Li ions consumption. Meng et al. [21] investigated the interfacial issues of an anode consisting of 99.9 wt% μm-Si (Figure 9a) with Li6PS5Cl as the electrolyte. It was found that the columbic efficiency was low at the first cycle but stabilized afterward, indicating that the interface and the side reactions between the Si and the electrolyte remained stable during cycling. This implied that the volumetric change of the Si does not lead to the continuous formation and growth of the SEI film that is frequently observed in the liquid electrolyte (Figure 9b).

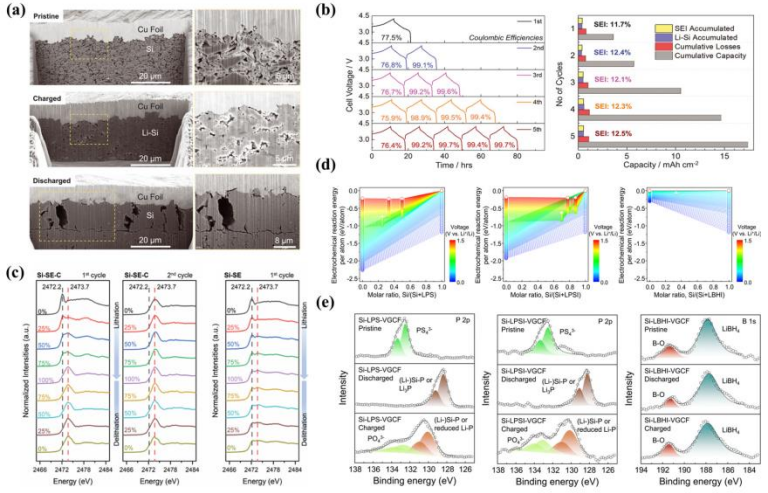

Figure 9: (a) Visualizing lithiation and delithiation of 99.9 wt % Si[21]. (b) Quantifying effects of SEI growth[21](c) Operando XANES investigating the chemical stability of SSE in Si composite anodes [102]. "Reproduced with permission from [Cao, Daxian, et al.], [Advanced Energy Materials]; published by [WILEY - VCH VERLAG GMBH & CO.], [2023]"(d) Calculated electrochemical reaction energies between Si and SSEs [15]. (e) Ex-situ XPS spectra of P 2p from Si+75Li2S-25P2S5(LPS)+VGCF, P 2p from Si+70(0.75Li2S-0.25P2S5)-60LiI(LPSI)+VGCF, and 1s from Si+3LiBH4-LiI(LBHI)+VGCF[15]. "Reproduced with permission from [Huang, Yonglin, et al.], [Energy & environmental science]; published by [RSC Publishing], [2023]"

Although the solid-solid interfacial contact helps to mitigate the overgrowth of SEI, the side reactions and product composition at the Si/SSEs interfaces also play important roles in the performance of ASSBs. Among sulfide, oxide, and polymer SSEs [103], sulfide SSEs have attracted intensive attention due to their high ionic conductivity, good mechanical properties, and simple synthesis processes [104]. However, sulfide SSEs also suffer from low stability at low potentials when matched with Si anodes. The electrochemical stability of SSEs in the Si-based anode and the effect of carbon additives were investigated through in situ XANES by Zhu et al (Figure 9c) [102]. It was found that Li6PS5Cl decomposition mainly occurs during the lithiation of Si in the first cycle and can be exaggerated by the conductive carbon, forming products of Li2S, Li3P, and LiCl [105-106]. The peaks remained unchanged in the delithiation

process, indicating that the decomposition is irreversible and the products are relatively stable. Han et al. [15] performed first-principles calculations to understand the thermodynamic stability between various SSEs and Si. The calculations revealed that a variety of electrochemical reactions could occur between Si and sulfide electrolytes (75Li2S-25P2S5(LPS) and 70(0.75Li_2S-0.25P_2S_5)-60LiI(LPSI)) with an onset potential of 1.5 V vs. Li^+/Li (Figure 9d) and are mainly due to the interactions between Si and P, with the formation of SiP_2, SiP, and Li_5SiP_3 as possible products. In contrast, the stability between Si and 3$LiBH_4$-LiI(LBHI) is much better and reactions occur only in a very narrow range of potentials (0.38-0.36 V vs. Li^+/Li). The reaction mechanism was further analyzed by XPS tests (Figure 9e), which showed that sulfide SSEs can decompose into products such as Li_3P and can also react with Si to form products such as SiP, whereas no side reaction occurs between Si and LiBHI. As a result, a high-performance solid-state Si anode with 96.2% ICE and excellent electrochemical stability can be realized by using LBHI SSE.

4.2. Electrochemical-Mechanical Coupling Effects

A full understanding of electrochemical-mechanical coupling effects in Si-based ASSBs is key to elucidating the failure mechanism of Si anodes. Volume expansion of the Si can lead to stress and strain evolution and variation of the electrode structure, which may decrease the effective contacts, increase the impedance, and therefore cause cycling decay of ASSBs.

Appropriate external pressure can suppress the volume expansion of Si, which is effective in maintaining the interfacial contact of Si/SSEs and facilitating the cycling of the battery. In 2012, Lee et al. [107] reported the effect of applied external stress on the electrochemical performance of nm-Si. The capacity of the Si half cell nearly reaches the theoretical capacity when the applied pressure reaches 3 MPa. With an increased external pressure of 230 MPa (Figure 10a), the capacity of the battery is only half of that of the external pressure of 3 MPa when the applied pressure is 230 MPa. However, the increase in external pressure also is beneficial to the cycling stability

performance of the battery. The capacity of the battery with an external pressure of 3 MPa decreases rapidly to 76.1% of its initial value after 8 cycles. In contrast, the capacity of half cells with an external pressure of 150 MPa and 230 MPa still retains 87.3% and 99% after 20 cycles, respectively (Figure 10b). Higher external pressure decreases the capacity because constraining the volume expansion of Si material may result in incomplete lithiation of Si. And, lower external pressure affects the cycling performance because the electrode integrity degrades faster because of unrestrained volume change of electrodes. Therefore, a trade-off between capacity and cycling performance exists when choosing the optimized magnitude of external pressure [24]. Yamamoto et al. [40] found that as the pressure increased from 50 MPa to 75 MPa, the initial discharge capacity of Si|Li-In half cell increased from 2849 mAh/g to 3412 mAh/g with also a higher capacity retention of 64% after 140 cycles. By comparing the structure changing of the Si anode under different pressures, it was suggested that a higher pressure of 75 MPa can form large perpendicular cracks which relieves the stress and results in stable cycling instead of fine cracks.

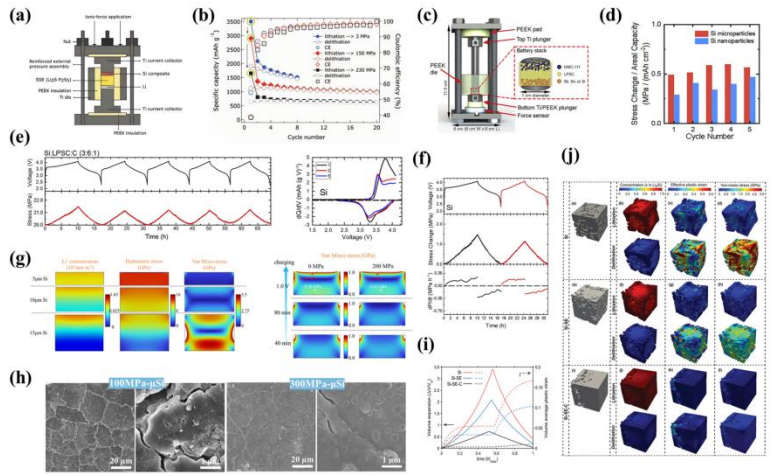

Figure 10: (a) Schematic of the ASSBs design [107]. (b) Electrochemical performance and CE of solid-state nano-Si anode cycled at a rate of C/20 under pressures of 3, 150, and 230 MPa [107]. "Reproduced with permission from [Piper, D. M et al], [Journal of the Electrochemical Society]; published by [IOP Publishing], [2012]"(c) Schematic of the cell assembly and the anode/LPSC/cathode stack within the cell[108]. (d)Particle size effect of Si on

stress [108]. (e) Electrochemical cycling and in situ stress measurements of Si anode composites in full cells [108]. (f)The galvanostatic curves in the top panel, the stress change in the middle panel, and the derivative of the stress with time in the bottom panel [108] "Reproduced with permission from [Han, Sang Yun et al], [Joule]; published by [Cell Press], [2021]"(g) Simulation for Si anodes with different Si-loading and stack pressures [109]. (h) The SEM images of the anode surface in close contact with the current collector side for the 100MPa and 300MPa μm-Si after 50 cycles [109]. "Reproduced with permission from [Tao, Jianming et al], [Energy Storage Materials]; published by [Elsevier], [2024]"(i) Volume expansion and contraction along with the volume average of effective plastic strain for different anode materials during the lithiation and delithiation[102]. (j) Structure evolution investigation of three types of the anode at pristine, end of lithiation, and delithiation stage. [102]. "Reproduced with permission from [Cao, Daxian et al], [Advanced Energy Materials]; published by [WILEY - VCH VERLAG GMBH & CO.], [2023]"

McDowell et al. [108] investigated the internal stress evolution of the Si anode during cycling in an ASSB with argyrodite-type SSE and NMC cathode (Figure 10c). The stress of the Si anode increases gradually during charging, reaches a maximum, and then decreases during discharging (Figure 10d). During the following cycles, the stress immediately after discharging does not return to the original value but increases somewhat, indicating that the electrode structure is irreversibly damaged. They also investigated the effect of Si particle size on stress. It was found that nanometer particles induced smaller stress change compared to microparticles, as the volumetric effect of smaller particles could be better accommodated by the internal voids between them (Figure 10e). Based on the dP/dt curves (stress change/time), it can be found that the rate of stress change is maximum at the end of charging and close to zero at the end of discharging. At the beginning of charging, the rate of stress change is small because the pores inside the electrodes buffer the stress change due to the volume expansion. However, the void diminishes with the charging process, which leads to an increased rate of stress change (Figure 10f). Zhu et al. [102] investigated strain and stress change of three types of anodes, Si, Si+SSE, and Si+SSE+C (Figure 10j). During the cycling, the plastic deformation and stress of the Si anode are the largest, while those of the Si+SSE electrode are smaller and those for the Si+SSE+C are the smallest, suggesting that both the SEE and C can alleviate the stress generated in Si. The deformation of the Si anode does not return to the original volume ratio (zero) at the

end of lithiation, indicating that the electrode structure is irreversibly damaged (Figure 10i). Recently, Tao et al. [109] investigated the performance decay of μm-Si anode in sulfide-based ASSBs with different Si loading and different external pressures. As the Si loading increases, the Li-ion concentration gradient and the hydrostatic stress gradient inside the Si electrode also increase, causing uneven stress distribution, and making the electrode susceptible to cracking, which is harmful to the cycling performance of the battery. Through the simulation, it was found that the applied pressure helps to reduce the unevenness of the stress inside the electrode, which reduces the possibility of electrode structure damage (Figure 10g). They found that the applied pressure has little effect on Li+ diffusion, but is advantageous to reduce the internal stress, the degree of electrode cracking, and the Li^+ concentration gradient (Figure 10h).

5. Summary and Perspective

With the merits of high specific capacity, high chemical stability, and low cost, Si anodes hold great promise to fulfill the promise of intrinsic safety and high energy density of ASSBs. This review summarizes the advantages and drawbacks, as well as the current research progress of Si and Si-based composite anodes with various structures and compositions, discusses the key issues of interface instability between Si and SSEs, and probes the electrochemical-mechanical coupling effects of Si-based anodes. The main perspectives and suggestions are summarized as follows:

(1) Since the designs, formulas, manufacturing processes, and working conditions of ASSBs deviate, the basic physiochemical requirements and application standards of Si anode remain not converged. Various Si anode structures with different electrode formulas and testing conditions have been investigated. Key influencing factors include the sizes, dimensions, and architectures. In general, μm-Si are prone to pulverization, void formation, and porosity change of the electrodes, which affect its cycling performance. nm-Si is beneficial because of better structure integrity, however, when applied in composite anode

with SSEs, may exacerbate the interfacial side reactions with SSEs due to its higher specific surface area, and could also have size-matching issues with micro-sized SSEs. Porous structured Si is an attractive choice because the connections between domains can improve the whole integrity and the pores can act as a buffer region accommodating the volume changes of the Si during cycling. Columnar Si array is also a promising architecture with volumetric changing at the lateral direction and a stable 2D lateral SEI that can be further stabilized by external pressure.

(2) Compositing Si with other materials proves an effective strategy to improve the cyclability and rate performances of Si. Carbon is a promising consistency in Si-based composite materials since it can serve as a coating material to restrict the volume change of Si, as a conductive network to improve the conductivity of the electrode, and as an active material contributing capacity. Li-Si alloys pose higher ICE, improved electronic and ionic conductivity, decreased hardness, and a smaller volume expansion, and therefore represent an attractive solution. However, simple, low-cost, and safe pre-lithiation or alloying methods and processes are required for wide application. Apart from carbon and alloys, conductive polymers and 2D materials with superior mechanical properties than inorganic materials were widely used to stabilize the structure and improve the performances of the Si anodes.

(3) The interface issues between the Si-based anode and SSEs are a focus of current research. The growth mechanism and composition of SEI in ASSBs deviate from that in liquid batteries. By reducing the contact interface between Si and SSEs, the SEI can be limited to a 2D plane, which can be kept relatively stable and inhibit excessive side reactions and successive Li ions consumption. Volume expansion of the Si can lead to stress and strain evolution, which can cause cracks, voids, and degradation of the electrode structure that is harmful to the cycling performance of Si anodes. Appropriate external pressure can suppress the volume expansion of Si, and maintain stabilized interfacial contact of Si/SSEs, and thus is an important factor in assessing the performances of the Si anodes.

To conclude, motivated by the urgent pursuit of safe and HED ASSBs, Si-based anodes have attracted intensive attention and witnessed significant advances in their performances and understanding of the failure mechanisms. Nonetheless, there remain many issues hindering their practical application. Some of these issues could be naturally solved by the progress on highly electrochemically stable and mechanically favorable SSEs. But others are inherent to Si itself and need to be conquered by collaboration from academia to industry. We envision that the perspectives and suggestions in this review could shed some light on the design and application of high-performance Si-based anodes accelerating the commercialization of ASSBs.

References

1. Goodenough JB, Park KS. The Li-ion rechargeable battery: A perspective. J. Am. Chem. Soc. 2013; 135: 1167–1176.
2. Grey CP, Hall DS. Prospects for lithium-ion batteries and beyond—A 2030 vision. Nat. Commun. 2020; 11: 62-79.
3. Jiang B, Sun Z, Liu M. China's energy development strategy under the low-carbon economy. Energy. 2010; 35: 4257–4264.
4. Kato Y, Hori S, Saito T, Suzuki K, Hirayama M, et al. High-power all-solid-state batteries using sulfide superionic conductors. *Nat.* Energy. 2016; 1: 16030.
5. Vedhanarayanan B, Seetha Lakshmi KC. Beyond lithium-ion: Emerging frontiers in next-generation battery technologies. Front. Batter. Electrochem. 2024; 3: 1377192.
6. Chan CK, Peng H, Liu G, McIlwrath K, Zhang XF, et al. High-performance lithium battery anodes using silicon nanowires. Nat. Nanotechnol. 2008; 3: 31–35.
7. Xiao Q, Fan Y, Wang X, Susantyoko RA, Zhang Q. A multilayer Si/CNT coaxial nanofiber LIB anode with a high areal capacity. Energy Environ. Sci. 2014; 7: 655–661.
8. Höltschi L, Jud F, Borca C, Huthwelker T, Villevieille C, et al. Study of Graphite Cycling in Sulfide Solid Electrolytes. J. Electrochem. Soc. 2020; 167: 110-558.

9. Bloi LM, Hippauf F, Boenke T, Rauche M, Paasch S, et al. Mechanistic insights into the reversible lithium storage in an open porous carbon via metal cluster formation in all solid-state batteries. Carbon. 2022; 188: 325–335.
10. Zhao M, Zhang J, Costa CM, Lanceros-Mendez S, Zhang Q, et al. Unveiling Challenges and Opportunities in Silicon-Based All-Solid-State Batteries: Thin-Film Bonding with Mismatch Strain. Adv. Mater. 2024; 36: 2308590.
11. Kang K, Meng YS, Breger J, Grey CP, Ceder G. Electrodes with high power and high capacity for rechargeable lithium batteries. Science. 2006; 311: 977–980.
12. Chen L, Fan X, Ji X, Chen J, Hou S, et al. High-Energy Li Metal Battery with Lithiated Host. Joule. 2019; 3: 732–744.
13. *Mineral Commodity Summaries 2021*; US Geological Survey: Reston, VA, USA, 2021.
14. Oh P, Yun J, Choi JH, Saqib KS, Embleton TJ, et al. Development of High-Energy Anodes for All-Solid-State Lithium Batteries Based on Sulfide Electrolytes. Angew. Chem. Int. Ed. Engl. 2022; 61: 202201249.
15. Huang Y, Shao B, Wang Y, Han F. Solid-state silicon anode with extremely high initial coulombic efficiency. Energy Environ. Sci. 2023; 16: 1569–1580.
16. Wang Y, Liu T, Kumar J. Effect of Pressure on Lithium Metal Deposition and Stripping against Sulfide-Based Solid Electrolytes. ACS Appl. Mater. Interfaces. 2020; 12: 34771–34776.
17. Doux JM, Nguyen H, Tan DHS, Banerjee A, Wang X, et al. Stack Pressure Considerations for Room-Temperature All-Solid-State Lithium Metal Batteries. Adv. Energy Mater. 2019; 10: 1903253.
18. Hopcroft MA, Nix WD, Kenny TW. What is the Young's Modulus of Silicon? J. Microelectromechan. Syst. 2010; 19: 229–238.
19. Cao D, Sun X, Li Y, Anderson A, Lu W, et al. Long-Cycling Sulfide-Based All-Solid-State Batteries Enabled by Electrochemo-Mechanically Stable Electrodes. Adv. Mater. 2022; 34: 2200401.
20. Li JY, Xu Q, Li G, Yin YX, Wan LJ, et al. Research progress regarding Si-based anode materials towards

practical application in high energy density Li-ion batteries. Mater. Chem. Front. 2017; 1: 1691–1708.
21. Tan DHS, Chen YT, Yang H, Bao W, Sreenarayanan B, et al. Carbon-free high-loading silicon anodes enabled by sulfide solid electrolytes. Science. 2021; 373: 1494–1499.
22. Trevey J, Jang JS, Jung YS, Stoldt CR, Lee SH. Glass-ceramic Li_2S-P_2S_5 electrolytes prepared by a single step ball billing process and their application for all-solid-state lithium-ion batteries. Electrochem. Commun. 2009; 11: 1830–1833.
23. Yamamoto M, Terauchi Y, Sakuda A, Takahashi M. Slurry mixing for fabricating silicon-composite electrodes in all-solid-state batteries with high areal capacity and cycling stability. J. Power Sources. 2018; 402: 506–512.
24. Wang X, He K, Li S, Zhang J, Lu Y. Realizing high-performance all-solid-state batteries with sulfide solid electrolyte and silicon anode: A review. Nano Res. 2022; 16: 3741–3765.
25. Lewis JA, Cavallaro KA, Liu Y, McDowell MT. The promise of alloy anodes for solid-state batteries. Joule. 2022; 6: 1418–1430.
26. Huo H, Janek J. Silicon as Emerging Anode in Solid-State Batteries. ACS Energy Lett. 2022; 7: 4005–4016.
27. Liu H, Sun Q, Zhang H, Cheng J, Li Y, et al. The application road of silicon-based anode in lithium-ion batteries: From liquid electrolyte to solid-state electrolyte. Energy Storage Mater. 2023; *55*: 244–263.
28. Song A, Zhang W, Guo H, Dong L, Jin T, et al. A Review on the Features and Progress of Silicon Anodes-Based Solid-State Batteries. Adv. Energy Mater. 2023; 13: 2301464.
29. Zhan X, Li M, Li S, Pang X, Mao F, et al. Challenges and opportunities towards silicon-based all-solid-state batteries. Energy Storage Mater. 2023; 61: 102875.
30. Sun Z, Yin Q, Chen H, Li M, Zhou S, et al. Building better solid-state batteries with silicon-based anodes. Interdiscip. Mater. 2023; 2: 635–663.
31. Dunlap NA, Kim S, Jeong JJ, Oh KH, Lee SH. Simple and inexpensive coal-tar-pitch derived Si-C anode composite for all-solid-state Li-ion batteries. Solid State Ion. 2018; 324: 207–217.

32. Trevey JE, Rason KW, Stoldt CR, Lee SH. Improved Performance of All-Solid-State Lithium-Ion Batteries Using Nanosilicon Active Material with Multiwalled-Carbon-Nanotubes as a Conductive Additive. *Electrochem.* Solid State Lett. 2010; 13: A154–A157.
33. Rana M, Rudel Y, Heuer P, Schlautmann E, Rosenbach C, et al. Toward Achieving High Areal Capacity in Silicon-Based Solid-State Battery Anodes: What Influences the Rate-Performance? ACS Energy Lett. 2023; 8: 3196–3203.
34. Liang J, Xiao K, Fang R, Rawal A, Lennon A, et al. High volumetric capacity nanoparticle electrodes enabled by nanofluidic fillers. Energy Storage Mater. 2021; 43: 202–211.
35. Gueon D, Ju MY, Moon JH. Complete encapsulation of sulfur through interfacial energy control of sulfur solutions for high-performance Li-S batteries. Proc. Natl. Acad. Sci. USA 2020; 117: 12686–12692.
36. Jain R, Lakhnot AS, Bhimani K, Sharma S, Mahajani V, et al. Nanostructuring versus microstructuring in battery electrodes. Nat. Rev. Mater. 2022; 7: 736–746.
37. Xu J, Liu L, Yao N, Wu F, Li H, et al. Liquid-involved synthesis and processing of sulfide-based solid electrolytes, electrodes, and all-solid-state batteries. Mater. Today Nano. 2019; 8: 100048.
38. Kim DH, Lee HA, Song YB, Park JW, Lee SM, et al. Sheet-type Li_6PS_5Cl-infiltrated Si anodes fabricated by solution process for all-solid-state lithium-ion batteries. J. Power Sources. 2019; 426: 143–150.
39. Miyazaki R, Ohta N, Ohnishi T, Takada K. Anode properties of silicon-rich amorphous silicon suboxide films in all-solid-state lithium batteries. J. Power Sources. 2016; 329: 41–49.
40. Yamamoto M, Terauchi Y, Sakuda A, Kato A, Takahashi M. Effects of volume variations under different compressive pressures on the performance and microstructure of all-solid-state batteries. J. Power Sources. 2020; 473: 228-595.
41. Dunlap NA, Kim J, Guthery H, Jiang CS, Morrissey I, et al. Towards the Commercialization of the All-Solid-State Li-ion Battery: Local Bonding Structure and the Reversibility of Sheet-Style Si-PAN Anodes. J. Electrochem. Soc. 2020; 167: 060522.

42. Stephan AK. Perfect combination: Solid-state electrolytes and silicon anodes? Joule. 2021; 5: 3074–3075.
43. Feng K, Ahn W, Lui G, Park HW, Kashkooli AG, et al. Implementing an in-situ carbon network in Si/reduced graphene oxide for high performance lithium-ion battery anodes. Nano Energy. 2016; 19: 187–197.
44. Okuno R, Yamamoto M, Kato A, Terauchi Y, Takahashi M. Microstructures of nanoporous-Si composite anodes in sulfide-based all-solid-state lithium-ion batteries. IOP Conf. Ser. Mater. Sci. Eng. 2019; 625: 012012.
45. Okuno R, Yamamoto M, Terauchi Y, Takahashi M. Stable cyclability of porous Si anode applied for sulfide-based all-solid-state batteries. Energy Procedia. 2019; 156: 183–186.
46. Okuno R, Yamamoto M, Kato A, Takahashi M. High Cycle Stability of Nanoporous Si Composites in All-solid-state Lithium-ion Batteries. J. Electrochem. Soc. 2022; 169: 080502.
47. Okuno R, Yamamoto M Kato A, Takahashi M. Stable Cyclability Caused by Highly Dispersed Nanoporous Si Composite Anodes with Sulfide-based Solid Electrolyte. J. Electrochem. Soc. 2020; 167: 140-522.
48. Cangaz S, Hippauf F, Reuter FS, Doerfler S, Abendroth T, et al. Enabling High-Energy Solid-State Batteries with Stable Anode Interphase by the Use of Columnar Silicon Anodes. Adv. Energy Mater. 2020; 10: 2001320.
49. Sakabe J, Ohta N, Ohnishi T, Mitsuishi K, Takada K. Porous amorphous silicon film anodes for high-capacity and stable all-solid-state lithium batteries. Commun. Chem. 2018; 1: 24.
50. Fridman K, Sharabi R, Elazari R, Gershinsky G, Markevich E, et al. A new advanced lithium ion battery: Combination of high performance amorphous columnar silicon thin film anode. *Electrochem.* Commun. 2013; 33: 31–34.
51. Wada M, Yin J, Tanabe E, Kitano Y, Tanase S, et al. Nanocomposite Anode Materials for Li-ion Batteries. Electrochemistry. 2003; 71: 1064–1066.
52. Piwko M, Thieme S, Weller C, Althues H, Kaskel S. Enabling electrolyte compositions for columnar silicon anodes in high energy secondary batteries. J. Power Sources. 2017; 362: 349–357.

53. Takamura T, Ohara S, Uehara M, Suzuki J, Sekine K. A vacuum deposited Si film having a Li extraction capacity over 2000 mAh/g with a long cycle life. J. Power Sources. 2004; 129: 96–100.
54. Phl N, Roozeboom F, Rah N, Baggetto L. 3-D integrated all-solid-state rechargeable batteries. *Adv*. Mater. 2007; 24: 19.
55. Lethien C, Zegaoui M, Roussel P, Tilmant P, Rolland N, et al. Micro-patterning of LiPON and lithium iron phosphate material deposited onto silicon nanopillars array for lithium ion solid state 3D micro-battery. Microelectron. Eng. 2011; 88: 3172–3177.
56. Huo H, Sun J, Chen C, Meng X, He M, et al. Flexible interfaces between Si anodes and composite electrolytes consisting of poly(propylene carbonates) and garnets for solid-state batteries. J. Power Sources. 2018; 383: 150–156.
57. Miyazaki R, Ohta N, Ohnishi T, Sakaguchi I, Takada K. An amorphous Si film anode for all-solid-state lithium batteries**.** J. Power Sources. 2014; 272: 541–545.
58. Chen C, Li Q, Li Y, Cui Z, Guo X, Li H. Sustainable Interfaces between Si Anodes and Garnet Electrolytes for Room-Temperature Solid-State Batteries. ACS Appl. Mater. Interfaces. 2018; 10: 2185–2190.
59. Xu K, Liu X, Guan K, Yu Y, Lei W, et al. Research Progress on Coating Structure of Silicon Anode Materials for Lithium-ion Battery. ChemSusChem. 2021; 14: 5135–5160.
60. Mazouzi D, Lestriez B, Roue L, Guyomard D. Silicon Composite Electrode with High Capacity and Long Cycle Life. J. Electrochem. Solid-State Lett. 2009; 12: A215–A218.
61. Poetke S, Hippauf F, Baasner A, Dörfler S, Althues H, et al. Nanostructured Si−C Composites As High-Capacity Anode Material for All-Solid-State Lithium-Ion Batteries. Batter. Supercaps. 2021; 4: 1323–1334.
62. Gu L, Han J, Chen M, Zhou W, Wang X, et al. Enabling robust structural and interfacial stability of micron-Si anode toward high-performance liquid and solid-state lithium-ion batteries. Energy Storage Mater. 2022; 52: 547–561.
63. Han X, Xu M, Gu LH, Lan CF, Chen MF, et al. Monothetic and conductive network and mechanical stress releasing

layer on micron-silicon anode enabling high-energy solid-state battery. Rare Met. 2024; 43: 1017–1029.
64. Kim J, Kim C, Jang I, Park J, Kim J, et al. Si nanoparticles embedded in carbon nanofiber sheathed with Li_6PS_5Cl as an anode material for all-solid-state batteries. J. Power Sources. 2021; 510: 230-425.
65. Pandey GP, Klankowski SA, Li Y, Sun XS, Wu J, et al. Effective Infiltration of Gel Polymer Electrolyte into Silicon-Coated Vertically Aligned Carbon Nanofibers as Anodes for Solid-State Lithium-Ion Batteries. ACS Appl. Mater. Interfaces. 2015; 7: 20909–20918.
66. Hu L, Yan X, Fu Z, Zhang J, Xia Y, et al. A "Reinforced Concrete" Structure of Silicon Embedded into an In Situ Grown Carbon Nanotube Scaffold as a High-Performance Anode for Sulfide-Based All-Solid-State Batteries. ACS Appl. Energy Mater. 2022; 5: 14353–14360.
67. Kim JY, Jung S, Kang SH, Park J, Lee MJ, et al. Graphite-Silicon Diffusion-Dependent Electrode with Short Effective Diffusion Length for High-Performance All-Solid-State Batteries. Adv. Energy Mater. 2021; 12: 2103108.
68. Lee J, Jin D, Kim JY, Roh Y, Lee H, et al. Dry Pre-Lithiation for Graphite-Silicon Diffusion-Dependent Electrode for All-Solid-State Battery. Adv. Energy Mater. 2023; 13: 2300172.
69. Yan W, Mu Z, Wang Z, Huang Y, Wu D, et al. Hard-carbon-stabilized Li–Si anodes for high-performance all-solid-state Li-ion batteries. Nat. Energy. 2023; 8: 800–813.
70. Zhang Z, Sun Z, Han X, Liu Y, Pei S, et al. An all-electrochem-active silicon anode enabled by spontaneous Li–Si alloying for ultra-high performance solid-state batteries. Energy Environ. Sci. 2024; 17: 1061–1072.
71. Han X, Zhou W, Chen M, Chen J, Wang G, et al. Interfacial nitrogen engineering of robust silicon/MXene anode toward high energy solid-state lithium-ion batteries. J. Energy Chem. 2022; 67: 727–735.
72. Zhang L, Lin Y, Peng X, Wu M, Zhao T. A High-Capacity Polyethylene Oxide-Based All-Solid-State Battery Using a Metal-Organic Framework Hosted Silicon Anode. ACS Appl. Mater. Interfaces. 2022; 14: 24798–24805.

73. Ng SH, Wang J, Konstantinov K, Wexler D, Chew SY, et al. Spray-pyrolyzed silicon/disordered carbon nanocomposites for lithium-ion battery anodes. J. Power Sources. 2007; 174: 823–827.
74. Zhang YQ, Xia XH, Wang XL, Mai YJ, Shi SJ, et al. Silicon/graphene-sheet hybrid film as anode for lithium ion batteries. Electrochem. Commun. 2012; 23: 17–20.
75. Song T, Xia J, Lee JH, Lee DH, Kwon MS, et al. Arrays of Sealed Silicon Nanotubes As Anodes for Lithium Ion Batteries. Nano Lett. 2010; 10: 1710–1716.
76. Song T, Lee DH, Kwon MS, Choi JM, Han H, et al. Silicon nanowires with a carbon nanofiber branch as lithium-ion anode material. J. Mater. Chem. 2011; 21: 12619–12621.
77. Kim JY, Park J, Lee MJ, Kang SH, Shin DO, et al. Diffusion-Dependent Graphite Electrode for All-Solid-State Batteries with Extremely High Energy Density. ACS Energy Lett. 2020; 5: 2995–3004.
78. Forney MW, Ganter MJ, Staub JW, Ridgley RD, Landi BJ. Prelithiation of silicon-carbon nanotube anodes for lithium ion batteries by stabilized lithium metal powder (SLMP). Nano Lett. 2013; 13: 4158–4163.
79. Xu H, Li S, Zhang C, Chen X, Liu W, et al. Roll-to-roll prelithiation of Sn foil anode suppresses gassing and enables stable full-cell cycling of lithium ion batteries. Energy Environ. Sci. 2019; 12: 2991–3000.
80. Chen J, Fan X, Li Q, Yang H, Khosh MR, et al. Electrolyte design for LiF-rich solid–electrolyte interfaces to enable high-performance microsized alloy anodes for batteries. Nat. Energy. 2020; 5: 386–397.
81. Kwon HJ, Hwang JY, Shin HJ, Jeong MG, Chung KY, et al. Nano/Microstructured Silicon-Carbon Hybrid Composite Particles Fabricated with Corn Starch Biowaste as Anode Materials for Li-Ion Batteries. Nano Lett. 2020; 20: 625–635.
82. Okuno R, Yamamoto M, Kato A, Takahashi M. Performance improvement of nanoporous Si composite anodes in all-solid-state lithium-ion batteries by using acetylene black as a conductive additive. Electrochem. Commun. 2022; 138: 107-288.

83. Zhu Y, Hu W, Zhou J, Cai W, Lu Y, et al. Prelithiated Surface Oxide Layer Enabled High-Performance Si Anode for Lithium Storage. ACS Appl. Mater. Interfaces. 2019; 11: 18305–18312.
84. Ge M, Cao C, Biesold GM, Sewell CD, Hao SM, et al. Recent Advances in Silicon-Based Electrodes: From Fundamental Research toward Practical Applications. Adv. Mater. 2021; 33: e2004577.
85. Ham SY, Sebti E, Cronk A, Pennebaker T, Deysher G, et al. Overcoming low initial coulombic efficiencies of Si anodes through prelithiation in all-solid-state batteries. Nat. Commun. 2024; 15: 29-91.
86. Iwamura S, Nishihara H, Ono Y, Morito H, Yamane H, et al. Li-rich Li-Si alloy as a lithium-containing negative electrode material towards high energy lithium-ion batteries. Sci. Rep. 2015; 5: 80-85.
87. Li X, Kersey-Bronec FE, Ke J, Cloud JE, Wang Y, et al. Study of Lithium Silicide Nanoparticles as Anode Materials for Advanced Lithium Ion Batteries. ACS Appl. Mater. Interfaces. 2017; 9: 16071–16080.
88. Sakuma M, Suzuki K, Hirayama M, Kanno R. Reactions at the electrode/electrolyte interface of all-solid-state lithium batteries incorporating Li-M (M = Sn, Si) alloy electrodes and sulfide-based solid electrolytes. Solid State Ion. 2016; 285: 101–105.
89. Zhou L, Zuo T, Li C, Zhang Q, Janek J, Nazar LF. $Li_{3-x}Zr_x(Ho/Lu)_{1-x}Cl_6$ Solid Electrolytes Enable Ultrahigh-Loading Solid-State Batteries with a Prelithiated Si Anode. ACS Energy Lett. 2023; 8: 3102–3111.
90. Ji W, Zhang X, Liu M, Ding T, Qu H, et al. High-performance all-solid-state Li-S batteries enabled by an all-electrochem-active prelithiated Si anode. Energy Storage Mater. 2022; 53: 613–620.
91. Cloud JE, Wang Y, Li X, Yoder TS, Yang Y, et al. Lithium silicide nanocrystals: Synthesis, chemical stability, thermal stability, and carbon encapsulation. Inorg. Chem. 2014; 53: 11289–11297.
92. Fan Z, Ding B, Li Z, Chang Z, Hu B, et al. In-Situ prelithiation of electrolyte-free silicon anode for sulfide all-solid-state batteries. eTransportation. 2023; 18: 100-277.

93. Kim M, Kim MJ, Oh YS, Kang S, Shin TH, et al. Design Strategies of Li-Si Alloy Anode for Mitigating Chemo-Mechanical Degradation in Sulfide-Based All-Solid-State Batteries. Adv. Sci. 2023; 10: e2301381.
94. Oh YS, Kim M, Kang S, Park JY, Lim HT. Redox activity of Li_2S-P_2S_5 electrolyte inducing chemo-mechanical failure in all-solid-state batteries comprising sulfur composite cathode and Li-Si alloy anode. *Chem.* Eng. J. 2022; 442: 136229.
95. Li H, Huang X, Chen L, Zhou G, Zhang Z, et al. The crystal structural evolution of nano-Si anode caused by lithium insertion and extraction at room temperature. Solid State Ion. 2000; 135: 181–191.
96. Yang L, Chen H, Jiang H, Wei YJ, Song W, et al. Failure mechanisms of 2D silicon film anodes: In Situ observations and simulations on crack evolution. Chem. Commun. 2018; 54: 3997–4000.
97. Xie L, Tang C, Bi Z, Song M, Fan Y, et al. Hard Carbon Anodes for Next-Generation Li-Ion Batteries: Review and Perspective. *Adv.* Energy Mater. 2021; 11: 2101650.
98. Lin HY, Li CH, Wang DY, Chen CC. Chemical doping of a core-shell silicon nanoparticles@polyaniline nanocomposite for the performance enhancement of a lithium ion battery anode. Nanoscale. 2016; 8: 1280–1287.
99. Janus R, Natkański P, Wach A, Drozdek M, Piwowarska Z, et al. Thermal transformation of polyacrylonitrile deposited on SBA-15 type silica. J. Therm. Anal. Calorim. 2012; 110: 119–125.
100. Obrovac MN, Krause LJ. Reversible Cycling of Crystalline Silicon Powder. J. Electrochem. Soc. 2007; 154: A103.
101. He Y, Jiang L, Chen T, Xu Y, Jia H, et al. Progressive growth of the solid–electrolyte interphase towards the Si anode interior causes capacity fading. Nat. Nanotechnol. 2021; 16: 1113–1120.
102. Cao D, Ji T, Singh A, Bak S, Du Y, et al. Unveiling the Mechanical and Electrochemical Evolution of Nanosilicon Composite Anodes in Sulfide-Based All-Solid-State Batteries. Adv. Energy Mater. 2023; 13: 2203969.
103. Zhao N, Khokhar W, Bi Z, Shi C, Guo X, et al. Solid Garnet Batteries. Joule. 2019; 3: 1190–1199.

104. Boulineau S, Courty M, Tarascon JM, Viallet V. Mechanochemical synthesis of Li-argyrodite Li_6PS_5X (X = Cl, Br, I) as sulfur-based solid electrolytes for all solid state batteries application. Solid State Ion. 2012; 221: 1–5.
105. Schwietert TK, Arszelewska VA, Wang C, Yu C, Vasileiadis A, et al. Clarifying the relationship between redox activity and electrochemical stability in solid electrolytes. Nat. Mater. 2020; 19: 428–435.
106. Tan DHS, Wu EA, Nguyen H, Chen Z, Marple MAT, et al. Elucidating Reversible Electrochemical Redox of Li_6PS_5Cl Solid Electrolyte. ACS Energy Lett. 2019; 4: 2418–2427.
107. Piper DM, Yersak TA, Lee SH. Effect of Compressive Stress on Electrochemical Performance of Silicon Anodes. J. Electrochem. Soc. 2012; 160: A77–A81.
108. Han SY, Lee C, Lewis JA, Yeh D, Liu Y, et al. Stress evolution during cycling of alloy-anode solid-state batteries. Joule. 2021; 5: 2450–2465.
109. Tao J, Han J, Wu Y, Yang Y, Chen Y, et al. Unraveling the performance decay of micro-sized silicon anodes in sulfide-based solid-state batteries. Energy Storage Mater. 2024; 64: 103082.

The book Surfaces, Interfaces, and Coatings Technology is a compilation of recent research advances covering fundamental aspects of chemistry and physics occurring at surfaces and interfaces.

VIDE LEAF

E-book Available
@
www.videleaf.com